Exciton-Polaritons in Thermal Equilibrium: From Bose-Einstein Condensation to Exciton-Polaritonics

by

Yongbao Sun

B.S. Chemical Physics, University of Science and Technology of China
(2010)

Submitted to the Department of Chemistry
in partial fulfillment of the requirements for the degree of

Doctor of Philosophy in Chemistry

at the

MASSACHUSETTS INSTITUTE OF TECHNOLOGY

February 2017

© Massachusetts Institute of Technology 2017. All rights reserved.

Signature redacted

Author . . . .
Yongbao Sun
Department of Chemistry

Signature redacted   January 27, 2017

Certified by. .   . . .
Keith A. Nelson
Haslam and Dewey Professor of Chemistry
Thesis Supervisor

Signature redacted

Accepted by . .   . .
Robert W. Field
Haslam and Dewey Professor of Chemistry
Chair, Department Committee on Graduate Theses

This doctoral thesis has been examined by a Committee of the
Department of Chemistry as follows:

Professor Moungi G. Bawendi... Signature redacted

Chairman, Thesis Committee
Lester Wolfe Professor of Chemistry

Signature redacted

Professor Keith A. Nelson......................................

Thesis Supervisor
Haslam and Dewey Professor of Chemistry

Signature redacted

Professor Jianshu Cao ....

Member, Thesis Committee
Professor of Chemistry

3

Exciton-Polaritons in Thermal Equilibrium:

From Bose-Einstein Condensation to Exciton-Polaritonics

by

Yongbao Sun

Abstract

Coherent control has been at the heart of the study of physical chemistry. Great advancement has been achieved in the past few decades in coherent control of classical systems by using spatially and temporally shaped electromagnetic waves. In this dissertation, we extend the concept of coherent control to a purely quantum mechanical collective system, namely, microcavity exciton-polariton Bose-Einstein condensates.

Microcavity exciton-polaritons, hereafter simply polaritons, are bosonic quasiparticles formed in a resonant semiconductor microcavity by coupling the excitonic polarizabilities in quantum wells to the transverse mode of the confined optical field in the cavity. The light-matter dual nature allows direct control of polaritons through either their excitonic or photonic components. By utilizing the fact that polariton-exciton and polariton-polariton interactions are repulsive, all-optical control of polaritons was realized. By shaping the intensity fronts of the optical beam incident on a microcavity, the potential landscape felt by polaritons can be easily tailored. This is the key ingredient of this dissertation work.

The light-matter dual nature endows polaritons a very small effective mass that is one hundred million times less than that of a hydrogen atom, leading to the observation of quantum phenomena such as condensation, superfluidity and quantized vortices at temperatures ranging from tens of Kelvin up to room temperatures. However, debates persist over whether the observed phenomena can be related to Bose-Einstein condensation because polaritons are not in thermal equilibrium. By applying all-optical trapping to a high-quality microcavity structure, polaritons at both spatial and thermal equilibrium were achieved across a broad range of densities and bath temperatures, as evidenced by the observed equilibrium Bose-Einstein distributions. A phase diagram for Bose-Einstein condensation of polaritons was produced for the first time, which agrees with the predictions of basic quantum gas theory.

The thermalization behavior depends crucially on the interactions among polaritons. By changing the underlying excitonic/photonic fractions in polaritons, the interaction strength of polaritons can be varied, leading to control between nonequilibrium and equilibrium behavior of the polariton gas. The interactions also play

a crucial role in polaritonic device operations. However, an accurate measurement of the polariton-polariton interaction strength has been not possible because of the difficulty in separating polaritons and excitons that are created by the same optical excitation. After propagating to the center of a sufficiently large optically induced annular trap, polaritons were separated from the incoherent populations of free carriers and hot excitons. The polariton interaction strength was then extracted from energies measured as a function of the polariton density. The measured interaction strength was about two orders of magnitude larger than previous theoretical estimates, putting polaritons squarely into the strongly interacting regime.

Optical control can also be utilized to directly manipulate polariton condensates. By tailoring the size and pumping intensity of the optical trap, polariton condensates can be switched among different high-order modes and the homogeneous condensate mode. The redistribution of spatial densities is accompanied by a superlinear increase in the emission intensity as a function of excitation power, implying that polariton condensates in this geometry could be exploited as a multistate switch. The parameters for reproducible switching between the high-order states in the optical trap have been measured experimentally, giving us a phase diagram for the mode switching. It will serve well to calibrate the implementation of an exciton-polaritonic multistate switch.

Thesis Supervisor: Keith A. Nelson
Title: Haslam and Dewey Professor of Chemistry

Acknowledgments

I am indebted to many outstanding individuals who provided invaluable support in different aspsects throughout my time at MIT. It would never be close to a point to finish my PhD without these people.

First and foremost, I would express my sincere gratitude to my research advisor Keith Nelson. Since the first meeting with him before joining the group, I have been significantly influenced by his enthusiasm in all aspects of science. His encyclopedic knowledge of optics and spectroscopy guided me through most of the research work presented in this dissertation. Besides, he has always been super encouraging which makes me feel I am much much better than I think of myself. I came join the group with some early success in computational condensed matter physics, but no knowledge in experimental physics and optics. After one year of hard time in learning, I started to doubt myself that I might not be capable of being an experimentalist as I thought, and even considered finding another research group and switching back to computational physics that I did in the college. However, it was the talk with Keith that made me decide to stay. I'm very grateful for his constant encouragement and support for scientific research and through family hardships. His patience in teaching me English grammars also allows me to have great improvement in scientific writing during the graduate study.

Professor David Snoke at the University of Pittsburgh acts as a second advisor throughout my PhD. We got to know each other when he took his sabbatical in my subgroup at the beginning of my second year, and have had a great collaboration since then. His proved expertise in exciton-polaritons and Bose-Einstein condensation guided me through formulating research ideas and designing experiments. Numerous discussions with David were always more than helpful for new measurements and analysis. David also helped me run though uncountable revisions of all my paper manuscripts in the prolonged battles with referees. It is such a distinct privilege to have him during my PhD.

Patrick Wen has been a fantastic mentor for my first three years. He taught me

7

from how to fold the lens tissue and clean up the optics all the way to align the entire 2D setup. We read through Yamamoto's lecture notes on condensation together, and discussed possible experimental ideas. I cannot imagine if I was able to survive without his teaching with great patience.

Yoseob Yoon joined the condensate subgroup three years ago. Chapter 7, in particular, would not be possible without his help. His questions always push me to learn more. I would also thank him for producing the nice-looking microcavity structure used in this dissertation.

Several collaborators contributed to the research in this dissertation with their expertise and advice. Professor Hakan Tureci and his student Saeed Khan at Princeton University provided detailed numerical simulations described in Chapter 7, which allow me to obtain a deeper understanding of the observed patterns described in Chapter 7. Professor David Snoke's students Gangqiang Liu and Mark Steger were extremely helpful in discussing experimental details, such as what thermal material I should use to mount the sample structure. They both visited MIT during my PhD. During his one-week trip, Mark helped a great deal in the calibration of the long-lifetime sample structure, which is extremely important given the quantitative characteristic of the work in this dissertation. Gangqiang was around for a month when we tried out the squeezed state generation and detection in optical traps. Professor Thomas Feurer at University of Bern was the person who introduced to me the world of quantum optics. The two-week stay at Bern with his students Baenz Bessire, Stefan Lerch, Sasha Schwarz, Manuel Unternaehrer and Professor Andre Stefanov allowed me to grasp the details in entanglement generation and detection. It saved me countless hours in designing the entangled-photon generation setup.

The Nelson group has been a tremendously great team to work with, for both science and fun. I would like to thank Xibin Zhou, Vasily Temnov and Zhao Chen. We were left in the small office in my first two years and 'had to' hang out ourselves for meals. Benjamin Ofori-Okai has been a good friend to talk about basketball and watch NBA in the midnight together. I would also like to thank Jian Lu for his help and accompany through many overnight THz measurements, and Prasahnt

Sivarajah for these long discussions regarding Rydberg polaritons and cavity quantum electrodynamics in THz frequencies. The rest of past and present Nelson group members also contribute to this dissertation in different aspects including Alexei Maznev, Harold Hwang, Longfang Ye, Felix Hofmann, Sharly Fleischer, Brad Perkins, Stephanie Teo, Colby Steiner, Samuel Teitelbaum, Jeffery Eliason, David Veysset, Doug Shin, Ilana Porter, Leora Cooper, Yaqing Zhang, Xian Li, Ryan Duncan, Ronny Huang, Yu-Hsiang Cheng, Pooja Tyagi, Brandt Pein, Jake Siegel, Keiichi Nakagawa, Deniz Bozyigit, Dmitro Martynowych, Frank Gao, and Tristan Pitt. I would also like to thank the group administrative assistant, Li Miao, for her help in placing equipment purchase orders and processing reimbursement.

A great community of friends surrounded me throughout my time at MIT. Xun Cai had been my roommate for about three years before he moved out to welcome his first child. Qing Liu is my meal mate in the past three years, and we have a great time preparing for job interviews together. Yan Gao has been my close friend since college times, and I cannot recall how many phone calls we have talking about optics, life and job hunting. I also cannot leave out Xu Zhang for our discussions of history, buddism and literature.

I am also thankful for my parents and grand-parents for their support and love throughout my life to pursue my PhD overseas. I feel deeply sorry to my grandpa that I was not able to be around when he was in bed and wanted to see me for the last time in his life, and now we cannot see each other forever. My father passed away three weeks before my thesis defense, and it was such a pity for not being able to have him around for my thesis defense and commencement. He was such a great father to back me up throughout my childhood until my wedding, and it would never be possible for me to receive the PhD degree without his support. Grandpa and dad, I believe you would also be in great joy to see me in regalia. I would also like to thank my parents-in-law for their constant encouragement and support, and their understanding in all difficult situations I faced up.

Finally, I owe my special gratitudes to my wife Jie Zhou. Although we have been physically separated by two hundred and fifty miles in the past six years, it has never

stopped her from always being right there to listen my complaints, encourage me through troughs, push me to achieve more, and here to celebrate my success. We laugh, we cry, we love, and we walk into the future together, hand in hand!

<div align="right">
Yongbao Sun

January 25, 2017
</div>

Contents

14

Appendices

Appendix A Generation and characterization of polarization-entangled photon states   **235**

List of Figures

Chapter 1

Introduction

1.1 Motivation and Background

The evolution of semiconductor electronics in the past few decades has signicantly advanced information processing and communication technologies, leading to increases in the CPU clock speed by more than five orders of magnitude. While higher speed of information processing is still in demand, the performance of conventional electronics has reached a fundamental bottleneck because of the ineffciency in the heat transfer and electronic resistive-capacitive delays in the subsystems [1]. Photonics have been demonstrated as a possible alternative, and great efforts have been devoted to the research of photonic circuits [2, 3, 4]. Recently, excitonics that utilizes electrostatically bound electron-hole pairs in solids is emerging as an interconnect between photonics and electronics. In excitonics, signal processing and communication can possibly be implemented with no need to undergo the conversion process in the information reception and processing. Moreover, the zero net charge of excitons could possibly incur no signal delays. Excitonic switches at high speeds have already been demonstrated with AlAs/GaAs coupled quantum wells [5, 6]. However, due to their heavy effective masses, which are typically about a tenth of the electron mass in vacuum, and limited lifetime, which is typically in the range of picoseconds to a few nanoseconds, excitons can only propagate about 1 nm up to 100 nm. This places significant challenges in device fabrication. Longer-lifetime indirect excitons have been proposed and demon-

strated as a way to solve this problem[7, 8]. However, the dark nature of indirect excitons does not allow direct control through optical means.

Exciton-polaritonics based on microcavity polaritons is emerging as a new candidate [9]. Microcavity polaritons are bosonic quasiparticles in resonant planar semiconductor microcavities: by placing quantum wells (QWs) at the antinodes of the confined modes in an optical microcavity, excitons in the QWs strongly couple to the confined photonic fields, leading to normal mode splitting into upper and lower branches of polaritons. The resulting polaritons have a combination of properties of both light and matter: they have a very light effective mass, on the order of 10^{-4} that of excitons, and can propagate over macroscopic distances up to millimeter length scale; their photonic components permit an easy access and manipulation of their properties; their excitonic fractions govern the interactions among polaritons, and by using a wedged cavity where the cavity width varies across the sample, we can tune the photon energy across the exciton resonance, thus leading to control of the interaction strength among polaritons.

The information content of polaritonics largely relies on the independent degrees of freedom of polaritons. Polaritons carry two spins from their photonic components, and can be directly accessed by controlling the polarization states (σ^+ and σ^-) of a resonant excitation beam. This opens up the way for the development of spin-based logic devices [10]. The angular momenta of polariton states can also be readily manipulated by using an incident field with spatially engineered Laguerre-Gaussian modes. Based on this, high-order vortices in microcavities have been reported [11, 12, 13].

This dissertation is focused on the development of optical trapping of polaritons, and the study of thermodynamic properties of the optically trapped polaritons. Polariton condensates at both spatial and thermal equilibrium were realized to study the phase boundary of the Bose-Einstein transition. The trapped condensates at different trapping geometries and powers are found to enable a possible all-optical multistate switch. By taking advantange of spatial separation between trapped polaritons and pump light, the interaction strength between polaritons is experimentally measured

24

for the first time. The result suggests the efficiency of the polaritonic devices could be much greater than anticipated.

In the remainder of this section, we summarize key results in this dissertation work. The significance of the results will also be presented.

1.1.1 Polariton condensates at thermal equilibrium

Exciton-polariton systems offer unique advantages for fundamental studies and applications based on their high-temperature condensation and on facile control and study of their properties through optical excitation and emission, but all previous experiments on polariton condensates have observed them quite far from equilibrium. This has lead to debate about whether polariton condensation is intrinsically a nonequilibrium effect, and it has limited the application of extensive theoretical results that describe atom condensates in equilibrium. By using very high-Q microcavities which yield long (almost 300 ps) polariton lifetimes, greatly exceeding the thermalization time of around 50 ps, we have directly observed equilibrium Bose-Einstein distributions of polaritons all the way up the condensate threshold density across a wide range of bath temperatures. From these distributions we extracted meaningful values of the chemical potential which yielded reliable values of the absolute polariton density. We were also able to verify the temperature-density phase diagram for the condensation transition.

Our results open up exciting new possibilities for studying and understanding condensates. Given that much of the theory of condensates has been done for a thermalized Bose gas, our results mean that all of this equilibrium theory can now be applied to polariton condensates. This is especially important in understanding interactions and many-body effects within the condensate. The spectrum of light emission from polaritons directly reveals the occupation numbers of the excited states at different energies, something that is not possible for atom condensates. At densities well above the condensation threshold, we see deviations from the Bose-Einstein distribution that clearly indicate many-body effects on the occupation numbers. Since we can assume equilibrium, the forms of the distributions we measure can be directly com-

pared to equilibrium many-body theories. That is a nontrivial task for theorists, but it is a hopeless task if the system is out of equilibrium, in which case there is no way to know whether the spectral features observed are due to many-body renormalization or nonequilibrium. The fact that we can vary the interaction strength and move the gas from equilibrium to out of equilibrium means that it is now possible to study the transition from nonequilibrium to equilibrium by varying the interaction strength. In atom gas experiments, while some nonequilibrium effects have been studied, the effect of nonequilibrium on the excitation spectrum has not been possible to study. Furthermore, given the flexibility in tailoring the potential landscape polaritons feel by shaping the geometry of an incident optical beam, quantum simulations of equilibrium many-body problems [14] such as quasi-Nambu-Goldstone modes [15, 16] and quantum phase transitions [17] are now also encouraging. The equilibrium polariton condensates also enable studies of the Higgs boson [18, 19] and evolution of early universe [20, 21, 22, 23] on the tabletop that can usually only be tested using particle accelerators.

1.1.2 Interaction strength among polaritons

It is no overstatement to say that the measurement of polariton-polariton interaction strengths has the potential to revolutionize all of polariton physics. For well over a decade, all of the theory of polaritons has assumed that they are weakly interacting in the low-density limit, based on theoretical calculations of the exciton-exciton interaction strength. By allowing polaritons to propagate over 20 μm to the center of a laser-generated annular trap, we were able to separate the polariton-polariton interactions from polariton-exciton interactions. By studying the energy renormalization of the polariton dispersions as the polariton density is increased, we experimentally obtained the first rigorous, quantitative measurement of the absolute value of the polariton-polariton interaction strength, and found it to be two orders of magnitude stronger than the theoretical prediction [24]. This will force a reanalysis of all previous results. It also promises to have great impact on the nonlinear optics field in general, as the nonlinearity which we report here is several orders of magnitude larger

26

than previous reported optical $\chi^{(3)}$ values in optical materials, albeit over a narrow wavelength range.

1.1.3 High-order modes in annular traps

Trapped polariton condensates from 0D to 1D and 2D in various geometries have been studied, and polaritonic switching and transistor behaviors have also been demonstrated. However, a complete study of the interactions among trapped states is missing, and the understanding of their formation mechanisms is mostly qualitative. We studied the entire family of trapped condensate modes in an annular optical trap. By varying the pump ring size and intensity, we observed that the trapped modes can be switched on successively. On the other hand, these modes are very stable as long as the pump conditions do not change. This indicates the trapped polariton condensates can be exploited for multistate switches, potentially enabling highly sensitive control over very large optical responses. We have also measured the mode boundaries, knowledge of which could serve well for device applications. Our theoretical study based on the generalized Gross-Pitaevskii equation suggests the switching between modes is determined by the balance between the outward flux loss of the polariton wavefunction and the overlap with pump-generated excitons which determines the amplification. The simulated phase boundary for the lowest-threshold mode agreed well with our experiments. We believe our results will open up exciting new possibilities for studying optically trapped polaritons and implementing polaritons in optical traps for device applications.

1.2 Outline of Dissertation

This dissertation is organized as follows. In Chapter 2, collective quantum phenomena including Bose-Einstein condensation (BEC) and superfluidity are reviewed. Chapter 2 focuses on BEC by first introducing BEC in the ideal non-interacting gas, followed by the Bogoliubov theory of BEC in the interacting gas. The semiclassical approach, the Grosso-Pitaevskii equation, is also presented. The chapter is concluded

by a review of observations of BEC of different particles in various systems. Chapter 3, the optical properties of quantum-well excitons and microcavity structures are reviewed in detail, followed by discussions of classical and quantum-mechanical treatments of exciton-polaritons in semiconductor microcavities. A comparison to phonon-polaritons is included in the end of the chapter. In Chapter 4, the details of experimental methodologies are described, including spatial shaping of the excitation beam, and the near-field and far-field photoluminescence imaging technique. In the same chapter, the experimental development of all-optical trapping of polaritons is presented. In Chapter 5, the thermodynamics and kinetics of polaritons and their condensates are discussed, followed by the observation of polariton condensates at both thermal and spatial equilibrium in a long-lifetime microcavity structure, and a discussion of the phase boundary of BEC. In Chapter 6, direct measurement of the polariton-polariton interaction strength is presented. Possible mechanisms that could explain the large value of the interaction strength observed in our experiments are also discussed. In Chapter 7, coherent control of polariton condensates with shaped optical beams and the possibility of using polariton condensates in the optical trap as a multistate switch are discussed. The dissertation is concluded by an outlook of future directions presented in Chapter 8.

Chapter 2

Bose-Einstein Condensation: Theory and Experiments

In a system of bosons in thermal equilibrium, when the interparticle spacing becomes comparable to their thermal de Broglie wavelength, the system undergoes Bose-Einstein condensation (BEC). Analogous to classical condensation where water vapor condenses on a cold surface and the motion of water molecules becomes highly restricted, the individual bosons in a Bose-Einstein condensate become completely correlated, and the system can be described as a single-particle wavefunction with a definitive phase factor. BEC is also accompanied by spontaneous emergence of long-range off-diagonal order, i.e., coherence. When interactions among the underlying particles are turned on, more peculiar properties such as dissipationless propagation and quantum depletion show up. Although BEC was predicted by Satyendra Nath Bose and Albert Einstein back 1924 [25, 26], experimental realization was hindered largely due to the fact that BEC phase only exists at extremely low temperatures, on the order of 10^{-7} K in atomic systems. With the advent of laser cooling and magneto-optical trapping, BEC of a very dilute and cold rubidium atomic gas was first realized in 1995 [27, 28, 29] at a temperature of 170 nK by Eric Cornell and Carl Wieman in Joint Institute for Laboratory Astrophysics (JILA), and later the same year by Wolfgang Ketterle here at MIT with sodium atoms cooled to 2 μK. For their pioneering work in the achievement of BEC in dilute gases of alkali atoms, and

early fundamental studies of the properties of the condensates, Eric Cornell, Wolfgang Ketterle and Carl Wieman were awarded the Nobel Prize in Physics in 2001. Since then, BEC has become an incredibly rapidly growing field of research, and has been observed with various atomic species [30] as well as quasiparticles in solids, including magnons in thin-film magnetic materials [31] and exciton-polaritons in semiconductor microcavities [32, 33, 34, 35]. Beyond being of fundamental interest, some effects of BEC have been exploited in applications. Because of their unique coherence properties, atomic condensates have been widely used in quantum optics and recently in quantum information processing for high-precision measurements [36]. The rising research in exciton-polariton condensates has also proved them to be an important complement to atomic condensates, and could be implemented in all-optical devices with better performance compared to contemporary electronic and photonic devices due to their light-matter dual nature [37].

The topic of Bose-Einstein condensation is treated in most textbooks on statistical mechanics and specialized journals on Bose-Einstein condensation itself, such as Refs. [38, 39, 40, 41]. In this chapter, only key physics of BEC that is relevant to this dissertation work will be presented. We start with a review of a simple model of non-interacting gas in Section 2.1. Despite its simplicity, the model is able to capture several important properties of BEC such as critical temperature and density, and condensation fraction. A discussion of trapped BEC in different dimensions will also be included. Section 2.3 describes the Bogoliubov theory of weakly interacting Bose gases. The effects of interactions on the ground state energy and excitation spectrum will also be discussed. We introduce the microscopic and macroscopic descriptions of BEC in Section 2.4. The spatial coherence and long-range off-diagonal order are derived based on field theories. The Gross-Pitaevskii equation, which is of a nonlinear Schrödinger equation form, is also covered. Lastly, the experimental realization of atomic BEC is reviewed, and some other systems in which condensation has been observed are briefly discussed.

2.1 Bose-Einstein Condensation of An Ideal Gas

For a system composed of non-interacting bosons in thermal equilibrium at a temperature T, the average occupation number of a single-particle state with an energy of E is given by the Bose-Einstein distribution

$$f(E) = \frac{1}{e^{(E-\mu)/k_B T} - 1} \tag{2.1}$$

where k_B is the Boltzmann constant, and μ is the chemical potential which is the amount of free energy incurred when adding or removing a particle from the system. In the high-temperature or low-density regime, quantum statistics becomes insignificant, and the quantum Bose-Einstein distribution in Eq. (2.1) becomes the classical Maxwell-Boltzmann distribution given by

$$f(E) = e^{-(E-\mu)/k_B T} \tag{2.2}$$

Figure 2-1(a) plots $f(E)$ for three different values of chemical potential when the temperature of the system is chosen to be 10 K. When μ is comparable to or less than $-k_B T$, the energy distribution is approximately a single exponential function, which is a straight line in the semi-log plot shown as the red curve in the figure. When $\mu \to 0^-$, there is a clear upturn around $E = 0$. As μ is further increased to a value of $-0.001 k_B T$, the particle occupancy at $E = 0$ is increased by more than three orders of magnitude, while it increases by less than a factor of 10 in the range of $E > 0.5$ meV. The nonlinear increase can be naively argued as a fact of decreasing cost incurred when adding particles to the ground state. Therefore, by changing the chemical potential, which is typically adjusted through the total number of particles in the system, the probability that particles occupy the ground state can be significantly increased. Fig. 2-1(b) plots the fraction of bosons occupying the energy of $E \sim E + dE$ in a uniform 3D system. Because the density of states for a uniform 3D system decays to zero as $E \to 0$ while the energy distribution $f(E)$ reaches its minimum when $E \to \infty$, particles are more likely to be found at
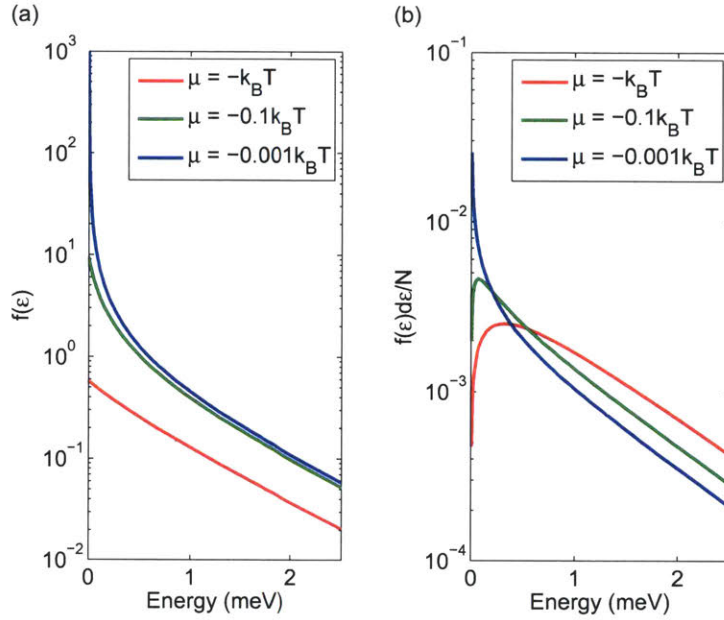
Figure 2-1: Particle occupancy for different values of chemical potential at 10 K. (a) The probability of bosons occupying different energy states. (b) The fraction of bosons occupying different energy states for a uniform 3D ideal gas.

a state with nonzero energy. However, when the chemical potential of the system is increased from $-k_BT$ to $-0.001\ k_BT$, the curve becomes monotonically decreasing as the energy increases, and the fraction of ground state populations increases by more than an order of magnitude and becomes dominant, indicating the possibility of a phase transition.

2.1.1 Onset of Bose-Einstein condensation

When bosons are in thermal equilibrium, we define the thermal de Broglie wavelength

$$\lambda_T = \frac{h}{\sqrt{2\pi m k_B T}} \tag{2.3}$$

where m is the mass of the boson and T is the temperature of the system. It is an ensemble average of the de Broglie wavelength of the individual boson, characterizing the furthest distance two particles can see each other. The length scale of λ_T at room

32
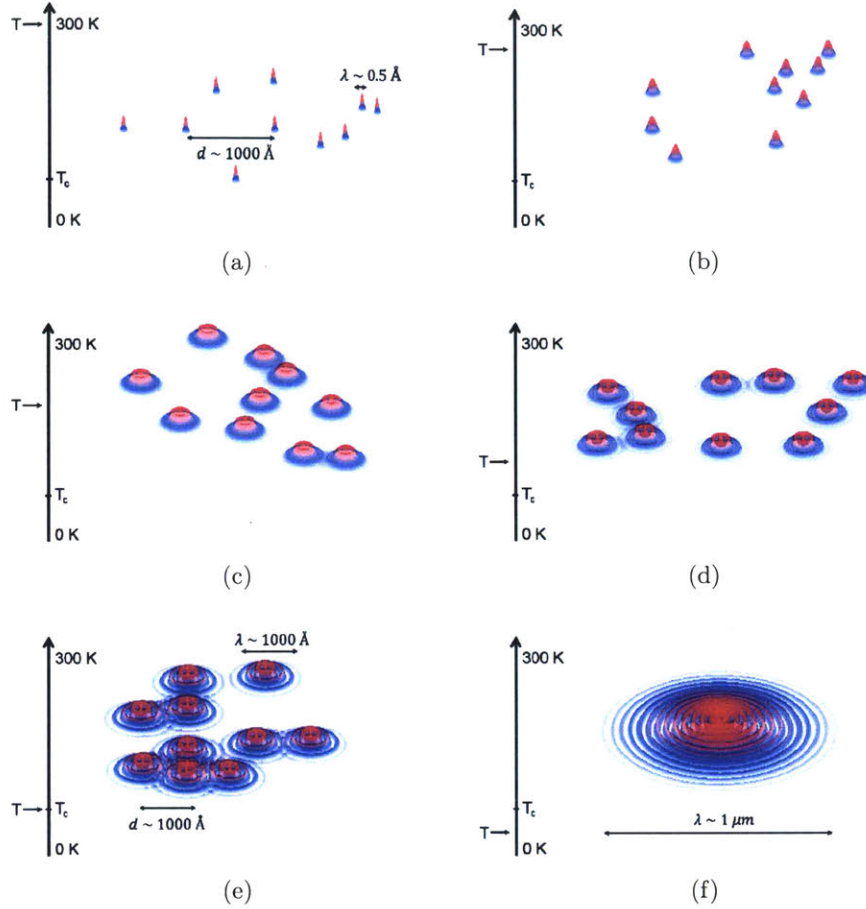
Figure 2-2: (a)-(f) Schematic illustration of the onset of condensation. The growing red-blue pillars indicate the thermal wavepackets of individual particles. Condensation occurs when the interparticle spacing d becomes comparable to the thermal de Broglie wavelength (λ_T). The condensate is a single-particle state, as shown in (f), where the individual constituents lose their identities.

temperature is shown in Table 2.1 for three different systems [42]. As can be seen, because λ_T is inversely related to the effective mass of the particle, it increases from sub-angstrom scale in atomic systems to macroscopic scale in polariton systems.

Quantum condensation occurs when the interparticle distance d is comparable to the thermal de Broglie wavelength λ_T, i.e., $\lambda_T \sim d$ such that individual particle wave-functions constructively interfere and become a macroscopic coherent wavepacket, forming the Bose-Einstein condensate. This condition is not satisfied under normal conditions, as indicated in Fig. 2-2. In order to achieve condensation, we could either

Systems	Atomic Gases	Excitons	Polaritons
Effective mass m^*/m_e	10^4	10^{-1}	10^{-5}
Interparticle spacing d	$1000\,\text{Å}$	$100\,\text{Å}$	$10\,\mu\text{m}$
de Broglie wavelength $\lambda_T(300\text{ K})$	$0.01\,\text{Å}$	$10\,\text{Å}$	$1\,\mu\text{m}$
Critical temperature T_c (K)	10 nK	100 mK	100 K

Table 2.1: Comparison of condensation conditions in different systems. Here m_e is the electron mass in vacuum.

increase the particle density or decrease the temperature of the system so that the thermal de Broglie wavelength is increased. In Fig. 2-2, the red-blue pillars indicate the wavepackets of single particles withcharacteristic length scales of λ_T. As can be seen from Figs. 2-2(a)-(f), the size of wavepackets grows as temperature T decreases. When T reaches a critical value T_c, condensation occurs because there is a significant amount of overlap among the wavefunctions of individual particles. As the system is further cooled down, it turns into a single-particle state with a coherent wavefunction spanning across a macroscopic length scale. The individual constituents in the condensate lose their separate identities, as illustrated in Fig. 2-2(f).

The onset of BEC can also be argued qualitatively based on basic thermodynamics. The total free energy of the system is given by

$$G = U - TS \tag{2.4}$$

that is, the sum of internal energy U and the contribution from randomization determined by the entropy S. Under normal conditions when the temperature of the system is high, particles in the system tend to distribute broadly across different quantum states in order to maximize the entropy part. However, when the temperature is close to zero, e.g., on the order of 10^{-7} K in ultracold atomic BEC systems, the decrease in the total free energy from randomization is negligible. The total free energy of the system could be significantly decreased if the internal energy could be reduced, which is realized by occupying a common lowest-energy state, i.e., the ground state, when condensation takes place.

Formal definition of the criticality of BEC. Although the thermodynamic argument is intuitive, it is difficult to be used to quantify the phase transition. A more formal definition of the critical BEC is given by Einstein and Yang [43] as follows. The total number of bosons in the system can be computed as

$$N(T, \mu) = N_0(T, \mu) + N_{th}(T, \mu) \tag{2.5}$$

where $N(T, \mu)$ is the total number of bosons in the system, and $N_0(T, \mu)$ and $N_{th}(T, \mu)$ are the number of particles in the ground state and the excited states. The T and μ dependence are explicitly expressed in N, N_0 and N_{th}. Bose-Einstein condensation happens when $\mu \to 0$ so that $N_0(T, \mu) \sim N(T, \mu)$. Here we use $\sim$ to indicate that the ground state population is comparable to the total number of bosons. Based on this, we could define the critical temperature and density as

$$N_{th}(T_c, \mu = 0) = N \tag{2.6}$$

This definition leads to the famous statement that BEC is a saturation of excited-state populations. Equation (2.6) can be used to find out the critical temperature given the total number of particles N, or to find out the critical density given the temperature of the system. We will calculate the critical conditions for various systems based on this in the following section.

Critical temperature and critical density in uniform 3D systems. The energy density of states for a free particle with mass m in a uniform 3D system with volume V is

$$g(E) = \frac{V}{4\pi^3} \left(\frac{2m}{\hbar^2} \right)^{\frac{3}{2}} \sqrt{E} \tag{2.7}$$

where $\hbar$ is the reduced Planck constant. The threshold of BEC can be found out as

$$N_c = N_{th}(T, \mu = 0) = \int_{0+}^{\infty} g(E) f(E) dE = \int_0^{\infty} \frac{g(E)}{e^{\beta E} - 1} dE \tag{2.8}$$

Substituting Eq. (2.7) into Eq. (2.8), and working out the algebra, we obtain

$$N_c = \frac{V}{4\pi^2} \left(\frac{2m}{\beta\hbar^2} \right)^{\frac{3}{2}} \zeta\left(\frac{3}{2} \right) \Gamma\left(\frac{3}{2} \right) \tag{2.9}$$

where $\zeta(\cdot)$ and $\Gamma(\cdot)$ are ζ and Γ functions, defined as

$$\Gamma(x) = \int_0^\infty t^{x-1} e^{-t} dt \tag{2.10}$$

and

$$\zeta(x) = \frac{1}{\Gamma(x)} \int_0^\infty \frac{t^{x-1}}{e^t - 1} dt \tag{2.11}$$

By defining the critical density as

$$n_c = \frac{N_c}{V} \tag{2.12}$$

and using the definition of the thermal de Broglie wavelength in Eq. (2.3), the criticality in Eq. (2.9) can be rewritten as

$$n_c \approx \frac{2.612}{\lambda_{T_c}^3} \tag{2.13}$$

or

$$n_c \lambda_{T_c}^3 \approx 2.612 \tag{2.14}$$

This equation clearly suggests that Bose-Einstein condensation happens when the phase space-density is about 2.6, consistent with the dimensionless analysis of the onset of quantum effects, that is, condensation occurs when the thermal de Broglie wavelength is comparable to the average interparticle distance.

2.1.2 BEC in 3D as a thermodynamic phase transition

Bose-Einstein condensation in 3D is a second-order phase transition with the specific heat experiencing a singularity in its first-order derivative with respective to temperature. Following the treatment in Ref. [44], the total energy of the system is calculated as

$$U = \int E g(E) f(E) dE = \frac{3}{2} k_B T \frac{V}{\lambda_T^3} g_{\frac{3}{2}}(Z) \tag{2.15}$$

where $Z = e^{\beta \mu}$ and

$$g_{\frac{3}{2}}(Z) = \frac{4}{3\sqrt{\pi}} \int_0^\infty dx x^{3/2} \frac{1}{Z^{-1} e^x - 1} \tag{2.16}$$

For $T < T_c$, $\mu = 0$ and $Z = 1$. The specific heat $C_V = \partial U / \partial T$ is obtained as

$$\frac{C_V}{k_B N} = \frac{15}{4} \frac{v}{\lambda_T^3} g_{\frac{3}{2}}(1) \tag{2.17}$$

and for $T > T_c$

$$\frac{C_V}{k_B N} = \frac{15}{4} \frac{v}{\lambda_T^3} g_{\frac{3}{2}}(Z) - \frac{9}{4} \frac{g_{\frac{3}{2}}(Z)}{g_{\frac{1}{2}}(Z)} \tag{2.18}$$

where $v = V/N$ is the specific volume. The specific heat has a characteristic cusp at $T = T_c$, and approaches to the classical value $3 k_B T / 2$ when $T \to \infty$, as shown in Fig. 2-3. This indicates that BEC in 3D is a second-order thermodynamic phase transition [40].

2.1.3 Condensation in low dimensions

Bose-Einstein condensation does not occur in uniform, infinite 1D and 2D systems since the energy density of states $g(E)$ does not vanish in the limit of $E \to 0$. However, it can be restored when an appropriate confining potential is applied.
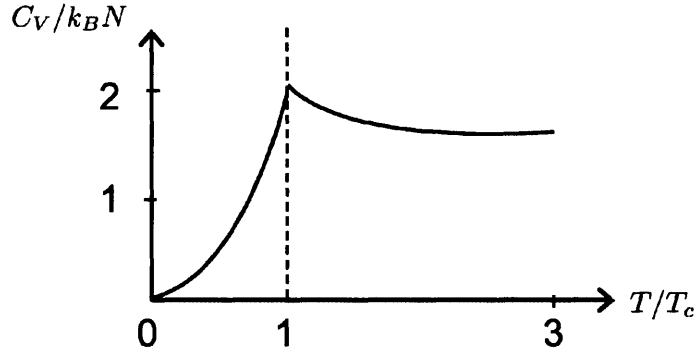
Figure 2-3: Figure taken from Ref. [44]. The specific heat of an ideal uniform gas in 3D in unit of $k_B N$ as a function of temperature T/T_c. At high temperatures, the curve approaches the classical limit $3/2$.

An ideal Bose gas in 1D systems. We consider a symmetric confining potential of the form

$$V(x) = V_0 \left(\frac{|x|}{L} \right)^\eta \tag{2.19}$$

where L is the length scale of the confinement, and V_0 is the height of the potential barrier. η can be regarded as a measure of the strength of confinement. The energy density of states becomes [45]

$$g(E) = \frac{\sqrt{2m}}{h} L \frac{E^{\frac{1}{\eta} - \frac{1}{2}}}{V_0^{\frac{1}{\eta}}} F(\eta) \tag{2.20}$$

with

$$F(\eta) = \int_0^1 \frac{y^{\frac{1-\eta}{\eta}}}{\sqrt{1-y}} dy \tag{2.21}$$

Figure 2-4(a) plots the 1D energy density of states for four different values of η. In the case of $\eta < 2$, the confinement allows the energy density of states to go to 0 when $E \to 0$. However, when $\eta = 2$, the energy density of states is energy-independent. When $\eta > 2$, the confinement is so strong that only the ground state is favored and $g(E)$ diverges as $E \to 0$. This will not support BEC any more.

38
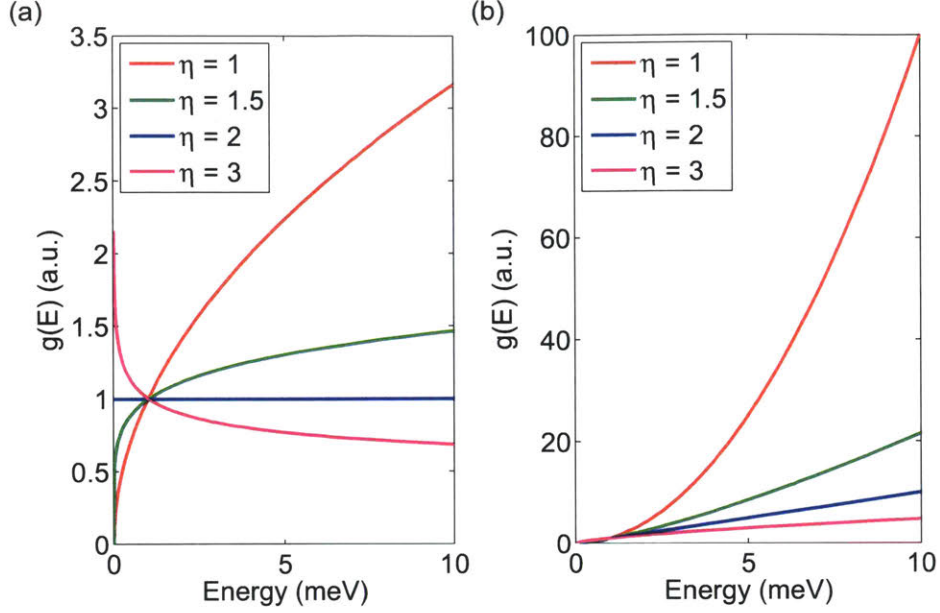
Figure 2-4: Energy density of states in confined 1D (a) and 2D (b) systems with different confinement constants.

Substituting Eq. (2.20) into Eq. (2.6), we get the criticality [44]

$$k_B T_c = \left[\frac{h}{2mL} \frac{V_0^{\frac{1}{\eta}}}{F(\eta)} \frac{1}{g_1(\eta, 0)} N \right]^{2\eta/(2+\eta)} \tag{2.22}$$

for 1D Bose-Einstein condensation when $0 < \eta < 2$, where $g_1(\eta, x)$ is the one-dimensional Bose function defined as

$$g_1(\eta, x) = \int_0^\infty \frac{y^{-\frac{1}{\eta} - \frac{1}{2}}}{e^{y-x} - 1} dy \tag{2.23}$$

An ideal Bose gas in 2D systems. Similar to the 1D case, infinite uniform 2D systems do not allow BEC because the energy density of states is energy-independent. We assume an isotropic two-dimensional confining potential

$$V(r) = V_0 \left(\frac{r}{a} \right)^\eta \tag{2.24}$$

39

where a is the size of the trap, and η and V_0 are the strength and height of the confining potential, respectively. This leads to a power-law-like energy density of states [45]

$$g(E) = \frac{2\pi^2 m a^2}{h^2} \left(\frac{E}{V_0}\right)^{\frac{2}{\eta}} \tag{2.25}$$

Figure 2-4(b) shows $g(E)$ for different values of η. As can be seen, for all values of η, the energy density of states readily converges to 0 when $E \to 0$, suggesting BEC is possible for any form of finite-size confinement in 2D systems. The criticality of BEC can be found to be [44]

$$k_B T_c = \left[\frac{h^2 V_0^{2\eta} N}{2\pi^2 m a^2 g_2(\eta, 0)}\right]^{\frac{2}{2+\eta}} \tag{2.26}$$

where $g_2(\eta, x)$ is the two-dimensional Bose function defined as

$$g_2(\eta, x) = \int_0^\infty \frac{y^{2/\eta}}{e^{y-x} - 1} dy \tag{2.27}$$

2.2 Off-Diagonal Long-Range Order in the Condensates

An intriguing feature of BEC is its extended coherence length well beyond the size of the underlying particle wavefunction, also known as the long-range off-diagonal order. This can be understood from the following derivation. Consider a system consisting of N bosons which can be described by a many-body wavefunction $\psi(r_1, r_2, \ldots, r_N)$. Here r_i is the position vector of the i-th particle, and ψ is symmetric under exchange of any pair of indices. In the general case, the system is a statistical mixture of mutually orthogonal states m with weights p_m. We then define the one-body density

matrix, better known as the first-order spatial correlation function, as

$$n^{(1)}(\boldsymbol{r}, \boldsymbol{r'}) = N \sum_m p_m \int d\boldsymbol{r}_2 d\boldsymbol{r}_3 \ldots \boldsymbol{r}_N \psi_m^*(\boldsymbol{r}, \boldsymbol{r}_2, \ldots, \boldsymbol{r}_N) \psi_m(\boldsymbol{r'}, \boldsymbol{r}_2, \ldots, \boldsymbol{r}_N)$$
$$= \left\langle \hat{\Psi}^\dagger(\boldsymbol{r}) \hat{\Psi}(\boldsymbol{r'}) \right\rangle \tag{2.28}$$

where $\hat{\Psi}^\dagger(\boldsymbol{r})$ and $\hat{\Psi}(\boldsymbol{r})$ are the field operators creating and annihilating a particle at position $\boldsymbol{r}$. The diagonal part $(\boldsymbol{r} = \boldsymbol{r'})$ of the one-body density matrix gives the particle density. The off-diagonal part $(\boldsymbol{r} \neq \boldsymbol{r'})$ describes the coherence established between distant points at $\boldsymbol{r}$ and $\boldsymbol{r'}$. To understand its behavior, consider the momentum distribution

$$n(\boldsymbol{p}) = \left\langle \hat{\Psi}^\dagger(\boldsymbol{p}) \hat{\Psi}(\boldsymbol{p}) \right\rangle \tag{2.29}$$

where $\hat{\Psi}(p) = (2\pi\hbar)^{-3/2} \int d\boldsymbol{r} \exp(i\boldsymbol{p} \cdot \boldsymbol{r}/\hbar) \hat{\Psi}(\boldsymbol{r})$ is the field operator in the momentum representation. In a homogeneous system, $n^{(1)}(\boldsymbol{r}, \boldsymbol{r'})$ only depends on the relative distance $\boldsymbol{s} = \boldsymbol{r} - \boldsymbol{r'}$, and $n^{(1)}(\boldsymbol{s})$ is the Fourier transform of the momentum distribution

$$n^{(1)}(\boldsymbol{s}) = \frac{1}{V} \int d\boldsymbol{p}\, n(\boldsymbol{p}) e^{-i\boldsymbol{p} \cdot \boldsymbol{s}/\hbar} \tag{2.30}$$

where V is the volume of the system. In a non-interacting BEC state, the lowest-energy state with momentum zero$(p = 0)$ is macroscopically occupied, exhibiting a singular behavior

$$n(\boldsymbol{p}) = N_0 \delta(\boldsymbol{p}) + \tilde{n}(\boldsymbol{p}) \tag{2.31}$$

where $\delta(\boldsymbol{p})$ is the delta function, and $\tilde{n}(\boldsymbol{p})$ is a smooth function approximating the excited-state distribution. By taking the Fourier transform of Eq. (2.31), we can show that, in the presence of BEC, the one-body density matrix $n^{(1)}(\boldsymbol{s})$ approaches

a non-zero value as $|s| \to \infty$

$$n^{(1)}(s)_{|s| \to \infty} \to \frac{N_0}{V} \tag{2.32}$$

This behavior was pointed out by Landau, Penrose and Onsager and is often referred to as off-diagonal long-range order [46, 47, 48], which was proposed by Yang et al. to identify Bose-Einstein condensation.

Following the discussion above, we can find out the scaling law of the first-order spatial correlation functions in different regimes. Below the condensation threshold, for a non-degenerate gas, the momentum distribution approaches the Maxwell-Boltzmann distribution [41]

$$n(p) = \exp(-\beta E(p)) = \exp(-p^2/2mk_BT) \tag{2.33}$$

Substituting this into Eq. (2.30), we find that there are only short-range correlations and $n^{(1)}(s)$ has a Gaussian form

$$n^{(1)}(s) = ne^{-\pi s^2/\lambda_T^2} \tag{2.34}$$

The above result explicitly shows that the one-body density tends to zero within a microscopic distance determined by the thermal de Broglie wavelength λ_T. On the other hand, when BEC forms, the low-energy states are strongly occupied and follow the Bose-Einstein distribution

$$n(p) = \frac{1}{e^{\beta E} - 1} \approx \frac{2mk_BT}{p^2} \tag{2.35}$$

Following the same calculations yields

$$n^{(1)}(s) \to n_0 + \frac{1}{(2\pi)^3} \frac{1}{s\lambda_T^2} \tag{2.36}$$

The first-order spatial correlation decays in a power-law fashion and remains finite in the long range. In the high-energy tail, the distribution still resembles the Maxwell-

Boltzmann distribution, and $n^{(1)}(s)$ falls as Gaussian. The change in the scaling law of the first-order spatial correlation function across BEC transition can thus be used to map out the phase boundary of the BEC transition. However, note that the off-diagonal long-range order will always decay to zero in confined systems, so this criterion is only suitable for infinite systems.

2.3 Effects of Interactions on Bose Einstein Condensates

When interactions are introduced among the bosons that form BEC, remarkable properties such as phase locking and superfluidity become possible. In this section, we discuss the Bogoliubov theory of weakly interacting Bose gases, and the effects of interactions on condensates, including renormalization of excitation spectrum, quantum and thermal depletion, and the mechanism of phase locking in BEC.

2.3.1 Hamiltonian of weakly interacting Bose gases and the lowest-order approximation

The Hamiltonian of the weakly interacting Bose gas in terms of the field operator $\hat{\psi}$ has the form [41, 44]

$$\hat{\mathcal{H}} = \int \left(\frac{\hbar^2}{2m} \nabla \hat{\psi}^\dagger(\boldsymbol{r}) \nabla \hat{\psi}(\boldsymbol{r}) \right) d\boldsymbol{r} + \frac{1}{2} \int \hat{\psi}^\dagger(\boldsymbol{r}) \hat{\psi}^\dagger(\boldsymbol{r}') V(\boldsymbol{r}' - \boldsymbol{r}) \hat{\psi}(\boldsymbol{r}) \hat{\psi}(\boldsymbol{r}') d\boldsymbol{r} d\boldsymbol{r}' \quad (2.37)$$

where $V(\boldsymbol{r}' - \boldsymbol{r})$ is the two-body scattering potential. For a uniform gas occupying a volume V, the field operator can be expanded in the plane-wave basis

$$\hat{\psi}(\boldsymbol{r}) = \frac{1}{\sqrt{V}} \sum_{\boldsymbol{p}} \hat{a}_{\boldsymbol{p}} e^{i\boldsymbol{p} \cdot \boldsymbol{r}/\hbar} \quad (2.38)$$

where $\hat{a}_p$ is the annihilation operator for a single-particle state of a plane wave with momentum p. Substituting Eq. (2.38) into Eq. (2.37) yields

$$\hat{\mathcal{H}} = \sum_p \frac{p^2}{2m} \hat{a}_p^\dagger \hat{a}_p + \frac{1}{2V} \sum_{p_1, p_2, q} V_q \hat{a}_{p_1+q}^\dagger \hat{a}_{p_2-q}^\dagger \hat{a}_{p_1} \hat{a}_{p_2} \qquad (2.39)$$

Here $V_q = \int V(r) \exp(-iq \cdot r/\hbar) dr$ is the Fourier transform of the two-body scattering potential. In a dilute system with low-density bosons, the scattering events that involve exchanges of large values of momenta are rare. Hence we could limit ourselves to small-momentum scattering events and approximate the actual scattering potential $V(q)$ with $V(q = 0) = g$, and rewrite the Hamiltonian in the form

$$\hat{\mathcal{H}} = \sum_p \frac{p^2}{2m} \hat{a}_p^\dagger \hat{a}_p + \frac{g}{2V} \sum_{p_1, p_2, q} \hat{a}_{p_1+q}^\dagger \hat{a}_{p_2-q}^\dagger \hat{a}_{p_1} \hat{a}_{p_2} \qquad (2.40)$$

2.3.2 Bogoliubov transformation and excitation spectrum

Since the ground state is occupied by a macroscopic number of particles in BEC, i.e., $N_0 \approx N$, one can neglect the quantum fluctuation of the system and replace the operator $\hat{a}_0$ with a c-number

$$\hat{a}_0 = \sqrt{N_0} \qquad (2.41)$$

First-order approximation. To a first-order approximation, we can neglect all the terms in Eq. (2.40) containing $p \neq 0$. The ground-state energy then takes the form

$$E_0 = \frac{N_0^2 V_0}{2V} \approx \frac{N^2 g}{2V} = \frac{1}{2} gnN \qquad (2.42)$$

where $n = N/V$ is the particle density of the system. The sign $\approx$ comes from the fact that $N_0 \approx N$ in BEC. This explains the fact that repulsive interactions lead to blueshifts in the energy spectrum as density increases.

Second-order approximation. Retaining all the quadratic terms in the particle operators with $\boldsymbol{p} \neq 0$, we obtain the decomposition of the Hamiltonian

$$\hat{\mathcal{H}} = \frac{V_0}{2V} \hat{a}_0^\dagger \hat{a}_0^\dagger \hat{a}_0 \hat{a}_0 + \sum_{\boldsymbol{p}} \frac{p^2}{2m} \hat{a}_{\boldsymbol{p}}^\dagger \hat{a}_{\boldsymbol{p}} + \frac{g}{2V} \sum_{\boldsymbol{p} \neq 0} \left(4 \hat{a}_0^\dagger \hat{a}_{\boldsymbol{p}}^\dagger \hat{a}_0 \hat{a}_{\boldsymbol{p}} + \hat{a}_{\boldsymbol{p}}^\dagger \hat{a}_{-\boldsymbol{p}}^\dagger \hat{a}_0 \hat{a}_0 + \hat{a}_0^\dagger \hat{a}_0^\dagger \hat{a}_{\boldsymbol{p}} \hat{a}_{-\boldsymbol{p}} \right)$$

(2.43)

We replace $\hat{a}_0^\dagger$ and $\hat{a}_0$ with $\sqrt{N}$ as we have done previously, and take into account that the particle number must be conserved in the sense

$$\hat{a}_0^\dagger \hat{a}_0 + \sum_{\boldsymbol{p} \neq 0} \hat{a}_{\boldsymbol{p}}^\dagger \hat{a}_{\boldsymbol{p}} = N$$

(2.44)

Neglecting all higher orders, the Hamiltonian is reduced to the form

$$\hat{\mathcal{H}} = \frac{1}{2} gnN + \sum_{\boldsymbol{p}} \frac{p^2}{2m} \hat{a}_{\boldsymbol{p}}^\dagger \hat{a}_{\boldsymbol{p}} + \frac{1}{2} gn \sum_{\boldsymbol{p} \neq 0} \left(2 \hat{a}_{\boldsymbol{p}}^\dagger \hat{a}_{\boldsymbol{p}} + \hat{a}_{\boldsymbol{p}}^\dagger \hat{a}_{-\boldsymbol{p}}^\dagger + \hat{a}_{\boldsymbol{p}} \hat{a}_{-\boldsymbol{p}} \right)$$

(2.45)

The third term in Eq. (2.45) presents the self-energy of the excited states due to the interaction, simultaneous creation of the excited states at momentum at $\boldsymbol{p}$ and $-\boldsymbol{p}$, and simultaneous annihilation of the excited states, respectively. By introducing the well known Bogoliubov transformation [49]

$$\hat{a}_{\boldsymbol{p}} = u_{\boldsymbol{p}} \hat{b}_{\boldsymbol{p}} + v_{-\boldsymbol{p}}^* \hat{b}_{-\boldsymbol{p}}^\dagger$$
$$\hat{a}_{\boldsymbol{p}}^\dagger = u_{\boldsymbol{p}}^* \hat{b}_{\boldsymbol{p}}^\dagger + v_{-\boldsymbol{p}} \hat{b}_{-\boldsymbol{p}}$$

(2.46)

where $u_{\boldsymbol{p}}$ and $v_{\boldsymbol{p}}$ are the transformation coefficients, and by imposing the bosonic commutativity between $\hat{b}_{\boldsymbol{p}}^\dagger$ and $\hat{b}_{\boldsymbol{p}}$, the explicit forms of $u_{\boldsymbol{p}}$ and $v_{\boldsymbol{p}}$ can be found as

$$u_{\boldsymbol{p}}, v_{-\boldsymbol{p}} = \pm \sqrt{\frac{p^2/2m + gn}{2\epsilon(p)} \pm \frac{1}{2}}$$

(2.47)

with

$$\epsilon(p) = \sqrt{\frac{gn}{m}p^2 + \left(\frac{p^2}{2m}\right)^2} \qquad (2.48)$$

In this picture, a real particle $\hat{a}_p$ is described as the superposition of the forward propagating many quasi-particles $u_p \hat{b}_p$ and the backward propagating many quasi-particles $v_{-p} \hat{b}_p^\dagger$. This suggests that a system of weakly interacting particles can be regarded as a system with collective excitations defined by $\hat{b}_p$, which are sometimes referred to as bogolons. Bogolons in a uniform BEC are similar to acoustic phonons in a solid, which will be discussed further in the following section. Substituting the Bogoliubov transformation Eq. (2.46) into Eq. (2.45), the Hamiltonian can be simplified to the diagonal form

$$\hat{\mathcal{H}} = E_0 + \sum_{p \neq 0} \epsilon(p) \hat{b}_p^\dagger \hat{b}_p \qquad (2.49)$$

where

$$E_0 = \frac{1}{2}gnN + \frac{1}{2}\sum_{p \neq 0}\left[\epsilon(p) - gn - \frac{p^2}{2m} + \frac{m(gn)^2}{p^2}\right] \qquad (2.50)$$

This suggests that we can treat the origina weaklyl interacting system defined by a_p as an effective non-interacting system defined by b_p.

2.3.3 Normalized ground state energy

A direct consequence of interaction leads to the correction of the ground state. By replacing the sum in Eq. (2.50) with an integral in momentum space, the ground state energy is found to be [43, 50]

$$E_0 = \frac{1}{2}gnN\left[1 + \frac{128}{15\sqrt{\pi}}(na^3)^{1/2}\right] \qquad (2.51)$$

where a is the s-wave scattering length defined as

$$a = \frac{gm}{4\pi\hbar^2} \qquad (2.52)$$

The second part in the sum is a perturbative correction to Eq. (2.42) since the Bogoliubov theory assumes $|a|n^3 \ll 1$ [49].

2.3.4 Excitation spectrum

The interaction renormalizes the excitations of the system of bosons profoundly. Within the framework of the Bogoliubov theory, the original system of interacting particles can now be described by the Hamiltonian for non-interacting quasi-particles given by $\hat{b}_p$ in Eq. (2.46) with a dispersion relation $\epsilon(p)$. In Fig. 2-5(a), we plot the excitation spectra for three different values of gn. As the interaction strength increases, the excitation spectrum renormalizes to a linear dispersion which is reminiscent of sound-wave dispersion. Mathematically, by letting $gn \to \infty$ or $p \to 0$ in Eq. (2.48), we obtain

$$\epsilon(p) = cp \qquad (2.53)$$

where we define the sound velocity as $c = \sqrt{gn/m}$. This linearized dispersion relation at low p is responsible for superfluidity, a flow with zero friction. Physically, the Bogoliubov theory suggests that the long-wavelength excitations of an interacting gas are sound-like waves. This can also be understood by examining the amplitudes of the new quasiparticles b_p. The solid and dashed lines in Fig. 2-5(b) show $|u_p|^2$ and $|v_{-p}|^2$ for three different values of interaction strength. As can be seen, in the low momentum limit, $|u_p|^2 \approx |v_{-p}|^2 \gg 1$, indicating that the long-wavelength excitations of the system are no longer single-particle like. Based on the Bogoliubov transformation in Eq. (2.46), the excitation b_p is a superposition of many real particles with opposite momentum values. As p increases, both amplitude values decrease, with $|u_p| \to 1$ and $|v_{-p}|^2 \to 0$, and they deceases faster for systems with weaker interactions. This
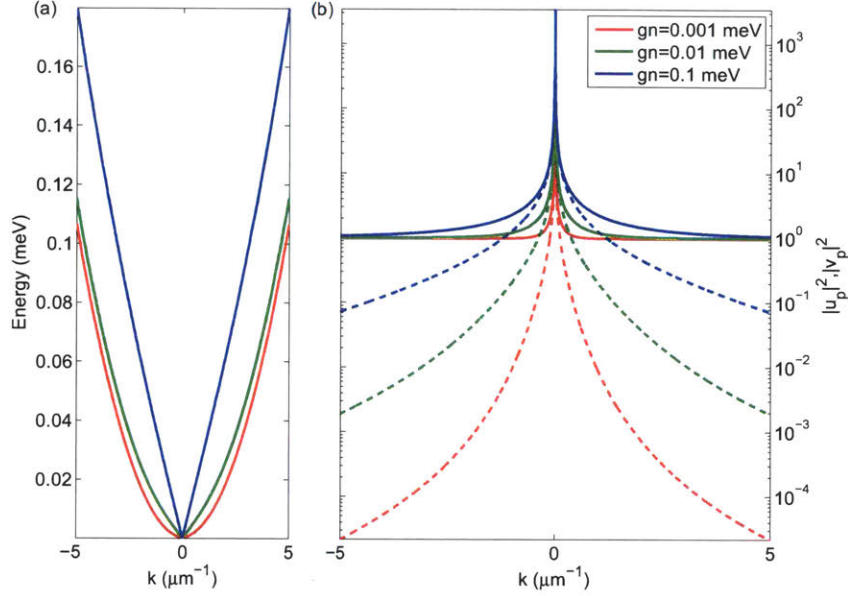
Figure 2-5: Spectra and amplitudes of collective excitations in an interacting Bose gas. The mass of the bosons is set to be $m = 9 \times 10^{-5} m_e$, with m_e being the electron mass in vacuum. (a) Spectra and (b) amplitudes of collective oscillations in an interacting Bose gas for different values of interaction strength. The solid and dashed lines in (b) are $|u_p|^2$ and $|v_{-p}|^2$, respectively.

leads to $\hat{a}_{\boldsymbol{p}} \approx \hat{b}_{\boldsymbol{p}}$, indicating that the single-particle excitation recovers in the short-wavelength and weak-interaction limit, which is also manifested in the excitation spectrum as it recovers the parabolic shape given by

$$\epsilon(p) = \frac{p^2}{2m} + gn \tag{2.54}$$

The transition between the collective excitation and the single-particle excitation takes place when $p^2/2m \approx gn$. Based on this, we define a characteristic length, called the healing length, as

$$\xi = \left.\frac{\hbar}{p}\right|_{\frac{p^2}{2m}=gn} = \sqrt{\frac{\hbar^2}{2mgn}} \tag{2.55}$$

for an interacting bosonic system. In the range of $r > \xi$, the system is classical, whereas it has to be described in the language of quantum mechanics when $r < \xi$.

48

2.3.5 Quantum and thermal depletion

The average number of quasi-particles N_p carrying momentum p must obey the Bose-Einstein distribution with the chemical potential $\mu = 0$, that is,

$$N_p = \left\langle \hat{b}_p^\dagger \hat{b}_p \right\rangle = \frac{1}{e^{\epsilon(p)/k_B T} - 1} \tag{2.56}$$

Using the Bogoliubov transformation Eq. (2.46), we obtain

$$N_p = \left\langle \hat{a}_p^\dagger \hat{a}_p \right\rangle = |v_{-p}|^2 + |u_p|^2 \left\langle \hat{b}_p^\dagger \hat{b}_p \right\rangle + |v_{-p}|^2 \left\langle \hat{b}_{-p}^\dagger \hat{b}_{-p} \right\rangle \tag{2.57}$$

Thus, the number of particles in the condensate can be calculated by

$$N_0 = N - \sum_{p \neq 0} N_p = N - \frac{V}{(2\pi\hbar^3)^3} \int d\boldsymbol{p} \left[|v_{-p}|^2 + \frac{|u_p|^2 + |v_{-p}|^2}{\exp(\beta\epsilon(p)) - 1} \right] \tag{2.58}$$

At absolute zero temperature $T = 0$, there is a finite leakage of particles into the excitation spectrum given by $|v_{-p}|^2$ even though the population of quasiparticles is zero, $\left\langle \hat{b}_p^\dagger \hat{b}_p \right\rangle = 0$. This fundamental leakage of particles from the condensate is referred to as quantum depletion, plotted as green lines in Fig. 2-6. At higher temperatures, the thermal population of quasiparticles, the second term in the integration, dominates. This extra leakage of particles from the condensate is called thermal depletion, shown as red lines in Fig. 2-6. Note that both quantum depletion and thermal depletion at low momentum are straight lines in the log-log plot, given by the power law scaling relationships. The explicit relations can be found by letting $p \to 0$ as

$$\lim_{p \to 0} N_p^{\text{(quantum)}} = \frac{\sqrt{mgn}}{2p} \tag{2.59}$$

and

$$\lim_{p \to 0} N_p^{\text{(thermal)}} = \frac{\sqrt{mk_B T}}{p^2} \tag{2.60}$$

49
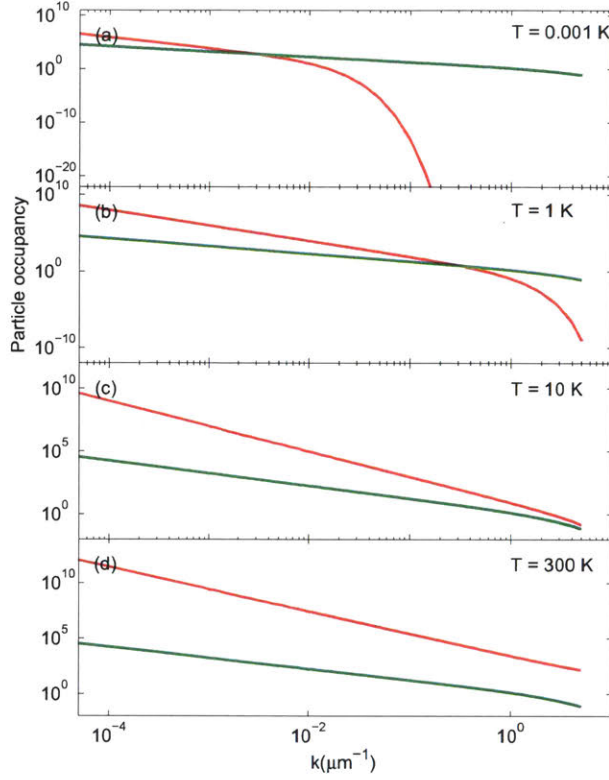
Figure 2-6: Quantum depletion (green) and thermal depletion (red) at different temperatures for a weakly interacting system with $gn = 0.1$. (a) $T = 0.001$ K, (b) $T = 1$ K (c), $T = 10$ K, and (d) $T = 300$ K.

As can be seen, quantum depletion is determined by the interaction strength gn, while thermal depletion depends on the temperature of the system. On the other hand, quantum depletion decays according to the power law $\sim 1/p^4$ when the momentum becomes large, while thermal depletion disappears according to $\sim e^{-\beta\epsilon(p)}$. The scaling laws of quantum depletion versus thermal depletion can often be used to determine if the system is weakly interacting in which case thermal depletion typically dominates.

2.3.6 Spatial coherence

Following the treatment in Ref. [44], when quantum depletion dominates, i.e., $N_p = |v_{-p}|^2$, the first-order spatial coherence function can be evaluated as

$$
\begin{aligned}
n^{(1)}(s) &= \frac{N_0}{N} + \frac{V}{N(2\pi\hbar)^3} \int dp N(p) e^{-ip \cdot s/\hbar} \\
&= \frac{N_0}{N} + \frac{V}{N(2\pi\hbar)^3} \int dp |v_{-p}|^2 e^{-ip \cdot s/\hbar} \\
&= \frac{N_0}{N} + \frac{V}{N\xi^3} D\left(\frac{s}{\xi}\right)
\end{aligned}
\tag{2.61}
$$

where we have defined the dimensionless function

$$
D\left(\frac{s}{\xi}\right) = \frac{1}{16\pi^3} \int dk \left(\frac{1+k^2}{\sqrt{k^4+2k^2}}\right) e^{-i(s/\xi)\cdot k}
\tag{2.62}
$$

Here $k = p\xi/\hbar$. For $s/\xi \gg 1$, the function $D(s/\xi)$ behaves like $\xi^2/\sqrt{32}\pi^2 s^2$, then we have [44]

$$
n^{(1)}(s) = \frac{N_0}{N} + \frac{1}{N} \frac{V}{\sqrt{32}\pi^2\xi} \frac{1}{s^2}
\tag{2.63}
$$

for an interacting Bose gas at $T = 0$. As can be seen, the interaction leads to the change of decay from Gaussian to power law. When thermal depletion dominates, the decay law of $n^{(1)}(s)$ is typically numerically evaluated due to its complexity.

2.3.7 Population fluctuations and phase locking

The interaction forces the condensate to acquire a particular phase as a coherent state rather than to have a random phase as a particle number eigenstate or statistical mixture of them [51]. This can be understood as the following. Consider the interaction part of the Hamiltonian

$$
\hat{\mathcal{H}}_B = \frac{1}{2V} \sum_q V_q \hat{a}_0^\dagger \hat{a}_0^\dagger \hat{a}_q \hat{a}_{-q} + h.c.
\tag{2.64}
$$

which allows virtual excitations of two particles out of the condensate. Here $h.c.$ stands for Hermitian conjugate. In order to take such a quantum depletion into account, we consider a variational state [52]

$$|\psi_0\rangle = e^{\phi\hat{a}_0^\dagger + \Sigma_q \lambda_q \hat{a}_q^\dagger \hat{a}_{-q}^\dagger}|0\rangle$$
$$= |\phi\rangle_0 \otimes \sum_q \left[|0\rangle_q|0\rangle_{-q} + \lambda_q|1\rangle_q|1\rangle_{-q} + \cdots\right] \qquad (2.65)$$

where λ_q is the variational parameter that needs to be minimized, and $|0\rangle$ is the condensate state at $T = 0$ with no thermal excitation. The Bogoliubov interaction energy is given by

$$E_B = \left\langle \psi_0 \left| \hat{\mathcal{H}}_B \right| \psi_0 \right\rangle = \sum_q \frac{V_q}{2V}(\phi_0^{*2}\lambda_q + c.c.) \qquad (2.66)$$

If we express the complex excitation amplitudes as $\phi = |\phi|e^{i\theta_0}$ and $\lambda_q = |\lambda_q|e^{i\theta_q}$, the expression above becomes

$$E_B = \sum_q \frac{V_q}{V}|\phi|^2|\lambda_q|\cos(2\theta_0 - \theta_q) \qquad (2.67)$$

Equation (2.67) is minimized when $2\theta_0 - \theta_q = \pi$, thus it is energetically favorable that the condensate has a well defined phase and the excitations are phase-locked to the condensate with a π phase difference. The reduced energy is macroscopic with $\Delta E = V_q|\phi|^2|\lambda_q|/V \sim gn_0\sqrt{N_q}$, where $n_0 = |\phi|^2/V$ is the condensate density and N_q is the average population in excited states in Eq. (2.57).

2.4 Theoretical Description of Condensates

Given the high density in a BEC, collisions between particles become important and must be taken into account in the description of condensed states. Our main goal in this section is to present the Gross-Pitaevskii equation, the analogue of the Schrödinger equation for the condensed state that has an additional nonlinear term

that describes the effects of collisions between underlying particles in the mean-field level. With this equation, we obtain the density distribution of the condensed state that differs from that obtained in the non-interacting case. However, we first sketch how the Gross-Pitaevskii equation is obtained and the conditions under which it is valid.

2.4.1 Field theoretic description of the condensed state

Taking into account the external potential $U(r)$, the many-body Hamiltonian in Eq. (2.37) can be cast into

$$\hat{\mathcal{H}} = \int \frac{\hbar^2}{2m}\hat{\psi}^\dagger(\boldsymbol{r}) \left(-\frac{\hbar^2}{2m}\nabla^2 + U(\boldsymbol{r}) \right) \hat{\psi}(\boldsymbol{r}) + \frac{1}{2} \int \hat{\psi}^\dagger(\boldsymbol{r})\hat{\psi}^\dagger(\boldsymbol{r}')V(\boldsymbol{r}' - \boldsymbol{r})\hat{\psi}(\boldsymbol{r})\hat{\psi}(\boldsymbol{r}')d\boldsymbol{r}d\boldsymbol{r}'$$

$$(2.68)$$

Since Bose-Einstein condensation occurs when the occupation number of the ground state becomes commensurate with the number of particles in the system, we may express the field operators in the Heisenberg representation as

$$\hat{\psi}(\boldsymbol{r}, t) = \psi(\boldsymbol{r}, t) + \delta\hat{\psi}(\boldsymbol{r}, t) \tag{2.69}$$

where $\psi(\boldsymbol{r}, t) = \left\langle \hat{\psi}(\boldsymbol{r}, t) \right\rangle$ is the mean value of the field operator representing the condensate wavefunction subject to the normalization condition

$$\int |\psi(\boldsymbol{r}, t)|^2 d\boldsymbol{r} = N_0 \tag{2.70}$$

and $\delta\hat{\psi}(\boldsymbol{r}, t)$ represents a perturbative deviation from the mean. The dynamics of the condensate is obtained from the Heisenberg equation of motion for the field operator

$$i\hbar\frac{\partial\hat{\psi}(\boldsymbol{r}, t)}{\partial t} = \left[\hat{\psi}(\boldsymbol{r}, t), \hat{\mathcal{H}} \right]$$

$$= \left[-\frac{\hbar^2}{2m}\nabla^2 + U(\boldsymbol{r}) + \int d\boldsymbol{r}\hat{\psi}^\dagger(\boldsymbol{r}, t)V(\boldsymbol{r} - \boldsymbol{r}')\hat{\psi}(\boldsymbol{r}', t) \right] \hat{\psi}(\boldsymbol{r}, t) \quad (2.71)$$

Substituting Eq. (2.69) back into Eq. (2.68) and retaining the mean-field components, we obtain the Gross-Pitaveskii equation for the condensate wavefunction

$$i\hbar\frac{\psi(\boldsymbol{r},t)}{\partial t} = \left(-\frac{\hbar^2}{2m}\nabla^2 + U(\boldsymbol{r}) + \int d\boldsymbol{r}\psi(\boldsymbol{r},t)V(\boldsymbol{r}-\boldsymbol{r}')\psi(\boldsymbol{r}',t)\right)\psi(\boldsymbol{r},t) \qquad (2.72)$$

The Gross-Pitaveskii equation is typically used to simulate the dynamics of the condensates in external confining potentials. It can also be used to simulate the spatial density distributions of stationary state.

2.4.2 Interactions in a dilute gas

It is an important feature of most experimentally produced BECs that while their density is very high, they are still dilute gases in the sense that the length a that characterizes collisions between particles is much smaller than the average interparticle spacing. Hence, two-body collisions dominate, and we may replace the true potential $V(\boldsymbol{r}-\boldsymbol{r}')$ with an effective interaction between bosons that is exact in the limit of large separations given by

$$V(\boldsymbol{r}-\boldsymbol{r}') = g\delta(\boldsymbol{r}-\boldsymbol{r}') \qquad (2.73)$$

Substituting Eq. (2.73) into Eq. (2.72), we find

$$i\hbar\frac{\psi(\boldsymbol{r},t)}{\partial t} = \left(-\frac{\hbar^2}{2m}\nabla^2 + U(\boldsymbol{r}) + g|\psi(\boldsymbol{r},t)|^2\right)\psi(\boldsymbol{r},t) \qquad (2.74)$$

which is the typical form of Gross-Pitaevskii equation used in atomic physics. By assuming that the stationary solution of Eq. (2.74) takes the form

$$\psi(\boldsymbol{r},t) = \psi(\boldsymbol{r})e^{-i\mu t/\hbar} \qquad (2.75)$$

54

with μ being the chemical potential, the time-independent Gross-Pitaevskii equation may be expressed as

$$\left(-\frac{\hbar^2}{2m}\nabla^2 + U(\boldsymbol{r}) - \mu + g|\psi(\boldsymbol{r},t)|^2 \right) \psi(\boldsymbol{r},t) = 0 \qquad (2.76)$$

which can be used to study the eigen-spectra of condensate systems.

2.4.3   The Bogoliubov equations

An alternative route to calculating the excitation spectrum of the condensate is to start from the Gross-Pitaevskii equation directly. We search for a perturbative solution that takes the form

$$\psi(\boldsymbol{r},t) = \psi_0(\boldsymbol{r})e^{-i\mu t}\left\{ 1 + \sum_{\boldsymbol{k}} \left(\alpha_{\boldsymbol{k}}e^{i(\boldsymbol{k}\cdot\boldsymbol{r}-\omega t)} + \beta_{\boldsymbol{k}}e^{-i(\boldsymbol{k}\cdot\boldsymbol{r}-\omega t)} \right) \right\}$$

$$= \psi_0(\boldsymbol{r})e^{-i\mu t} + \sum_{\boldsymbol{k}} \left\{ u_{\boldsymbol{k}}e^{i(\boldsymbol{k}\cdot\boldsymbol{r}-(\mu+\omega)t)} + v_{\boldsymbol{k}}e^{-i(\boldsymbol{k}\cdot\boldsymbol{r}+(\mu-\omega)t)} \right\} \qquad (2.77)$$

where $\mu_{\boldsymbol{k}}(\boldsymbol{r}) = \psi_0(\boldsymbol{r})\alpha_{\boldsymbol{k}}$ and $v_{\boldsymbol{k}}(\boldsymbol{r}) = \psi_0(\boldsymbol{r})\beta_{\boldsymbol{k}}$ are the excitation amplitudes of the forward propagating and backward propagating excitation waves with wavenumbers $\pm\boldsymbol{k}$. $\mu = g|\psi_0(\boldsymbol{r})|^2$ is the chemical potential. Substituting Eq. (2.77) into Eq. (2.74) and collecting terms for $e^{i(\boldsymbol{k}\cdot\boldsymbol{r}-(\mu+\omega)t)}$ and $e^{-i(\boldsymbol{k}\cdot\boldsymbol{r}+(\mu-\omega)t)}$, we obtain the following eigenvalue equation for the two excitation waves

$$\begin{pmatrix} \frac{\hbar k^2}{2m} + \mu & \mu \\ -\mu & -\frac{\hbar k^2}{2m} - \mu \end{pmatrix} \begin{pmatrix} u_{\boldsymbol{k}} \\ v_{\boldsymbol{k}} \end{pmatrix} = \omega \begin{pmatrix} u_{\boldsymbol{k}} \\ v_{\boldsymbol{k}} \end{pmatrix} \qquad (2.78)$$

It is straightforward to find the eigenvalues given by

$$\omega = \pm\sqrt{\omega_k(\omega_k + 2\mu)} \qquad (2.79)$$

where $\hbar\omega_k = \hbar^2 k^2/2m$ is the kinetic energy of a non-interacting free particle. Equation (2.79) has the same form as the excitation spectrum we obtained in Eq. (2.48) based on the Bogoliubov theory.

55

2.5 Realization of Bose-Einstein Condensation

Bose-Einstein condensation was considered for a long time as a somewhat unrealistic peculiarity of the Bose gas. For many years the only example of a Bose condensed system was superfluid helium ^{4}He [53, 54]. However, due to strong interactions in ^{4}He, many salient features of BEC were not observed; for instance the condensate fraction does not exceed 10%. The first unambiguous proof for a BEC in a weakly interacting system came from atomic physics in 1995 where a dilute cloud of rubidium atoms [27] was cooled down to nanokelvin temperatures. A sharp distribution in velocity space appeared, as shown in Fig. 2-7, which is probably the most widely used example when demonstrating the idea of BEC. As shown in the figure, just before the appearance of a Bose-Einstein condensation, atoms follow the Maxwell-Boltzmann distribution and spread out in the velocity map. Upon the formation of the condensate, a significant population at zero velocity is observed, accompanied with a thermal tail. After further evaporation, as is called for the final step in BEC preparation, the thermal tail is significantly compressed, leaving a population of nearly pure condensate. Since 1995, BEC has been observed in various atomic systems, such as alkali atoms ^{85}Rb [55], ^{23}Na [28], ^{7}Li [29], ^{39}K [56], ^{41}K [57], and ^{133}Cs [58], and two-electron atoms such as ^{4}He [59, 60], ^{170}Yb [61], ^{174}Yb [62], ^{176}Yb [63], ^{40}Ca [64], ^{84}Sr [65], ^{86}Sr [66, 67], ^{88}Sr [68], and also ^{1}H [69] and ^{52}Cr [70]. Extension to atomic species beyond these relatively abundant atomic species is still an active field of research [71, 72, 73].

For realization of BEC, the most challenging part is to cool the system down to sub-micro Kelvin, a temperature that is more than six orders of magnitude lower than that in the deep universe. The most important condition in the quest for such low temperatures is total isolation from the outside world. This is achieved by spatial trapping of atomic gases in a magneto-optical trap, when temperatures of order of 10 μK are attained by laser cooling [74]. In the decisive step of evaporative cooling, the most energetic atoms escape the trap when the confining potential is lowered [75], and hence the temperature of the remaining gas falls below the critical temperature to undergo BEC. More experimental details about these techniques can be found in
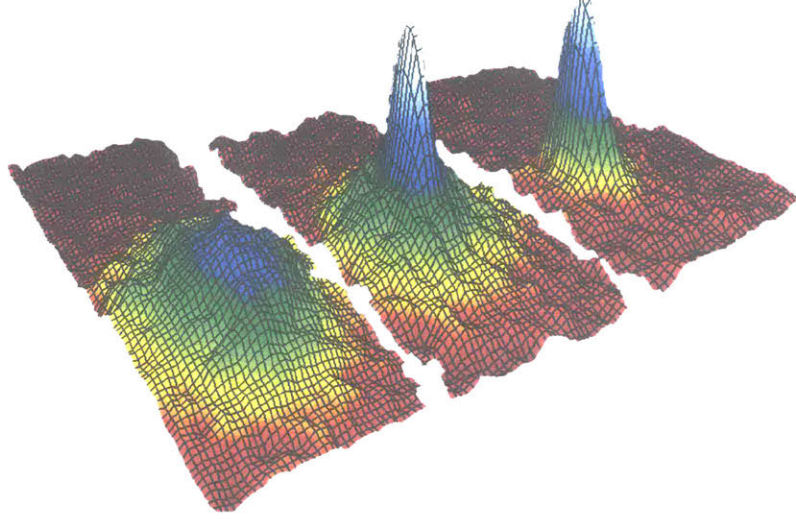
Figure 2-7: Figure courtesy of the Nobel prize committee. Velocity distributions for a gas of rubidium atoms at different temperatures. Left: above the critical temperature. Middle: at the critical temperature. and Right: below the critical temperature, confirming the discovery of a new phase of matter.

textbooks [40, 51].

Following the success in the realization of condensation in atomic systems, a proposal was made in 1996 with regard to the BEC of exciton-polaritons. Exciton-polaritons are hybrid quasi-particles consisting of quantum-well (QW) excitons and microcavity photons in semiconductor planar microcavities [76] . By dressing QW excitons with microcavity photons, new bosonic quasiparticles called exciton-polaritons with extremely light effective masses are produced. Exciton-polaritons can overcome the localization and inhomogeneous broadening problem via their spatially extended wavefunctions compared to atomic systems, leading to a 10-fold increase in the critical temperature when quantum phenomena become important. Indeed, condensation of polaritons with some signatures of BEC has been realized ranging from liquid helium temperature all the way up to room temperature [32, 33, 34, 35, 77, 78, 79]. Figure 2-8 shows the condensation of polaritons in a CdTe-based microcavity at 5 K. Similar features such as spectral and momentum narrowing were observed upon the formation of condensation. However, compared to atomic BEC, condensation of polaritons is still much less explored mainly due to slow progress in the fabrication
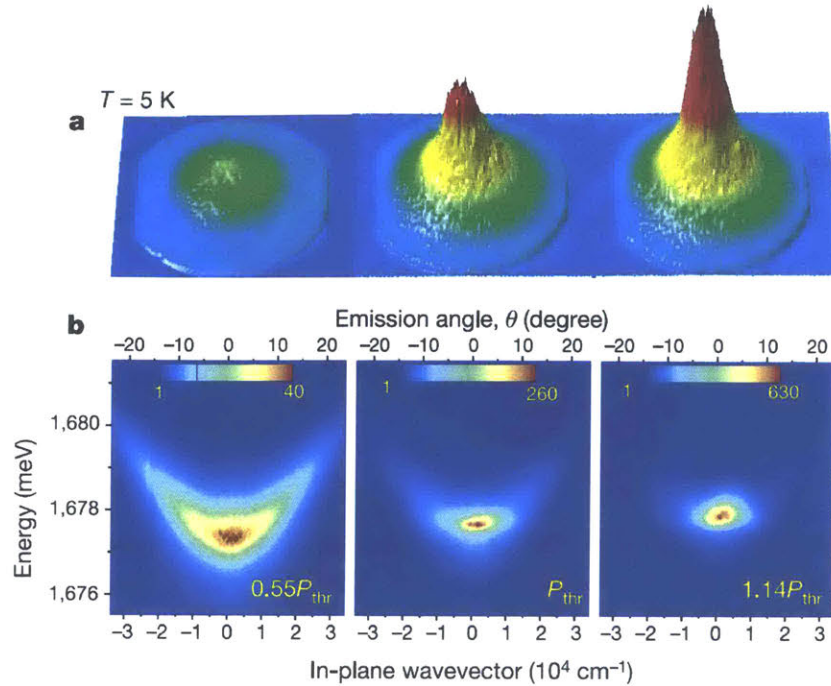
Figure 2-8: Figure taken from Ref. [33]. Far-field emission measured at 5 K for three excitation intensities. (a) Pseudo-3D images of the far-field emission within the angular cone of $\pm 23°$, with the emission intensity displayed on the vertical axis in arbitrary units. With increasing excitation power, a sharp and intense peak is formed in the center of the emission distribution, $\theta_x = \theta_y = 0°$, corresponding to the lowest momentum state $k_\parallel = 0$. (b) Same data as in (a) but resolved in energy.

of high-quality samples.

The concept of Bose-Einstein condensation finds applications in many systems other than ultracold atoms and exciton-polaritons. Historically, the first of these were superconducting metals where the bosons are pairs of electrons with opposite spin. Collective magnetic excitations in magnetic materials such as magnons have also been shown to undergo condensation under appropriate conditions [31]. On the other hand, the search of exciton condensation is still an ongoing effort due to various experimental challenges, although it has been proposed by Moskalenko et al. dated back to 1962 [80, 81]. Table 2.1 compares the conditions of condensation with atomics, excitons and polaritons. Because the effective masses of the quasiparticles can be engineered to be much less than the atomic masses, the critical temperature of the

condensation is significantly increased all the way up to room temperature.

Fermions can also undergo Bose-Einstein condensation when they pair up by neutron-neutron interactions and proton-proton interactions [82, 83]. The most celebrated example is conventional superconductivity in metals [84] where a pair of electrons at the Fermi surface are bound together by phonons to allow condensation of the charged pair, that is, superconductivity. The possibility of mesons, either pions or kaons, forming a Bose-Einstein condensate in the cores of neutron stars has been widely discussed [85, 86, 87, 88]. It is a wonder of nature that Bose-Einstein condensation of atoms is analogous to neutron stars, whose temperatures are 20 orders of magnitude different. This equivalence has been exploited to simulate the evolution of early universe [89]. In the fields of nuclear and particle physics, the idea of Bose-Einstein condensation also helps in understanding the vacuum as a condensate of quark-antiquark pairs, the so-called chiral condensates [90, 91].

2.6   Conclusion

Condensation is a purely quantum mechanical phenomenon manifested by macroscopic occupation of the ground state when the thermal de Broglie wavelength of the bosonic particle is comparable to the interparticle spacing in the system. Some salient features of condensates can be understood based on thermodynamic treatment of the non-interacting ideal gas. When the underlying particles are interacting, more peculiar features such as quantum depletion and phase-locking emerge, which can be understood in light of the Bogoliubov theory. BEC has been realized in various systems from ultracold atomic gases to elementary excitations in solids, in particular exciton-polaritons in microcavities, which will be the focus of this dissertation.

Chapter 3

Excitons and Exciton-Polaritons in Microcavities

An exciton is a hydrogen-like quasiparticle in solids that is formed when an electron and a hole are bound together by Coulomb interaction after a photoexcitation above the bandgap. Excitons play a central role in energy transport in solid-state materials ranging from light harvesting antennas in bacteria and green plants to the excitonic switches and other optical logical units. Instead of describing the change in the motion of 10^{23} atoms and their constituents in full detail, by using the exciton formalism, light-matter interactions in solids are understood as the creation and annihilation of excitons as well as scattering events involving excitons. Depending on their size compared to the unit cell of their host lattice, excitons can be categorized as either Frenkel excitons [92] or Wannier-Mott excitons [93, 94]. Frenkel excitons are typically tightly bound to host molecules, while Wannier-Mott excitons can delocalize over tens of lattice sites. By reducing the dimension of the hosting lattice, quantum confinement will lead to an increase in the overlap between the electron and hole wavefunctions and to quantization of the electron and hole energy levels, thereby changing the behavior of excitons dramatically. Exciton levels in zero-dimension quantum dots have similar characteristics to atomic energy levels, with fully quantized sharp emission peaks. When separating the electron and hole in real space, typically by introducing a heterostructure, the dipole moments of the excitons can be significantly increased.

The lifetime of this type of excitons is also increased because the spatial separation reduces the rate of electron-hole recombination.

The properties of excitons can be further altered by dressing it with confined photons. By placing an exciton medium, typically a two-dimensional quantum well (QW), at the antinodes of an optical cavity that is resonant with the excitonic transitions in the QW, strong coupling between the confined light mode and excitonic polarizabilities in the QW leads to the formation of exciton-polaritons [95, 96]. Exciton-polaritons in a microcavity are composite two-dimensional bosonic quasiparticles with an extremely low effective mass that is typically about 10^{-5} of the free electron mass. One can view the polaritons as photons with nonlinear interactions many orders of magnitude higher than those in typical optical materials due to their excitonic components. Alternatively, they can be viewed as dressed excitons which are given much longer diffusion length, with propagation distances up to millimeters [97, 98]. The light effective mass inherited from the cavity photon also allows for quantum phenomena, such as Bose-Einstein condensation [33, 34], superfluidity [99], quantized vortices [100, 11, 12, 101, 102], and macroscopic quantum states [103, 104], to be observed at temperatures from tens of Kelvin up to room temperatures [77, 78, 79]. More importantly, the light-matter dual nature of polaritons permits probing in a direct way by examining the properties of those photons that couple out the cavity due to finite cavity reflectivity. Additionally, the repulsive interaction from excitonic constituents can be exploited for the manipulation of polaritons to realize all-optical transistors [105] and switches [10].

In this chapter, excitons and exciton-polaritons are discussed. We start with a fully quantum description of excitons, and derive the binding energy as well as the Bohr radius of excitons in Section 3.1. Excitons in quantum wells are discussed in Section 3.2, including the modification of the wavefunction and binding energy due to quantum confinement. Section 3.3 presents an overview of optical microcavities. Several characteristic measures of the quality of microcavities such as Q-factor and finesse are introduced. The Purcell enhancement of spontaneous emission is also discussed. In Section 3.4, we present a detailed review of microcavity polaritons. Both

semiclassical and fully quantum approaches are used to compute optical reflectance and exciton-photon coupling. A comparison between exciton-polaritons and phonon-polaritons concludes the chapter.

3.1 Excitons as Bosons

At low excitation densities, typically in a range where the interparticle spacing is much larger than the excitonic radius a_B, i.e, $na_B^3 \ll 1$, excitons can be regarded as bosons. When excitation densities increas, electrostatic screening becomes so strong that electrons and holes cannot effectively bind any longer. At sufficiently high densities, the fermionic characteristics of electrons and holes cannot be neglected, and the system forms an electron-hole liquid [106, 107]. Such a liquid cannot be solidified but remains a liquid even down to $T = 0$ K.

3.1.1 Quantum description of excitons

Following Hanamura and Haug [108, 109], the Hamiltonian of electronic systems has the form

$$\hat{\mathcal{H}} = \int dr \hat{\Psi}^\dagger(r)\hat{\mathcal{H}}_0(r)\hat{\Psi}^\dagger(r) + \frac{1}{2} \int drdr'\hat{\Psi}^\dagger(r)\hat{\Psi}^\dagger(r')\hat{V}(r - r')\Psi(r)\Psi(r') \quad (3.1)$$

where $\hat{\mathcal{H}}_0(r)$ is the Hamiltonian of the single electron that takes into account the band structure of the solid, and $\hat{V}(r)$ is the Coulomb interaction in the solid. The field operator for electrons $\hat{\Psi}$ can be expanded in terms of the Bloch waves

$$\Psi(r) = \frac{1}{\sqrt{N}} \sum_{k;j=c,v} \hat{a}_{kj}u_{kj}(r)e^{ik\cdot r} \quad (3.2)$$

Here $j = c, v$ denote the conduction and valence band, $u_{kj}(r)$ is the Bloch wavefunction, N is the number of unit cells of the lattice, and $\hat{a}_{kj}^\dagger$ and $\hat{a}_{kj}$ are fermionic creation and annihilation operators for an electron, respectively. For the valence band, we introduce the hole creation operator $\hat{b}_{-k}$ to replace the electron annihilation

operator

$$\hat{a}_{kv}^{\dagger} = \hat{b}_{-kc}$$ (3.3)

because annihilation of a valence band electron in a state with a wavevector k, spin σ and charge $-e$ can be equivalently treated as the creation of a hole in a state with the opposite wavevector $-k$, flipped spin $\bar{\sigma}$ and charge $+e$. For the conduction band, we simplify the notation as

$$\hat{a}_{kc} = \hat{a}_k$$ (3.4)

Substituting Eq. (3.2) and Eq. (3.4) into Eq. (3.1), and neglecting number non-conserving terms, we obtain the Hamiltonian for a direct two-band semiconductor in the form of [109]

$$
\hat{\mathcal{H}} = \sum_{k} E_e(k)\hat{a}_k^{\dagger}\hat{a}_k + \sum_{k} E_h(k)\hat{b}_k^{\dagger}\hat{b}_k
$$
$$
+ \frac{1}{2} \sum_{k_1,k_2,k_3,k_4} V_{k_1,k_2,k_3,k_4}^{cccc}\hat{a}_{k_1}^{\dagger}\hat{a}_{k_2}^{\dagger}\hat{a}_{k_3}\hat{a}_{k_4} + \frac{1}{2} \sum_{k_1,k_2,k_3,k_4} V_{-k_1,-k_2,-k_3,-k_4}^{vvvv}\hat{b}_{k_1}^{\dagger}\hat{b}_{k_2}^{\dagger}\hat{b}_{k_3}\hat{b}_{k_4}
$$
$$
- \sum_{k_1,k_2,k_3,k_4} \left(V_{k_1,k_3,k_2,k_4}^{cvvc} - V_{k_1,k_3,k_4,k_2}^{cvcv} \right) \hat{a}_{k_1}^{\dagger}\hat{b}_{k_2}\hat{b}_{k_3}\hat{a}_{k_4}
$$ (3.5)

where $\hat{a}_k$ and $\hat{b}_k$ are the annihilation operators for electrons and holes in the conduction and valence band, respectively, and

$$V_{k_1,k_2,k_3,k_4}^{ijlm} = \langle k_1 i, k_2 j | \hat{V} | k_3 l, k_4 m \rangle$$ (3.6)

is the direct and exchange interactions between electrons and holes due to the Coulomb potential $\hat{V}$. In the effective-mass approximation, $E_e(k)$ and $E_h(k)$ are the kinetic

energies of an electron or a hole with effective masses m_e and m_h, respectively

$$E_e(k) = E_g + \hbar^2 k^2 / 2m_e \qquad (3.7)$$

$$E_h(k) = \hbar^2 k^2 / 2m_h \qquad (3.8)$$

where E_g is the bandgap energy. Now consider the eigenvalue equation for a general electron-hole pair state,

$$\hat{\mathcal{H}}|x\rangle = E|x\rangle \qquad (3.9)$$

with

$$|x\rangle = \sum_{\boldsymbol{k},\boldsymbol{k}'} A_{\boldsymbol{k},\boldsymbol{k}'} \hat{a}_{\boldsymbol{k}}^{\dagger} \hat{b}_{\boldsymbol{k}}^{\dagger} |0\rangle \qquad (3.10)$$

Substituting Eq. (3.16) into Eq. (3.9), we obtain

$$[E_e(k) + E_h(k') - E)A_{\boldsymbol{k},\boldsymbol{k}'} - \sum_{\boldsymbol{k},\boldsymbol{k}'} \left(V_{\boldsymbol{k},-\boldsymbol{l}',-\boldsymbol{k}',\boldsymbol{l}}^{cvvc} - V_{\boldsymbol{k},-\boldsymbol{l}',-\boldsymbol{l},-\boldsymbol{k}'}^{cvcv} \right) A_{\boldsymbol{k},\boldsymbol{k}'} = 0 \qquad (3.11)$$

For Wannier excitons, the plane-wave factors in Eq. (3.2) and the Coulomb potential $\hat{V}$ are slowly varying functions which change very little in one unit cell, hence Eq. (3.6) can be computed by first integrating the Bloch functions in one unit cell, and then summing over all unit cells weighted by the plane-wave factors. The slow-varying envelope also leads to quasi-orthogonality of the periodic function u in the long-wavelength limit

$$\frac{1}{v_0} \int_{\text{unit cell}} u_{\boldsymbol{k}\approx 0,c}^{*}(\boldsymbol{r}) u_{\boldsymbol{k}\approx 0,c}(\boldsymbol{r}) d\boldsymbol{r} \approx 1 \qquad (3.12)$$

$$\frac{1}{v_0} \int_{\text{unit cell}} u_{\boldsymbol{k}\approx 0,c}^{*}(\boldsymbol{r}) u_{\boldsymbol{k}\approx 0,v}(\boldsymbol{r}) d\boldsymbol{r} \approx 0 \qquad (3.13)$$

65

where v_0 is the volume of the unit cell. In this case, the exchange integral can be neglected, and the Coulomb interaction can be greatly simplified as

$$\hat{V}_{k,-l',-k',l}^{cvvc} = \frac{1}{N_{\text{cell}}^2} \int dr\, dr' \frac{e^2}{\epsilon|r - r'|} e^{i(l-k)\cdot r + i(l'-k')\cdot r'} \tag{3.14}$$

Taking the Fourier transform of (3.11) with the approximated Coulomb interaction, we obtain the Wannier equation for an exciton [93]

$$\hat{\mathcal{H}}_{ex}\Phi(r_e, r_h) = E\Phi(r_e, r_h) \tag{3.15}$$

with

$$\hat{\mathcal{H}}_{ex} = -\frac{\hbar^2}{2m_e}\nabla^2 - \frac{\hbar^2}{2m_h}\nabla^2 + E_g - \frac{e^2}{\epsilon|r - r'|} \tag{3.16}$$

where the two-particle wavefunction can be expressed in terms of the amplitudes $C_{k,k'}$ as

$$\Phi(r_e, r_h) = \sum_{k,k'} C_{k,k'} e^{ik\cdot r_e + ik'\cdot r_h} \tag{3.17}$$

By introducing the relative coordinate $r = r_e - r_h$ and the center-of-mass coordinate $R = (m_e r_e + m_h r_h)/(m_e + m_h)$, the center-of-mass motion and the relative motion can be separated by means of

$$\Phi(r_e, r_h) = \phi_n(r)\frac{1}{V}e^{iK\cdot R} \tag{3.18}$$

where K corresponds to the center-of-mass momentum. The resulting equation of the relative motion is

$$\left(-\frac{\hbar^2}{2m_r}\nabla_r^2 - \frac{e^2}{\epsilon_0\epsilon r} + E_{b,n}\right)\phi_n(r) = 0 \tag{3.19}$$

where $m_r = m_e m_h/(m_e + m_h)$ is the reduced mass. Equation (3.19) has the form of the standard Schrödinger equation for a hydrogen atom. The total energy of the pair

66

is then given by

$$E(K, n) = E_g - E_{b,n} + \frac{\hbar^2 K^2}{2(m_e + m_h)} \tag{3.20}$$

with the binding energy of the pair being

$$E_B = \frac{\hbar^2}{2a_B^2 m_r} \tag{3.21}$$

and $E_{B,n} = E_b/n^2$. Here a_B is the exciton Bohr radius, defined as,

$$a_B = \frac{4\pi\epsilon_0\epsilon\hbar^2}{e^2 m_r} \tag{3.22}$$

As can be seen, the exciton Bohr radius is an intrinsic material property determined by the electrostatic permittivity ϵ and the reduced mass of the exciton m_r. Excitons in inorganic semiconductors are typically much more delocalized than those in organic materials and molecules. Now the light-matter interaction in the two-band model can be defined as

$$|x\rangle = \hat{e}_{\mathbf{K},n}^{\dagger}|0\rangle \tag{3.23}$$

with the exciton creation operator

$$\hat{e}_{\mathbf{K},n}^{\dagger} = \sum_{\mathbf{k},\mathbf{k}'} \delta_{\mathbf{K},\mathbf{k}+\mathbf{k}'} \phi_n(\mathbf{l}) \tag{3.24}$$

Here $|0\rangle$ is the ground state of the system, $\mathbf{l} = (m_h\mathbf{k} - m_e\mathbf{k}')/(m_e + m_h)$, and $\phi_n(\mathbf{l})$ is the Fourier transform of $\phi_n(\mathbf{r})$. Working out the algebra, we find the commutation relations of the exciton operators are

$$[\hat{e}_{\mathbf{K}',n'}, \hat{e}_{\mathbf{K},n}] = 0 \tag{3.25}$$

$$[\hat{e}_{\mathbf{K}',n'}^{\dagger}, \hat{e}_{\mathbf{K},n}^{\dagger}] = 0 \tag{3.26}$$

$$[\hat{e}_{\mathbf{K}',n'}, \hat{e}_{\mathbf{K},n}^{\dagger}] = \delta_{\mathbf{K}\mathbf{K}'}\delta_{nn'} - \mathcal{O}(n_{exc}a_B^3) \tag{3.27}$$

Therefore, excitons can be considered approximately bosonic particles in the low-density regime when $n_{exc} \ll 1/a_B^3$, i.e., the interparticle spacing of excitons is much larger than their Bohr radius. At high densities, when an electron-hole liquid forms, the light-matter interaction cannot be fully described by uncorrelated excitons any longer.

3.1.2 Properties of excitons in different materials

Depending on the dielectric screening ϵ of the system, the exciton Bohr radius can vary from a few angstroms to tens of nanometers. Frenkel excitons are those excitons that are typically bound tightly to their host lattice, with binding energies on the order of 100 meV. At present they are widely studied in organic materials where they dominate the optical absorption and emission spectra. Unlike Frenkel excitons, Wannier-Mott excitons have relatively small binding energies on the order of a few meV. Between Frenkel and Wannier-Mott excitons, there are so-called charge-transfer excitons which are spatially separated electron-hole pairs having a spatial extension on the order of the crystal lattice constant. The lowest-energy charge-transfer exciton usually extends over two nearest-neighbor molecules in a molecular crystal and creates a donor-acceptor complex. In table 3.1 we list the binding energies E_B and Bohr radii

crystal	E_g (eV)	m_r/m_0	E_B (meV)	a_B (Å)
GaAs	1.519	0.066	4.1	150
CdTe	1.606	0.089	5.0	80
GaN	3.426	0.770	26.4	28
InSb	0.237	0.014	0.5	860
MoS$_2$ (monolayer)	3.4	~ 1	480	8

Table 3.1: Exciton properties in different systems

a_B for different materials. Here E_g is the band gap of the material, and m_r/m_0 is the ratio of the exciton mass to the electron mass in vacuum.

3.2 Quantum Well Excitons

When spatial confinement is introduced in the host lattice, the properties of excitons can be altered significantly. Depending on the relative values of layer thickness L and exciton Bohr radius a_B, excitons behave differently. In the limit of $L \gg a_B$, called the thin-film regime, the excitonic Rydberg energy R_y is much bigger than the quantization energy $\hbar^2/m_e L$, and thus the excitons are only weakly perturbed by the confinement. The internal electron-hole wavefunction is undistorted, but the exciton center-of-mass motion is quantized. In the limit of $L \sim a_B$, called the quantum well regime, the excitonic Rydberg energy is comparable to or smaller than the quantization energy of the subbands, and thus quantization of both electron and hole subbands occurs. The distortion of the internal exciton wavefunction due to a decrease of the average electron-hole separation leads to an increase in the binding energy. In the limit of $L \ll a_B$, tunneling of electrons and holes becomes innegligible, thus leading to a reduction in the electron-hole wavefunction overlap and a decrease in the binding energy.

3.2.1 Quantum confinement

With the advance of epitaxial growth techniques of molecular beam epitaxy, semiconductor materials can be fabricated with atomic monolayer precision, giving rise to novel structures such as two-dimensional (2D) quantum wells, 1D quantum wires and 0D quantum dots. A QW is a thin-layer narrow-bandgap semiconductor material sandwiched between two barrier layers of wider bandgap materials, as shown in Fig. 3-1. The emission wavelength depends on the QW dimensions and is different from the bandgap energy of either semiconductor. The QW thickness is comparable to the exciton Bohr radius, hence the motions of the electrons and holes are confined perpendicular to the QW plane, which is referred to as the z direction by convention. The wavefunctions along this direction are reminiscent of particle-in-a-box states, as shown in Fig. 3-2, and their energy levels are quantized, leading to the formation of multiple energy bands in the in-plane energy dispersion relations, with a typical
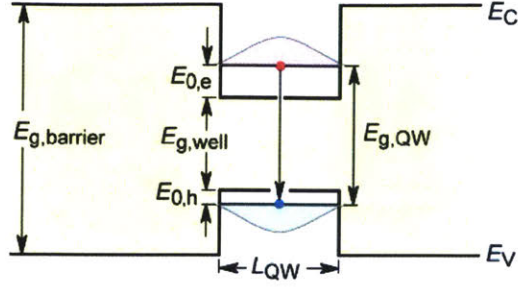
Figure 3-1: A schematic illustration of the band edge alignment of a quantum well.
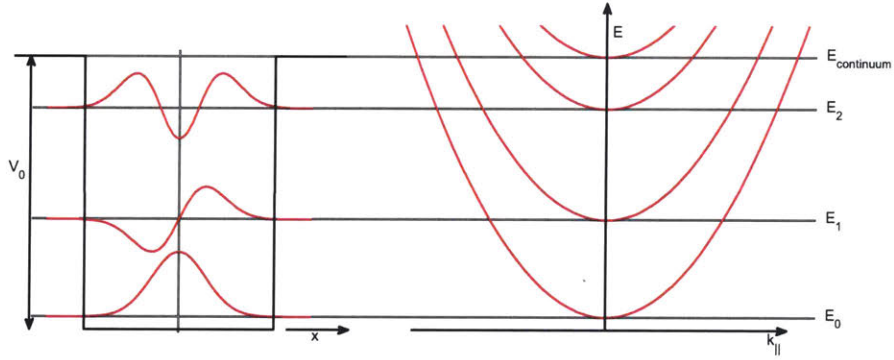
Figure 3-2: The wavefunctions of bound states within a quantum well (left) and corresponding in-plane energy dispersions of those states (right).

energy separation on the order of 10 meV in GaAs QWs. Due to the quantization, the energy dependence of the density of states (DOS) changes from $\propto \sqrt{E}$ in 3D (blue dashed line) to step functions in 2D (red solid line), as shown in Fig. 3-3.

3.2.2   QW exciton binding energy

To take into account the confining potential of the QW, we rewrite Eq. (3.16)

$$\left(-\frac{\hbar^2}{2m_e}\nabla_e^2 - \frac{\hbar^2}{2m_h}\nabla_h^2 + U_e(z_e) + U_h(e_h) - \frac{e^2}{4\pi\epsilon_0\epsilon|\boldsymbol{r}_e - \boldsymbol{r}_h|} \right) \Phi(\boldsymbol{r}_e, \boldsymbol{r}_h) = E\Phi(\boldsymbol{r}_e, \boldsymbol{r}_h)$$

$$(3.28)$$
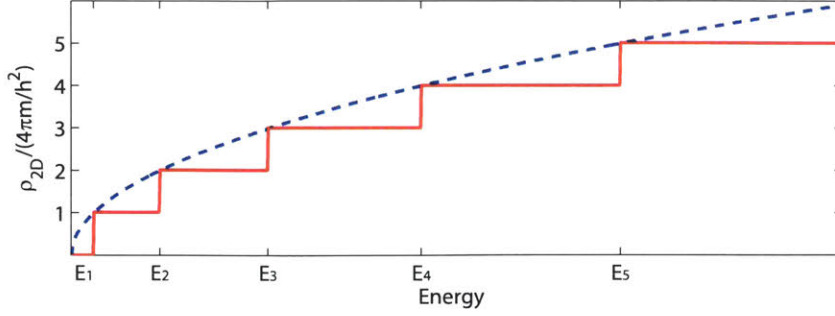
Figure 3-3: Energy density of states (DOS) of excitons in a quantum well (red solid line) and in the bulk (dashed blue line).

with $U_{e,h}(z_{e,h})$ being the confining potentials for electrons and holes in the z direction, which are assumed to be step functions at the well boundaries for simplicity. Therefore, we decompose the wavefunction of exciton's motion as

$$\Phi(\boldsymbol{r}_e, \boldsymbol{r}_h) = F(\boldsymbol{R})f(\boldsymbol{\rho})U_e(z_e)U_h(z_h) \tag{3.29}$$

where $\boldsymbol{R}$ is the center-of-mass coordinate and $\boldsymbol{\rho} = \boldsymbol{\rho}_e - \boldsymbol{\rho}_h$ is the in-plane electron-hole relative motion. The four components in Eq. (3.29) describes the exciton center-of-mass motion, the relative electron-hole motion in the plane of the QW, and the electron and hole motion normal to the plane, in order. They satisfy

$$\left\{ -\frac{1}{\rho}\frac{\partial}{\partial\rho}\left(\frac{\hbar^2}{2m_r}\frac{\partial}{\partial\rho}\rho\right) - \frac{e^2}{4\pi\epsilon_0\epsilon}\iint \frac{|U_e(z_e)|^2|U_h(z_h)|^2}{\sqrt{\rho^2 + (z_e - z_h)^2}}dz_e dz_h \right\} f(\rho) = -E_B^{QW} f(\rho) \tag{3.30}$$

and

$$\left\{ -\frac{\hbar^2}{2m_{e,h}}\nabla_{e,h}^2 + U_{e,h} - \frac{e^2}{4\pi\epsilon_0\epsilon}\iint \frac{|f(\rho)|^2|U_{e,h}(z_{e,h})|^2}{\sqrt{\rho^2 + (z_e - z_h)^2}}2\pi\rho d\rho dz_{e,h} \right\} U_{e,h}(z_{e,h}) = E_{e,h}U_{e,h}(z_{e,h}) \tag{3.31}$$

71
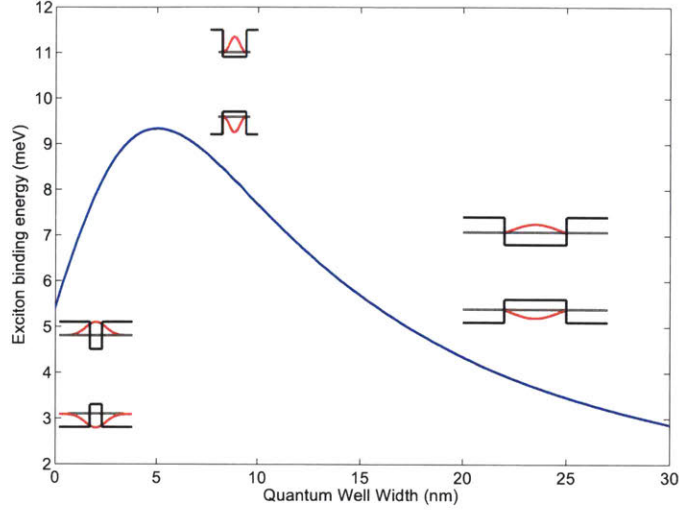
Figure 3-4: Exciton binding energy as a function of the QW width. The insets are schematic illustrations of the QW potential and wavefunctions of electron and hole for different QW widths.

where $E_{e,h}$ are the electron and hole confining energies, and E_B^{QW} is the exciton binding energy in the QW, which can be expressed explicitly as [9]

$$E_B^{QW}(a) = -\frac{\hbar^2}{2m_r a^2} + \frac{e^2}{4\pi\epsilon_0\epsilon} \iiint \frac{|f(\rho)|^2 |U_e(z_e)|^2 |U_h(z_h)|^2}{\sqrt{\rho^2 + (z_e - z_h)^2}} 2\pi\rho d\rho dz_e dz_h \qquad (3.32)$$

where a is the width of the QW. Figure 3-4 plots the exciton binding energy as a function of the well width computed from Eq. (3.32) with a finite barrier. As is seen, the binding energy increases if the exciton confinement strengthens, but as the width is further decreased, the spatial overlap across the confinement direction between the electron and hole wavefunctions decreases significantly, eventually leading to a decrease in the binding energy. On the other hand, in an ideal 2D QW with an infinite barrier height, i.e., $|U_{e,h}(z_{e,h})|^2 = \delta(z_e, z_h)$, one can find the binding energy of the two-dimensional exciton exceeds by a factor of four compared to the bulk exciton binding energy

$$E_B^{QW} = 4E_B \qquad (3.33)$$

72

where E_B is given by Eq. (3.21).

3.2.3   Optical transition in quantum wells

The oscillator strength of bulk excitons is defined as

$$f = \frac{2m_r\omega}{\hbar}|\langle u_v|e\cdot r|c_v\rangle|^2\frac{V}{\pi a_B^3} \tag{3.34}$$

where e is the polarization vector of the incident field, and $|u_v\rangle$, $|c_v\rangle$ are the valence band and conduction band wavefunctions, respectively. In quantum wells, in order to account for the quantum confinement, the oscillator strength is averaged over the growth direction

$$f = \frac{2m_r\omega}{\hbar}|\langle u_v|e\cdot r|c_v\rangle|^2\frac{S}{\pi a_B^2}\left|\int U_e(z)U_h(z)dz\right|^2 \tag{3.35}$$

More importantly, the lack of full translational invariance relaxes the requirement of momentum conservation in the growth direction. In contrast to bulk excitons, QW excitons with in-plane momenta $\hbar k_\parallel$ interact with a continuum of photon modes with the same in-plane momentum but arbitrary longitudinal momentum $\hbar k_z$. This is referred to as mesoscopic enhancement.

3.3   Optical microcavities

A resonator is a device or system that exhibits resonant behavior, that is, it naturally oscillates at some frequencies, called resonant frequencies. A guitar is an example of mechanical resonators. Similarly, an optical microcavity is an optical resonator in the sense that it is in resonance with optical light frequencies. An optical resonator has a dimension close to the wavelength of optical light, typically on the order of microns, leading to the term "microcavity". By utilizing either total internal reflection at the boundary between two dielectrics or destructive interference from distributed Bragg reflectors (DBRs), light modes are confined as standing waves inside microcavities.

In this section, we discuss some key characteristics and experimental fabrication of optical microcavities.

3.3.1 Planar microcavities based on DBRs

One example of optical microcavities is the planar microcavity in which two flat mirrors are brought into close proximity so that only a few multiples of half wavelengths of optical light can fit in between them. Metal mirrors and dielectric mirrors can be
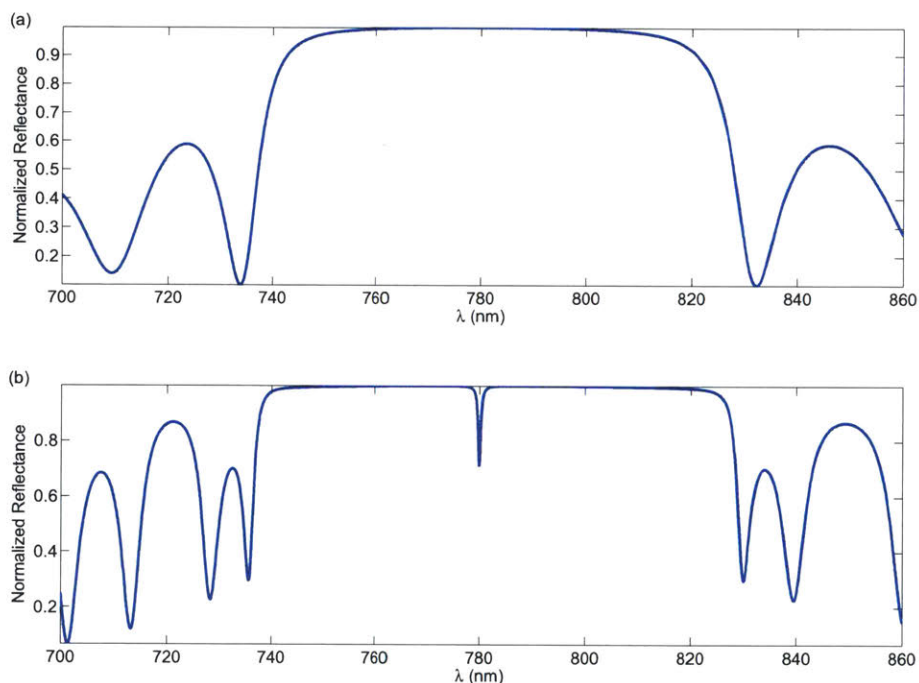
Figure 3-5: Simulated white light reflection spectra of the top DBR (a) and a $3\lambda/2$ microcavity structure (b).

employed in the construction of the cavity. A more popular choice is a DBR, which is made of layers of alternating high and low refractive indices, each layer with an optical thickness of $\lambda/4$, where λ is the resonant wavelength of the cavity. Light reflections from each interface destructively interfere, creating a stop band for transmission. In Fig. 3-5(a), we plot the simulated white light reflection spectrum of a DBR consisting of 14 pairs of AlAs/AlGaAs alternating layers. The reflectivity of the DBR in the range of 760 nm and 800 nm reaches $> 99\%$, forming the stop band. Away from the

stop band, the reflectivity decreases dramatically. Therefore, the DBR can be utilized as a high-reflectance mirror when the wavelength of the incident light is within the stop band.
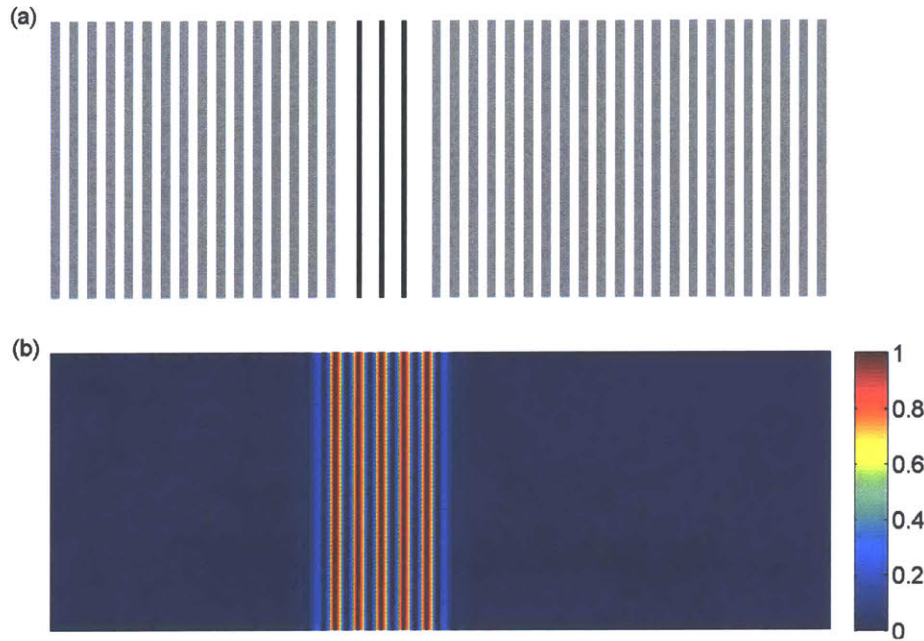
Figure 3-6: (a) A schematic illustration of the planar microcavity structure. The dark and light gray alternative layers indicate the distributed Bragg reflectors (DBRs) that are used to confine the light in the cavity. Sets of quantum wells (QWs) are shown as the black lines. (b) The calculated electric field energy distribution in the cavity.

When two such high-reflectance DBRs are separated with an optical thickness equal to an integer multiples of $\lambda/2$, an optical resonator with a resonance wavelength of λ is formed. Figure 3-6(a) shows a typical structure of such a microcavity. The light and dark gray layers indicate the alternating $\lambda/4$ DBRs, and the center region is the cavity where resonant photons are confined. The simulated white light reflection spectrum is shown in Fig. 3-5(b). The reflection dip at $\lambda = 780$ nm in the stop band gives the cavity resonance wavelength. We also show the stationary energy distributions of the electric field inside the cavity in Fig. 3-6(b). The peak-node structure indicates that the photon field inside the cavity is a standing wave. Some energy of the fields leaks into the DBRs, but most of the energy remains inside the cavity. In the next section, we will review some key physical measures that

characterize the cavity quality.

3.3.2 Characteristics of microcavities

Q-factor and finesse. The quality factor, better known as Q-factor, is simply defined as the ratio of a resonance cavity wavelength λ and the full width at half maximum (FWHM) bandwidth ($\delta\lambda$) of the resonance:

$$Q = \frac{\lambda}{\delta\lambda} \qquad (3.36)$$

If the thickness of the cavity is half of the resonance wavelength λ, Q is the average number of round trips that a photon travels inside the cavity before it couples out. Hence it is proportional to the confinement time in the unit of the optical period. The finesse of a cavity is defined as the ratio of the free spectral range $\Delta\lambda$, which is the frequency spacing between two successive reflected intensity maxima or minima, to the FWHM of a resonance $\delta\lambda$, that is,

$$\mathcal{F} = \frac{\Delta\lambda}{\delta\lambda} \qquad (3.37)$$

Provided that the pair of mirrors that form the cavity have reflectivities of R_1 and
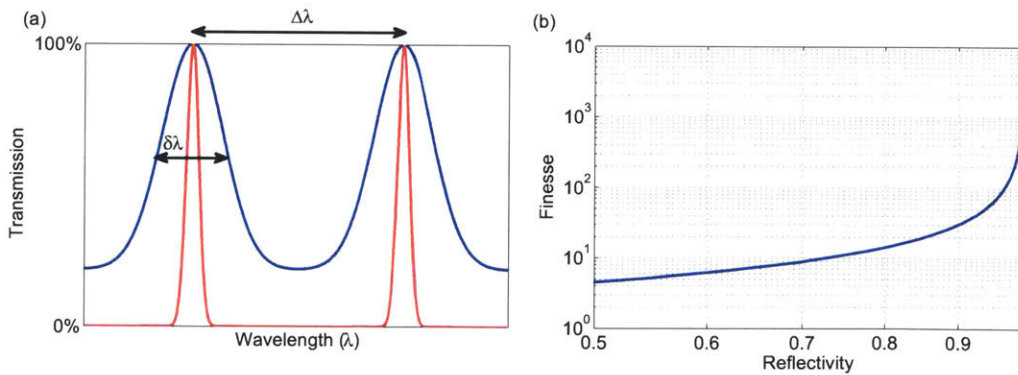
Figure 3-7: (a) The mode spectra of a cavity with a finesse of $\mathcal{F} = 18$ (red) and $\mathcal{F} = 3.6$ (blue). (b) The finesse as a function of reflectivity. Very high finesse factors require highly reflective mirrors.

76

R_2, the finesse can be directly computed as

$$\mathcal{F} = \frac{\pi(R_1 R_2)^{1/4}}{1 - (R_1 R_2)^{1/2}} \tag{3.38}$$

It is an intrinsic measure of the ability of the cavity to confine optical fields excluding propagation effects within the cavity as does the Q factor, and is related to the Q factor as

$$Q = \frac{n_{\text{eff}} L_{\text{cav}}}{\lambda} \mathcal{F} \tag{3.39}$$

where n_{eff} is the effective index of refraction of the cavity, and L_{cav} is the length of the cavity. In typical microcavities, we have $\lambda \sim L_{\text{cav}}$, and the Q factor is approximately the same as the finesse.

Figure 3-7(a) shows the mode spectra of two optical cavities with different Q factors. The resonance linewidth is much narrower in a high-finesse cavity, indicating the time the photons spend in the cavity is longer. High finesse is achieved by using high-reflectivity mirrors for the cavity. However, the increase in finesse is marginal until a reflectivity of $R > 95\%$ is realized, as shown in Fig. 3-7(b).

Intracavity field enhancement. The electric field is confined to standing waves inside the cavity, and the peak field strength is significantly enhanced compared to that in free space by a factor of

$$\frac{E_{\text{cavity}}}{E_{\text{free}}} \approx \frac{1}{1 - R} \tag{3.40}$$

where R is the total power reflectivity off the DBRs in a round trip. In a typical planar microcavity, this quantity ranges from 20 to 1000.

Angular dispersion of a cavity field. The dispersion of the photons is modified in the presence of the cavity. The total energy of the confined photons is calculated

as

$$E_{\text{cav}} = \frac{\hbar c}{n_{\text{eff}}}\sqrt{k_\perp^2 + k_\parallel^2} \tag{3.41}$$

where $k_\perp = 2\pi n_{\text{eff}}/\lambda$ is the longitudinal wave number given by the cavity confinement, and $k_\parallel$ is the in-plane wave number. There is a one-to-one correspondence between the incident angle θ and each resonance with in-plane wave number $k_\parallel$

$$k_\parallel = n_{\text{eff}}\frac{2\pi}{\lambda}\tan\left[\arcsin\left(\frac{\sin\theta}{n_{\text{eff}}}\right)\right] \approx \frac{2\pi}{\lambda}\theta \tag{3.42}$$

Because there is no confinement in the plane, we have $k_\parallel \ll k_\perp$, and then

$$E_{\text{cav}} \approx \frac{\hbar c}{n_{\text{eff}}}k_\perp\left(1 + \frac{k_\parallel^2}{2k_\perp^2}\right) = E_{\text{cav}}(k_\parallel = 0) + \frac{\hbar^2 k_\parallel^2}{2m_{\text{cav}}} \tag{3.43}$$

with the cavity photon effective mass defined as

$$m_{\text{cav}} = \frac{E_{\text{cav}}(k_\parallel = 0)}{c^2/n_{\text{eff}}^2} \tag{3.44}$$

where c is the light speed in vacuum. The cavity effective mass is typically on the order of 10^{-5} of the electron mass in vacuum. Rearranging Eq. (3.44), we would get the "energy-mass relation" as

$$E_{\text{cav}}(k_\parallel = 0) = m_{\text{cav}}v^2 \tag{3.45}$$

where v is the group velocity of the light in the cavity given by c/n_{eff}.

Purcell effect. By placing an emitter inside the cavity, the spontaneous emission rate can be significantly enhanced [110, 111, 112] due to the change of the photon density of states (DOS). Figure 3-8 illustrates the photon DOS in vacuum and in a single-mode cavity. The vacuum DOS has a typical parabolic shape, while the cavity DOS becomes Lorentzian. The spontaneous emission rate Γ for an emitter-vacuum,
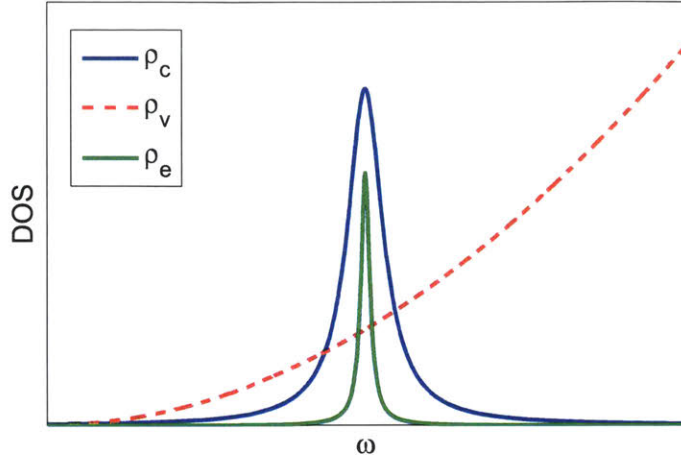
Figure 3-8: Density of states of the vacuum ρ_v, a single-mode cavity ρ_c and an emitter ρ_e as a function of ω.

or emitter-cavity, system is dictated by Fermi's golden rule

$$\Gamma = \frac{2\pi}{\hbar^2}|\mathbf{d}\cdot\mathbf{E}(\mathbf{r},t)|^2\rho(\omega) \tag{3.46}$$

for the case of an electric dipole $\mathbf{d}$ interacting at position $\mathbf{r}$ and time t with the light field $\mathbf{E}(\mathbf{r},t)$. As a result, the ratio of the spontaneous emission rate in the cavity Γ_c to that in vacuum Γ_v is [112]

$$\frac{\Gamma_c}{\Gamma_v} = \frac{3Q(\lambda/n_{\text{eff}})^3}{4\pi^2 V_{\text{eff}}}\frac{\delta\omega^2}{4(\omega_e-\omega)^2+\delta\omega^2}\frac{|\mathbf{E}(\mathbf{r})|^2}{|\mathbf{E}_{\text{max}}|^2}\left(\frac{\mathbf{d}\cdot\mathbf{E}(\mathbf{r})}{dE}\right)+f \tag{3.47}$$

where ω_e and ω are the frequencies of the emitter and cavity resonance, respectively, $\delta\omega$ is the linewidth of the cavity resonance, $\mathbf{E}(\mathbf{r})$ is the electric field amplitude in the cavity, and $|\mathbf{E}_{\text{max}}|^2$ is the maximum intensity. This ratio allows the emitter in the cavity emit much faster than that in the bulk. The term

$$F_P = \frac{3Q(\lambda/n_{\text{eff}})^3}{4\pi^2 V_{\text{eff}}} \tag{3.48}$$

depends only on parameters of the cavity, and is known as the Purcell factor. It determines the upper limit of such an enhancement. The second part in Eq. (3.47)

shows the effect of detuning on the efficiency of enhancement. The lifetime of the emitter can be made arbitrarily long by detuning it away from the cavity resonance, until it is limited by other nonradiative losses given by f. The last two terms underline the effect of the cavity field distribution and the alignment of the dipole with the electric field. In order to achieve a greater enhancement, the emitter is typically placed at the antinode of the cavity field.

Purcell enhancement of spontaneous emission [112] is neatly demonstrated in
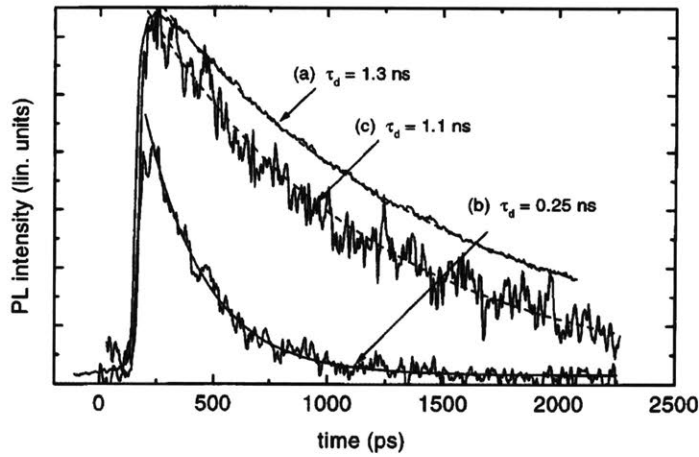
Figure 3-9: Figure taken from Ref. [112]. Time-resolved photoluminescence for a quantum dot when placed in a bulk material (a) or inside a pillar microcavity (b) and (c). In case (b) the dot is in resonance with the single mode of the cavity and decays about five times quicker than when it is coupled to a continuum of modes in the bulk. In case (c) the dot is detuned from the cavity mode and as a result displays only a small enhancement of its lifetime as compared to the bulk case.

Fig. 3-9 where the photoluminescence decays were recorded for a quantum dot placed in a bulk material or inside a cavity. Comparing (a) and (b), a factor of 5 enhancement was achieved. When detuning the cavity away from the frequency of the quantum dot emission, only a small enhancement of its lifetime is achieved, as seen in Fig. 3-9(c).

3.3.3 Other realizations of microcavities

The confinement methods employed in the fabrication of microcavities fall into three categories, as shown in Fig. 3-10. While the DBR-based planar microcavities usually

80

provide ultrahigh finesse, the whispering-gallery modes of silica and quartz micro-spheres have received considerable attention [113, 114, 115, 116, 117, 118]. Whispering-
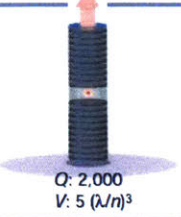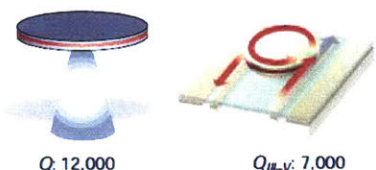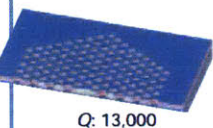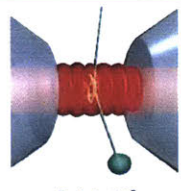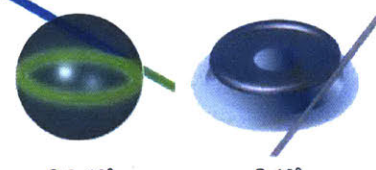
Figure 3-10: Figures taken from Ref. [118]. The microcavities are organized by column according to the confinement method used and by row according to high Q and ultrahigh Q. Small mode volume and ultrasmall mode volume are other possible classifications that are somewhat complementary to this scheme. Upper row: micropost [112], microdisk [119, 120], semiconductor [95], polymer add/drop filter [121], photonic crystal cavity [122]. Lower row: Fabry-Perot bulk optical cavity [123, 124], microsphere [116], microtoroid [125]. n is the material refractive index, and V, if not indicated, was not available. Microsphere volume V was inferred using the diameter noted in the cited reference and finesse (F) is given for the ultrahigh-Q Fabry-Perot as opposed to Q. Two Q values are cited for the add/drop filter: one for a polymer design, Q_{Poly}, and the second for a III-V semiconductor design, $Q_{\mathrm{III-V}}$.

gallery resonators are typically dielectric spherical structures in which waves are confined by continuous total internal reflection. Excellent surface finish is crucial for maximizing Q, and the formation of spheres through surface tension provides a near atomically smooth surface, with only a few nanometers or less of surface roughness. The bulk optical loss from silica is also exceptionally low and record-high Q factors of 8×10^9 and finesses of 2.3×10^6 have been obtained [115, 116]. Nevertheless, one of the remaining issues is the difficulty of tuning the wavelengths of the cavity modes, and efficiently coupling light into and out of the whispering-gallery mode.

Microcavities based on photonic crystals can provide extremely small mode volumes with even higher Q-factors [126], shown in the right column of Fig. 3-10, which are advantageous for many applications. The main issues for such microcavities are

the difficulty of their fabrication, the large surface area in proximity to the active area which produces non-radiative recombination centers and traps diffusing electron-hole pairs, and the difficulty in tuning their cavity resonances. Furthermore, Q values in fabricated structures are well below theoretical optima [127].

3.4 Microcavity Polaritons

When placing a QW in an optical microcavity, strong coupling between excitons in QWs and confined photons in the cavity leads to the normal-mode splitting into microcavity polaritons. Different theoretical schemes have been proposed to describe the exciton-photon coupled system in a planar microcavity. The semiclassical approach models the active medium as a Lorentz oscillator, and is convenient for the computation of the reflectivity, transmission and absorption. On the other hand, the quantum theory treats the light-matter interaction as the vacuum Rabi coupling, and is more advantageous for the computation of photoluminescence. It also plays a crucial role in understanding quantum phenomena such as Bose-Einstein condensation, superfluidity and quantized circulation with microcavity polaritons.

3.4.1 Semiclassical description

In the semiclassical theory of microcavity polaritons, Maxwell's equations are solved together with a constitutive relation between the electric field and displacement field. In calculating the optical response of a semiconductor microcavity, each layer except the active medium, typically semiconductor QWs, can be modeled by a local, frequency-independent dielectric constant $n(z)$. The QWs contain the additional excitonic contribution, which depends on frequency with a resonant form and gives an intrinsically nonlocal dielectric response. We take the z axis along the growth direction, and the electric field satisfies the following wave equation in the frequency

domain in each layer of the microcavity

$$\left[n^2(z)\frac{\omega^2}{c^2} + \frac{\partial^2}{\partial z^2} \right] \mathbf{E}(z,\omega) = -4\pi\frac{\omega^2}{c^2}\mathbf{P}(z,\omega) \tag{3.49}$$

The resonant polarization density $\mathbf{P}$ is zero in the DBRs and spacers. In the QW, to the lowest order, the polarization can be modeled as a Lorentzian oscillator,

$$\chi(\omega) = -\frac{\mu_{cv}}{\omega - \omega_0 + i\gamma} \tag{3.50}$$

where μ_{cv} is the transition dipole momentum matrix element, ω_0 is the resonance of the exciton $1s$ state, and γ is the dephasing rate of the $1s$ exciton state. A solution to Eq. (3.49), the electric field in each dielectric layer, with refractive index n, is written as the sum of right $E^+(z,\omega)$ and left $E^-(z,\omega)$ propagating waves:

$$E(z,\omega) = E^+(z,\omega) + E^-(z,\omega) \tag{3.51}$$

Given an arbitrarily defined initial field of a form given by Eq. (3.51), $E(0,\omega) = E^+(0,\omega) + E^-(0,\omega)$, the propagation of the electric field through DBRs and spacer layers is treated by the standard transfer matrix formalism. In transfer matrix method, the optical field after traveling a distance L can be found by multiplying a vector of the right and left going fields with a propagation matrix M:

$$\begin{pmatrix} E^+(L,\omega) \\ E^-(L,\omega) \end{pmatrix} = M \begin{pmatrix} E^+(0,\omega) \\ E^-(0,\omega) \end{pmatrix} \tag{3.52}$$

For the propagation of optical fields through a layer of material with a refractive index n, the change in the optical fields is given by a phase factor acquired from the propagation over the length of the material. In this case, the transfer matrix M is given by:

$$M = \begin{pmatrix} e^{ikL} & 0 \\ 0 & e^{-ikL} \end{pmatrix} \tag{3.53}$$

where $k = n\omega/c$ is the wave number in the material. When the optical field crosses an interface from left to right, where materials of refractive indices n_1 and n_2 are on the left and right side of the interface, the transfer matrix that relates the field amplitudes on the right to those on the left of the interface is

$$\begin{pmatrix} E_R^+ \\ E_R^- \end{pmatrix} = M_{1 \to 2} \begin{pmatrix} E_R^+ \\ E_R^- \end{pmatrix} \tag{3.54}$$

with

$$M_{1 \to 2} = \frac{1}{2n_2} \begin{pmatrix} n_1 + n_2 & n_1 - n_2 \\ n_1 - n_2 & n_1 + n_2 \end{pmatrix} \tag{3.55}$$

The propagation through the QW has the added complication of the resonant polarization. Denoted by M_{QW}, the transfer matrix that propagates the first-order field amplitudes through the QW in the thin well limit, i.e., $L \to 0$, is [128]

$$M_{\mathrm{QW}} = \begin{pmatrix} 1 + \beta_r & -\beta_r \\ \beta_r & 1 - \beta_r \end{pmatrix} \tag{3.56}$$

with

$$\beta_r = i\frac{2\pi\omega}{n_s c}\chi(\omega) \tag{3.57}$$

where n_s is the refractive index of the QW. Eventually, the propagation of the optical fields through the entire structure can be calculated by transforming the incident field using the total transfer matrix

$$M = \prod_i M_i \tag{3.58}$$

where the product is over all the layers of the semiconductor microcavity structure. The reflectivity and transmission are related to the matrix elements of M as

84
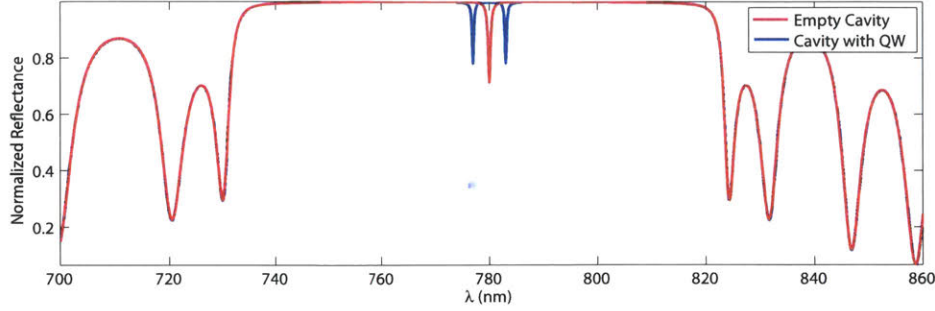
Figure 3-11: Simulated white light reflection spectrum of a $3\lambda/2$ microcavity structure with a QW embedded at the antinodes. The red line is the white light reflection spectrum from the same cavity without the QW.

$$R = \left| \frac{M_{21}}{M_{22}} \right|^2 \tag{3.59}$$

$$T = \left| M_{11} - \frac{M_{12}M_{21}}{M_{22}} \right|^2 \tag{3.60}$$

$$A = 1 - R - T \tag{3.61}$$

In Fig. 3-11, we plot the simulated white light reflectance from a $3\lambda/2$ microcavity structure consisting of 20 and 24 pairs DBRs at the top and bottom, respectively. The DBRs are GaAs and AlAs alternating layers. The refractive indices are chosen to be $n_{\mathrm{GaAs}} = 3.43$ and $n_{\mathrm{AlAs}} = 2.97$. The $1s$ exciton has a resonance at 780 nm and a dephasing rate of 0.05 THz. As can be seen, due to the presence of the exciton medium, the reflectance shows two dips around the original dip at 780 nm, which can be attributed to upper and lower polariton emissions. The upper and lower polariton states can be obtained easily using the quantum description in the following section.

3.4.2 Quantum description

The quantum description of microcavity polaritons is most commonly used when studying Bose-Einstein condensation. It starts with the exciton-photon coupling Hamiltonian under the rotating-wave approximation

$$\mathcal{H} = \sum_{\boldsymbol{k}_\parallel} E_X(\boldsymbol{k}_\parallel) a_{\boldsymbol{k}_\parallel}^\dagger a_{\boldsymbol{k}_\parallel} + \sum_{\boldsymbol{k}_\parallel} E_C(\boldsymbol{k}_\parallel) b_{\boldsymbol{k}_\parallel}^\dagger b_{\boldsymbol{k}_\parallel} + \sum_{\boldsymbol{k}_\parallel} \hbar\Omega(\boldsymbol{k}_\parallel)(a_{\boldsymbol{k}_\parallel}^\dagger b_{\boldsymbol{k}_\parallel} + a_{\boldsymbol{k}_\parallel} b_{\boldsymbol{k}_\parallel}^\dagger) \tag{3.62}$$

85

where $a_{k_\parallel}$ and $b_{k_\parallel}$ are the exciton and cavity photon annihilation operators, $E_C(k_\parallel)$ is the energy of the cavity mode given by Eq. (3.43), and $E_X(k_\parallel)$ is the energy of the exciton transition which typically varies by less than $10\,\mu\text{eV}$ in the range of relevant $k_\parallel$. Ω is the coupling strength between the cavity photon and excitonic transitions, which is usually referred to as the Rabi energy. For a QW exciton, the coupling strength is [129]

$$\Omega = e\sqrt{\frac{f}{8\epsilon L m_e S}} \int d^2 r_\parallel dz F_{k_\parallel,n}(r_\parallel, z) v_{k'_\parallel,n'}(r_\parallel, z) \tag{3.63}$$

where f/S is the excitonic oscillator strength per unit area, and $F(\cdot)$ and $v(\cdot)$ are the center-of-mass wavefunctions of the two-dimensional excitons and the longitudinal mode of the cavity photons

$$F_{k_\parallel,n}(r_\parallel, z) = \sqrt{\frac{2}{L}} \sin\left(\frac{\pi n(z - z_0)}{L}\right) \frac{e^{ik_\parallel \cdot r_\parallel}}{\sqrt{S}} \tag{3.64}$$

$$v_{k'_\parallel,n'} = \sqrt{\frac{2}{L}} \sin\left(\frac{\pi n' z}{L_{\text{eff}}}\right) \frac{e^{ik'_\parallel \cdot r_\parallel}}{\sqrt{S}} \tag{3.65}$$

where n and n' are integers indicating the parity of the wavefunctions. As can be seen, Ω does not depend on the incident field, but only on the cavity volume through f. In fact, it is the dipole interaction between the cavity vacuum field and the excitonic transition.

In order to achieve strong coupling, the coupling strength must be stronger compared to the cavity photon decay rate γ_c and exciton decay rate γ_x. If $\Omega \ll \gamma_x, \gamma_c$, the system is in the weak-coupling regime, and the spontaneous emission is irreversible. It is not appropriate to describe the system using the Hamiltonian in Eq. (3.62). In reality, the limiting factor is typically the radiative decay of the cavity γ_c, and tremendous of efforts have been devoted to the development of high-Q cavities to allow the study of strong light-matter coupling.

In the limit of strong coupling, the Hamiltonian in Eq. (3.62) can be diagonalized

with the Hopfield transformation

$$\hat{P}_{\boldsymbol{k}_\parallel} = X(\boldsymbol{k}_\parallel)\hat{a}_{\boldsymbol{k}_\parallel} + C(\boldsymbol{k}_\parallel)\hat{b}_{\boldsymbol{k}_\parallel} \tag{3.66}$$

$$\hat{Q}_{\boldsymbol{k}_\parallel} = -C(\boldsymbol{k}_\parallel)\hat{a}_{\boldsymbol{k}_\parallel} + X(\boldsymbol{k}_\parallel)\hat{b}_{\boldsymbol{k}_\parallel} \tag{3.67}$$

The coefficients, $X(\boldsymbol{k}_\parallel)$ and $C(\boldsymbol{k}_\parallel)$, are called the exciton and cavity Hopfield coefficients and are given by [130]

$$|X(\boldsymbol{k}_\parallel)|^2 = \frac{1}{2}\left(1 + \frac{\delta(\boldsymbol{k}_\parallel)}{\sqrt{\delta^2(\boldsymbol{k}_\parallel) + \Omega^2}}\right) \tag{3.68}$$

$$|C(\boldsymbol{k}_\parallel)|^2 = \frac{1}{2}\left(1 - \frac{\delta(\boldsymbol{k}_\parallel)}{\sqrt{\delta^2(\boldsymbol{k}_\parallel) + \Omega^2}}\right) \tag{3.69}$$

with cavity detuning defined as

$$\delta(\boldsymbol{k}_\parallel) = E_C(\boldsymbol{k}_\parallel) - E_X(\boldsymbol{k}_\parallel) \tag{3.70}$$

Substituting Eq. (3.67) into Eq. (3.62) yields

$$\hat{\mathcal{H}} = \sum_{\boldsymbol{k}_\parallel} E_{LP}(\boldsymbol{k}_\parallel)\hat{P}^\dagger_{\boldsymbol{k}_\parallel}\hat{P}_{\boldsymbol{k}_\parallel} + \sum_{\boldsymbol{k}_\parallel} E_{UP}(\boldsymbol{k}_\parallel)\hat{Q}^\dagger_{\boldsymbol{k}_\parallel}\hat{Q}_{\boldsymbol{k}_\parallel} \tag{3.71}$$

which is a Hamiltonian with no interaction terms. The new operators $\hat{P}_{\boldsymbol{k}_\parallel}$ and $\hat{Q}_{\boldsymbol{k}_\parallel}$ give the excitations of the resulting system, and are typically referred to as the lower and upper polariton annihilation operators, respectively. The energies of the new states are given by:

$$E_{LP/UP}(\boldsymbol{k}_\parallel) = \frac{1}{2}\left[E_X(\boldsymbol{k}_\parallel) + E_C(\boldsymbol{k}_\parallel) \mp \sqrt{\Omega^2 + \delta^2(\boldsymbol{k}_\parallel)}\right] \tag{3.72}$$

Figure 3-12 plots the energies $E_X(\boldsymbol{k}_\parallel)$, $E_C(\boldsymbol{k}_\parallel)$, $E_{LP}(\boldsymbol{k}_\parallel)$, and $E_{UP}(\boldsymbol{k}_\parallel)$ as a function of $\boldsymbol{k}_\parallel$ for three different values of $\delta(k_\parallel = 0)$. The energies are calculated using Eq. (3.72) and parameters: $\Omega = 10.84$ meV and $E_X(0) = 1604.6$ meV. Because the effective mass of cavity photons is typically 10^5 times lighter than the vacuum electron mass,
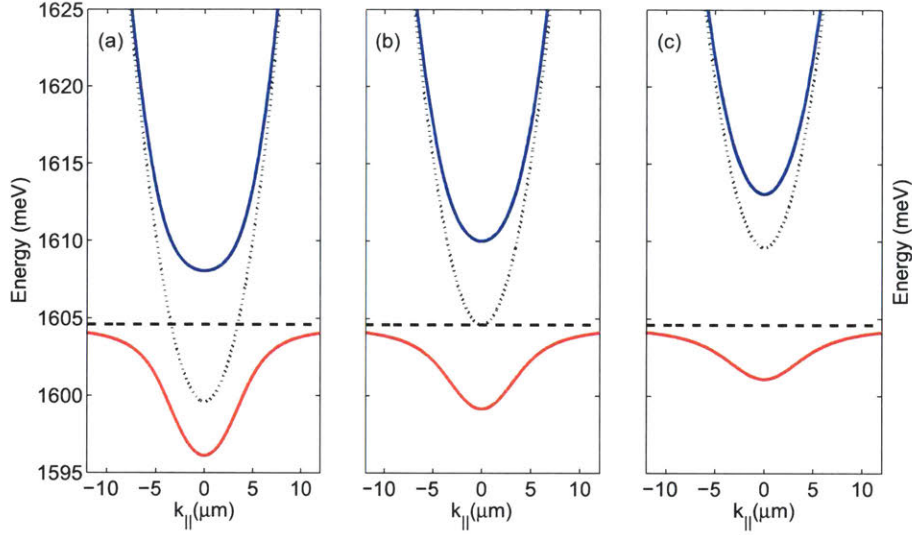
Figure 3-12: Dispersion curves of polariton modes at three representative cavity detunings (a) $\delta = -5$ meV, (b) $\delta = 0$ meV, and (c) $\delta = 5$ meV. The dotted lines show the confined cavity modes, and the dashed lines show the bare exciton modes. The blue and red solid lines indicate the upper polariton (UP) and lower polariton (LP) branches, respectively, arising from the strong coupling between cavity modes and exciton modes. Our sample parameters were used in the calculations.

and about 10^3 times less than that of excitons in a GaAs quantum well structure, $E_X(\boldsymbol{k}_\parallel)$ is essentially constant with $\boldsymbol{k}_\parallel$. As the cavity detuning $\delta(\boldsymbol{k}_\parallel)$ is varied, the excitonic fractions in the lower polariton states are also varying. As seen in Fig. 3-12, the energies and shapes of the polariton dispersion curves depend strongly on the cavity detuning: positive detunings result in lower polaritons that are more exciton-like, with heavier effective masses and stronger interactions with phonons and other carriers, while negative detunings result in lower polaritons that are more photon-like, with smaller effective masses and weaker interactions with phonons and other carriers.

In practice, the cavity detuning can be changed by using a wedged microcavity, shown in Fig. 3-13. The length of the cavity increases monotonically along one direction of the QW plane so that the energy of the cavity mode can be tuned relative to the exciton resonance energy, allowing us to experimentally tune $\delta(k_\parallel = 0)$. We show the lower and upper polariton energies at different positions in such a wedged struc-
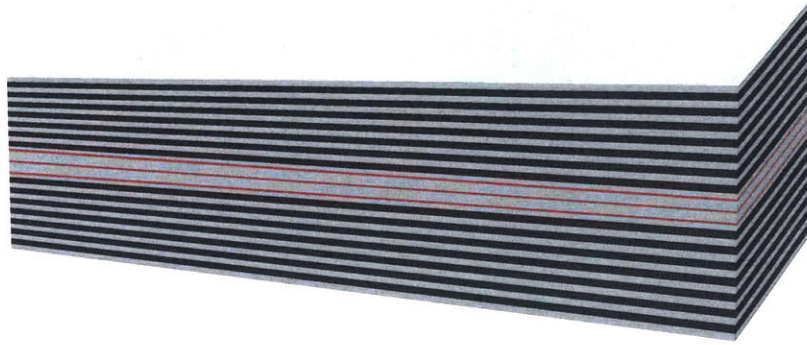
Figure 3-13: A schematic illustration of a wedged $3\lambda/2$ microcavity. The dark and light gray alternative layers indicate the distributed Bragg reflectors (DBRs) that are used to confine the light in the cavity. The red layers indicate the QWs that are placed at the antinodes of the confined electric fields.

ture in Fig. 3-14(a). The dashed lines are energies of cavity photons and excitons. A small slope is also included in the exciton energies to account for the change of QW width across the sample. When we move away from the resonance of cavity photons and excitons indicated by the intersection of the two dashed lines, the lower and upper polariton energies are asymptotic to the cavity photon and exciton energies, respectively, suggesting the change in the characteristics of polaritons. This dependence can be clearly seen in Fig. 3-14(b), where the exciton fractions $|X(k_\parallel = 0)|^2$ for lower and upper polaritons are plotted.

3.4.3 Comparison to bulk polaritons

In general, polaritons are bosonic quasiparticles resulting from strong coupling of electromagnetic waves with electric or magnetic dipole-carrying excitations. Whenever the polariton picture is valid, the model of photons propagating freely in crystals is not sufficient. For example, the coupling of an infrared photon with an optical phonon gives rise to phonon-polaritons, and the coupling of surface plasmons with light results in surface plasmon-polaritons. A cavity is not indispensable to realize strong coupling although it could enhance the coupling. In Fig. 3-15, we show the dispersions for both phonon-polaritons in a bulk crystal and exciton-polaritons in the cavity. The red and blue lines give lower and upper polaritons, the green lines
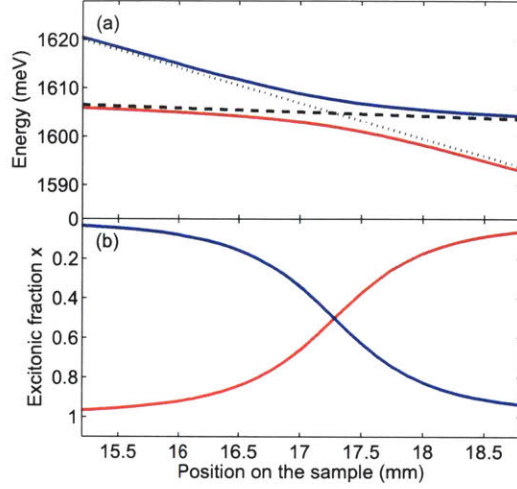
Figure 3-14: (a) The calculated upper polariton (blue line) and lower polariton (red line) ground state ($k_\parallel = 0$) energies at different positions in a wedged microcavity structure. The dashed line indicates the exciton energies, and the dotted line shows the cavity energies. (b) Excitonic fractions of upper polaritons (blue line) and lower polaritons (red line) at different sample positions.

represent the light modes, and the black lines stand for the phonons and excitons in Fig. 3-15(a) and (c), respectively. As can be seen, both phonon-polaritons in the bulk crystal and exciton-polaritons in the microcavity show the signatures of avoid crossing, which is a manifestation of strong coupling. The dispersions have similar asymptotic behavior as k increases. However, due to the coupling to an optical cavity, the lower exciton-polaritons have an effective mass with finite value. On the other hand, the bulk lower phonon-polaritons have an infinite mass due to the linear dispersion relation. This clearly demonstrates the importance of the cavity for the observation of quantum condensation in exciton-polariton systems.

The density of states is evaluated using [131]

$$D_2(E) = \frac{1}{2\pi^2} \int_E \frac{dl}{|\nabla E|} \tag{3.73}$$

for 2D exciton-polaritons, and using

$$D_3(E) = \frac{1}{4\pi^3} \int_E \frac{dS}{|\nabla E|} \tag{3.74}$$
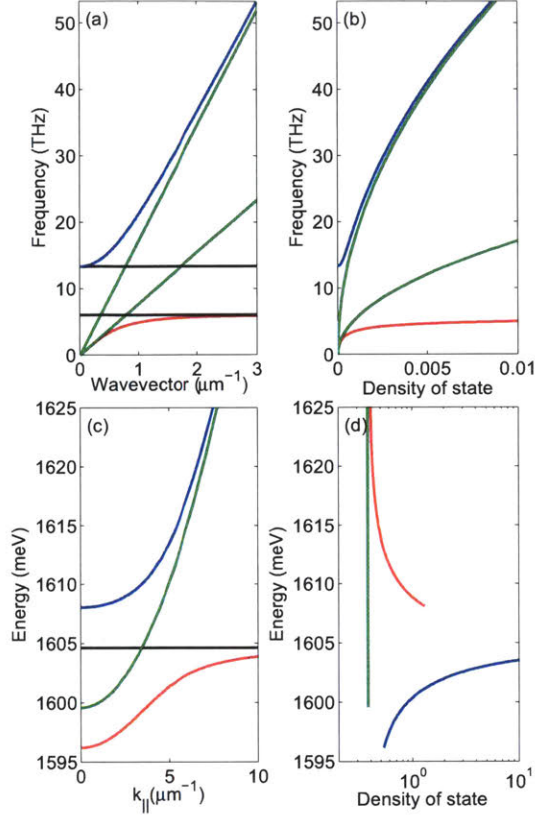
Figure 3-15: (a) Phonon-polariton dispersions in a bulk crystal. (b) Density of states of phonon-polaritons in the bulk crystal. (c) Exciton-polariton dispersions in a microcavity. (d) Density of states of exciton-polaritons in a cavity. Red and blue lines give lower and upper polaritons, green lines represent photon modes, and black lines stand for the material modes.

for 3D phonon-polaritons. The results are plotted in Fig. 3-15(b) and (d). For microcavity exciton-polaritons, the density of states is quasi-constant given its two dimensionality, and is never zero because of the confinement of the cavity, while the density of states approaches zero as $k \to 0$ for lower phonon-polaritons.

3.4.4 Going beyond the strong coupling regime

When the coupling energy is comparable to the energy levels, i.e., $\Omega \sim E$, the rotating-wave approximation is not valid any more. The electrons, holes and photons need to be treated on the same footing [32]. It is a consequence of subband mixing of higher-orbital excitons, and is typical in confined intersubband transitions. This is called

the ultrastrong-coupling regime. In this regime, lower polaritons consist of excitons with even smaller effective Bohr radii and larger binding energies, while the opposite holds for upper polaritons.

Chapter 4

Experimental Methodologies

In this chapter, experimental methodologies involved in this dissertation work are discussed in detail. We start with an overview of the experimental setup for photoluminescence imaging in Section 4.1. In Section 4.2, the principle of spatial shaping based on a spatial light modulator is presented. Included is the calibration of spatial light modulator and the Gerchberg-Saxton algorithm that can be exploited to improve the quality of spatial shaping. The principles of near-field imaging and far-field imaging are explained in Section 4.3. We also discuss the implementation and calibration of the imaging setup in this section. The density of k states on the CCD, which is an important quantity in converting the CCD counts to the polariton number, is also covered in the same section. In Section 4.4, we discuss initial experiments performed with our sample in order to characterize its properties and estimate important parameters. These are the basic experiments that should be performed on any new sample, to make sure that the observed effects are consistent with previous knowledge. In Section 4.5, the mechanisms for the formation of polaritons and their condensates through optical excitation are reviewed in detail, followed by a review of tools to control polaritons and their condensates in Section 4.6, including fabrication methods and optical trapping. Given the quantitative results involved in this dissertation work, we conclude this chapter by a discussion of the weighted least-squares approach that is used in the data analysis, as well as the numerical algorithm used to extract the excitation profile.

4.1 Experimental Setup

A schematic illustration of the experimental setup used in this dissertation is shown in Fig. 4-1. The following notations are used. L: lens, AOM: acousto-optic modulator, M: mirror, PH: pinhole, IM: imaging plane, SLM: spatial light modulator, S: sample, OL: objective lens, NPBS: non-polarizing beam splitter. The output of a continuous-wave (c.w.) laser is first modulated by an AOM with a duty cycle of 0.5% at 1 kHz, and then magnified by a telescope formed by L2 and L3. A pinhole PH1 is placed at the focal point of L2 to clean up the spatial mode of the beam after the AOM. The beam is then shaped into an annular pattern by the SLM. The annular pattern is transformed to the right size on the sample by two pairs of telescopes L5/L6 and L7/OL. A 90R/10T non-polarizing beam splitter (NPBS) is used to reflect 90% of the excitation beam intensity and 10% of the resulting photoluminescence intensity. Ideally, a dichroic mirror should be in the place of the NPBS. However, since the excitation beam and photoluminescence are separated by 50 nm in wavelength, it is not trivial to fabricate such a dichroic mirror with good optical efficiency and small wavefront distortion. The photoluminescence after the photoexcitation is collected by the same objective lens, and then imaged downstream in either the far-field or thenear-field geometry. A longpass filter is placed at the entrance of the spectrometer CCD to allow only PL to pass through. The details of the major equipment involved in the optical setup are described below.
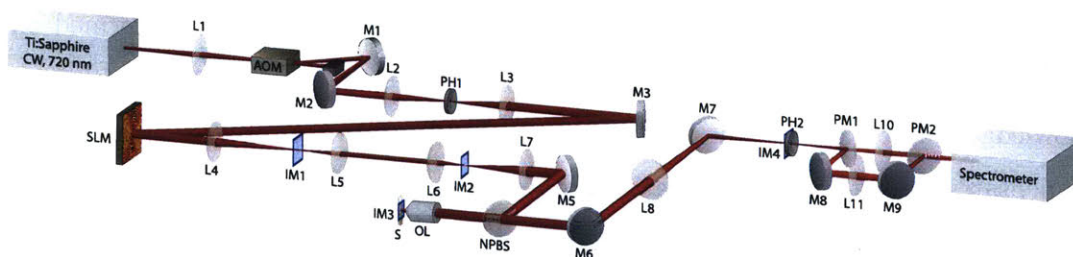
Figure 4-1: A schematic illustration of the experimental setup. The following notations are used in the figure. L: lens, AOM: acousto-optic modulator, M: mirror, PH: pinhole, IM: imaging plane, SLM: spatial light modulator, S: sample, OL: objective lens, NPBS: non-polarizing beam splitter.

94

Excitation laser. The excitation laser is a SolsTiS 1000 model from MSquared Lasers. It is a c.w. Ti:Sapphire laser with a spectral linewidth of <50 kHz when the reference cavity lock is applied. The output beam has a diameter of <0.4 mm and a divergence of <1.5 mrad with horizontal polarization. It also offers a wide range of tuning in wavelength from 700 nm to 950 nm, with a peak power of 2.6 W at 780 nm. The output power at 720 nm, which is the excitation wavelength that is used in most experiments in this dissertation, is ~1.2 W. The laser power is controlled by a $\lambda/2$-waveplate and a polarizer. The orientation of the polarizer is fixed so that the output polarization is horizontal, and the rotation of the waveplate is controlled by a motorized precision rotation stage from Thorlabs (Model PRM1Z8).

Acousto-optic modulator. The AOM is an MT250-0.5-800 model from AAOpto-Electronics. It shapes the incident c.w. beam into a pulsed output with a specific duty cycle and frequency controlled by the driving radio frequency (RF) wave based on the acousto-optic effect. The RF input of the AOM is provided by a four-channel digital delay and pulse generator, model DG535, from Stanford Research Systems. The clear aperture of the AOM is 0.5 mm × 2 mm. The input polarization has to be horizontal in order to achieve the maximum diffraction efficiency. A diffraction efficiency of 92% at 720 nm is obtained in the lab. Slight adjustment of the RF power and the orientation of AOM are needed when a different wavelength is used. The rise and fall times are 160 ns, but is not significant compared to the 5 μs on-time of the AOM. To avoid unwanted damages, the optical excitation density has to remain below 5 W/mm^2.

Spatial light modulator. The SLM used in the setup is a phase-only model from Holoeye with an addressing level of 8-bit and a full HD resolution of 1920 × 1080. This high resolution does come at a cost: the fill factor is only 87%. While this is good for pixelated devices, it leads to a 40% power loss. The best realized efficiency at 720 nm is typically 30%. In order to achieve the best diffraction efficiency, the input polarization has to be aligned with the long axis of the surface of the SLM.

The SLM communicates with the computer via a DVI port. To avoid unwanted damages, the optical excitation density has to remain below $2\,\mathrm{W/cm^2}$. Note that the optical flatness of this SLM is not ideal for temporal shaping but an appropriate compensation function is applied.

Objective lens. The objective lens is a 46-144 model from Edmund Optics with a $10\times$ magnification. It has a working distance of $33.5\,\mathrm{mm}$ and an effective focal length of $20\,\mathrm{mm}$. Its numerical aperture (N.A.) is 0.28, which corresponds to a spatial resolution of $\sim$1.3 µm in the range of wavelengths used in the experiments.

Cryostat. The microcavity structure is kept in an open-loop ST-300MS cryostat from Janis Research Company Inc. The design of the cryostat allows a wide acceptance angle of the optical excitation beam up to 75°. The rectangular window block is made of sapphire to give the best optical transmission in the near infrared range. The chamber is kept in a vacuum of 3×10^{-3} torr via mechanical pumping. Temperatures between $5\,\mathrm{K}$ and $325\,\mathrm{K}$ can be achieved through the combination of liquid helium cooling and a thermocouple controlled by a temperature controller from LakeShore (model 331). In order to save helium and avoid sudden temperature changes in the sample which produces mechanical strain and can cause sample cracking, the sample is cooled down to $10\,\mathrm{K}$ from room temperature in 3 to 4 hours. Apiezon N Grease is applied on the substrate of the microcavity structure in order to obtain good thermal contact with the cold finger. This vacuum grease exhibits extremely low vapor pressure at ambient temperatures, 6×10^{-10} torr at $20\,\mathrm{°C}$, which is further lowered at cryogenic temperatures. However, it needs to be replaced after a few experimental cycles since frequent thermal contraction and expansion degrade the contact. Note that although the silver paste from SPI Supplies can give better thermal contact, it is not used in the lab because silver paste leads to a permanent mounting of the sample on the cold finger. If not healed properly, it could result in sample cracking during cooling.

96

Spectrometer CCD. The spectrometer is a 300i model and the CCD is a Pixis 100 model, both from Princeton Instruments. The grating installed in the spectrometer has a groove spacing of 1200/mm, and should be calibrated using an atomic gas-discharge lamp before any spectrally resolved measurements. The calibration can be performed with WinSpec which is software that is provided by Princeton Instruments. The CCD has a dimension of 100×1340 with an individual pixel size of 20 µm. Both spectrometer grating and CCD can be controlled by WinSpec or a home-built Lab-View program. The LabView program allows a fully automated continuous recording of images on the CCD.

4.2 Shaping Excitation Beam based on SLM

The easiest setup imaginable with a two-dimensional SLM is to aim a monochromatic laser at it, and observe the far-field diffraction when different phase patterns are applied. Using simple variations on this basic recipe, the Holoeye HEO1080P SLM is calibrated and implemented for spatial beam shaping. We will discuss the calibration of the SLM, the principle of spatial shaping, and the Gerchberg-Saxton algorithm that could be exploited to improve the quality of spatial shaping in this section.

4.2.1 Implementation

The Holoeye HEO1080P Phase Only Modulator is connected to a computer through a DVI cable and is set up as a second monitor. The Windows desktop can then be extended to the second monitor, and anything that is displayed on the extended desktop will be displayed on the SLM. In practice, displaying phase masks is done either by manually selecting a 2944×1080 (monitor size + SLM size) pixel wallpaper (set to tile) in Windows, or automatically through a user interface provided by Holoeye. While the device only uses the green color channel, it is often easier to use a greyscale image which of course works equally well. The SLM has an 8-bit addressing depth, meaning that each pixel can be given a green or gray color level from 0 to 255. The device can be connected with a serial cable, after which new calibration data can be

loaded. The procedures for data loading, gamma curve correction and potentiometer adjustment are well explained in manuals on the CD-ROM that is delivered with the SLM.

4.2.2 Calibration of the SLM

Once powered up, the SLM converts a driving electric signal into an optical phase shift for every one of the 2 million pixels in the liquid-crystal display. The relation between the SLM input (256 levels as set on the computer) and the output optical phase shift (up to 2π) has to be determined by careful calibration. We followed the method that is suggested by Holoeye in the manual of the SLM. Using an opaque plate, usually a paper block made of blackout material, with two slits, a collimated input beam is split into two distinct beams as shown in Fig. 4-2. These two beams reflect off the SLM and are focused to one spot on a camera where an interference pattern can be observed. Since the two beams are incident on different halves of the SLM, the phase difference between the two beams can be independently controlled with a binary phase mask provided by the user interface of the SLM. If a varying phase delay is applied to one of the beams, the interference fringes will shift on the camera. This shift is a good measure of the phase delay and is directly related to the driving voltage. By constructing a grayscale-to-phase-shift plot and numerically fitting it to a 14th-order polynomial [132], we obtain a lookup table, streamlining the process of calculating the grayscale mask pattern from the desired phase pattern. The grayscale-to-phase information should be loaded to the SLM through the serial port after calibration. Note that the calibration is crucial for shaping efficiency if a very different wavelength is used.

4.2.3 Principle of spatial shaping

The general principle of spatial shaping is illustrated in Fig. 4-3. The input plane indicates the surface of the SLM which is placed at the Fourier plane of the lens, and the output plane indicates the conjugate Fourier plane. To quantitatively describe
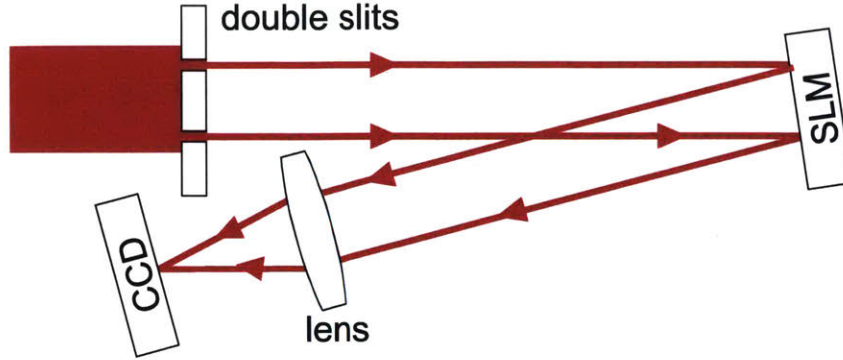
Figure 4-2: A schematic illustration of the experimental setup used for the calibration of an SLM. The input beam is split by two slits, and then incident on two different sides of the SLM. The reflected light off the SLM is recombined by a lens before the CCD.

the beam shaping process, we assume the input field as a coherent plane wave
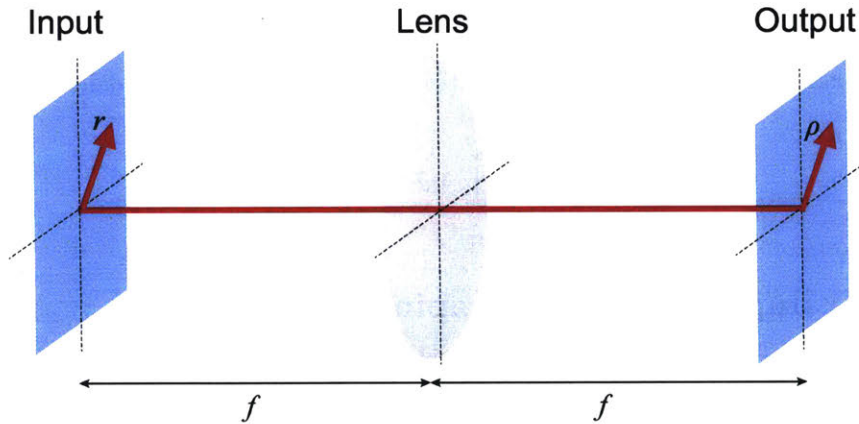
Figure 4-3: A schematic illustration of the spatial shaping highlighting the relationship between the beam geometry in the input and output planes. A lens of focal length f projects the Fourier transform of the input field onto the output plane.

$$E_0(\boldsymbol{r}) = A_0(\boldsymbol{r})\exp(i\Phi_0) \tag{4.1}$$

where the $\boldsymbol{r}$ independence in the phase Φ_0 is a result of the plane-wave assumption. The SLM provides a phase modulation $\Phi^{\mathrm{SLM}}(\boldsymbol{r})$, and the electric field after the input plane has a modified wavefront

$$E^{\mathrm{in}}(\boldsymbol{r}) = E_0(\boldsymbol{r})\exp(i\Phi^{\mathrm{SLM}}(\boldsymbol{r})) \tag{4.2}$$

99

In a typical spatial shaping setting, we know the distribution of the field at the output plane, denoted as $I^f(\boldsymbol{\rho}) = |E^f(\boldsymbol{\rho})|^2$. Based on Fourier optics, $E^f(\boldsymbol{\rho})$ and $E^{\mathrm{in}}(\boldsymbol{r})$ are Fourier transform pairs. Putting everything together, we have

$$\left| \mathcal{F}\left[A_0(\boldsymbol{r}) e^{i\Phi^{\mathrm{SLM}}(\boldsymbol{r})} e^{i\Phi_0} \right] \right|^2 = \left| \mathcal{F}\left[A_0(\boldsymbol{r}) e^{i\Phi^{\mathrm{SLM}}(\boldsymbol{r})} \right] \right|^2 = I^f(\boldsymbol{\rho}) \tag{4.3}$$

where $\mathcal{F}$ indicates the Fourier transform. It can be solved nominally as

$$\exp\left[i\Phi^{\mathrm{in}}(\boldsymbol{r}) \right] = A_0^{-1}(\boldsymbol{r}) \mathcal{F}^{-1}\left[\sqrt{I(\boldsymbol{\rho})} \exp(i\Phi(\boldsymbol{\rho})) \right] \tag{4.4}$$

where $\Phi(\boldsymbol{\rho})$ is the phase front at the output plane, and for simplicity we assume the electric field at this plane is also a plane wave, and therefore it is not dependent on $\boldsymbol{\rho}$. In practice, we also assume a uniform distribution for the beam incident on the SLM when calculating the phase distribution applied to the SLM, yielding

$$\exp\left[i\Phi^{\mathrm{in}}(\boldsymbol{r}) \right] = \mathcal{F}^{-1}\left[\sqrt{I(\boldsymbol{\rho})} \right] \tag{4.5}$$

4.2.4 Examples of spatial shaping

In the work of this dissertation, the excitation beam is typically shaped into an annular pattern. In order to achieve this, the axicon phases as shown in Figs. 4-4(a)-(c) are applied to the surface of the SLM. The resulting beam profiles at the output plane calculated from 2D fast Fourier transformation are shown in Figs. 4-4(d)-(f), respectively. As can be seen, the radius of the annular pattern can be controlled by changing the spatial periodicity of the phase pattern, with a smaller periodicity corresponding to a larger annulus. By deliberately changing the gamma value, which is a nonlinear map from grayscale to grayscale and is used to tune the contrast of the pattern applied on the SLM, the light intensity distribution can be adjusted. This principle is illustrated in Fig. 4-5, where a binary axicon phase is applied. The even orders of the annular pattern are significantly suppressed by applying such a 0-1 binary transformation of the original 8-bit phase pattern. In practice, nonlinear
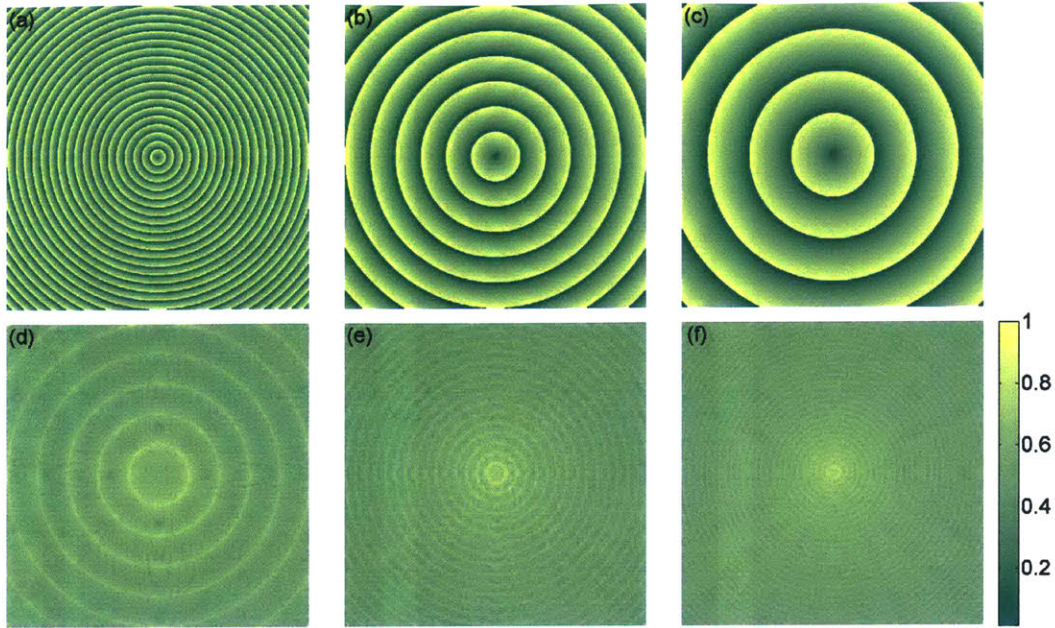
Figure 4-4: (a)-(c) Axicon phases on the SLM for different spatial distributions. (d)-(f) The resulting intensity profiles at the output plane calculated from the 2D fast Fourier transformation corresponding to the modulations of (a)-(c), respectively. The colorbar represents relative intensities for (d)-(f) and relative phases $(0 - 2\pi)$ for (a)-(c).

gamma corrections have to be applied in order to suppress all high-order annuli.

4.2.5 Gerchberg-Saxton algorithm

The Gerchberg-Saxton (GS) algorithm can be applied to solve Eq. (4.4) to improve the spatial shaping quality. It was originally proposed in 1972 by R. W. Gerchberg and W. O. Saxton to solve the problem of phase retrieval of a field at two different planes [133]. At those two planes, only the field amplitudes are known and given that the fields are related by the Fourier transform. Nowadays, this algorithm has also been extensively used to calculate phase-only diffractive optical elements to be used as beam shapers. The steps for the implementation of the GS algorithm are summarized in the following [134, 135, 136]:

1. A field with an amplitude given by the square root of the target profile and a constant phase is taken.
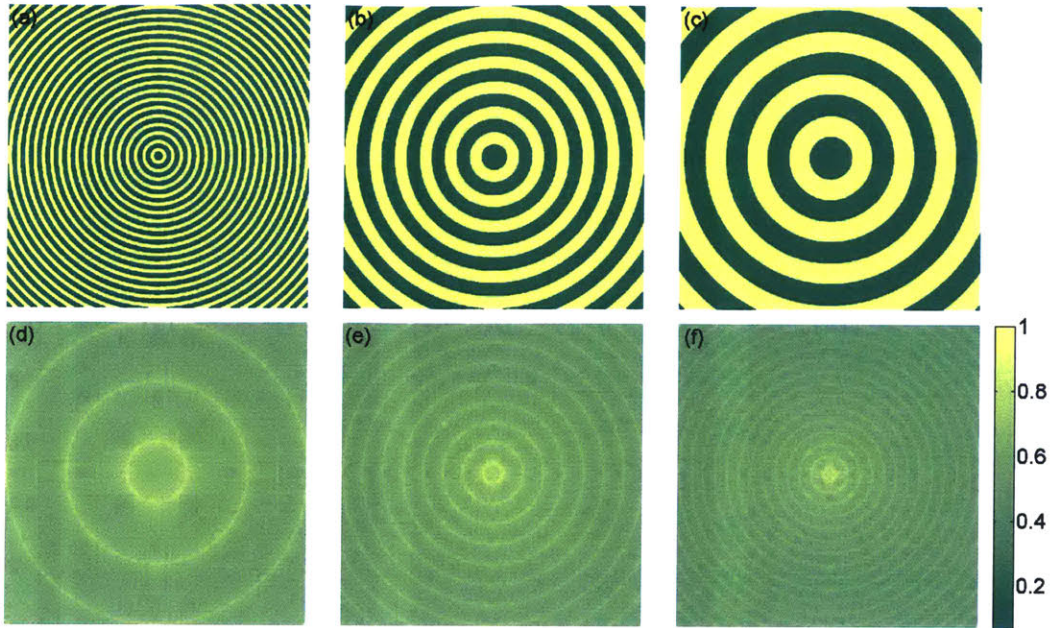
Figure 4-5: (a)-(c) Binary axicon phases on the SLM for different spatial distributions. (d)-(f) The resulting intensity profiles at the output plane calculated from the 2D fast Fourier transformation corresponding to the modulations of (a)-(c), respectively. The colorbar represents relative intensities for (d)-(f) and relative phases (0 and 2π) for (a)-(c).

2. The field is propagated from the image plane to the object plane.

3. The amplitude information is discarded, leaving only the phase information for the phase mask.

4. The amplitude and phase of the illumination field are added to the phase information to obtain the resulting object field.

5. The field is propagated from the object plane to the image plane.

6. The resulting reconstructed image (square of the field amplitude) is compared with the target profile. By using the correlation between both images defined in Eq. (4.6) as a criterion, a decision is taken to step out of or continue the iterations.

7. The phase from the reconstructed image is combined with the field amplitude obtained from the target profile, and the process is repeated from step 1.
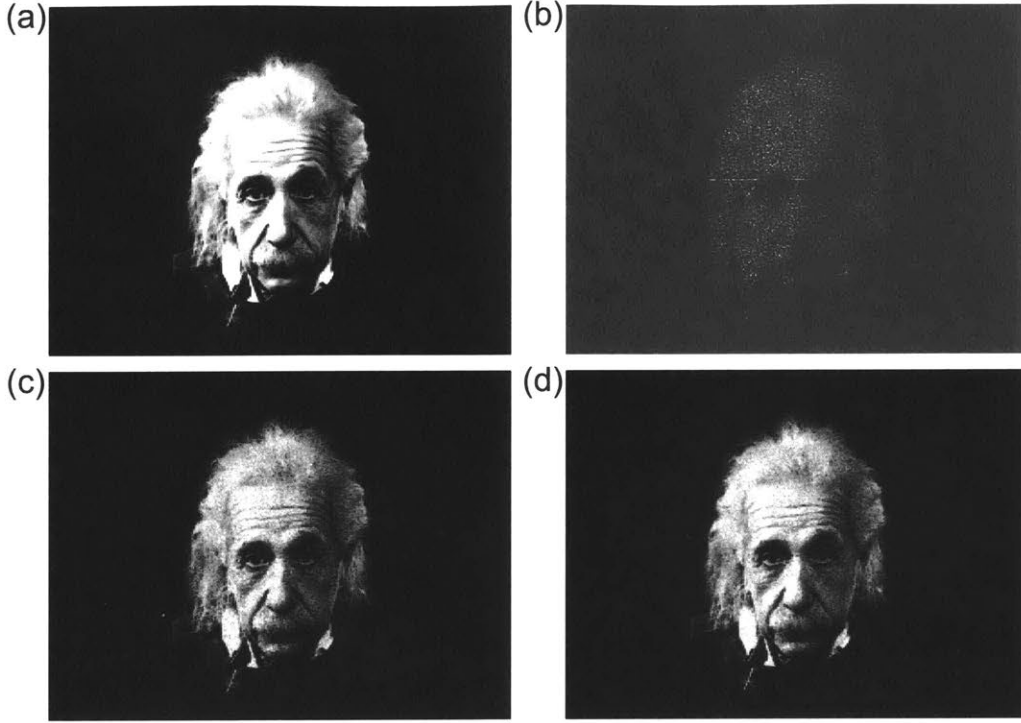
Figure 4-6: (a) The target profile. (b)-(d) The calculated profiles based on the Gerchberg-Saxton algorithm for 3 (b), 64 (c) and 128 (d) iterations, respectively.

The correlation between two matrices of the same dimension is defined as

$$\rho = \frac{\sum_{m,n}(T_{mn} - \bar{T})(C_{mn} - \bar{C})}{\sqrt{\left(\sum_{m,n}(T_{mn} - \bar{T})^2\right)\left(\sum_{m,n}(C_{mn} - \bar{C})^2\right)}} \qquad (4.6)$$

where T and C are the target profile and calculated profile, and $\bar{T}$ and $\bar{C}$ are the average values of T and C, respectively. In Fig. 4-6, we plot the calculated profile at the image plane for 3 different iterations starting from a Gaussian profile. The target profile is shown in Fig. 4-6(a), and Fig. 4-6(b) shows the calculated profile after 3 iterations. It has already had some signatures similar to the target profile. When iterations of 64 and 128 are used, the difference between the calculated images is negligible, as shown in Figs. 4-6(c) and (d).

The convergence of the GS algorithm can be quantitatively measured by the statistical correlation ρ between the target profile and the calculated profile defined in

103

Eq. (4.6). Figure 4-7 plots ρ between the target profile in Fig. 4-6(a) and the calculated profiles with different number of iterations. As can be seen, ρ approaches to unity in ~ 20 iterations, indicating the GS algorithm converges in a fairly quick manner.
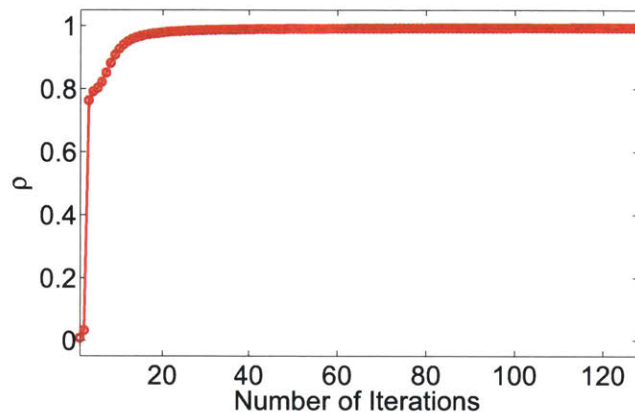
Figure 4-7: The correlation between the target profile and the calculated profiles in Fig. 4-6 as a function of number of iterations in the Gerchberg-Saxton algorithm.

4.3 Measuring Photoluminescence

In this section, we describe the photoluminescence imaging setup, as was first implemented in the Nelson group in 2011 [137]. With this setup, we can measure energy-resolved photoluminescence in both real and k space. The real space is also referred to as near field, while the k space is called far field in the exciton-polariton community. Lowpass filtering in both real space and k space is also possible by placing a pinhole at either the image plane or the Fourier plane.

4.3.1 Near-field imaging

The setup for near-field imaging is schematically shown in Fig. 4-8. The combination of two pairs of a $4f$-imaging system allows a relay imaging of the object plane (the sample plane in photoluminescence measurements) to the image plane (the entrance slit of the spectrometer in photoluminescence measurements) in the near-field geom-
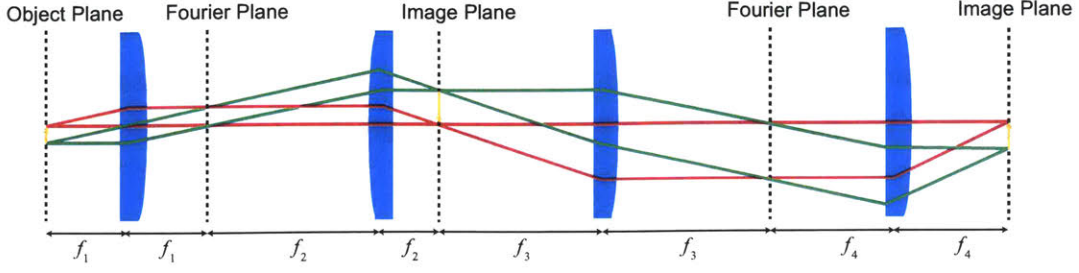
Figure 4-8: The four-lens combination forms two $4f$ imaging systems to relay image the object (the yellow arrow) from the object plane to the final image plane. In k-space imaging, the last lens is removed, and the object is imaged to the Fourier plane after f_3. The intermediate image plane and Fourier plane can be used to perform lowpass filtering in either real or k space.

etry. The resulting image at the image plane is a real-space image of the object plane with a magnification given by

$$\gamma = \frac{f_4 f_2}{f_3 f_1} \tag{4.7}$$

In the current setup implemented in the lab, we have $f_1 = 2\,\text{cm}$, $f_2 = 80\,\text{cm}$, and $f_3 = f_4 = 10\,\text{cm}$, so a magnification of $\gamma = 40$ is realized. A flip mirror in front of the spectrometer allows us to direct light to a charged-coupled device (CCD) camera for imaging purposes (not shown in Fig. 4-8). Figure 4-9(a) and (b) show representative real-space images of density distributions of polaritons when an annulus with a diameter of $42\,\mu\text{m}$ is used to excite the microcavity structure.

The same setup can also be used for making a position- (x-) and energy- (E-) resolved measurement. In this case, the entrance slit of the spectrometer is nearly completely closed, so that only the part of the light with $y \approx 0$ enters the spectrometer. In addition, the grating is aligned in such a way that it directs the first-order diffraction to the spectrometer CCD, allowing the transformation of a one-dimensional position-resolved image into a position- and energy-resolved image. By spatially and spectrally resolving the horizontal slice indicated by the dashed white line, the energy profile along the horizontal axis is obtained as shown in Fig. 4-9(b). This potential landscape will be discussed in detail in Section 4.6.

In order to eliminate the propagation effect of polaritons when resolving the po-

tential landscape, it is crucial to apply k-space filtering before imaging the photolumi-
nescence to the spectrometer CCD. In this case, an iris is placed at the intermediate
Fourier plane to allow only $k \approx 0$ components of the photoluminescence to pass
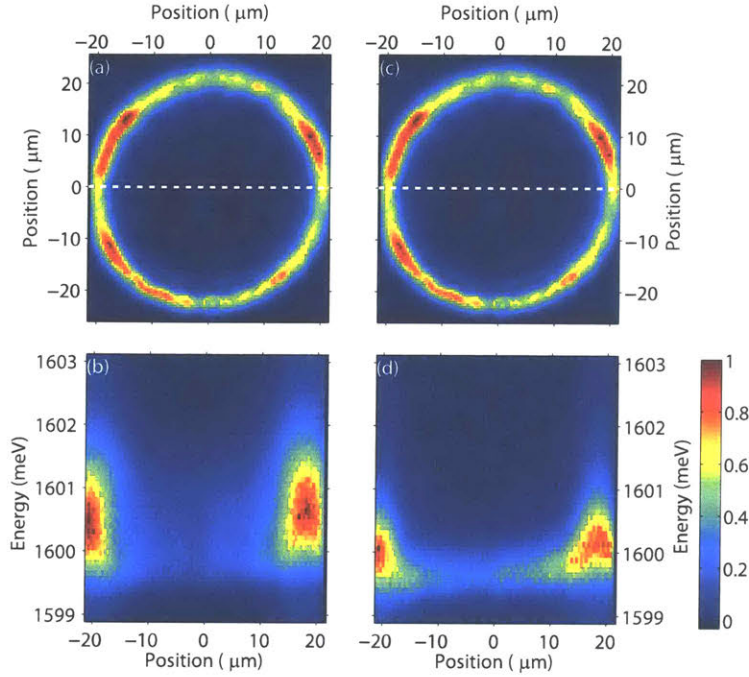
Figure 4-9: (a) Spatial distributions of polaritons without k-space filtering. (b) Spatial
distributions of polaritons with k-space filtering. (c) Energy-resolved spatial distributions of
polaritons without k-space filtering. (d) Energy-resolved spatial distributions of polaritons
with k-space filtering.

through. The resulting image is shown in Fig. 4-9(d). Because we eliminate the
high-k components, the total signal is weaker compared to Fig. 4-9. Spatial distribu-
tions of polaritons become narrow as expected, since polaritons convert the potential
energy to their kinetic energies as they accelerate away from the pump region, and
the k-space filter eliminates the high-k components. On the other hand, the reduc-
tion in the barrier height at the pump region when k-space filtering is applied is a
result of elimination of exciton photoluminescence, since excitons are formed from
phonon-carrier scattering and typically occupy high-k states.

4.3.2 Far-field imaging

A traditional way to acquire a far-field image is to place a screen at infinity. The k coordinates of this image would then correspond to the angles incident on the screen. A more compact setup is composed of three lenses by taking out the last lens in Fig. 4-8. As can be seen, the exiting rays with the same azimuthal angle on the object plane are imaged to the same position on the Fourier plane of f_3, but rays with different angles do not overlap on the Fourier plane. In this way, a far-field image of the original object is created, and the coordinates of the generated image on the Fourier plane have one-to-one correspondence to the emission angles on the object plane, which can then be translated to the transverse momentum, better known as in-plane momentum $k_\parallel$ in the polariton community, defined as

$$k_\parallel = \frac{2\pi}{\lambda} \sin \theta \qquad (4.8)$$

where we implicitly assume that the emission wavelength λ is not angle-dependent. This is a reasonable assumption for this dissertation work because the energies of polariton states within the numerical aperture of the current setup vary by less than 0.3%, as seen in Figs. 4-10(c) and (d). Similarly, by nearly closing the slit so that only the signal corresponding to $k_y \approx 0$ passes through, and aligning the grating to send a spectrally resolved image to the CCD camera, one can record the momentum-(k_x-) and energy- (E-) resolved image. In this case, the resolved momentum k_x is essentially the same as the total in-plane momentum $k_\parallel$ since only photons with $k_y \approx 0$ are detected.

Figure 4-10(a) shows the momentum distributions of polaritons when an annulus with a diameter of 42 µm is used to excite the microcavity structure. The accumulation of polaritons at a nonzero momentum is merely a result of the cavity gradient which provides a potential for polaritons to accelerate away. By spatially selecting the vertical slice indicated by the dashed white line using the spectrometer slit, and spectrally resolving the photoluminescence that passes through the slit, the energy profile along the vertical axis can be obtained, shown in Fig. 4-9(c). The resulting

image is referred to as the energy dispersion $E(k)$ of polaritons. As can be seen, because we integrate over the entire sample area in this plot, the energy distribution is smeared out since polaritons at different sample positions have different energy dispersions in this wedged microcavity.
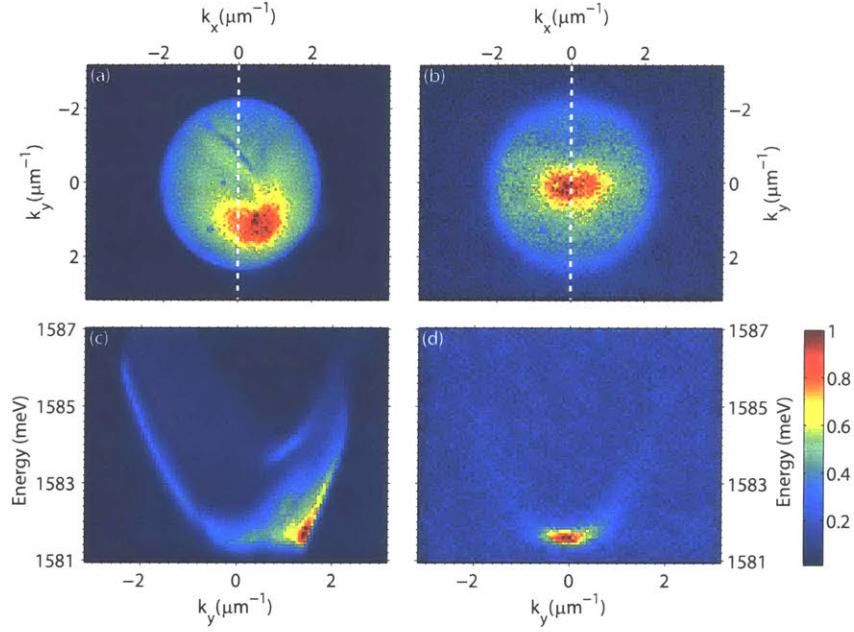
Figure 4-10: (a) Momentum distributions of polaritons without real-space filtering. (b) Momentum distributions of polaritons with real-space filtering. (c) Energy-resolved momentum distributions of polaritons without real-space filtering. (d) Energy-resolved momentum distributions of polaritons with real-space filtering.

In order to eliminate the spatial inhomogeneity, we place a spatial filter with a diameter of $500\,\mu\text{m}$ in the reconstructed real-space image plane downstream after f_2 in Fig. 4-8. This corresponds to an integration of a region that is $5.5\,\mu\text{m}$ away from the optical axis on the sample. The resulting filtered emissions are displayed in Figs. 4-10(b) and (d). As expected, the emissions have more localized momentum distributions than the previous case. Note that spatial filtering is crucial in order to obtain a dispersion relation if it is subsequently used to extract the energy distributions $N(E)$ of polaritons. This will be heavily discussed in Chapter 5.

108

4.3.3 White light reflection

In order to characterize the reflection dip of the microcavity structure, the sample is illuminated by white light. A flashlight is typically used to produce the white light and is aligned with the excitation path before the non-polarizing beam splitter, as indicated in Fig. 4-1. The reflected white light is imaged to the far-field geometry and spectrally resolved. The orientation of the flashlight and diameter of the iris are adjusted so that a reflection spectrum with high signal-to-noise ratio is obtained on the spectrometer CCD.

4.3.4 Implementation of the imaging setup

The near-field and far-field imaging setups implemented in the lab are shown in Fig. 4-11 and Fig. 4-12, respectively. As can be seen, the emission shares common path until the reconstructed image plane, indicated by the black dashed line, and near-field and far-field imaging paths differ afterwards. The near-field imaging is implemented with a one-lens imaging geometry, where the distance between L2 and the image plane as well as the distance between L2 and the entrance slit of the spectrometer are set at twice the focal length of L2. In the far-field geometry, the focal length of L3 is chosen as the distance from L3 to the entrance of the spectrometer equals the distance from the image plane to L3. To make it convenient to switch between the near-field geometry and far-field geometry, M5, M6 and L3 are set up as movable optics. The following procedures can be carried out if the setup needs to be reconstructed.

1. Position a collimated beam directly into the entrance of spectrometer slit and align it to the center of the CCD camera.

2. Place L3 in the beam path and move it back and forth so that the focal point on the screen is tightest.

3. Set up M6 and M2.

4. Send a collimated beam from L3 to L1, and the position of the L1 is found when the output beam is collimated again.

109

5. Set up M1 and OL. The position of OL is determined by the sum of the focal lengths of L1 and OL, and is initially laid out by measuring the distance using a meter tape.

6. Place the sample on a stage, and take out L1 from the beam path.

7. Send a collimated beam from the excitation path, and direct the beam to the CCD through the far-field imaging path. Move the position of the sample mount so that a tight focal point is found on the spectrometer CCD.

8. Take out M6 and L3, and set up M3, M4, M5 and L2.

9. Send a white light from the excitation path, and aim at the edge of the sample. Align L2 so that a sharp image with high contrast is formed on the spectrometer CCD.
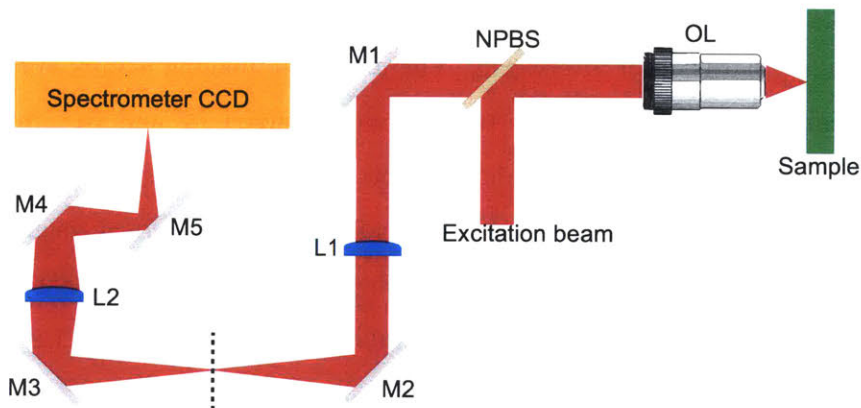
Figure 4-11: A schematic illustration of the near-field imaging setup used for this dissertation work.

Note that the positions of OL and L2 are approximately correct after the initial implementation. A further calibration is needed in order to perform near-field and far-field imaging to a high degree of precision. The following procedures are suggested to be carried out.

1. Place a 1D phase mask at the sample position. This can be done by taking out L1 and imaging the reflected light in the far-field geometry and checking the collimation of the reflected light.

110
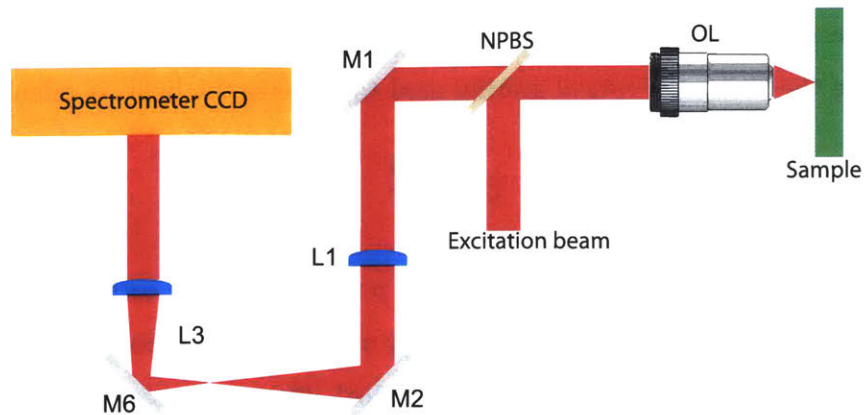
Figure 4-12: A schematic illustration of the far-field imaging setup used for this dissertation work.

2. Put L1 back in the beam path, and send a white light into the excitation path.

3. Move the OL while keeping fixed the relative distance between the phase mask and the OL until a sharp far-field image of the phase mask is obtained. The far-field image is an array of spots that is rotated by 90° with respect to the original phase mask array.

At this point, the far-field imaging path should be well calibrated and ready to use. The near-field imaging path is calibrated by the following procedures.

1. Send a white light into the excitation path, and aim it at the edge of the sample.

2. Move L2 along the optical axis so that a sharp edge of the sample is observed on the CCD camera.

4.3.5 Optical efficiency of the imaging path

The optical efficiency of the imaging path is an important factor, since it is crucial when we convert the CCD counts to the polariton number. In this case, a flat mirror is placed at the sample position and aligned to the focal plane of the objective lens that collects the photoluminescence in our experiments. A collimated laser beam at 780 nm is sent to the excitation path and is focused by a microscope objective. The retro-reflected light is collected by the same objective lens, and propagated though

the far-field imaging path. The overall efficiency of the optical path, including the efficiency of the CCD and optical grating used to disperse the light, is calculated as

$$\xi = \frac{Ch\nu}{P} \tag{4.9}$$

where P is the power measured at the sample position, C is the corresponding CCD counts per second, and $h\nu$ is the photon energy of the excitation beam. The quantity ξ can also be estimated by multiplying the optical efficiency factors of each optic in the imaging system including the quantum efficiency of the dispersing grating and spectrometer CCD.

4.3.6   Density of k states on the CCD

Let (k_x, k_y) label the Cartesian coordinate in reciprocal space at the sample plane, and let (x_F, y_F) label the Cartesian coordinate on the CCD. Define the angle θ as the emitting angle with respect to the normal of the sample plane, and ϕ as the azimuthal angle of the emission at the sample plane, as shown in Fig. 4-13, thus we have
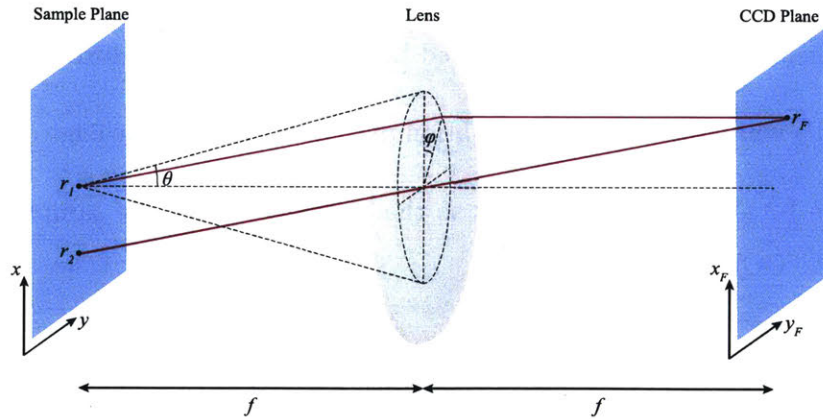
Figure 4-13: Two rays at r_1 and r_2 emitting into the same angle (θ, ϕ) are imaged onto the same position r_F on the Fourier plane.

$$k_\parallel = k \sin \theta \tag{4.10}$$

$$\tan \phi = \frac{k_y}{k_x} \tag{4.11}$$

112

where $k_\|$ and k are the magnitudes of the in-plane momentum and the total momentum, with the x and y components being k_x and k_y, respectively. The function $k(\theta)$ can be obtained from the dispersion relation as

$$k = \frac{1}{2\hbar c}\left(E_x + E_c + \frac{\hbar^2}{2m}k_\|^2 - \sqrt{\left(E_x - E_c - \frac{\hbar^2}{2m}k_\|^2\right)^2 + \Omega^2}\right) \qquad (4.12)$$

where E_x and E_c are the exciton energy and cavity energy at $k_\| = 0$, and Ω is the Rabi energy. Connecting the coordinates on the sample plane to the Cartesian coordinates on the CCD plane (x_F, y_F), we find the corresponding relation

$$x_F = \rho f \tan\theta \cos\phi \qquad (4.13)$$

$$y_F = \rho f \tan\theta \sin\phi \qquad (4.14)$$

In the implementation of the far-field imaging setup, we have a few more lenses to relay image the Fourier plane of the lens to the CCD plane as depicted in Fig. 4-12, and the magnification from the Fourier plane to the CCD plane is given by ρ here. Putting all the pieces together yields

$$x_F = \rho f \tan\left(\arcsin\frac{k_\|}{k}\right)\cos\left(\arctan\frac{k_y}{k_x}\right) \qquad (4.15)$$

$$y_F = \rho f \tan\left(\arcsin\frac{k_\|}{k}\right)\sin\left(\arctan\frac{k_y}{k_x}\right) \qquad (4.16)$$

where we express the angles θ and ϕ using k and $k_\|$.

Neglecting polariton dispersion. The area element will be connected through the Jacobian as

$$dx_F dy_F = \frac{\partial(x, y)}{\partial(k_x, k_y)} dk_x dk_y \qquad (4.17)$$

As a first-order approximation, we neglect the polariton dispersion and assume the emission wavenumber k is angle-independent. The Jacobian is evaluated as

$$\frac{\partial(x_F, y_F)}{\partial(k_x, k_y)} = \begin{vmatrix} \frac{\partial x_F}{\partial k_x} & \frac{\partial x_F}{\partial k_y} \\ \frac{\partial y_F}{\partial k_x} & \frac{\partial y_F}{\partial k_y} \end{vmatrix} = \frac{\gamma^2 f^2}{k^2 \cos^4 \theta} \tag{4.18}$$

Therefore,

$$dx_F dy_F = \frac{\gamma^2 f^2 \lambda^2}{4\pi^2 \cos^4 \theta} dk_x dk_y \tag{4.19}$$

The transformation can be understood from Fig. 4-14. Figure 4-14(a) shows the reciprocal space at the sample plane, and k_x and k_y are uniformly spaced. Figure 4-14(b) displays the one-to-one correspondence of k_x and k_y on the CCD. Clearly k_x and k_y become sparse at high angles, indicating the decrease of the density of k states at high angles [138]. The blue circles indicate our field of view.
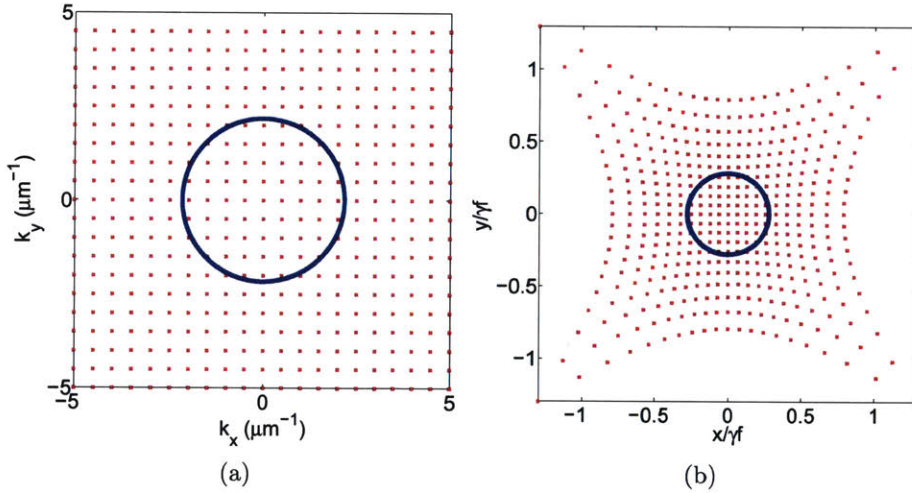
Figure 4-14: Mapping of Fourier plane to the spectrometer CCD. (a) Reciprocal space at the sample plane, k_x and k_y are uniformly spaced. (b) One-to-one correspondence of k_x and k_y on the CCD. The blue circles indicate our field of view.

Taking the fact that the total number of states should be conserved,

$$dn = \frac{S}{4\pi^2} dk_x dk_y = D dx dy \tag{4.20}$$

114

where $S/4\pi^2$ is the density of k states in the reciprocal space, S is the sample area, and D is the density of k state on the CCD. Therefore,

$$D = \frac{S}{\gamma^2 f^2 \lambda^2} \cos^4 \theta \qquad (4.21)$$

Consequently, the number of states per pixel can be computed as

$$M = DA = \frac{SA}{\gamma^2 f^2 \lambda^2} \cos^4 \theta \qquad (4.22)$$

where A is the area of a single CCD pixel. Removing the θ dependence by using the relation in Eq. (4.10), we obtain

$$M = \frac{SA(k^2 - k_\parallel^2)^2}{4\pi^2 \gamma^2 f^2 k^2} \qquad (4.23)$$

Taking into account the polariton dispersion. When taking into account the angle-dependence in the emission wavenumber k, we approximate the dispersion relation in Eq. (4.12) as a quadratic relation in order to simplify the calculation of the Jacobian

$$k = k_0 + \frac{\hbar}{2mc} k_\parallel^2 \qquad (4.24)$$

where $k_0 = E_0/\hbar c$, and E_0 is the ground state energy at $k_\parallel = 0$. Working out the Jacobian gives

$$\frac{\partial(x_F, y_F)}{\partial(k_x, k_y)} = \begin{vmatrix} \frac{\partial x}{\partial k_x} & \frac{\partial x}{\partial k_y} \\ \frac{\partial y}{\partial k_x} & \frac{\partial y}{\partial k_y} \end{vmatrix} = \frac{\rho^2 f^2 \left(k^2 - akk_\parallel\right)}{(k^2 - k_\parallel^2)^2} \qquad (4.25)$$

with $a = \hbar/mc$. Therefore,

$$dn = \frac{S}{4\pi^2} dk_x dk_y = \frac{S}{4\pi^2} \frac{(k^2 - k_\parallel^2)^2}{\rho^2 f^2 (k^2 + akk_\parallel)} dx dy \qquad (4.26)$$

115

the density of k states per pixel on the CCD is

$$M = \frac{SA(k^2 - k_\parallel^2)^2}{4\pi^2\rho^2 f^2(k^2 - akk_\parallel)} \qquad (4.27)$$

Compared to Eq. (4.23), a correction of $akk_\parallel$ is added to the denominator. Overall, the factor M gives a correction of $\sim 12\%$ at the edge of our field of view compared to $k_\parallel = 0$, and it is crucial to include in converting the energy dispersions $E(k)$ to the energy distributions $N(E)$, which will be the focus of Chapter 5.

4.4   Microcavity Structures

The structure of the sample used in this dissertation is shown in Fig. 4-15: three sets of four 7-nm GaAs quantum wells (QWs) are embedded at three antinodes in a $3\lambda/2$ microcavity, with the front and back distributed Bragg reflectors (DBRs) composed
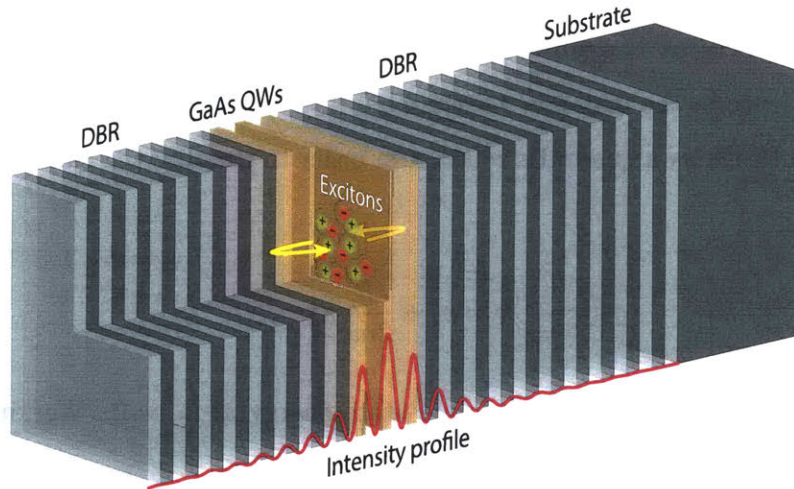
Figure 4-15: Schematic illustration of the microcavity structure used in this dissertation. The red lines indicate the intensity distribution of the confined optical field. The dark and light gray alternate layers are the distributed Bragg reflectors (DBRs) that are used to confine the light in the cavity. Quantum wells (QWs) are shown as the orange layers.

of 32 and 40 pairs, respectively, of $Al_{0.2}Ga_{0.8}As/AlAs$ $\lambda/4$ layers. The cavity region is indicated as the orange section, and red lines show the intensity distributions of the confined light modes in the cavity. This microcavity structure is identical to

semiconductor microcavity structures with short polariton lifetimes [34] except that the number of layers in the DBRs is doubled. This leads to an significant increase in the lifetime of the trapped cavity field to about 135 ps, implying a polariton lifetime of 270 ps at $\delta = 0$, which has been verified by transport measurements under both non-resonant excitation [97] and resonant excitation [98]. The microcavity structure is wedged along one direction as shown in Fig. 3-13, which allows tuning of the photon resonance across the exciton resonance, thus allowing control of exciton fractions in polariton states.

Although the concept of doubling the number of DBR layers is simple, the fabrication is not trivial because it requires much longer fabrication times, approximately 30 hours of molecular-beam epitaxy (MBE), with tight control during the entire growth process. If the growth process is not well controlled, inhomogeneities in the lower levels will be amplified in higher levels.

4.4.1 Optical selection rules in GaAs

The electrons and holes that compose the excitons in bulk GaAs originate in the underlying atomic orbitals of the Ga and As atoms. The covalent bonding between Ga and As atoms gives rise to an s-orbital like conduction band and a p-orbital like valence band. To determine the optical selection rules, we must consider the total angular momentum of each particle. The total angular momentum $\mathbf{J}$ is the sum of the particle spin $\mathbf{S}$ and the orbital angular momentum $\mathbf{L}$,

$$\mathbf{J} = \mathbf{L} + \mathbf{S} \tag{4.28}$$

Since holes arise from electrons, both electrons and holes have spins of $|\mathbf{S}| = \frac{1}{2}$. On the other hand, the orbital angular momentum of an electron in the conduction band is $|\mathbf{L}| = 0$ since the parity of the conduction band is s-orbital like. Thus the total angular momentum of the electron is $|\mathbf{J}| = \frac{1}{2}$. However, the orbital angular momentum of the hole is $|\mathbf{L}| = 1$ as a result of the p-orbital like parity of the valence band. Hence the hole is a $|\mathbf{J}| = \frac{3}{2}$ system and we have $|\mathbf{J}| = \frac{3}{2}$ and $|\mathbf{J}| = \frac{1}{2}$. Holes

with $|\mathbf{J}| = \frac{1}{2}$ resides in the so-called split-off band. At the gamma point $\mathbf{k} = 0$, they are separated by about $0.5\,\mathrm{eV}$ from holes with $|\mathbf{J}| = \frac{3}{2}$ in our sample, and are not resonant with the excitation laser, therefore are not considered throughout this dissertation. Putting it altogether, this leaves two possible total angular momentum values, $m_j = \pm\frac{1}{2}$, for an electron, and four possible values, $m_j = \pm\frac{3}{2}, \pm\frac{1}{2}$, for a hole. We typically refer to the holes with $m_j = \pm\frac{3}{2}$ as heavy holes (hh), and the holes with $m_j = \pm\frac{1}{2}$ as light holes (lh). Light holes and heavy holes are degenerate at $k = 0$ in bulk semiconductors. In quantum wells, confinement lifts the degeneracy, leaving the heavy hole band at a lower energy. Since the heavy hole and light hole bands are split by $30\,\mathrm{meV}$ in the long-lifetime structure we obtained from Princeton, and the confined light is close to the resonance of they heavy hole excitons, we only consider polaritons arising from heavy-hole excitons in this dissertation. The band structure is summarized in Fig. 4-16(a).
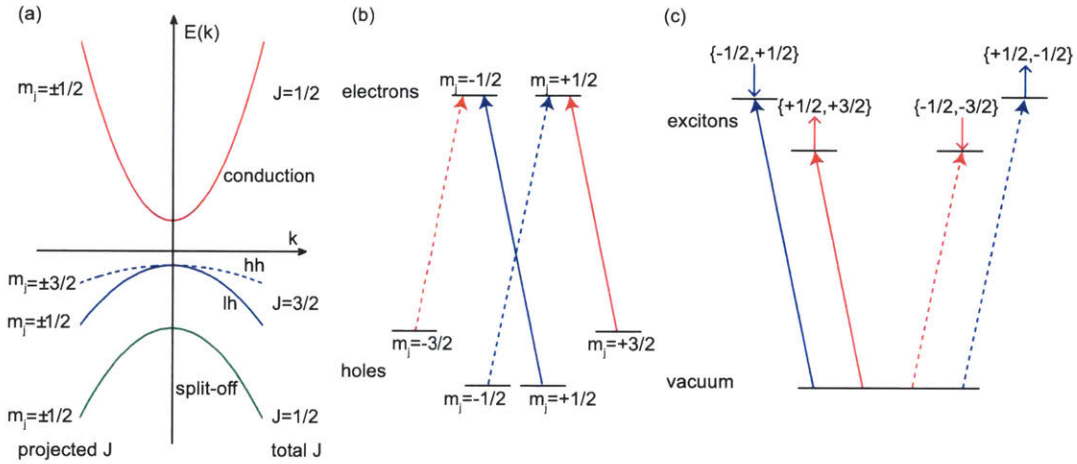
Figure 4-16: (a) A schematic diagram of the energy band structure of a bulk GaAs crystal. The three lowest states are the split-off band, light-hole and heavy-hole states in the valence band, and the highest state is the conduction band. The total angular momenta J and their projections on the growth axis J_z are also shown next to the band structure. (b) Energy states and optical transition selection rules for zero in-plane momentum. The dashed (solid) arrows represent right circularly (left circularly) polarized light. (c) Energy states and optical transition selection rules in the exciton basis set.

Because of angular momentum conservation, the absorption of a single photon causes a change in the total angular momentum by ± 1 given that a photon has a total angular momentum of $|\mathbf{J}| = 1$. The allowed optical transitions between electrons and

118

holes are shown in Fig. 4-16(b). As can be seen, all the connected states have a total angular momentum difference of $\Delta m_j = \pm 1$, corresponding to excitation with a left circularly polarized light (dashed lines) or with a right circularly polarized light (solid lines).

The optical transition can be more conveniently described in the exciton basis [139], as shown in Fig. 4-16(c). In the exciton representation, the right circularly polarized (σ^+) with the right energy will create a spin-up heavy-hole exciton (but a spin-down heavy-hole exciton), and vice versa. The vacuum is the unexcited system.

4.4.2 Polariton spin and pseudospin

The picture described above is valid in the strong coupling regime, so there are similar relations between the photon polarization and the polariton angular momentum. A σ^+ photon creates a $|+1\rangle$ polariton and a σ^- photon creates a $|-1\rangle$ polariton. A linearly polarized photon creates a polariton in the superposition state $\frac{1}{\sqrt{2}}(|+1\rangle + e^{2i\phi}|-1\rangle)$, which corresponds to a polariton with a spin oriented in the plane of the quantum well. This leads to a common description of the polariton system as a pseudospin-1/2 system, and the polariton states $|+1\rangle$ and $|-1\rangle$ are represented by the pseudospin states $|\uparrow\rangle$ and $|\downarrow\rangle$, respectively. The pseudospin representation can be advantageous when describing quantum-optical phenomena in microcavities.

4.4.3 Characterization of long cavity lifetime

The quality of the sample varies from batch to batch, hence it is important to measure the lifetime of the microcavity structure to see if it is reasonably long (>100 ps). Without performing time-resolved measurements, the following calibration [140] can be carried out for this purpose.

In this measurement, the polaritons were excited incoherently by using an above-bandgap c.w. laser, and the resulting photoluminescence was imaged onto the CCD camera in the near-field geometry. A spatial filter was also placed in the Fourier plane to allow only $k \approx 0$ components to pass through. Spectrally resolved near-field

emissions for different cavity detunings are shown in Fig. 4-17. The horizontal axis displays spatial position, and the vertical axis displays the lower polariton emission energy. When the cavity detuning is −5.7 meV, as shown in Fig. 4-17(e), polaritons are mostly localized at the excitation spot, but when the cavity is significantly negatively detuned at −35.9 meV, long-range propagation as far as 500 μm is observed with high-quality samples, as shown in Fig. 4-17(a). The results can be qualitatively understood by the change in the effective masses of polaritons for different cavity detunings. The polaritons are lighter and can propagate further when the cavity detuning is more negative and polaritons are mostly photon-like. Interestingly, only up-hill (toward thinner cavity widths) propagation was observed for all different cavity detunings in our measurement.

A possible mechanism for the observation of uphill propagation of the polariton fluid is shown in Fig. 4-18. A reservoir of free carriers is created under c.w. non-resonant pumping. The free carriers then relax down to the high-momentum exciton states via LO-phonon scattering and exciton scattering. Further scattering with acoustic phonons turns excitons into polaritons. At the pump region, a significant fraction of polaritons undergo polariton-polariton scattering and reach $k = 0$, leading to a bright emission at the pump region. In the meantime, some fraction of polaritons ballistically accelerate away from the pump spot. In the uphill direction, the kinetic energy of polaritons is lost in surmounting the cavity gradient, and eventually the polaritons become stationary, i.e., $k_\parallel \approx 0$, at which point their emission gets through the k-space filter and they enter the field of view. On the other hand, in the downhill direction, the cavity gradient provides an additional acceleration for polaritons, and they remain outside of the field of view. Based on the decay of photoluminescence in the uphill direction, the lifetime of polaritons can be estimated.

4.4.4 Characterization of sample parameters

The cavity length varies as a function of position on the sample. In order to characterize the energy detuning of the cavity mode from the exciton energy, δ, the energy of the lower polariton was measured as a function of position. For those measurements,
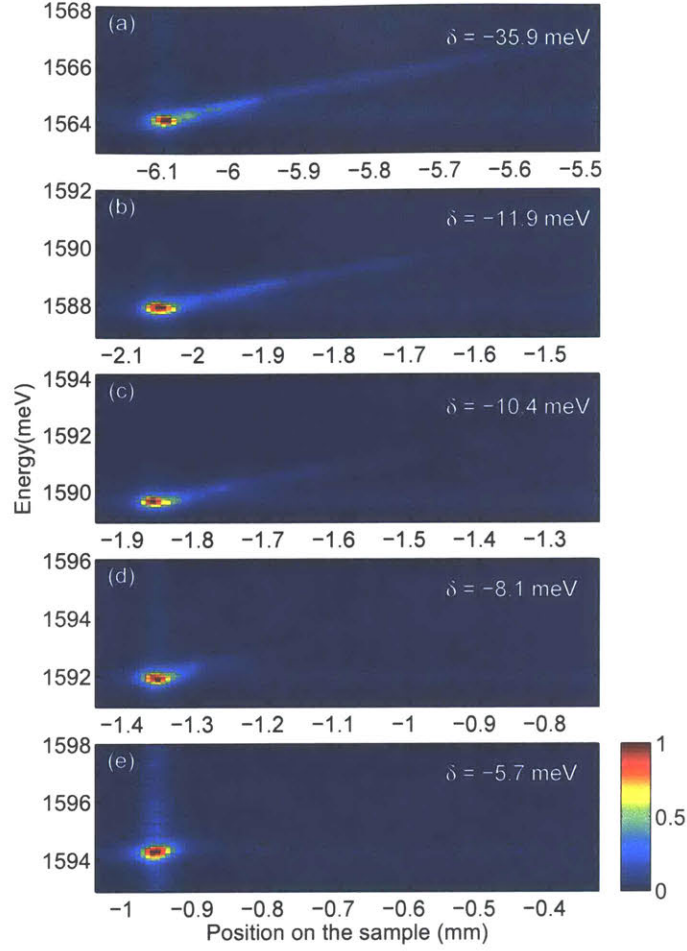
Figure 4-17: Long-range polariton propagation along the wedged direction of the sample under c.w. non-resonant excitation. Spectrally resolved near-field emissions for different cavity detunings (δ). The horizontal axis displays the sample position, with zero sample position corresponding to the zero cavity detuning and negative sample position corresponding to the negative cavity detuning. The vertical axis displays the LP emission energy at $k = 0$. Since the polariton effective mass becomes lighter when the cavity is more negatively detuned, the polaritons propagate further.

the output of the c.w. laser was directly focused onto the surface of the sample as a Gaussian spot with a FWHM diameter of about 5 μm. The power of the c.w. laser was kept as low as possible to eliminate any energy renormalization of the dispersion curves from increased densities. In order to isolate the photoluminescence from a single position on the sample, a pinhole was placed in the reconstructed near-field image plane downstream show in Fig. 4-11. The pinhole was centered on the excita-
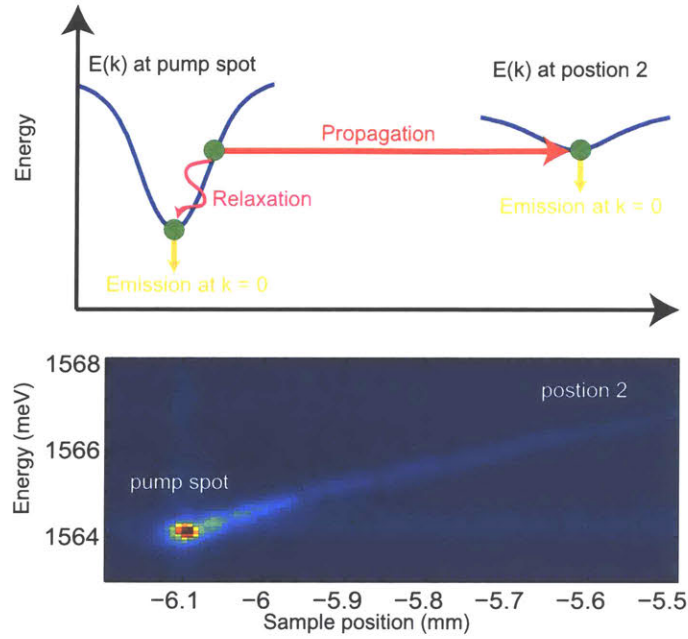
Figure 4-18: Due to the cavity gradient, the ground state energy of polaritons increases upon the uphill direction. At the pump region, a significant fraction of polaritons undergo polariton-polariton scattering and reach $k = 0$, leading to bright emission at the pump region. In the meantime, some fraction of polaritons at different stages of relaxation ballistically accelerate away from the pump spot with different amounts of kinetic energy in the form of in-plane momentum. In the uphill direction, the kinetic energy of polaritons is gradually lost in overcoming the cavity gradient, and $k_\parallel$ reduces to ≈ 0 and the polaritons enter the field of view. This occurs at different distances from the pump region, depending on the in-plane momentum of the polaritons when they left that region. On the other hand, in the downhill direction, the cavity gradient provides additional acceleration for polaritons, and they remain outside of the field of view. Based on the decay of photoluminescence in the uphill direction, the lifetime of polaritons can be estimated.

tion pump spot so that the emission around the excitation spot was collected. Some representative far-field images at different cavity detunings are shown in Fig. 4-19. As can be seen, the ground state energy increases as the detuning is increased because the cavity energy is higher as we move to more excitonic detunings. The spectral linewidth of the photoluminescence at $k_\parallel$ also increases as a manifestation of the increased interactions between polaritons and other species including excitons and free carriers. The entire set of dispersion curves is used to determine the cavity gradient and the Rabi splitting. We use the nonlinear least-squares to fit the data set to the
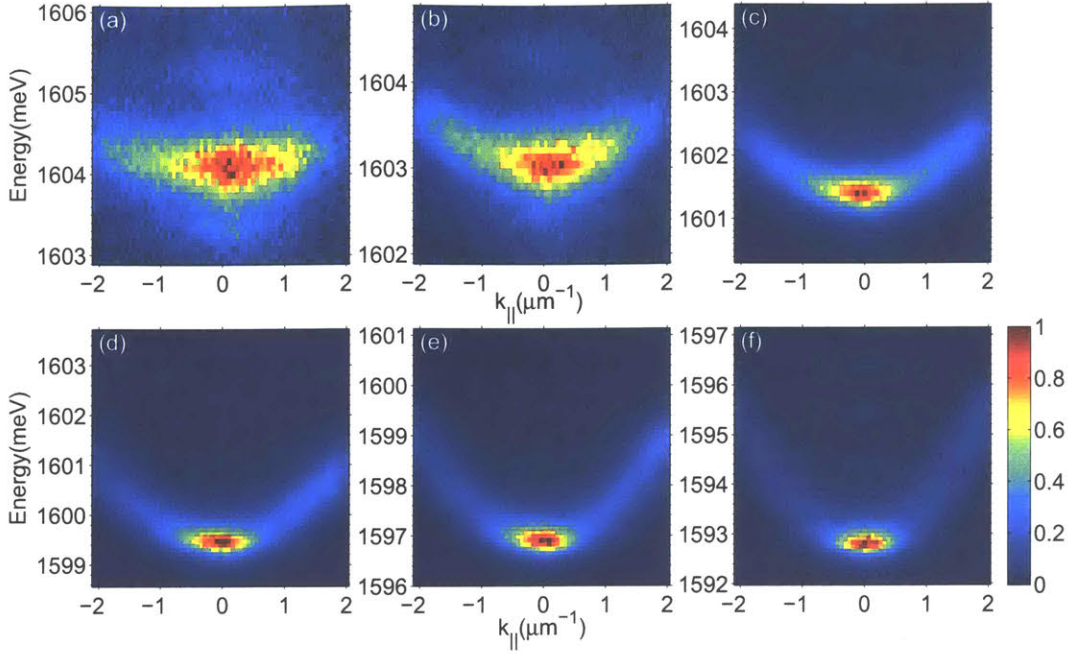
Figure 4-19: Spatially filtered spectrally resolved far-field polariton photoluminescence in long-lifetime samples at different cavity detunings. The photoluminescence is shown as a function of both in-plane wave vector $k_{\parallel}$ and energy. The spatial filter was centered on the optical pump spot which was focused at a position on the sample corresponding to a cavity detuning energy, δ, of (a) 9.47 meV, (b) 5.91 meV, (c) 2.36 meV, (d) -1.19 meV, (e) -4.75 meV, and (f) -9.49 meV.

model

$$E(k,x) = \frac{1}{2}\left(2E_x + (g_x + g_c)(x - x_{res}) + \frac{\hbar^2}{2m}k^2 - \sqrt{\left((x - x_{res})(g_x - g_c) - \frac{\hbar^2}{2m}k^2\right)^2 + \Omega^2}\right)$$

(4.29)

where we also assume a gradient for the exciton energy. g_x and g_c are the exciton and cavity energy gradients, respectively. x_{res} is the resonance position of the sample, x is the current position, and m is the effective mass of bare photons which is experimentally determined by fitting the polariton dispersion collected at a detuning

123

of -30 meV to a parabola. The fitted parameters in Eq. (4.29) are

$$E_x = (1603.20 \pm 1.69)\,\mathrm{meV}$$

$$g_x = (-2.46 \pm 2.40)\,\mathrm{meV/mm}$$

$$g_c = (-12.26 \pm 2.36)\,\mathrm{meV/mm}$$

$$x_{res} = (17.12 \pm 0.25)\,\mathrm{mm}$$

$$\Omega = (10.84 \pm 2.83)\,\mathrm{meV} \tag{4.30}$$

The results are summarized in Fig. 4-20. The energy of the dispersion relation at $k = 0$ is used to map out the energy of the lower polariton as a function of position, shown in Fig. 4-20 as blue circles. The energies of the lower polariton for very short and long cavity lengths are asymptotic to the energies of the uncoupled exciton and cavity modes, respectively, shown as the black dashed lines. The energy difference between the two modes gives the detuning energy, $\delta = E_c - E_x$, which is used to label the dispersion curves in Fig. 4-19. We also plot the fitted LP energies using Eq. (4.29), and the fitted values agree well with the measured energies.
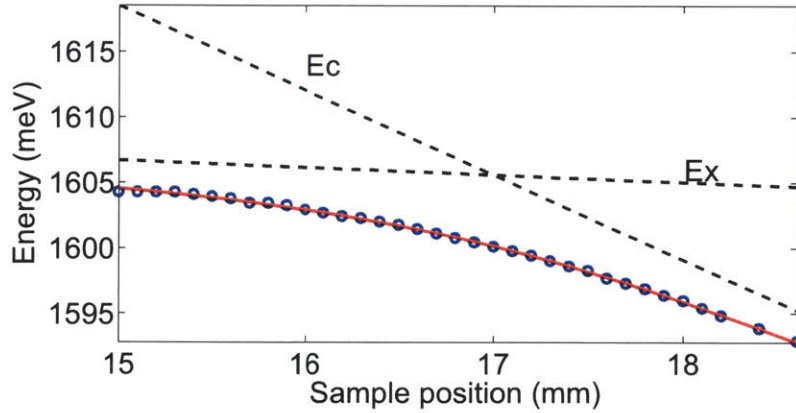
Figure 4-20: The ground state energy of polaritons as a function of sample positions in the long-lifetime microcavity. The blue circles are measured ground state energies at different sample position, and the red line is the fit using Eq. (4.29). Black dashed lines are the fitted bare cavity energy and exciton energy.

4.5 Realization of Quantum Condensation in Microcavities

Quantum condensation of microcavity polaritons is usually referred to as dynamic condensation owing to the parametric process that drives the formation of polariton condensates. In this section, we briefly review the details of experimental realization of quantum condensation with polaritons.

Non-resonant excitation. A c.w. laser with its photon energy far above the polariton resonance, typically matching one of the reflection dips above the stop band, is used to create a reservoir of free carriers, as shown in Fig. 4-21(a). This excitation scheme is referred to as non-resonant excitation.

Formation of thermalized exciton reservoir. After non-resonant excitation, the free carriers relax to the exciton dispersion by scattering with LO phonons. This process confers very large momenta to excitons, leading to decoupling between excitons and photons, as shown in Fig. 4-21(b). Excitons then lose energy and momentum by multiple scattering events with acoustic phonons. A thermalized exciton reservoir is then created in the vicinity of the light cone around $k_{rad} = 10\,\mu m^{-1}$, where polaritons are formed, as illustrated in Fig. 4-21(c). Polaritons are strongly coupled to light and can radiatively decay on a much faster timescale, on the order of $100\,ps$ in the long-lifetime structure. Furthermore, the density of states decreases dramatically given the change of the energy dispersion in the low-k region. Competition between slow polariton-acoustic phonon scattering and fast polariton radiative recombination prevents the system from reaching thermal equilibrium in short-lifetime microcavity structures, producing the so-called relaxation bottleneck region [141, 142].

Parametric scattering at the magic angle Figure 4-21(d) depicts the relaxation in the low-k region, where polariton-polariton scattering [143, 144, 145, 146, 147] results in the relaxation of polaritons into the ground state at $k = 0$. At an angle known as the magic angle, the polariton-polariton scattering becomes very efficient because
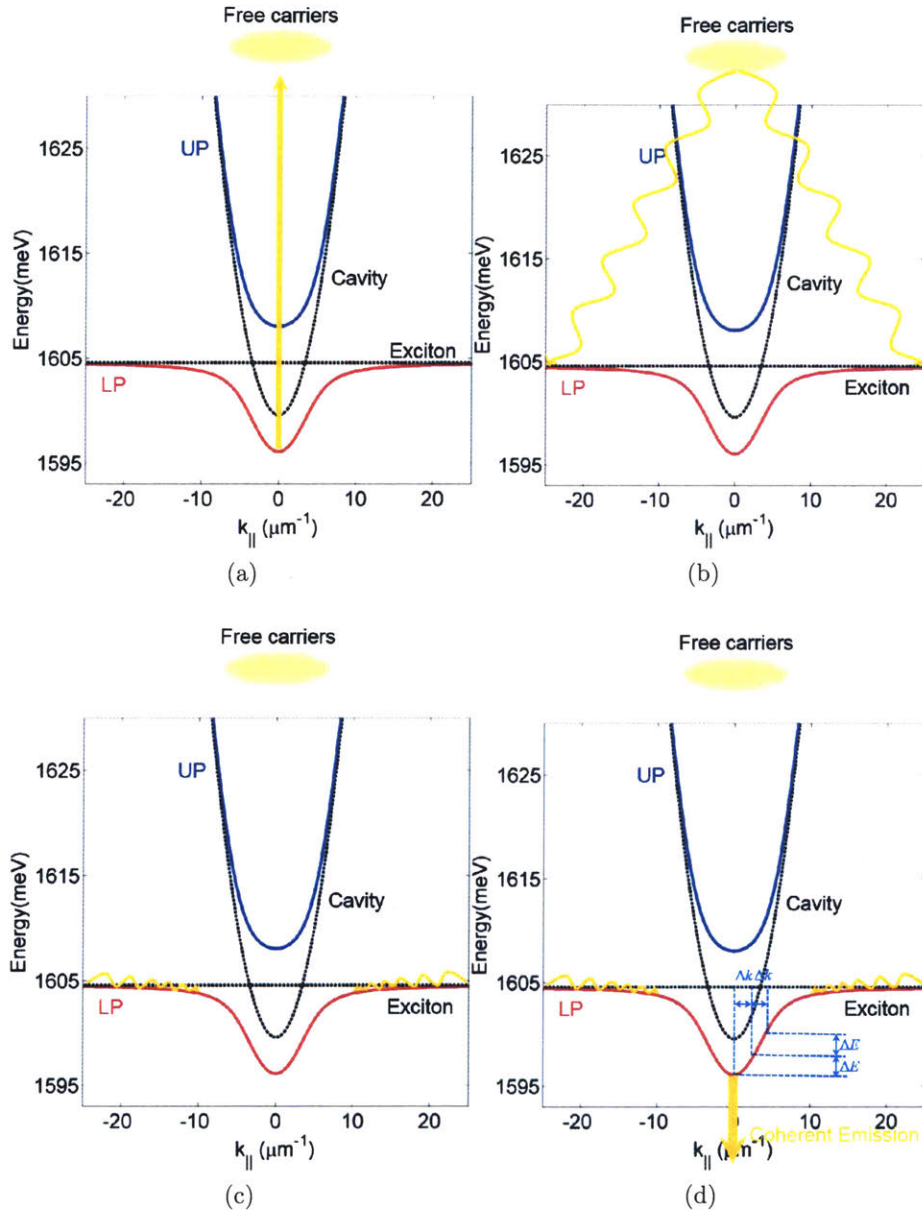
Figure 4-21: A schematic illustration of formation of polariton condensates. (a) Non-resonant pumping excites a reservoir of free carriers. (b) The free carriers scatter with LO phonons and become non-radiative. (c). Excitons scatter with acoustic phonons, and produce a thermalized exciton reservoir at the bottleneck region. (d) Further scattering with acoustic phonons becomes inefficient at the bottleneck region, and polariton-polariton scattering takes place. At the inflection point of the energy dispersion, polariton-polariton scattering becomes very efficient. Once the ground state population reaches unity, Bose amplification takes place, and drives polariton condensation.

it can satify both the exact energy and momentum conservation, as illustrated in the figure. When the occupation of the ground state reaches unity, Bose amplification takes place and stimulates other polaritons into the ground state, causing macroscopic occupation of the ground state to occur and formation of quantum condensates.

4.6 All-Optical Trapping of Microcavity Polaritons

Exciton-polaritons in semiconductor microcavities have emerged as model systems for studying many-body effects, nonclassical states of light and matter, and quantum phase transitions in solid state. Furthermore, because of the extremely small effective mass, the operational temperature for polaritonic devices that exploit these properties can be as high as room temperature, presenting promising opportunities to create low-threshold, fast-operation nonlinear devices such as polariton switches and transistors. This rapid developing research on exciton-polaritons presents an urgent demand for control and manipulation of polaritons and their condensates. In this section, we review previously reported techniques to confine polaritons, followed by a detailed discussion of the experimental development of all-optical trapping in the Nelson group.

4.6.1 Previous approaches to confine polaritons

The tools to spatially manipulate polaritons rely on trapping either the excitonic components or the photonic components of the polaritons. Figure 4-22(c) illustrates a stress trap induced by a sharp metal tip with a diameter of 50 μm [34]. Because the bandgap of the semiconductor critically depends on the distance between two nearest atomic neighbors, the local strain introduces a redshift to the exciton energy, resulting in the formation of a parabolic potential for polaritons. The implementation of this technique led to the first successful demonstration of quantum condensation of exciton-polaritons in a GaAs-based microcavity under strictly non-resonant and non-local pumping, taking advantage of the diffusion of polaritons into the trap.

A somewhat related technique, which also exploits a modification of the local strain environment to manipulate the polariton potential landscape, is the application
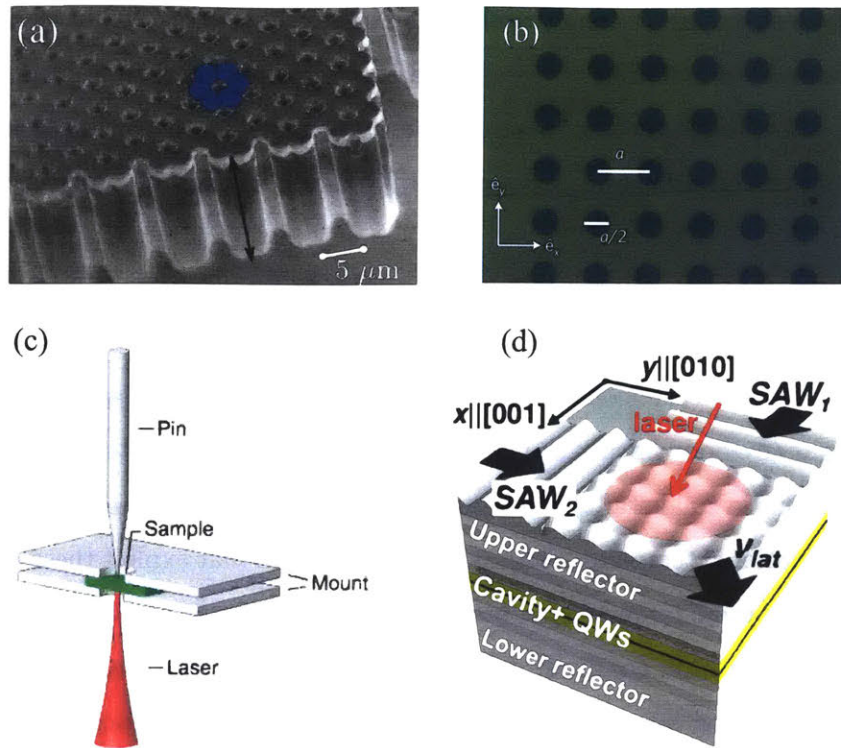
Figure 4-22: Different approaches to control of polaritons and their condensates. (a) Figure taken from Ref. [148]. An SEM image of a patterned microcavity structure grown by electron-beam lithography. (b) Figure taken from Ref. [149]. An SEM image of a patterned microcavity structure formed by depositing metallic thin films on the surface after fabricating the microcavity. (c) Figure taken from Ref. [34]. A schematic illustration of a stress trap. (d) Figure taken from Ref. [150]. A schematic illustration of confining polaritons by applying surface acoustic waves.

of surface acoustic waves (SAWs) to the polariton system [150, 151], as illustrated in Fig. 4-22(d). The cavity length and the refractive index of the cavity material are locally modified in the presence of the acoustic wave, which leads to a change of the local resonance condition and hence to optical confinement. The rise and fall time of the acoustic wave can be on the order of 10 ns, thus providing a dynamic approach to confinement of polaritons.

A comparatively simple, yet very efficient method to create polariton confinement in a grown microcavity structure is the deposition of metallic thin films on the sample surface [152, 149], shown in Fig. 4-22(b). The metal mask changes the boundary conditions of the electromagnetic wave with respect to a semiconductor-air interface

and creates an optical node. As a result, a modest shift in the energy of the optical resonance can be observed (on the order of 0.1–1 meV), which leads to an effective photonic confinement. The beauty of this approach lies in its simplicity, and many pioneering experiments with polaritons in periodic potential landscapes were initially carried out with such samples, including the observation p- and d-wave condensation [152, 149, 153].

Owing to the high flexibility and maturity of electron beam lithography and etching technologies, two-dimensional arrays of micropillars of almost any geometry can be fabricated easily [154, 155, 156, 157, 158]. Figure 4-22(a) shows an SEM image of an array of micropillars aligned in a honeycomb lattice configuration [148]. This lattice configuration provides an analogy to a graphene-type structure, and Dirac points have also been observed at specific locations in the Brillouin zone. Although these techniques are able to create well defined potential trap profiles, they are necessarily static and determined at the time of sample fabrication.

4.6.2 Optical trapping of polaritons

The carrier and exciton reservoir, which is created by the excitation laser, provides a flexible way to create potentials for the polaritons because excitons created by a laser field in the same structure have much larger effective mass than the polaritons: the typical polariton mass is less than 10^{-4} times that of electron mass, while the free exciton mass is of the order a tenth of the electron mass in GaAs quantum wells. Therefore, the excitons created by a laser pulse are essentially static as seen by polaritons, and the mean-field repulsion energy of the excitons acts as a static potential energy barrier. By using spatial light modulators to shape the optical excitation beam, confinement of almost any geometry can be readily implemented. Based on optical trapping, many intriguing phenomena have been observed including the formation of the macroscopic high-order quantum states [103, 159] and demonstration of polaritons with defined chirality [160].

In this dissertation, spatially varying potential barriers for polaritons are created by pumping the microcavity structure with an annulus of usually 42 μm in diameter.
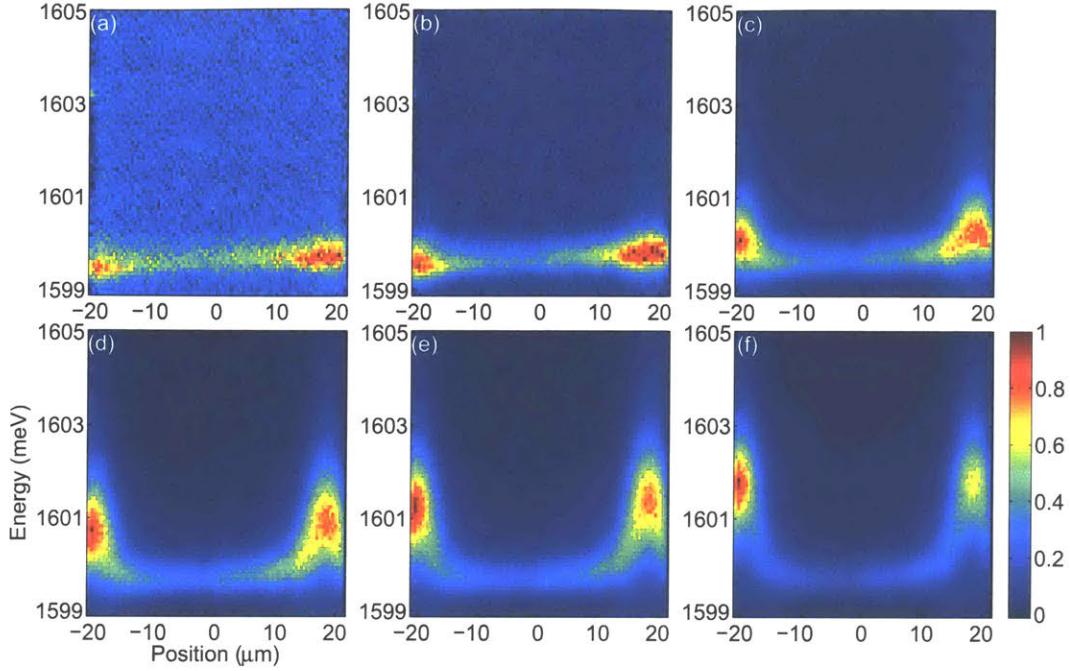
Figure 4-23: Energy-resolved real-space emission as excitation power increases. The pump powers are $P = 54.5$ mW, $P = 129.2$ mW, $P = 404.7$ mW, $P = 639.6$ mW, $P = 774.0$ mW and $P = 881.7$ mW in (a)-(f), respectively.

Figure 4-23 shows the spectrally resolved emission as a function of position on the sample for different pump powers. As can be seen in Fig. 4-23(a), when the pump level is low, polaritons remain in the vicinity of the pump region. The linear slope is a result of cavity gradient due to the spatially varying cavity thickness. As the pump power is increased, the energy shift at the pump region increases due to the accumulation of high densities of hot carriers and excitons, and a potential barrier for polaritons is formed.

The height of the barrier as a function of the integrated intensity of the photoluminescence is shown in Fig. 4-23, along with the energy shift in the center of the trap at $x = 0$. In the range of accessible pump powers, the energy shifts at the pump region always exceed the energy shifts in the center of the trap, suggesting polaritons are confined. The confinement of polaritons can also be identified by comparing Fig. 4-25 with Fig. 4-19. When polaritons are not trapped, as shown in Figs. 4-25(d)-(f), they can accelerate ballistically away from the pump spot, and lead to smeared dispersion
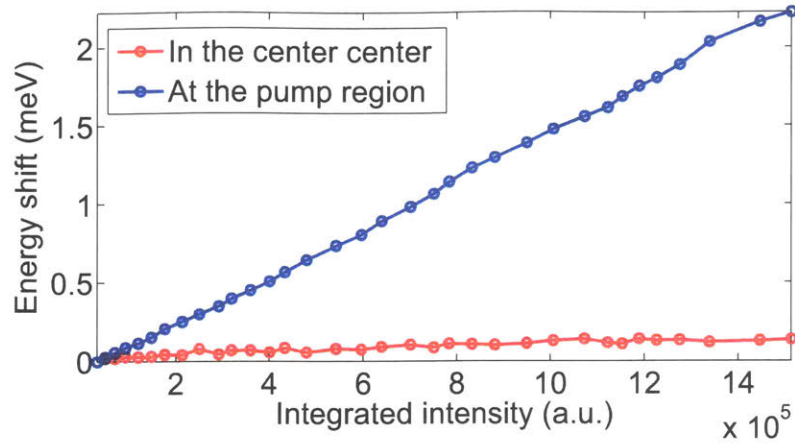
Figure 4-24: Trap height as a function of integrated photoluminescence intensity at both the pump region (blue circles) and the center of the trap (red circles).
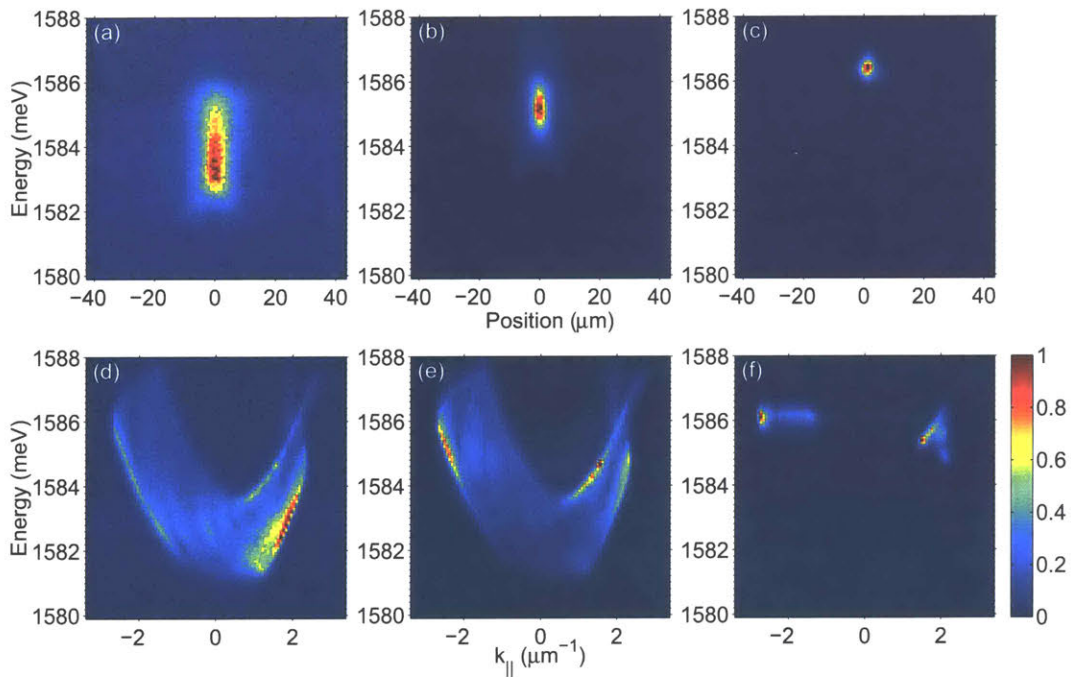
Figure 4-25: Spectrally resolved near-field (a)-(c) and far-field images (d)-(f) of the photoluminescence with a Gaussian excitation profile for pump powers 0.4 mW (a) and (d), 23.4 mW (b) and (e), and 1019 mW (c) and (f).

curves. On the other hand, when polaritons are confined in the center, they are able to reach spatial equilibrium, indicated in Fig. 4-19. In fact, the trapped polaritons can even reach thermal equilibrium when the cavity detuning is close to resonance

or positive. This will be discussed heavily in Chapter 5. In Fig. 4-23, we also show the spectrally resolved near-field emission patterns when a Gaussian spot is used to excite the microcavity. In this case, polariton condensates are formed on top of the exciton reservoir.

4.7 Numerical Techniques in Data Analysis

The ordinary least-squares approach is equivalent to maximum-likelihood estimates in statistics if the data set does not experience heteroscedasticity. Heteroscedasticity refers to the statistical phenomenon when subsets of a collection of random variables have different variabilities from others. Since the uncertainties in each of the individual data points are not necessarily the same in our experiments, an ordinary least-squares approach would fail to give an accurate inference of the parameters in our model. A weighted least-squares estimate has been developed to solve this problem.

4.7.1 Weighted least-squares estimate

The weighted least-squares estimate has been used to estimate some important quantities in the measurements, including the determination of the pure exciton-exciton interaction strength in Chapter 6. Here a summary of the key concepts of weighted least-squared regression is presented.

For a regression model

$$Y = X\beta + \varepsilon \tag{4.31}$$

where Y is an $n \times 1$ column vector with n indicating the number of data points, X is an $n \times p$ matrix with p indexing the number of independent loading factors, and β is a $p \times 1$ vector of these independent factors. ε is the set of residuals which are

assumed to be independently normally distributed, with a covariance matrix

$$\text{Var}(\varepsilon) = \begin{pmatrix} \sigma_1^2 & 0 & \cdots & 0 \\ 0 & \sigma_2^2 & \cdots & 0 \\ \vdots & \vdots & & \vdots \\ 0 & 0 & \cdots & \sigma_n^2 \end{pmatrix} \tag{4.32}$$

The weighted least-squares regression is conducted to minimize

$$Q(\beta) = \| w \cdot (\boldsymbol{Y} - \boldsymbol{X}\beta) \|_2^2 \tag{4.33}$$

where w is a $n \times 1$ vector for the weights on different measurements of Y. By differentiating the equation with respect to β, the estimator is found to be

$$\hat{\beta} = \left(\boldsymbol{X}^T \boldsymbol{W} \boldsymbol{X}\right)^{-1} \boldsymbol{X}^T \boldsymbol{W} \boldsymbol{Y} \tag{4.34}$$

where $\boldsymbol{W}$ is a diagonal matrix whose entries are the weights w, and the $1 - \alpha$ uncertainty is given by

$$\Delta \hat{\beta}_k = s_k t_{1-\alpha/2, n-p-1} \quad k = 1, 2, \cdots, p \tag{4.35}$$

where t is the $1 - \alpha/2$ percentile of the student t distribution with degrees of freedom of $n - p - 1$. The sample standard deviation is estimated as

$$s_k = \sqrt{\frac{\sum_{i=1}^{n} e_i^2}{n - p - 1} c_{k,k}} \tag{4.36}$$

where $c_{k,k}$ is the diagonal element of $\left(\boldsymbol{X}^T \boldsymbol{W} \boldsymbol{X}\right)^{-1}$, and

$$e = \sqrt{w} \cdot \left(\boldsymbol{Y} - \boldsymbol{X}\hat{\beta}\right) \tag{4.37}$$

For the extrapolation, or prediction in the statistical sense, the value of regressand is

given by the matrix $\boldsymbol{\mathcal{X}}$. Therefore, the mean of the predicted regressor is simply

$$\boldsymbol{\mathcal{Y}} = \boldsymbol{\mathcal{X}}\hat{\beta} \tag{4.38}$$

and the uncertainty associated with the prediction/extrapolation is given by

$$\Delta\boldsymbol{\mathcal{Y}} = \mathcal{S}t_{1-\alpha/2,n-p-1} \tag{4.39}$$

with

$$\mathcal{S}^2 = \boldsymbol{\mathcal{X}}^T \left(\boldsymbol{X}^T\boldsymbol{W}\boldsymbol{X}\right)^{-1}\boldsymbol{\mathcal{X}}u \tag{4.40}$$

and

$$u = \sum_{i=1}^{b} \frac{e_i^2}{n-p-1} \tag{4.41}$$

This is used in extrapolating the pure excitonic interaction strength in Chapter 6.

4.7.2 Least-squares fitting of ellipses

All the measurements in this dissertation were taken with annulus excitation profiles. Because of the imperfections of the imaging setup, the excitation profile is usually an ellipse with an eccentricity close to 0. We extract the lengths of major and minor axes of the ellipse and report their geometric average as the radius of the excitation profile. The least-squares fit to an ellipse is not trivial because the parametric form of an ellipse is not an injective function. An injective function is a one-to-one function that never maps distinct elements of its domain to the same element of its codomain. Exponential functions are injective while trigonometric functions are not injective. We follow the algorithm proposed by Walter Gander et al. [161], and the idea is summarized in the following.

An ellipse is parameterized by the quadratic equation

$$x^T A x + b^T x + c = 0 \tag{4.42}$$

where $x = (x_1, x_2)$ is a point coordinate in 2D, A is a 2×2 matrix, b is a 2×1 vector, and c is a scalar that all need to be determined. Because the equation is typically over-determined, that is, there are more data points than the number of parameters, solving the original fitting is effectively carried out as

$$x_i^T A x_i + b^T x_i + c \approx 0 \tag{4.43}$$

for all data points with x_i, with the constraint

$$a_{11}^2 + 2a_{12}^2 + a_{22}^2 = 1 \tag{4.44}$$

Regrouping the parameters as

$$\mathbf{v} = (b_1, b_2, c)^T \tag{4.45}$$

$$\mathbf{w} = (a_{11}, \sqrt{2}a_{12}, a_{22})^T \tag{4.46}$$

and defining the coefficient matrix

$$S = \begin{pmatrix} x_{11} & x_{12} & 1 & x_{11}^2 & \sqrt{2}x_{11}x_{12} & x_{12}^2 \\ \vdots & \vdots & \vdots & \vdots & \vdots & \vdots \\ x_{m1} & x_{m2} & 1 & x_{m1}^2 & \sqrt{2}x_{m1}x_{m2} & x_{m2}^2 \end{pmatrix} \tag{4.47}$$

where m is the number of data points, we find that Eq. (4.43) can be rewritten as

$$S \begin{pmatrix} \mathbf{v} \\ \mathbf{w} \end{pmatrix} \approx 0 \tag{4.48}$$

with constraints $\|w\| = 1$. This problem can then be solved by a standard linear algebra approach, for example, singular value decomposition. Figure 4-26 shows one ex-
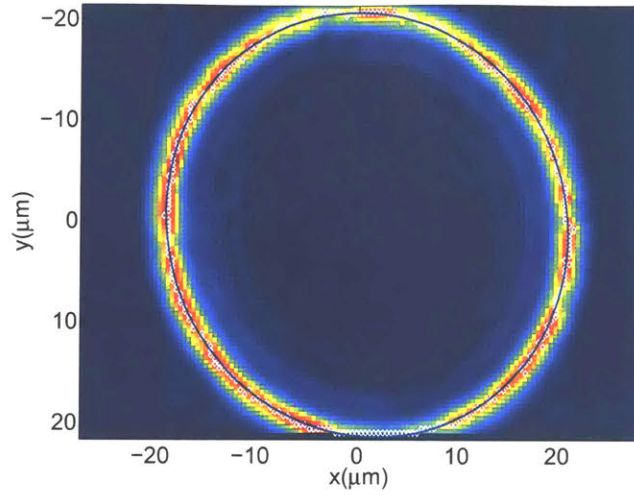
Figure 4-26: An illustration of fitting an annular excitation profile using the Walter and Gander's algorithm. The white diamonds are those with maximum intensity values along the profile, and the solid blue line is the fit.

ample of the fitted annular profile. The lengths of major and minor axes are $19.87\,\mu m$ and $21.29\,\mu m$, respectively, and their geometric average $20.57\,\mu m$ $(=\sqrt{19.87 \times 21.29})$ is used as an approximation to the radius of an ideal annular profile.

Chapter 5

Exciton-polariton Bose-Einstein Condensation in Thermodynamic Equilibrium

The experimental realization of Bose-Einstein condensation (BEC) of atoms has triggered wide exploration of macroscopic quantum effects, including superfluidity and quantized vortices. However, the ultralow temperature of atomic condensates hinders further applications. Polaritons in semiconductor microcavities have been used to demonstrate quantum effects such as condensation [32, 33, 34] and superfluidity [99] in much elevated temperatures, but polariton lifetimes are typically too short (due to photon escape from the cavity) to permit thermal equilibration following emergence of a coherent state [162, 163, 164, 165]. Although polariton experiments and theories have shown that a great number of canonical features of condensation persist in nonequilibrium, debates persist over whether polariton condensates can be called Bose-Einstein condensates [166, 167, 168], in part related to the question of whether polariton condensation is intrinsically a nonequilibrium effect. It is thus of fundamental importance to investigate whether polariton condensates can reach thermal equilibrium. Of course, strictly speaking, BEC cannot occur in an ideal infinite 2D system, but it has been shown [38, 169, 170, 171] that a 2D Bose gas in a large but finite trap has the same threshold behavior as a 3D Bose gas in a finite trap of the

same type. We can thus talk of an equilibrium BEC in 2D and 3D finite trapped systems using the same language.

In this chapter, we will discuss the first unambiguous observation of Bose-Einstein condensation of optically trapped polaritons in thermal equilibrium in a high-Q microcavity. In Section 5.1, the thermodynamic properties of polaritons and their condensates in previous experiments with short-lifetime microcavities are briefly reviewed. The challenges in realizing a polariton gas with full thermalization are also discussed. In Section 5.2, experimental methodologies are described, followed by discussions of signatures of quantum condensation in Section 5.3. In Section 5.4, we present the experimental realization of polariton condensates in true thermal equilibrium over a wide range of polariton densities and bath temperatures. Details of how to convert the measured CCD counts to the absolute polariton populations as well as how to extract the chemical potentials and temperatures from the measured distributions are included. Section 5.5 shows that the equilibrium behavior of polariton gases and their condensates depends crucially on the interaction strength among polaritons. By adjusting the cavity detuning to allow polaritons to become more photon-like, the equilibrium gas reverts back to nonequilibrium. In Section 5.7, we discuss the first measurement of a density-temperature phase diagram for Bose-Einstein condensation of polaritons. The measured phase boundary agrees well with the prediction of basic quantum gas theory, indicating that polariton condensation is a true phase transition. We conclude this chapter with a discussion of possible experiments exploiting the properties of BEC in thermodynamic equilibrium.

5.1 Condensation in Short-Lifetime Microcavities

In this section, we will briefly review the energy distributions $N(E)$ of polariton gases in short-lifetime microcavities, in particular, polariton condensates in a k-space trap with a CdTe-based microcavity and in a real-space trap with a GaAs-based microcavity. We will also discuss in detail early efforts in the study of the thermodynamic properties of polaritons and their condensates.

5.1.1 Polariton condensation far from equilibrium

Due to the steep dispersion of polaritons within the light cone, as shown in Fig. 3-12, the particle number loss rate of polaritons through polariton-phonon and polariton-polariton scattering at in-plane momentum $k_{||} = 0$ is significantly reduced; hence a large polariton population can accumulate around $k_{||} = 0$ to allow quantum condensation even in short-lifetime samples. However, unlike atomic condensates, polariton condensates are typically transient due to their limited lifetimes determined by leak-
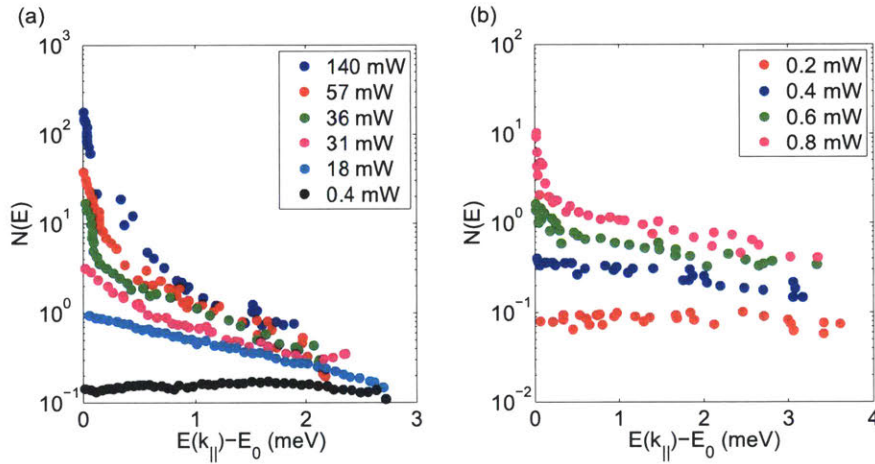
Figure 5-1: (a) Adapted from Ref. [33]. The measurements were performed with a CdTe-based microcavity with a lifetime of approximately 1 ps at positive cavity detunings $\delta = 3 \sim 8$ meV. The excitation laser was tuned about 100 meV above the polariton resonance with a uniform top-hat geometry of 35 μm diameter. (b) Adapted from Ref. [34]. The measurements were performed with a GaAs-based microcavity with a lifetime of approximately 2 ps at a detuning of $\delta = -10$ meV before applying the stress. The potential trap created by the mechanical stress exerted by a rounded-tip pin is about 50 μm in diameter. The excitation laser has an excess energy of 129 meV, and the photoluminescence was collected from the center of the trap.

age of the cavity. The energy distributions $N(E)$ of the resulting condensates are highly nonequilibrium because polaritons couple out of the cavity before they equilibrate with each other and the host lattice. In Fig. 5-1, we show the distributions of the polaritons created non-resonantly from below threshold to well above threshold in short-lifetime cavities [33, 34]. The plots are adapted from the two earliest experimental demonstrations of polariton condensation in Refs. [33] an [34]. In Fig. 5-1(a), a CdTe-based microcavity with a cavity lifetime of 1 ps was used, and the excitation

laser was carefully shaped into a uniform top-hat shape to eliminate inhomogeneities within the pump region. In Fig. 5-1(b), a GaAs-based microcavity with a cavity lifetime of 2 ps was used. Unlike the previous case, mechanical stress was applied to the microcavity to induce a potential trap so that polaritons could reach spatial equilibrium, i.e., become concentrated, inside the trap. Although the nature of quantum condensation was verified by the observation of spontaneous emergence of long-range coherence in both cases, both systems did not reach thermal equilibrium. As can be seen, polaritons follow Maxwell-Boltzmann distributions at low pump powers, as evidenced by straight lines in the semi-log plot. When the pump power is further increased, a condensate-like peak shows up around the ground state, but the entire distribution cannot be fitted by the equilibrium Bose-Einstein model. This has led to a common description of a polariton condensate as "nonequilibrium condensate", and also has prevented any determination of an equilibrium phase diagram which subsequently led to debate whether polariton condensation is a thermodynamic phase transition.

5.1.2 Formation of polariton condensates in thermodynamic and kinetic regimes

Two earlier works have addressed in depth the mechanism of condensate formation and thermalization of polaritons in short-lifetime samples. In Ref. [172], the polariton condensate in a CdTe-based microcavity was studied over a wide range of pump powers and bath temperatures. Depending on the cavity detuning which in turn determines the interaction strength among polaritons, polariton condensates in thermodynamic and kinetic regimes were identified. In Fig. 5-2, the pump power was kept at $P = 10.2$ mW, and the cavity detuning was chosen to be $\delta = 6.8$ meV, which corresponds to an exciton fraction of 62.7% in the polaritons; therefore polaritons were strongly interacting. This led to full thermalization of polaritons at high bath temperatures where the bottleneck effect was weak, as evidenced by the good fits to the Maxwell-Boltzmann distribution. As the bath temperature was decreased, a
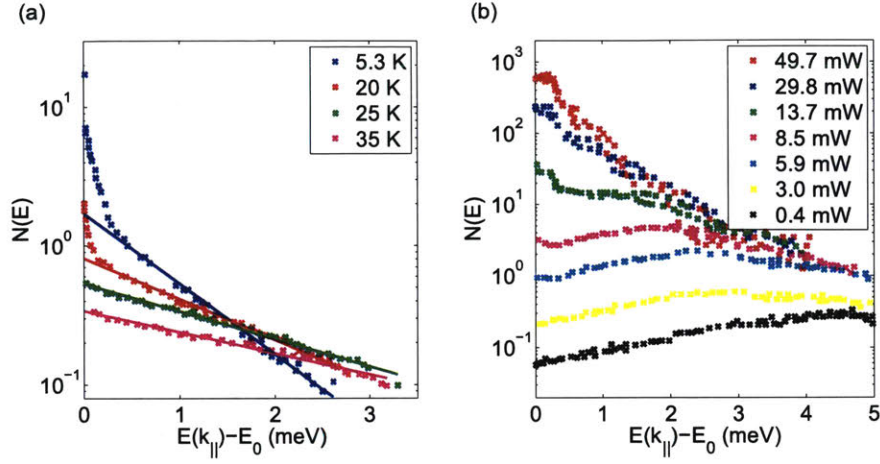
Figure 5-2: Thermodynamic and kinetic regimes of polaritons created non-resonantly in a CdTe-based microcavity with a cavity lifetime of ~1 ps. Adapted from Ref. [172]. (a) Energy distributions (dots) and corresponding best fits to the equilibrium Bose-Einstein distribution (solid lines) collected at a cavity detuning of $\delta = 6.8$ meV at different bath temperatures while the power of the excitation laser was kept at $P = 10.2$ mW. (b) Energy distributions collected at a cavity detuning of $\delta = -1$ meV at different pump powers while the lattice temperature was kept at $T = 5.2$ K.

condensate-like peak showed up at $E = 0$ due to the decrease in the critical threshold, but the overall distribution became nonequilibrium. The best fit to an equilibrium Bose-Einstein distribution missed the data by about a factor of 10 at low energies, leading to difficulty in extracting the chemical potential and temperature of polariton gases at the onset of condensation, similar to the case in Fig. 5-1. This regime was identified as the thermodynamic regime, as the polariton gas could reach thermal equilibrium under right conditions. In Fig. 5-2(b), the lattice temperature was kept at $T = 5.2$ K, and the cavity detuning was chosen to be $\delta = -1$ meV to make polaritons less interactive. The polaritons in this case never reached full thermalization at all pump powers. The hump at $E = 2$ meV is a signature of the well-known bottleneck effect in polariton relaxation. Condensation showed up when the pump power was above $P = 10.2$ mW, because of Bose amplification of the ground state and depletion of polaritons in the bottleneck region when $N(E = 0) = 1$. This has led to the classification of this regime as the kinetic regime. Although this work was able to identify the roles of interaction strength in thermalization and polariton condensation, there

141

was no comparison of the data at different densities, so that the meaningfulness of the fit values of chemical potential (in particular, the prediction of the absolute number of particles from the chemical potential) could not be verified, and questions regarding whether polariton condensates can reach thermal equilibrium remained unanswered.

In a later work in Ref. [173], the effect of interaction strength on the thermalization of polariton condensates was systematically investigated by changing the cavity detuning. Signatures of condensates in thermal equilibrium were also reported. In this work, an intense pulsed laser was used to excite a short-lifetime microcavity structure, which gave a rapidly changing temperature and density of polaritons on the time scale of tens of picoseconds. It could be argued, however, that on short time scales of 1–2 picoseconds, the gas could be considered to be in quasi-equilibrium. The time evolution of the polariton temperatures at four selective detunings is plotted
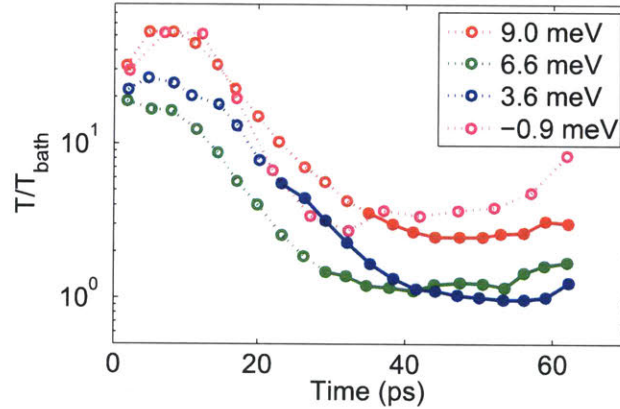
Figure 5-3: Figure adapted from Ref. [173]. Time evolution of normalized polariton temperature T/T_{bath} at cavity detunings of $\delta = 9.0$ meV (red), $\delta = 6.6$ meV (green), $\delta = 3.6$ meV (blue), and $\delta = -0.9$ meV (magenta). An intense picosecond laser pulse was used to excite polaritons in a GaAs-based microcavity with a cavity lifetime of $\tau_c = 2$ ps at an incident angle of 50° with respect to the sample surface normal. The excitation profile is a Gaussian with a diameter of 50 μm. Here closed symbols are the temperatures extracted by fitting the corresponding distributions to an equilibrium Bose-Einstein model. Open symbols denote cases when polaritons are not fully thermalized, and these temperature values do not correspond to actual temperatures and are plotted rather as references to help qualitatively understand the dynamics.

in Fig. 5-3 for a fixed pump power of $P \approx 3P_{th}$, where P_{th} is the pump power at the threshold. The corresponding excitonic fractions are 76.5%, 70.8%, 62.1%, and

46.9%, respectively. The closed symbols are the temperatures extracted by fitting the corresponding distributions to an equilibrium Bose-Einstein model, and open symbols are plotted as references to help qualitatively understand the dynamics. As seen in this figure, the thermalization time is at least 20 ps for positive detunings, and for negative detunings, thermal equilibrium is never established within 60 ps. This work suggests that the thermalization of polaritons is determined by the cavity lifetime and the interaction strength. However, debates arise over whether meaningful thermodynamic properties of the polariton gas, specifically the validity of the fits of distributions to the equilibrium Bose-Einstein model, can be extracted from the experimental data given the fact that with a single Gaussian laser excitation spot, the potential-energy profile felt by the polaritons is strongly renormalized, leading to both self-trapping of the condensate in a small, quasi-harmonic potential inside the laser spot [174], and free streaming away from the spot [175]. In general, it has been shown that integration of a spatially inhomogeneous distribution can lead to misleading fits to a Bose-Einstein distribution [176]. Nevertheless, based on reasonable assumptions for density and temperature variations, fits with an average temperature and chemical potential [177] can still be obtained, which suggest that the polariton gas should reach thermal equilibrium provided that the cavity lifetime is longer than their thermalization time and polariton condensation is true Bose-Einstein condensation with a well defined density-temperature phase diagram.

Later work by the same group [13] with the same short-lifetime structure used a large laser spot with a flat intensity profile and resonant detuning that gave a longer mean free path to reduce the spatial inhomogeneity. In this configuration, the spatial coherence properties were measured. The power law for the spatial coherence was found to depend crucially on the nonequilibrium nature of the polariton gas [13, 178].

These early attempts in addressing the thermalization behavior of polaritons and their condensates were important steps in understanding polariton condensation. However, they clearly do not resolve the debate, as terms such as "intrinsic nonequilibrium character" and "far from equilibrium" have still been widely used in the literature in the past two years [179, 180, 181, 182, 183].

5.1.3 Challenges in reaching thermodynamic equilibrium

As discussed above, the key challenge in polariton systems is to achieve long polariton lifetime, longer than their thermalization time. Since the thermalization time for the polariton gas was at least 20 ps for polaritons that are mostly exciton-like, and most samples used in previous experiments have polariton lifetimes on the order of a few picoseconds [184], this suggests that an improvement of the cavity Q by at least an order of magnitude is needed, which is not trivial for GaAs fabrication technology. A great effort has been devoted in designing and fabricating the long-lifetime cavity structure. A detailed recipe regarding the sample structure and sample fabrication are discussed in Chapter 4. The new microcavity structure has a Q of ~320,000 and a cavity photon lifetime of 135 ps. This corresponds to a polariton lifetime of 270 ps at resonance, which has been confirmed by the long-range (millimeter scale) propagation of polaritons created through either resonant [98] or non-resonant optical excitations [97].

5.2 Trapping Polaritons in a Flat-Bottom Potential Barrier

In general, it has been shown that integration of a spatially inhomogeneous distribution can lead to misleading fits to a Bose-Einstein distribution [176]. In order to guide polaritons toward equilibrium with a specified location and geometry, we made a spatial trap. In this section, we will describe the generation of a flat-bottom potential trap, and the dispersion relations $E(k)$ of the optically trapped polaritons. Details of the optical trapping can be found in Chapter 4.

5.2.1 Generation of flat-bottom potential trap

In principle, any well defined potential barrier can be used to trap polaritons and guide them to spatial equilibrium. However, even a simple harmonic trap will lead to a change of the density of polariton states, and deconvolution is needed to extract
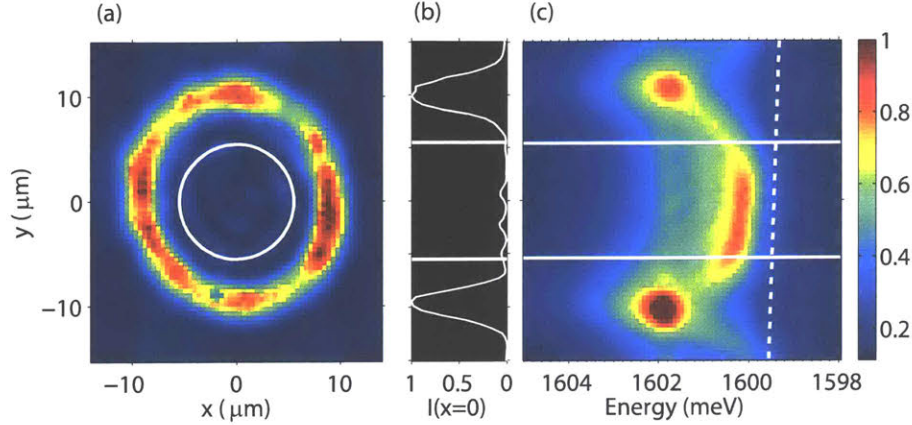
Figure 5-4: (a) Reflection of the excitation beam from the sample surface. The white circle indicates the region of the sample that is observed in photoluminescence imaging measurements after spatial filtering. (b) Normalized excitation light intensity along the $x = 0$ line through the center of the excitation ring pattern shown in (a). (c) Spectrally resolved photoluminescence along $x = 0$. The photoluminescence within the solid white lines is collected and imaged onto the spectrometer CCD in the far-field geometry for the polariton distribution measurements. The dashed white line indicates the photon energy gradient deduced from the low-density spectrum.

their energy distributions $N(E)$ from measured k-space dispersions. To simplify the problem, we made a flat-bottom potential barrier. The flat potential in the center of the trap results in a density of states invariant of polariton energies, which greatly reduces the complexities in retrieving the distributions $N(E)$.

In order to generate a flat-bottom potential trap, we shaped the Gaussian beam into an annulus structure with a diameter of 19 μm, as shown in Fig. 5-4. The formation of a 2D polariton trap was verified by measuring the energy of the lower polariton state as a function of sample position. A near-field image of the sample surface was imaged onto the entrance slit of an imaging spectrometer. The spectrometer slit selected the $x = 0$ slice of the near-field image and was then spectrally dispersed on the spectrometer CCD. The resulting image, plotted in Fig. 5-4(c) for the case of moderate pump powers below the condensation threshold, shows the intensity of the photoluminescence (PL) emitted by lower polaritons as a function of both the PL energy and the sample position. The white dashed line indicates the emission energies at very low pump powers; the slope of this line arises from the wedge of the cavity

145
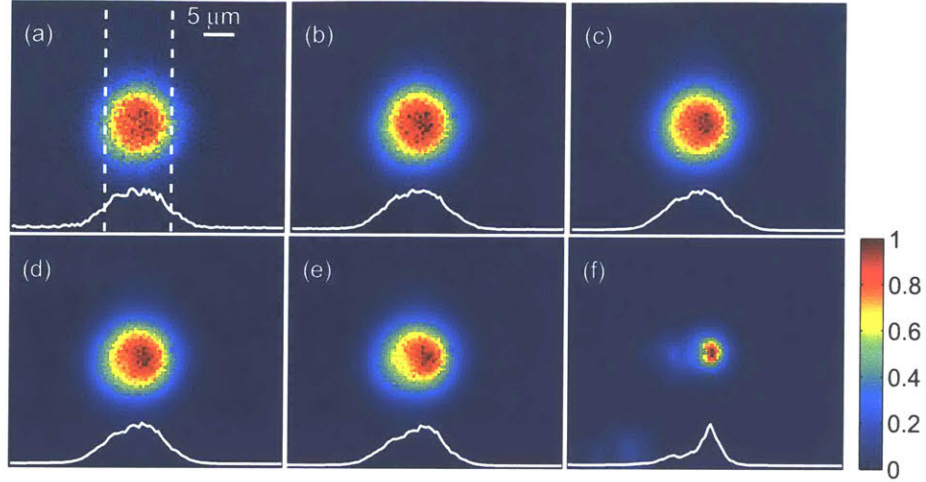
Figure 5-5: Spatial distributions of polaritons at different excitation densities. (a) $P = 0.09\,P_c$, (b) $P = 0.31\,P_c$, (c) $P = P_c$, (d) $P = 2.42\,P_c$, (e) $P = 3.26\,P_c$, and (f) $P = 5.71\,P_c$, where P_c denotes the threshold pumping power. The dashed line indicates the collection region, and the solid line is the cross section of the horizontal slice at the center. The long tail from (f) is from the scattering of the neutral density filter used to attenuate the emission.

thickness shown in Fig. 5-4, which causes a gradient in the cavity photon energy. At the pump region, there is a blueshift of the polariton energy due to their interactions with each other as well as from repulsive interactions between polaritons and excitons and free carriers. As indicated in Fig. 5-4(c), the barrier is not constant around the ring, varying by about 0.2 meV from one side to the other due to inhomogeneity in the pump intensity. The barrier is slightly wider than the laser profile, because excitons propagate up to 1 μm.

The potential landscape is nearly flat in the region from -5.5 μm to 5.5 μm indicated by the white circle in Fig. 5-4(a) and the horizontal lines in Fig. 5-4(b) and 5-4(c). PL was collected from only this region for determinations of the polariton energy distributions as discussed below. The nearly flat potential profile corresponds to a constant density of states in 2D. Additionally, a nearly homogeneous distribution was established in the field of view. Figure 5-5 plots the spatial distributions for pump powers from below to far above the condensation threshold. PL from the barrier was spatially filtered out, since otherwise the emission patterns would be dominated by

146
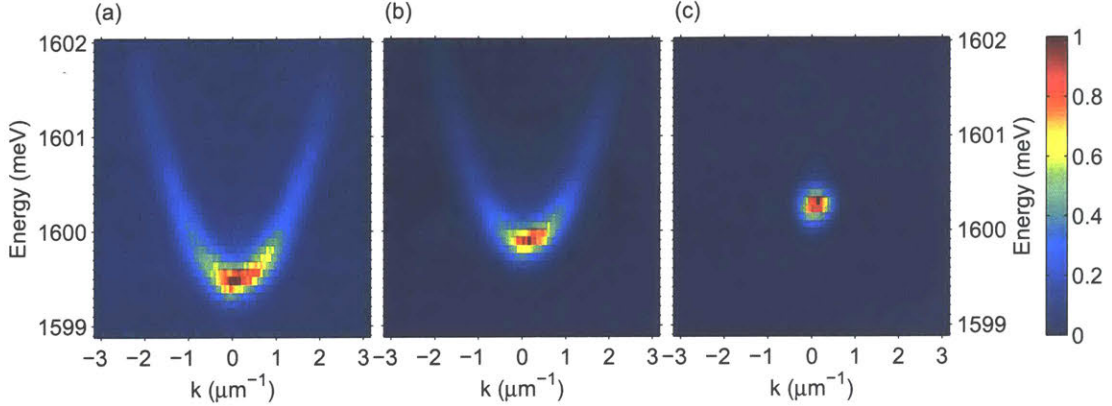
Figure 5-6: Representative far-field energy dispersions in the center of the trap at pump powers of $P = 88$ mW (a), $P = 451$ mW (b), and $P = 711$ mW (c).

the PL at the pump region, particularly at low pump powers. Within the collection region, indicated by the dashed line, the spatial distributions vary by less than 20% over the field of view below the threshold in (a)-(b), at threshold in (c), and above the threshold in (d)-(e). As seen in this figure, the real-space profiles remain similar over a broad range of polariton densities, evidenced by the plots of horizontal slices at the centers shown in Fig. 5-5 as the white solid lines. When the system was pumped very hard, self-trapping of the polariton condensate was observed. The homogeneous spatial distribution is also evidenced by little change in the energy-resolved emission intensities across the field of view within the boundaries of the white solid lines as seen in Fig. 5-4(c).

5.2.2 Dispersion relation of optically trapped polaritons

Polaritons in the center of trap reach equilibrium in k space. In Fig. 5-6, we show the dispersion relations for pump powers of $P = 88$ mW(a), $P = 451$ mW (b), and $P = 711$ mW (c). These dispersions clearly distinguish themselves from the dispersion of untrapped polaritons which are smeared out in the direction of the propagation, as seen in Fig 4-25. The levels of the energy dispersions also blueshift, which is a manifestation of repulsive interactions among trapped polaritons.

147

5.3 Signatures of Quantum Condensation

Under right conditions, condensation of a large population of polaritons was observed in the trap, evidenced by k-space narrowing, superlinear increase in emission intensities and spontaneous emergence of coherence.

k-space narrowing. Figure 5-6 shows a series of angle-resolved spectra at different pump powers. Above the condensation threshold as the pump power is increased, there is a dramatic narrowing of the range of momenta that polaritons occupy. We integrated the spectra along the energy axis, and calculated the FWHM at different pump powers. The resulting plot is shown in Fig. 5-7(c). At low pump powers, polaritons have a broad k-space distribution with a FWHM of 3.4 μm^{-1}, and this decreases to 0.6 μm^{-1} when condensation occurs.

Superlinear increase in emission intensity. Figure 5-7(a) shows the integrated emission intensities in the field of view as a function of pump power. With increasing excitation power, the emission intensity increased linearly in the range of $P = 200$ mW to $P = 600$ mW. Upon condensation, an increase of the emission intensity by more than four orders of magnitude was observed. This threshold-like behavior was also reported in early condensation experiments with short-lifetime cavities [33, 34], and is a direct result of Bose amplification of the ground state population. In Fig. 5-7(a), we also plot the ground state energies at $k_{||} = 0$ at different excitation powers. As can be seen, the ground state shifts by about 1.4 meV in the range of pump powers used. The shift is significantly smaller than the Rabi energy, which is calibrated to be 10.84 meV for this sample. Therefore, the system remains in the strong coupling regime even above the condensation threshold. In practice, a loss of strong coupling is typically accompanied by a second threshold corresponding to the onset of photon lasing, and is fairly straightforward to identify in experiments [174]. However, this is absent in our measurements.
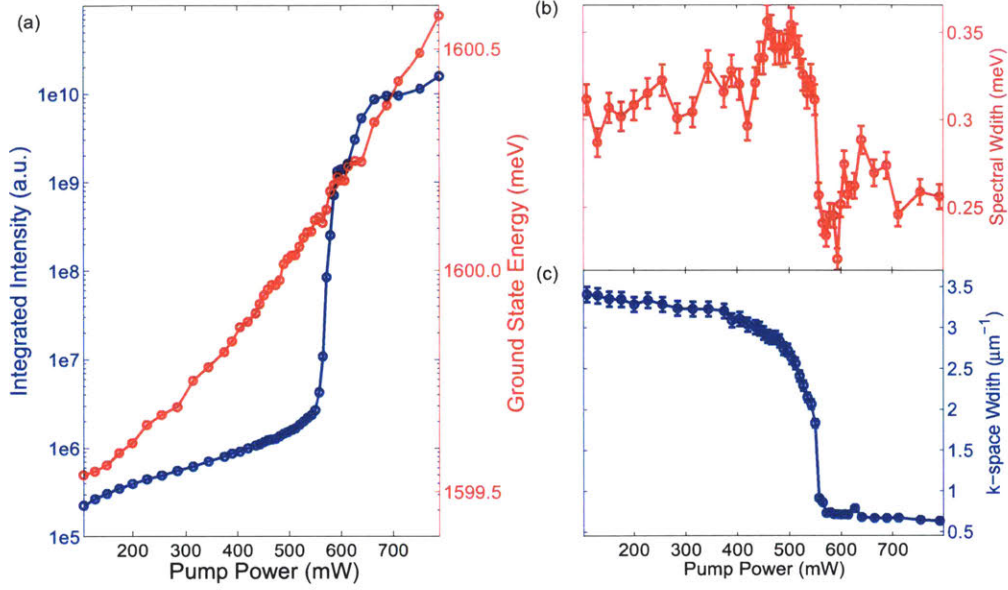
Figure 5-7: Signatures of quantum condensation in the center of the trap at a detuning of $\delta = 0$ meV and a bath temperature of $T = 12.5$ K plotted as a function of pump power. (a) The integrated intensity in the field of view (blue), and the ground state energy at $k_{\parallel} = 0$ (red). (b) Spectral width at $k_{\parallel} = 0$. (c) The k-space FWHM.

Spectral narrowing. Spontaneous emergence of coherence is expected when quantum condensation occurs. This is shown in Fig. 5-7(b). As can be seen, the spectral width at $k_{\parallel} = 0$ first increases as the pump power increases because incoherent scattering becomes more frequent as there are more polaritons in the system. When condensation happens, the linewidth decreases by a factor of 3, indicating an increase of coherence in the system.

Similar signatures of condensation were also observed for all temperatures we studied, and in Fig. 5-8, we show the same analysis as above but with a higher lattice temperature $T_{\text{bath}} = 25.0$ K. As can be seen, the onset of condensation is accompanied by a nonlinear increase in emission intensities, and spontaneous emergence of coherence leads to spectral narrowing. k-space narrowing was also observed at this temperature.

149
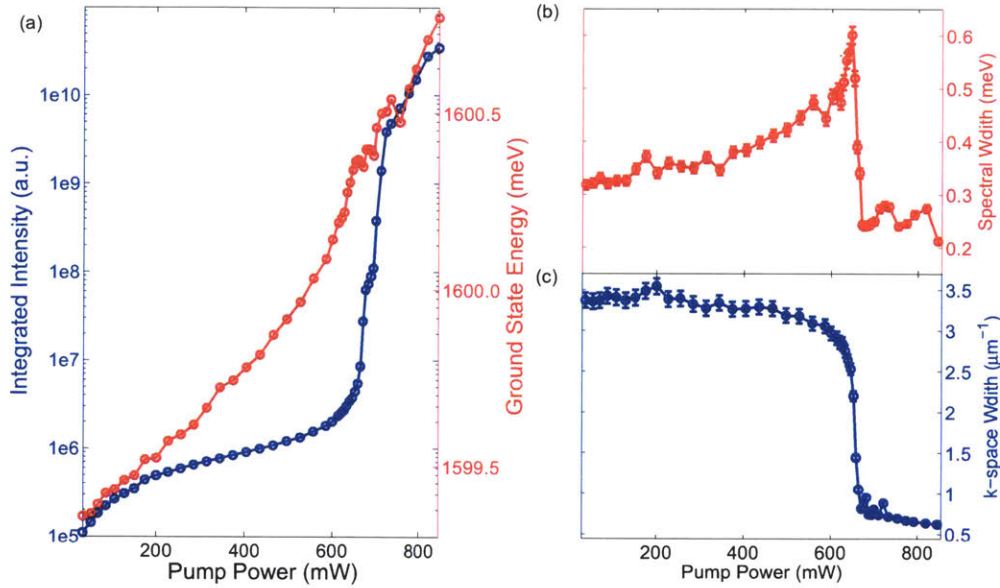
Figure 5-8: Signatures of quantum condensation in the center of the trap at a detuning of $\delta = 0$ meV and a bath temperature of $T = 25.0$ K plotted as a function of pump power. (a) The integrated intensity in the field of view (blue), and the ground state energy at $k_{||} = 0$ (red). (b) The spectral width at $k_{||} = 0$. (c) The k-space FWHM.

5.4 Polariton Gas Reaching Thermal Equilibrium

In this section, we will discuss in detail how to extract the intensity distribution $I[E(k)]$ from a raw tiff image collected in the experiment, and how to convert the intensity distribution to the occupancy of polariton states $N(E)$, followed by how to fit the distribution $N(E)$ to obtain the temperature T and chemical potential μ.

5.4.1 Extracting polariton dispersion $E(k)$

Preprocess the tiff image. The raw image collected in the experiment is saved in the 16-bit tiff format, with intensity counts ranging from 0 to 65535. The raw image is imported into the data analysis module as a matrix $I(x, y)$ with dimensions 100×1340. The dimension of the image is determined by the camera CCD, since the CCD has 1340 and 100 pixels in the horizontal and vertical dimensions, respectively. The vertical dimension is used to resolve k, and the horizontal dimension is the
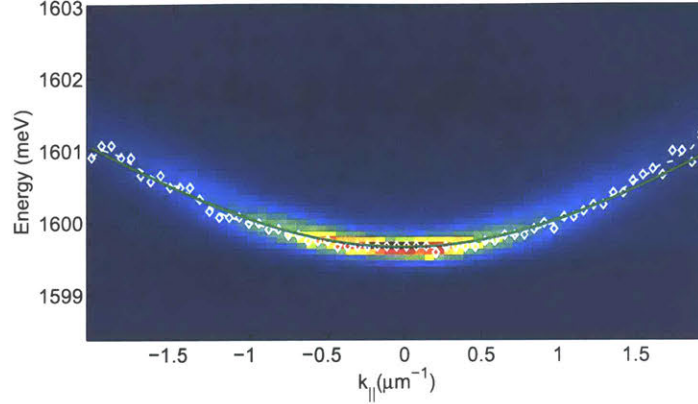
Figure 5-9: A far-field energy dispersion of polaritons in the center of the trap at a bath temperature of $T = 12.5$ K and at a detuning of $\delta = 0$ meV. The white diamonds give the raw energy dispersion relation extracted as the data points with maximum intensity values for each vertical slice. The white dashed line is the running average of the raw dispersion relation. The green line is the fit to the lower-polariton dispersion relation in Eq. (3.72).

emission energy. The background signal is taken to be the mean of the rightmost 140 columns, which is subtracted from $I(x, y)$. The raw image is then cut to leave only the region of interest, and rotated clockwise by 90 degrees to give a normal view of the polariton dispersion, as shown in Fig. 5-9. Let $I(E, k)$ denote the truncated matrix.

Binning $I(E, k)$ over k. Binning is performed in the following way to smooth out the raw image. Starting from the center column, every consecutive specified number of columns are binned to yield one single vertical slice for each bin. For example, let $-3, -2, -1, 0, 1, 2, 3$ denote the column index. If we choose a three-column running average, the bins are taken as the arithmetic average of $(-3, -2, -1)$, $(-2, -1, -0)$, $(-1, 0, 1)$, $(0, 1, 2)$, and $(1, 2, 3)$. Typically, we bin over only 3 columns. The k of each bin is taken to be the k of the center slice. The binned image is slightly smaller than the raw image along the k dimension.

Extracting the dispersion relation $E(k)$. Each column in the resulting binned image is traversed. For each column, we find the maximum intensity point, and the corresponding E and k are taken to be $E(k)$, shown as white diamonds in Fig. 5-9.

151

The white dashed line is a five-point running average of the white diamonds. The intensity counts $I[E(k)]$ for each k state are taken as the sum of the intensities of each vertical slice. Due to the one-to-one correspondence between E and k given by the dispersion relation $E(k)$, we hereafter simply denote it as $I(E)$.

Fitting the dispersion $E(k)$ to theoretical model. In order to calculate the Hopfield coefficients for the subsequent calculations, we fit the dispersion to the theoretical model, which has the following form

$$E(k) = \frac{1}{2}\left(E_x + E_c + \frac{\hbar^2}{2m}k^2 - \sqrt{\Omega^2 + \left(E_x - E_c - \frac{\hbar^2}{2m}k^2\right)^2}\right) \tag{5.1}$$

where E_x and E_c are the exciton and cavity resonance energies, and m is the effective mass of bare photons. Note careful unit conversion has to be taken because we use meV for the energy and degree for the k. E_x is the only free parameter inferred by the nonlinear least-squares fitting. A typical fitted dispersion is shown as the green line in Fig. 5-9. We will use the fitted $E(k)$ in all calculations below.

5.4.2 Converting $I(E)$ to energy distribution $N(E)$

In order to convert the intensity distribution $I(E)$ to the energy distribution $N(E)$, we need to take into account the angle-dependent radiative lifetime of polaritons as well as the angle-dependent density of k states in the Fourier plane, i.e., the plane of the CCD, in additional to an efficiency factor that converts the photon counts to the occupancy.

The angle-dependent radiative lifetime is taken into account through the excitonic fractions of each k state, which are calculated as

$$x(k) = \frac{1}{2}\left(1 + \frac{\delta(k)}{\sqrt{\delta(k)^2 + \Omega^2}}\right) \tag{5.2}$$

with cavity detuning defined as

$$\delta(k) = E_c + \frac{\hbar^2}{2m}k^2 - E_x \tag{5.3}$$

The lifetime correction factor is computed as

$$\tau_{LP}(k) = \tau_c \left(\frac{x(k)}{10} + \frac{1 - x(k)}{1} \right)^{-1} \tag{5.4}$$

by assuming the lifetime of pure excitons to be 10 times longer than that of cavity photons, and the bare cavity photon lifetime τ_c is experimentally determined to be 135 ps.

The density of k states $M(k)$ can be computed following the basic theory of Fourier optics as discussed in Chapter 4. Putting everything altogether, we get the occupancy by using

$$N(E) = \eta I(E) \tau_{LP}(k) / M(k) \tag{5.5}$$

where η is the efficiency factor, which is determined carefully using the experimental calibration (see Chapter 4 for details). It can also be obtained by adjusting its value to achieve the best goodness-of-fit. In the calculation, the energy dispersion $E(k)$ is used to convert $\tau_{LP}(k)$ and $M(k)$ to $\tau_{LP}(E)$ and $M(E)$.

Since we have both positive and negative k's in the dispersion relation $E(k)$, we can get two sets of energy distributions $N(E)$. We arithmetically average both sides of $N(E)$ to get the final $N(E)$. The resulting distributions $N(E)$ for different pump powers are shown as dots in Fig. 5-10. Because a single efficiency factor is used in extracting all the distributions $N(E)$ at different excitation densities, wecan deduce the relative occupation numbers from the vertical scale of Fig. 5-10.
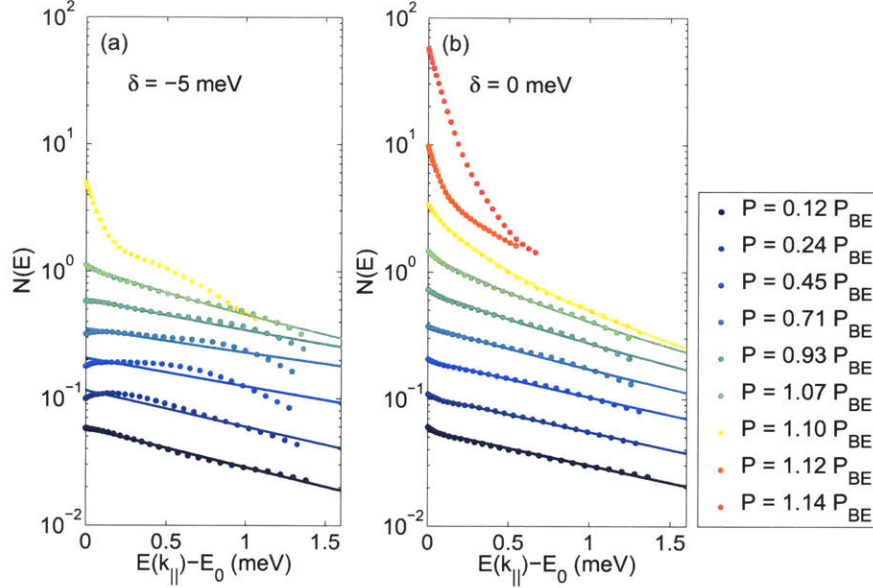
Figure 5-10: Energy distributions of polaritons in the center of the trap at (a) $\delta = -5$ meV (weak interactions, nonequilibrium) and (b) $\delta = 0$ meV (strong interactions, equilibrium) at different pump powers at a bath temperature of $T_{bath} = 12.5$ K. The solid curves are best fits to the equilibrium Bose-Einstein distribution in Eq. (5.6). The fitted values of T and μ are shown in Fig. 5-12. The threshold powers P_{BE} are 382 mW and 443 mW for detunings $\delta = -5$ meV and $\delta = 0$ meV, respectively.

5.5   Varying Polariton Gas from Nonequilibrium to Equilibrium

To see the effect of interactions on thermalization, $N(E)$ was measured at two different cavity detunings, $\delta = -5$ meV and $\delta = 0$ meV, for a series of pump powers. The detuning δ is the energy difference between the cavity resonance and exciton energy at $k_{||} = 0$. Changing the detuning changes the underlying excitonic fraction of the polaritons, which governs their interactions. Positive values of detunings indicate polaritons are more exciton-like, while negative values of detunings give polaritons which are mostly photon-like. Here $\delta = 0$ meV and $\delta = -5$ meV correspond to excitonic fractions of 50% and 30%, respectively. This indicates that the polaritons with $\delta = -5$ meV have interactions which are weaker by a factor of 3 than those at $\delta = 0$ meV, and less thermalization is expected.

154

The measured distributions $N(E)$ at both detunings and various pump powers are shown in Fig. 5-10. The pump powers are reported in terms of the threshold power, P_{BE}, defined below. The sample was immersed in a helium bath that was kept at a temperature $T_{bath} = 12.5$ K for both detuning positions. The measured values of $N(E)$ were fit to a Bose-Einstein distribution, given by

$$N_{BE}(E) = \frac{1}{e^{(E-\mu)/k_B T} - 1},\tag{5.6}$$

where T and μ are the temperature and chemical potential of the polaritons, respectively, and k_B is the Boltzmann constant. The ground state ($k_{||} = 0$) of the lower polariton shifts to a higher energy as the density increases, due to the repulsive polariton-polariton interactions. We defined the ground state energy in each case as $E = 0$ so that $\mu = 0$ corresponds to the condition for Bose-Einstein condensation. The best fits of the data to $N_{BE}(E)$ were determined using T and μ as free parameters in nonlinear least-squares regressions, and are shown as solid curves in Fig. 5-10.

When the polariton states are negatively detuned and have very weak interactions, the fits to the Bose-Einstein distribution are poor. As seen in Fig. 5-10(a), for the case of $\delta = -5$ meV, at low density the distribution has a reasonable fit to a Maxwell-Boltzmann distribution (which corresponds to a single exponential, i.e., a straight line on a semi-log plot), but as the polariton density is increased, the distribution is no longer fully thermal. The hump at $E = 0.5$ meV is a manifestation of the bottleneck effect, as was also observed in Ref. [172]. As the density is increased further, a peak occurs which is condensate-like, but the rest of the distribution does not fit the Bose-Einstein functional form in Eq. (5.6), indicating that the polaritons are not in thermal equilibrium. This behavior is similar to that seen in many other experiments with short-lifetime polaritons, e.g. Ref [33, 172], and is consistent with a nonequilibrium polariton condensate. The nonequilibrium distribution has been reproduced by numerical solution to the quantum Boltzmann equation [185]. Despite the long cavity lifetime, the photon-like polaritons with weak interactions do not reach thermal equilibrium.

155

In contrast, $N(E)$ at $\delta = 0$ is well described by $N_{BE}(E)$ for all pump powers up to $P = 1.1P_{BE}$. At pump powers well below P_{BE}, $N(E)$ is well described by a single exponential function, i.e., a Maxwell-Boltzmann distribution. Between $P = 0.9P_{BE}$ and $P = 1.1P_{BE}$, an upturn in the distribution at $E = 0$ meV is observed, indicating that $N(E)$ deviates from Maxwell-Boltzmann statistics and must be described by a Bose-Einstein distribution with the reduced chemical potential $|\mu/k_BT| < 1$. The fit values of T and μ used in Fig. 5-10(b) are shown in Fig. 5-12 as the blue symbols. As seen in this figure, when the density is increased, T decreases from around 20 K to a lowest value of 13.9 ± 0.2 K and μ/k_BT smoothly goes from -2.93 ± 0.16 to -0.28 ± 0.01. For pump powers greater than $1.1P_{BE}$, a condensate in the ground state appears. This peak cannot be fit to an ideal Bose-Einstein distribution, and we believe that the reason is the appearance of many-body effects such as the Bogoliubov linear spectrum and depletion of the condensate due to interactions. In the thermodynamic limit, the condensate peak should be delta-function like, which is broadened in the presence of finite-size fluctuations [186]. The high-energy tails of the top two curves have the same absolute values, indicating that the populations in the excited states saturate when there is a condensate, consistent with a Bose-Einstein condensation phase transition for bosons in thermal equilibrium.

The upturn in the shape of $N(E)$ in the low-energy states unambiguously distinguishes $N(E)$ as a Bose-Einstein distribution rather than a Maxwell-Boltzmann distribution. Previous reports using short-lifetime samples [173, 172] showed fits of $N(E)$ without the clear upturn near $E = 0$ at excitonic detunings; although a condensate peak appeared in some cases, there was not a clear density-dependent evolution from a thermal Maxwell-Boltzmann distribution to a degenerate Bose-Einstein, non-condensed distribution. Furthermore, short-lifetime samples thermalized only when the microcavity was positively detuned [173] and the polariton characteristics were mostly exciton-like so that the motion of the polaritons was severely restricted. In contrast, the long-lifetime polaritons seen here at zero detuning follow Bose-Einstein statistics throughout the phase transition and propagate to fill the trap in spatial equilibrium.
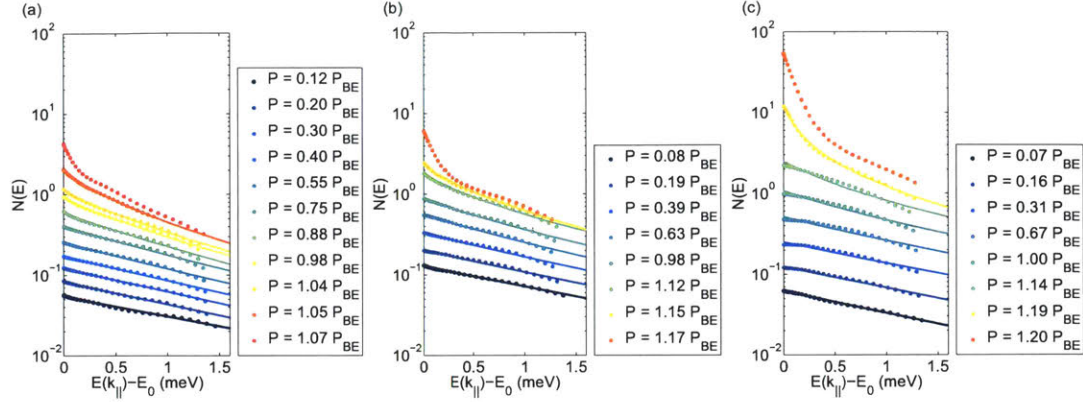
Figure 5-11: Energy distributions of polaritons (dots) and the best fits to the equilibrium Bose-Einstein model (solid lines) at bath temperatures of $T = 10.0$ K (a), $T = 17.5$K (b), and $T = 25.0$ K (c), with corresponding threshold pump powers $P_{BE} = 435$ mW, $P_{BE} = 474$ mW, and $P_{BE} = 557$ mW, respectively.

We emphasize that not only the curvature of the fits in Fig. 5-10 but also the absolute vertical scale of the fits is constrained by the values of μ. We do not have a free parameter to change the overall intensity scaling factor for each individual curve. The data points give the absolute occupation numbers as indicated by the vertical scale in addition to the relative occupation numbers at different pump powers. When the value of μ in the Bose-Einstein distribution is increased toward zero, this increases the absolute value of $N_{BE}(E)$. Thus, the fits are tightly constrained by the requirement that we fit not only the shape of the distribution but also the relative heights of all the curves with only two parameters, T and μ, for each individual distribution $N(E)$. This constraint is reflected in the very small relative uncertainties in the fitted values of μ shown in Fig. 5-12(b).

5.6 Characteristics of Polariton Condensates in Equilibrium

The bath temperature was also varied in the range of 10.0–25.0 K. Good thermalization was achieved across this range, as seen in Fig. 5-11, where the energy distributions $N(E)$ at three other bath temperatures, i.e., $T_{\text{bath}} = 10.0$ K, $T_{\text{bath}} = 17.5$ K,

and $T_{\text{bath}} = 25.0$ K are shown for a series of pump powers. As seen in the figure, the distributions at all temperatures fit well to the equilibrium Bose-Einstein model in Eq. (5.6), up to a ground-state occupation number $N(0) \sim 2\text{–}3$. At higher densities, the distributions deviate slightly from the equilibrium Bose-Einstein model. This is not surprising, since many-body effects play an important role when there is a large ground state occupation.

In Fig. 5-12, we plot the fitted values of T and $\mu/k_B T$ for different pump powers for bath temperatures of $T_{\text{bath}} = 12.5$ K and $T_{\text{bath}} = 22.5$ K. As can be seen, when the bath temperature is low, i.e., $T_{\text{bath}} = 12.5$ K, the fit values of T at low densities are
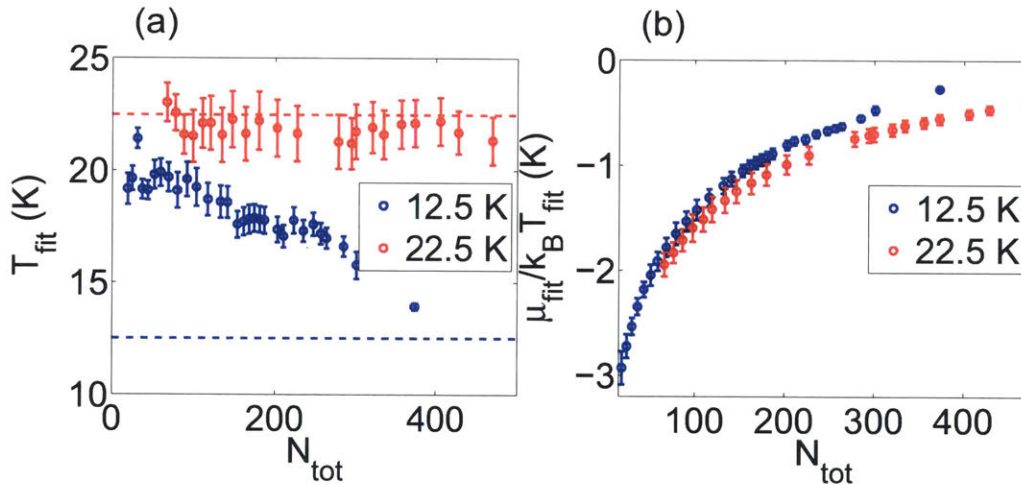
Figure 5-12: Fitted values of polariton distributions as a function of pump power. Errorbars indicate 95% confidence intervals from the fits. (a) Effective temperatures of polaritons for bath temperatures $T_{\text{bath}} = 12.5$ K (blue points) and $T_{\text{bath}} = 22.5$ K (red points) at different pump powers extracted by fitting the energy distributions (shown in Fig. 5-10b for the 12.5 K case) to the equilibrium Bose-Einstein model. The dashed lines indicate the helium bath temperatures. (b) Reduced chemical potential $\alpha = \mu/k_B T_{\text{fit}}$ for bath temperatures $T_{\text{bath}} = 12.5$ K (blue points) and $T_{\text{bath}} = 22.5$ K (red points) at different pump powers .

much higher than T_{bath} and at higher densities they settle to temperatures slightly above T_{bath}, while for a bath temperature of $T_{\text{bath}} = 22.5$ K, the fitted temperatures stay pinned to the bath temperature, within the uncertainty. The chemical potential increases smoothly toward zero in each case as the density is increased. A similar trend was also observed for all other bath temperatures.

5.7 Phase Diagram of Bose-Einstein Condensation of Polaritons

Now that we have well defined temperatures ranging over which thermal equilibrium is established, it is straightforward to determine the phase diagram of polariton Bose-Einstein condensation. In this section, we will describe how the total number of polaritons is calculated, and how the threshold for Bose-Einstein condensation is picked. The effective temperatures of polaritons at the threshold are also examined. With well defined temperatures and total polariton numbers, the phase diagram of Bose-Einstein condensation is for the first time measured experimentally.

5.7.1 Computing N_{tot} in the trap

Since the polaritons are well characterized by the fits to Bose-Einstein distributions, we obtain the total number of polaritons by extrapolating the fitted distributions $N(E)$ of polaritons as shown in Fig. 5-11 and 5-10(b) to high energies, and then integrating over the energy, and multiplying by the density of states, using the standard formula

$$N_{tot} = \int_0^{E=20\,\text{meV}} N(E)D(E)dE \qquad (5.7)$$

with density of states defined as

$$D(E) = \frac{gAm_{LP}}{2\pi\hbar^2} \qquad (5.8)$$

where A is the area of the trap, m_{LP} is the effective mass of the lower polariton, and $g = 2$ accounts for the spin degeneracy of the polaritons. $E = 20$ meV is used for the upper bound of integration so that the energy distributions above $E = 20$ meV are negligible. Fig. 5-13 shows the deduced occupation number from Eq. (5.7) as the pump power is increased, using the fit values of T and μ in $N(E)$ at each pump power, for the case of bath temperature $T_{bath} = 12.5$ K.
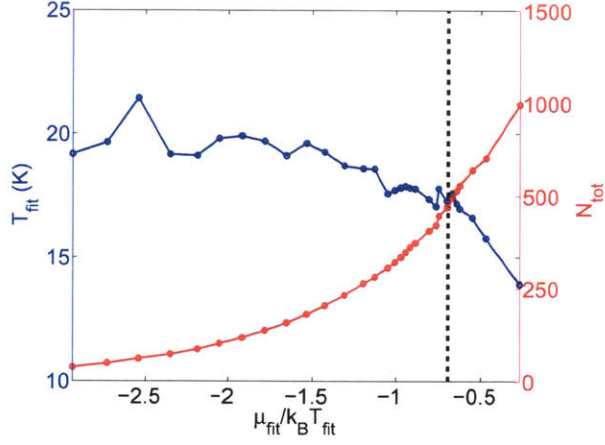
Figure 5-13: The effective temperatures of polaritons T_{fit} (blue) and total number of polaritons N_{tot} (red) at different reduced chemical potentials at a bath temperature of $T_{bath} = 12.5$ K. The vertical dashed line indicates the threshold of the Bose-Einstein degeneracy, i.e., $-\mu/k_B T = \ln 2$.

5.7.2   Defining the threshold of Bose-Einstein condensation

Defining the threshold for Bose-Einstein condensation in a two-dimensional system with a flat potential is problematic, because unlike the three-dimensional case, the density of states is flat in two dimensions, and the energy distribution $N_{BE}(E)$ given by Eq. (5.6) evolves continuously into one which is sharply peaked at $E = 0$ as density increases. We can define the threshold for crossover from classical to Bose-Einstein statistics as the case when $N(0) \sim 1$, or we can define the threshold for condensation, or quasi-condensation, when $N(0) \gg 1$, e.g., $N(0) \sim 10$. Whichever threshold for $N(0)$ we pick, Eq. (5.9) implies the same scaling law, namely that the total number N_{tot} at the critical threshold will be proportional to the temperature T. This is equivalent to a dimensional analysis of the onset of quantum effects when the thermal de Broglie wavelength λ_T is comparable to the average interparticle distance r_s, which for a two-dimensional system is

$$r_s \sim n^{-1/2} \sim \lambda_T \sim \sqrt{\frac{\hbar^2}{m k_B T}}. \tag{5.9}$$

160
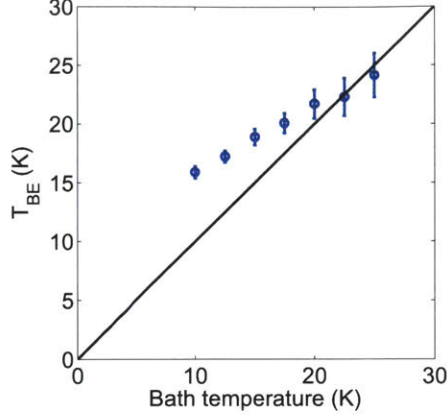
Figure 5-14: The critical temperature as a function of lattice temperature for $\delta = 0$ meV. Errorbars indicate 95% confidence intervals from the fits. The solid black line indicates $T_{BE} = T_{\text{bath}}$.

and therefore $n \propto T$.

To determine the the phase diagram, i.e., to check the scaling law in Eq. (5.9), we want to plot the total number N_{tot} at critical threshold as a function of the fit value of T at the threshold. The values of N_{tot} were obtained from Eq. (5.7), and plotted as a function of $\mu/k_B T_{\text{fit}}$ in Fig. 5-13 for the data at a bath temperature of $T = 12.5$ K. We define the threshold of quantum degeneracy as the onset of Bose amplification, i.e., $N(k_{\parallel} = 0) = 1$. This corresponds to a value of $\mu/k_B T = -\ln 2$, shown by the black dashed line in Fig. 5-13. For a given bath temperature, the critical temperature T_{BE} and the critical polariton number N_{BE} are then picked to give the value that is closest to the black dashed line. This also defines the threshold pump power, P_{BE}, as the laser power at which the polaritons reach the critical threshold for quantum degeneracy.

5.7.3 Thermalization of polariton gas at critical point

Based on this methodology, N_{BE} values were determined for a series of T_{bath} values ranging from 10.0 K to 25.0 K. The fit values of T at the onset of Bose-Einstein statistics are plotted in Fig. 5-14(a), showing the general trend of T_{BE} slightly higher than T_{bath}, as discussed earlier. The relative deviation is highest at lowest bath

161
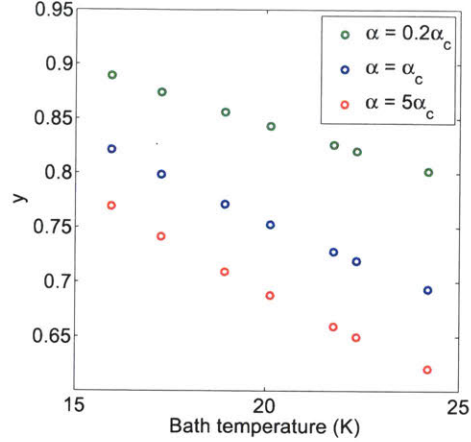
Figure 5-15: The fractions of polariton populations in the field of view as a function of bath temperature for chemical potentials of $\alpha = 0.2\alpha_c$ (green), $\alpha = \alpha_c$ (blue), and $\alpha = 5\alpha_c$ (red), with $\alpha_c = -\ln 2$ being the critical value of Bose-Einstein condensation.

temperature, when the heat capacity of the sample is lowest, allowing the local sample temperature to rise more due to the laser heating.

The phase diagram of the Bose-Einstein condensation, i.e., the relation of N_{BE} to T_{BE} is shown in Fig. 5-14(b). The black line is the best fit of a linear proportionality. Within the uncertainty, the data are consistent with a linear increase T in threshold with N_{BE}, consistent with the expected phase boundary of a weakly interacting boson gas in two dimensions implied by the relation Eq. (5.9). This line can be viewed as a phase boundary: above the line, the gas is quantum-degenerate, and below it, the gas is classical.

5.7.4 Replot of phase diagram

Figure 5-14(b) shows the phase diagram deduced by fitting the $N(E)$ data to a Bose-Einstein distribution, and then integrating the fit curve using Eq. (5.7). This method allows us to account for the high-energy tail of the particle distribution which extends outside of our detected range, due to the fact that high-energy states correspond to high $k_{\parallel}$, which give light emission outside the numerical aperture of our collection lens. This correction is highly necessary because the fractions of the polaritons that remain

outside the numerical aperture are not negligible. Figure 5-15 plots the fraction of polaritons in the field of view defined in Eq. (5.10).

$$y = \frac{\int_0^{E_{max}} N(E)dE}{\int_0^\infty N(E)dE} \tag{5.10}$$

The fraction outside our field of view is particularly high for low densities and high temperatures when the polaritons have broad energy distributions. About 30% of the polaritons would be missed if the correction were not performed. Figure 5-16(a) plots the phase diagram with N_{tot} computed from summing the CCD counts per second defined below in Eq. (5.11)

$$N_{int} = \sum_i \frac{N_i \tau_i}{\xi M_i} \tag{5.11}$$

where N_i, τ_i and M_i are the CCD counts per second, the lifetime of the polariton state, and the density of k states at pixel i, respectively. ξ accounts for the overall optical efficiency of the collection setup, including the loss in the dispersive grating and the quantum efficiency of the CCD. The black line is the best linear fit $y \propto x$. As can be seen, this plot deviates from linearity. The deviation is a result of the change in the fraction of polaritons in the field of view at different temperatures.

Figure 5-16(b) shows a correction to Fig. 5-16(a), using the integrated CCD counts within the field of view, but adding a correction for the high-energy tail outside our field of view, based on the fits to the Bose-Einstein distribution. The particle numbers plotted in Fig. 5-16(b) are therefore

$$N_{tot} = N_{int} + \frac{gmS}{2\pi\hbar^2} \int_{E_{max}}^{E=20 \text{ meV}} N(E)dE \tag{5.12}$$

where N_{int} is determined using Eq. (5.11), E_{max} is the maximum energy in the field of view, and the temperature and chemical potential in $N(E)$ are taken from the fitted values of Bose-Einstein distributions. The polariton population beyond the upper bound $E = 20$ meV of the integration is negligible. The black line is a fitted linear relation. The difference is negligible compared to Fig. 5-14(b), which is not surprising
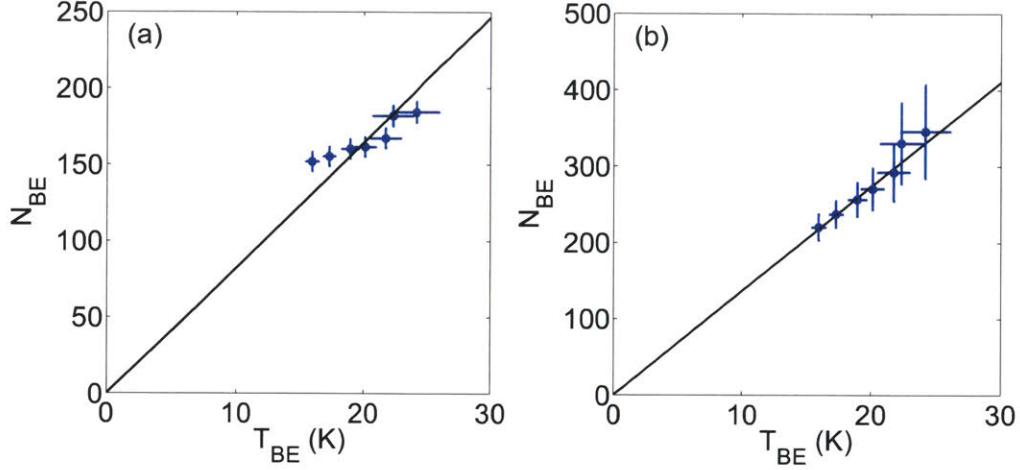
Figure 5-16: Phase diagram of polariton Bose-Einstein condensation with N_{BE} including only polariton populations in the field of view (a) and with N_{BE} corrected for the polariton populations outside our field of view (b). Horizontal errorbars are from the fits, and vertical errorbars are calculated from uncertainties in temperature, chemical potential and photon counting.

because the fits to the Bose-Einstein distribution fall closely on top of the data at all temperatures. Compared to Fig. 5-16(a), the linear proportionality is improved because of the inclusion of polariton populations at high energies which are outside of our field of view.

5.7.5 Quantitative measure of degree of thermalization

We define the degree of thermalization as

$$\mathrm{DOT} = \frac{N_{fit}^c}{N_{int}^c} \tag{5.13}$$

where N_{fit} is total number of polaritons in the field of view implied by the fitted distribution. The superscript c indicates the values of N chosen at the critical point of Bose degeneracy. This quantity can also be used as a quantitative measure of the overall quality of Bose-Einstein fitting. Figure 5-17 plots the DOT at the critical threshold $\mu/k_B T = -\ln 2$ for the data shown in the phase diagram. As can be seen, this factor varies within 5% for most of the temperatures. This confirms full
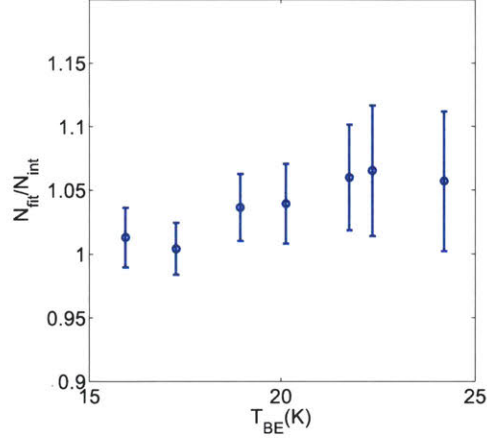
Figure 5-17: Degree of thermalization at different bath temperatures. Errorbars are calculated from uncertainties in fitted temperature, chemical potential and counting photons.

thermalization of the polariton gas in the range of studied temperatures. The slight increase in the DOT might come from the temperature-dependent emission rate of polaritons, which was not taken into account in the current data analysis routine.

The DOT can also be interpreted as a check of the number of polaritons in the field of view. We can also perform the check in the following way. Similar to the previous way, we compared the values of $N(E)$ from our fits to the Bose-Einstein distribution to independent data for the occupation number obtained from estimating the total photon emission rate. The process for obtaining the latter was as follows.

1. A laser light with known power was sent through a pinhole at the sample plane, and the total CCD counts per second corresponding to this were measured. This gave a factor ξ defined by $dN_{CCD}/dt = \xi dN_{phot}/dt$.

2. The density of k-states for the trap was calculated from the trap size, assuming a flat potential, as $N_s = g\Delta k_x \Delta k_y (A/(2\pi)^2)$, where A is the area of the trap and g accounts for the spin degeneracy.

3. With the spectrometer imaging the k-space (Fourier) plane, the range $\Delta k_x \Delta k_y$ per pixel was estimated from the polariton dispersion in the photonic limit, where the effective mass of the cavity photons is known, giving the energy as a

165

function of in-plane k. This was cross-checked with estimates based on the ray geometry of the lens system which mapped emission angles from the sample to off-axis lateral shifts in the Fourier plane, as discussed in Chapter 4. The ranges $\Delta k_x \Delta k_y$ per pixel from these two methods agree within our level of uncertainty.

4. The rate of photon emission was related to the total number of polaritons N in steady state using the relation $dN/dt = N/\tau$, i.e., $N = (dN/dt)\tau$, where τ is the radiative lifetime of the polaritons, calculated using the Hopfield polariton coefficients discussed in Chapter 3.

The occupation number can then be estimated, independent of the fits, as

$$
\begin{aligned}
N(E) &= \frac{(dN_{CCD}/dt)(2\pi)^2 \tau}{gA\Delta k_x \Delta k_y \xi} \\
&\equiv C\frac{dN_{CCD}}{dt}.
\end{aligned}
\tag{5.14}
$$
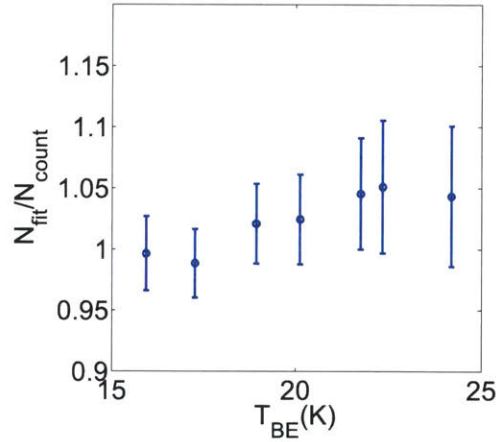
Figure 5-18: Comparison to the critical density using fitted distributions (N_{fit}) and using photon counting (N_{count}). Errorbars are calculated from uncertainties in fitted temperature, chemical potential and counting photons.

Because several of these numbers are estimates, there is some uncertainty in the overall multiplier C which takes into account all of these factors. On the other hand, the values of $N(E)$ from fits to the Bose-Einstein distribution do not have any overall multiplier, with their absolute value set by the values of chemical potential μ. The

factor C was adjusted for best fit of $N(E)$ to the CCD data, but had to be the same for all data sets taken with the same optical setup. Figure 5-18 shows the ratio of the value of C used for the fits to the nominal value of C obtained from photon counting using Eq. (5.14) at various temperatures in a single experimental run. As seen in this figure, the predictions from the fits and the predictions from the photon counting estimate fell within the range of uncertainty of the photon counting method in every case.

5.8   Outlook and Conclusions

It has been a longstanding assumption that Bose condensation effects seen in polariton systems are a direct result of the quantum nature of the system when $r_s \sim \lambda_T$, but up to now it has not been possible to directly test this. By using high-quality microcavities with lifetimes over an order of magnitude longer than those of previous samples, polaritons in a two-dimensional flat optical trap are seen to unambiguously show thermal Bose-Einstein statistics. This clearly distinguishes polariton condensation from the conventional lasing effect in semiconductor materials.

Now that we have samples in which true equilibrium can be established, new experiments are possible to test theoretical predictions of interacting Bose gases which have been elusive in cold atom experiments. For example, studies can be conducted of the excitation spectrum of the interacting Bose gas, and of the crossover from 2D to 1D equilibrium which can be controlled by spatial shaping of the excitation light to make tailored potential energy landscapes. Characteristics of the nonequilibrium state can also be studied systematically by varying the cavity detuning to control the polariton interaction strength and by varying the excitation profile to engineer the potential landscape. Dynamical relaxation into the equilibrium state can also be studied by using pulsed rather than c.w. excitation followed by time-resolved measurements, as well as the coherence properties as the system passes through the Berezinsky-Kosterlitz-Thouless transition. The results are also encouraging for applications in quantum simulation of condensed matter system that exploit equilibrium

BEC properties.

Chapter 6

Direct Measurement of Polariton-Polariton Interaction Strength

Excitons have been at the heart of semiconductor physics. In energy-harvesting systems such as the leaves of a green plant, when a photon of sunlight is absorbed by a chlorophyll molecule, the solar energy is converted into the excited state of the molecule, forming an exciton. Excitons then transport energy between molecules in the leaf, and ultimately mediate the conversion of sunlight into electric energy. Excitonic devices have emerged as new interconnect technologies between traditional electronic and photonic devices, and present a great pontential advantage over their traditional counterparts because the zero net charge allows excitonic devices to operate without the resistive-capacitive delays that retard conventional electronics. Excitonic switches at high speeds have already been demonstrated in AlAs/GaAs coupled quantum wells [5]. Excitons also play very important roles in the fundamental understanding of semiconductors, laying the foundation of high-order complexes such as biexcitons and triexcitons. Topologically protected excitons in thin films have also been predicted as novel candidates that could permit scattering-free propagation for long distances [187].

The observation of quantum condensation at room temperature with microcav-

ity polaritons presents great opportunities in exploiting polaritons as model systems to study both many-body physics and macroscopic quantum coherence. Observations such as higher-band p- and d-wave condensates in periodic potentials [152, 149] offer the possibility to study fundamental many-body interactions in high-temperature superconductivity with microcavity polaritons. Predictions of the quantum blockade regime in dilute polariton systems have gained significant attention [188, 189, 190, 191]. This effect would allow us to exploit the fascinating properties of polaritons in integrated quantum light sources [192, 193, 194], sources of entangled and indistinguishable photons [195, 196, 197, 198, 199, 200, 201], and to generate polariton number states in microcavity traps, paving the way for the study of quantum phase transitions and Bose-Hubbard physics with light. Furthermore, the light-matter dual nature of polaritons has been exploited in realizing all-optical circuits. The past decade witnessed the demonstration of exciton-polaritonic devices such as spin switches [10] and optical transistors [105].

While many of the effects depend crucially on the role of the interactions among underlying excitons and polaritons, the experimental determination of the interaction strength is notoriously difficult. In this Chapter, we will discuss the first direct measurement of polariton-polariton interaction strength. We will first review previous attempts in determining the exciton-exciton interaction strength as well as polariton-polariton interaction strength in Section 6.1. By using the high-Q microcavity structure, we were able to allow polaritons to propagate away from the pump region. The conditions for the complete separation between the polaritons and the exciton reservoir are carefully examined in Section 6.2. In Section 6.3, we discuss the spatial and spectral profiles of trapped polaritons in the center of the annular potential profile. In order to determine the interaction strength, the density of polaritons in the field of view has to be carefully calibrated. Two ways to compute the density of polaritons are presented in Section 6.4. The measured interaction strength between polaritons is discussed in Section 6.5. The measured quantity is two orders of magnitude greater than previously expected, and is manifested at high densities through the saturation of the energy shift as a function of density, which was covered

in Section 6.6. We conclude the chapter by a discussion of possible mechanisms that could contribute to the large values obtained in our measurements.

6.1 Previous Attempts in Determining Exciton-Exciton Interaction Strength

In this section, we will briefly review the difficulty involved in determining the exciton-exciton and polariton-polariton interaction strengthd, as well as previous attempts in the study of the interaction strengths.

6.1.1 Direct Measurement of Exciton-Exciton Interaction Energy

The main complication in the experimental measurement of exciton-exciton interaction strength is the calibration of the exciton density. On the one hand, generating excitons involves absorption of photons with uncertainties in the absorption coefficient and in the efficiency of exciton formation. On the other hand, given their shallow energy dispersion (energy varies by $\sim 10\,\mu\text{eV}$ within $5\,\mu\text{m}^{-1}$), most excitons can easily scatter with acoustic phonons or collide with each other, and become non-luminescent. In general, the overlap of the excitonic region of the spectrum with other electronic states such as electron-hole plasmas, biexcitons and trions makes it difficult to identify purely excitonic signal.

In order to avoid the density calibration, Voros et al. [202] suggest the determination of exciton-exciton interaction strength through the relationship between the energy shift Δ and spectral linewidth Γ approximated as

$$\Delta E = gn \tag{6.1}$$

$$\Gamma = 4\pi g^2 n D(E) \tag{6.2}$$

where g is the interaction strength, n is the density of the excitons, and $D(E)$ is the

density of states per unit area at the average thermal energy. In a two-dimensional system, the density of states is constant and equal to $m/\pi\hbar^2$. Since both quantities are linear with density, the ratio of the two will be independent of density. By using a high-quality sample with extremely low inhomogeneous broadening and disorder, Voros et al. were able to measure the linewidth as a function of energy shift to a high precision. A spatial trap induced by mechanical strain was applied to the microcavity sample, leading to the formation of a confinement potential of 3 meV in 500 µm. The spatial trap not only prevented excitons from diffusing out of the field of view, but also reduced the nonradiative decay significantly. Figure 6-1 shows typical spatially resolved spectra at different densities, taken at times long after a quasi-c.w. laser pulse. The change in the emission energy is a result of the decrease in the exciton
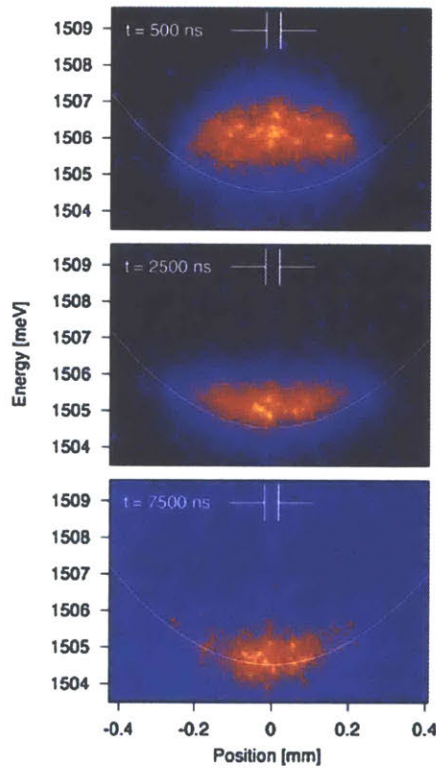
Figure 6-1: Figure adapted from Ref. [202]. Spatially resolved luminescence spectra from indirect excitons in coupled quantum wells at T = 5 K, confined in a two-dimensional trap, at different waiting times after the initial photoexcitation.

density due to exciton recombination. By extracting the spectral linewidth and energy

shift at different times from Fig. 6-1, a nonlinear dependence was observed, as shown in Fig. 6-2. By taking into account the many-body correlations of the excitons, Voros et al. were able to reproduce the nonlinear dependence to a high precision, shown as the solid fits in the figure. However, the calculations had to be made using explicit assumptions in the form of many-body correlations, thus complicating the determination of the exciton-exciton interaction strength g.
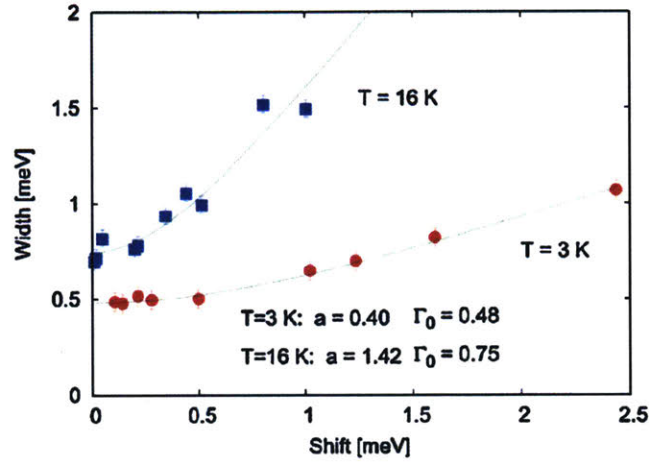
Figure 6-2: Figure adapted from Ref. [202]. Half width at half maximum of the exciton luminescence line as a function of the spectral shift at two temperatures. The solid lines are fits of the theory discussed in the text to the experimental values.

6.1.2 Measurement of Exciton-Exciton Interaction Energy through Polaritons

The difficulty in calibrating the density of interacting particles can be avoided by resonantly coupling excitons in quantum wells (QWs) to confined photon modes in a very high-Q planar microcavity, forming exciton-polaritons. The deep dispersion of exciton-polaritons, as can be seen in Fig. 3-12, prevents polaritons from undergoing non-radiative decay through scattering with optical phonons. However, experimental determination of the polariton interaction strength has been nearly as difficult. The main challenge in previous experiments for measuring the polariton-polariton interacting strength has been to establish the absolute density of the polaritons in-

dependent of any excitons or free carriers that may be present. When the polaritons are generated by non-resonant laser excitation, not only polaritons but also bare excitons are created. This leads to a population of excitons of unknown density. If structures with short lifetime (ca. 2 ps) are used, the polaritons do not travel far from the cloud of excitons. Therefore, when a shift of the energy of the polariton state is observed, it is not possible to determine how much of this shift is due to direct polariton-polariton interaction and how much is due to polariton-exciton interaction. In principle, there may also be free carriers created near the laser excitation region, which also interact with the polaritons. Furthermore, the non-resonantly generated polaritons ballistically escape away from the pump region, and some fraction becomes non-luminescent. Alternatively, if polaritons are created resonantly, they typically have a highly non-equilibrium and coherent distribution that does not allow easy extraction of the energy renormalization of the particles.

In order to localize polaritons spatially, Ferrier et al. [154] formed a semi-infinite potential barrier for polaritons as shown in Fig. 6-3. Repulsive interaction with the excitonic reservoir is responsible for condensation in the optical trap formed between the excitation area and the wire end. The separation of the exciton reservoir from polaritons was claimed to be realized upon the formation of the condensate since the real-space distribution of the condensates narrows. By measuring the shift of the lowest energy polariton state in the semi-infinite optical trap, the interaction strength between polaritons was extracted to be $g = 9\,\mu eV \cdot \mu m^2$. The results are summarized in Fig. 6-4. The black squares are the measured energy shift at different pump powers. By assuming the measured energy shift at low powers comes exclusively from the polariton-reservoir interaction, and the shift is linearly dependent on the pump power, shown as the red dashed line, the blue shift as a result of polariton-polariton interactions was taken as the difference between the black curve and the red dashed curve, and is shown as the blue curve. Clearly this measurement suffers from several weaknesses. First, the interactions among condensed polaritons are assumed to be the same as those among normal polaritons. Second, the linear extrapolation of the energy shift as a function of pump power needs to be carefully justified. Furthermore,
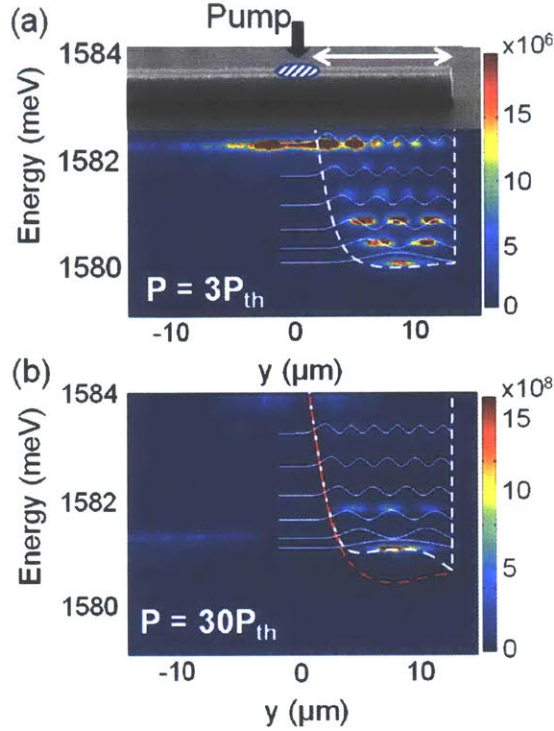
Figure 6-3: Figure adapted from Ref. [154]. Spatially and spectrally resolved emission of a microwire excited 15 µm from its end for $P = 3P_{th}$. White lines: Calculated polariton states confined by the potential shown in white dashed line which includes interaction with the excitonic reservoir. Inset: Scanning electron micrograph of the microwire with schematic representation of excitonic reservoir in dashed blue. (b) Same as (a) for $P = 30P_{th}$.

polaritons do not reach spatial equilibrium, and possibly lack of thermal equilibrium as well. The role of confined condensates states in the energy shift is not obvious.

6.2 Separating Polaritons from Exciton Reservoir

We used the very high-Q microcavity under non-resonant excitation. The high Q implies long polariton lifetime, 200 ps or longer, which allows the polaritons to propagate well away from the laser excitation region. By propagating polaritons to the center of a sufficiently big optically induced annular trap, we can separate polaritons from the population of free carriers and hot excitons. The polariton interaction strength can then be extracted from the spectral data at the center of the trap. In this Section,
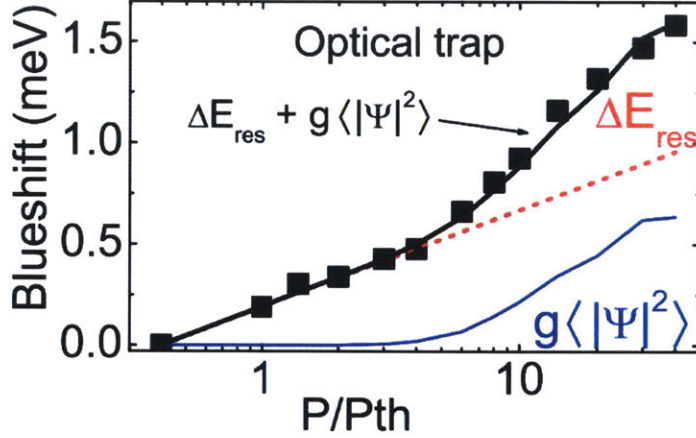
Figure 6-4: Figure taken from Ref. [154]. Measured blueshifts of the lowest energy polariton state in an semi-infinite optical trap with a diameter of 15 μm.

we will present a detailed discussion of how the polariton signal is isolated.

6.2.1 Determining the diameter of the annulus

The annular trap in this work was formed by irradiating a spatial light modulator (SLM) with the axicon phase imposed on the surface. The excitation beam is from an MSquared continuous wave (c.w.) laser, as discussed in Chapter 4. By changing the spatial periodicity of the axicon phase pattern, a ring with a diameter in the range of 30 − 100 μm can be created on the sample surface. In order to completely separate polaritons from the exciton reservoir, the size of the ring has to be sufficiently big. It is well known that excitons can propagate up to 100 nm in typical inorganic [203, 204] and organic systems [205, 206]. This limited range of propagation is also the main obstacle for an optical transient grating measurement of the exciton diffusion length in these systems. Therefore, a ring with a diameter of 50 μm should well serve this purpose. Nonetheless, a careful determination whether excitons from the pumping region diffuse into the field of view has been carried out. Figure 6-5 shows the energy shifts for the ground state of the lower polaritons for different sizes of the ring trap when the density of the polaritons in the field of view is $1.2\,\mu m^{-2}$ (kept constant by keeping the photon emission intensity of the polaritons constant)

at a cavity detuning of $\delta = -0.14$ meV. As can be seen, when the trap size is greater than 25 μm, corresponding to a distance of 12.5 μm from the generation region on the perimeter to the center of the trap, the energy of the ground state remains almost the same, which confirms that the energy renormalization only comes from the contribution of polariton-polariton interactions in the center of the trap, where excitons do not exist. On the other hand, when the trap size is smaller than 15 μm, the blueshift is twice the amount we obtained from a big trap, because the edges of the pump region leak into the field of view. This also emphasizes that a long-lifetime microcavity is necessary in order to obtain clean blueshifts in a large trap.
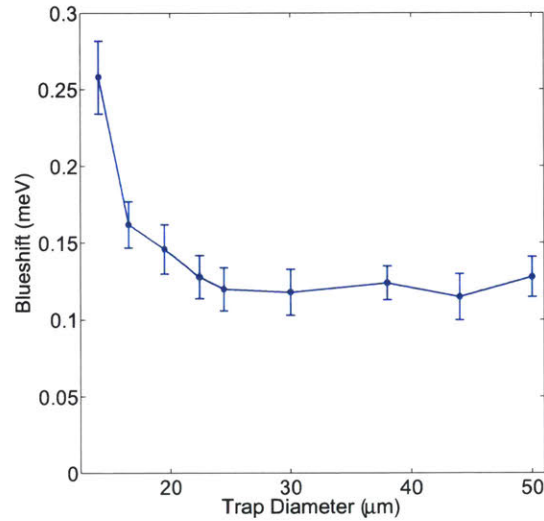
Figure 6-5: Blue shift of the $k_{||} = 0$ state for different ring trap sizes at the cavity detuning of $\delta = -0.14$ meV when the density of the polaritons in the center of the trap is $n = 1.2\,\mu m^{-2}$. The errorbars are standard deviations of estimated energy shifts.

The upper bound of the diffusion length of the incoherent excitons generated from non-resonant excitation has also been measured using a single excitation spot in a different trapping geometry. An excitation laser with a Gaussian intensity profile with a FWHM of approximately 8 μm was used to excite the microcavity sample to generate a population of incoherent excitons as well as polaritons, using the same non-resonant excitation method as for the ring generation discussed above, but in a stress-generated trap of the type presented in Ref. [34]. Figure 6-6 shows the PL of the lower polaritons with $k_{||} = 0$. At the excitation region around $x = 0$, the detuning

is $\delta = 2.3$ meV. The red dashed line corresponds to the sum of the single-particle energy of the lower polariton at low density in this region, found by measuring the $k_{||} = 0$ PL energy at a very low density, and a fit of emission energies to a Gaussian
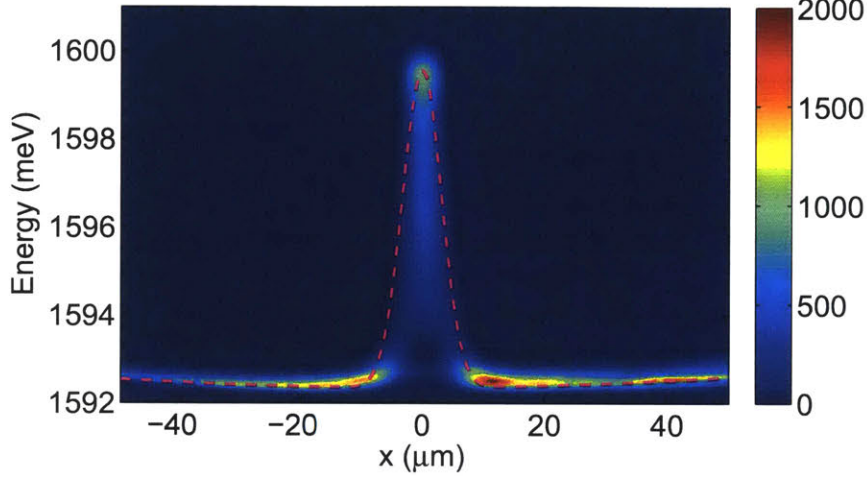
Figure 6-6: $k_{||} \simeq 0$ polariton energies under a Gaussian-shaped spot excitation at a cavity detuning of $\delta = 2.3$ meV in a stress trap. The red dashed line is a sum of the bare single-particle energy and a fit to Gaussian profile $y = A\exp(-x^2/\Delta x^2)$, with the diffusion length of the excitons and free carriers determined from the fit as $\Delta x = 7.5\,\mu$m. The lattice temperature was approximately 8 K.

profile $A\exp(-x^2/\Delta x^2)$. The fitting gives a FWHM of 7.5 μm and a height of 7.2 meV. Because the generation of the polaritons is done at a single spot in this case, the excitation density must be much higher to get a number of polaritons in the trap comparable to the ring generation case. In the case shown in Fig. 6-6, the polariton density is still below the condensation threshold, but the blue shift at the excitation spot is much larger than that of the excitation ring region for the experiments reported here; the blue shift of the excitation region was at most 4 meV in the experiments. The diffusion of the excitons can be seen from the energy shift of the polaritons in the vicinity of the excitation region. At $x = \pm 10\,\mu$m, the blue shift of the polariton energy reduces to 0.2 meV. Based on this, the upper bound of the exciton diffusion length was estimated to be 5.3 μm. At regions that are $>20\,\mu$m away from the center of the excitation region, the energy shift of the polariton ground state is negligible.

This confirms that the exciton reservoir at the pump region does not leak into

the center of the trap where the energy shift data will be determined. Although this experiment with a single spot in a stress trap does not have conditions identical to those of the laser-generated ring trap, it should overestimate, not underestimate, the effect of diffusion of the excitons. First, the density at the excitation spot was higher, as evidenced by the much stronger blue shift, so the pressure pushing excitons outward should be stronger. Also, the lattice temperature was lower, which should give a higher exciton diffusion constant.

Based on this observation, we choose an annulus with a diameter of $42\,\mu$m for the further experiments. A real-space image of the excitation profile is shown in Fig. 6-7. The dashed circle in Fig. 6-7(a) and the dashed line in Fig. 6-7(b) indicate the
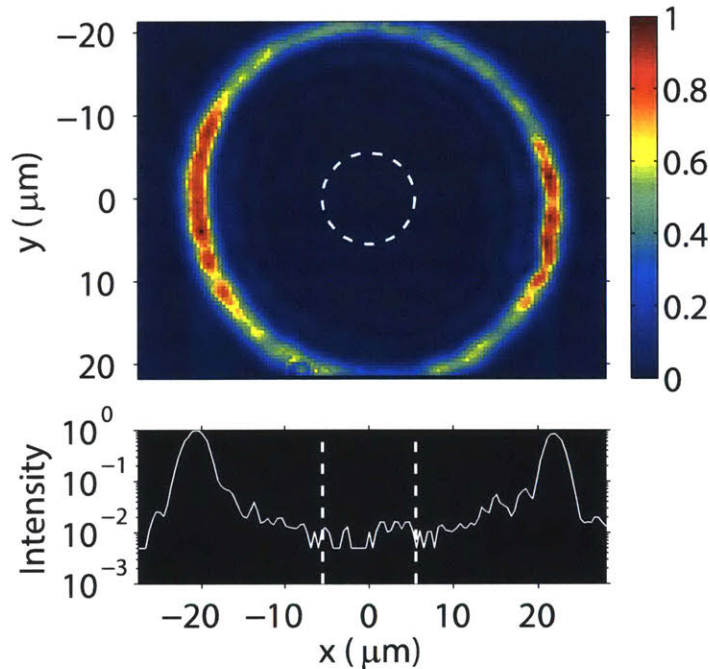
Figure 6-7: (a) The real-space image of the laser reflection, which is a ring with a diameter of $42\,\mu$m. The white dashed circle indicates the region where the photoluminescence (PL) is collected. (b) The white solid line is the cross section of the $y = 0$ slice that is selected by the entrance of the imaging spectrometer and then energy-resolved. The white dashed line indicates the position of the pinhole.

collection region defined by a spatial filter placed at the reconstructed real-space plane downstream. The $y = 0$ slice was selected by the spectrometer slit and then spectrally dispersed to get the emission energy. Fig. 6-7(b) shows the intensity profile of the

179

$y = 0$ slice. We also measured the integrated light intensity in the collection region with and without a neutral density filter, and determined that the light intensity in the collection region is ~2000 times smaller than that in the pumping region. This is crucial to the quality of the measurement, for otherwise, light in the collection region can create excitons and free carriers which can lead to an additional shift of the polariton energy. As discussed below, typical energy shifts of the polaritons in the collection region are about 10% of the energy shift in the pumping region. Assuming that the exciton density is proportional to the pump intensity, the energy shift of the polaritons in the collection region cannot come from the excitons.

6.2.2 Trapping polaritons in the center of the annulus

The potential profile induced by the annulus pumping was examined by applying k-space filtering with an iris at the Fourier plane of the objective. Typical spatially
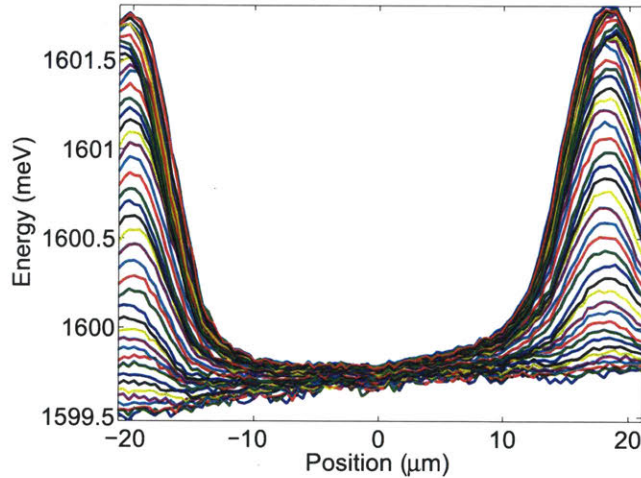
Figure 6-8: Blue shift of the $k_\parallel = 0$ state at the pumping region in an annular trap with a diameter of 35 μm as a function of pump power for $\delta = 1.06$ meV. The slope of the emission energy is a result of cavity wedge.

and spectrally resolved emission was shown in Fig. 4-9(d). By fitting each vertical slice $I(E)$ in the figure to a Gaussian function $I = A \exp(-(E - E_0)^2/2\sigma^2) + B$ with free parameters A, E_0, σ and B independently, and taking the fitted E_0 for all the different positions as the potential profile, the resulting plot is shown in Fig. 6-8 for

180

different pump powers. As is seen, the potential profile around $x = 0$ is nearly flat in all the densities, due to the polariton population finding a common chemical potential in equilibrium. Meanwhile, the height of the barrier increases as the pump power is increased. The slope in the potential profile is a result of the spatially varying cavity width.

The accumulation of the polaritons in the center of the trap can be seen in Fig. 6-9. It shows the energy shift at the pump region with a diameter of 35 μm for different pump powers, but all below the condensation threshold, so there is no condensate. The polariton density is significantly higher on the left side of the trap, as a result of optical trapping. The fact that the blue shift is asymmetric, larger inside the trap than outside it, is further evidence that it does not arise from exciton diffusion. Exciton diffusion from the generation region should be symmetric, as excitons flow both inward and outward. The density of polaritons is not expected to be symmetric, unlike the excitons, because polaritons stream away from the barrier when there is no trap [140], while they accumulate in the trap when there is an energy minimum to collect them. The total number of polaritons as a function of pump power in the field
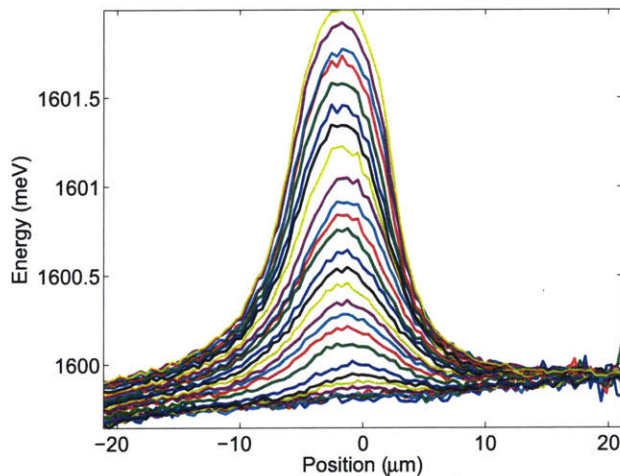
Figure 6-9: Blue shift of the $k_{||} = 0$ state at the pumping region in an annular trap with a diameter of 35 μm as a function of pump power for $\delta = 1.06$ meV. The slope of the emission energy is a result of the cavity wedge. The left edge of the plot is toward the center of the trap.

of view, indicated by the dashed circle in Fig. 6-7(a), is plotted in Fig. 6-10(b). As

is seen, the measured number of polaritons increased linearly with pump excitation density in the low-density regime below the condensation threshold.

6.3   Interactions of Polaritons inside the Trap

6.3.1   Energy shift of $k_{||} = 0$ states at different intensities

Under the mean-field approximation, at low particle density, the blue shift of the ground state energy is linearly dependent on the particle density n, i.e.,

$$\Delta E = gn \tag{6.3}$$

where ΔE and n are the blue shift and particle density, respectively. In the absence of many-body correlations, the slope g is density independent.

In order to determine the energy shift of the ground state, we spectrally resolved the emission in the field of view and imaged it to the far-field geometry to obtain the dispersion relation. Figure 6-10(c) shows a typical energy-resolved emission pattern in the far-field geometry at low excitation power, and Fig. 6-10(d) shows a case of high excitation power, but below the condensation threshold. As can be seen, the ground state polariton energies, indicated by the horizontal dotted and dashed lines, are blue shifted due to repulsive interactions among polaritons. In order to determine the ground state energy at zero excitation density, we linearly extrapolate the measured blue shifts to zero density. All the blue shifts are then reported with respect to this energy. As shown in Fig. 6-10(a), the blue shift increases linearly with the polariton density, agreeing with the mean-field theory. This confirms that the interaction strength g does not depend on the density of the polaritons in this regime.
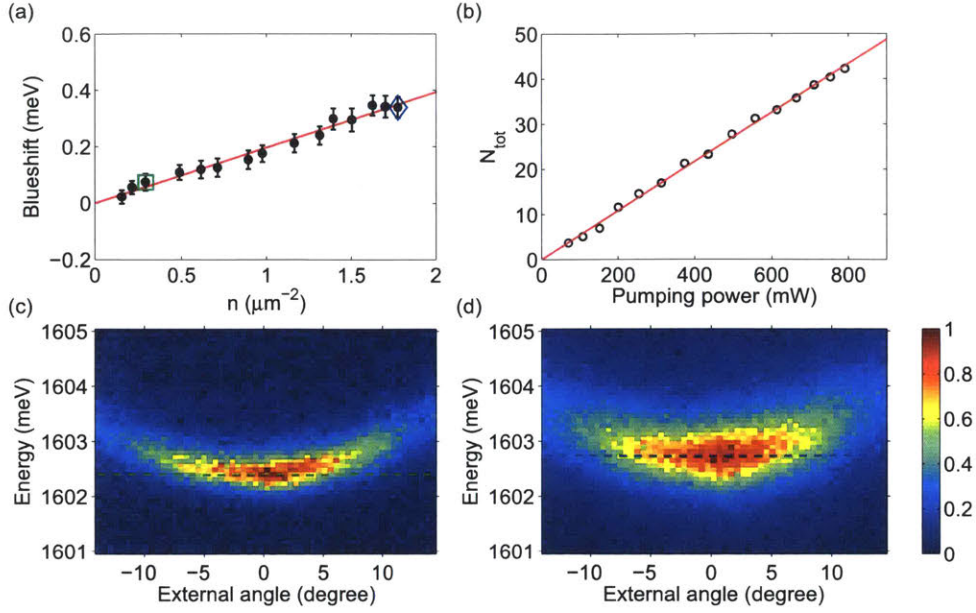
Figure 6-10: (a) Blue shifts of ground state energies at different polariton densities at a detuning of $\delta = 6.29$ meV. (b) Polariton number in the field of view at different pumping powers. (c)-(d) Typical energy-resolved dispersions corresponding to the data points indicated by the green square (c) and blue diamond (d) in (a), both at low densities when there is no condensate. The dashed lines are the assigned energies of the ground state of polaritons.

6.3.2 Spectral profile of $k_{||} = 0$ states at different intensities

There is also a Lorentzian spectral broadening which arises from the interactions. To a good approximation, when there is no condensate, this spectral broadening can be seen as simply the uncertainty energy given by $\Delta E = \hbar/\Delta t$, where Δt is the average incoherent scattering time. This broadening also gives a measure of the polariton-polariton interaction strength. At low density, the emission profile deviates away from the Lorentzian profile and resembles the Voigt profile, which accounts for the disorder-induced inhomogeneous broadening, as discussed in the following.

The emission profiles at $k_{||} = 0$ at different excitation densities for the detunings in Figs. 6-10 are shown in Fig. 6-11 to 6-17. The background signal is not subtracted,

and the solid lines are the fit to a Voigt lineshape, given by

$$V(E; \sigma, \gamma, E_0, A, c) = A \int_{-\infty}^{\infty} G(E'; \sigma, E_0) L(E - E'; \gamma, E_0) dE' + c \qquad (6.4)$$

where $G(E; \sigma, E_0)$ is the Gaussian profile

$$G(E; \sigma, E_0) = \frac{e^{-(E-E_0)^2/2\sigma^2}}{\sigma\sqrt{2\pi}} \qquad (6.5)$$

and $L(E; \gamma, E_0)$ is the Lorentzian profile

$$L(E; \gamma, E_0) = \frac{1}{\pi} \frac{\gamma}{(E - E_0)^2 + \gamma^2}; \qquad (6.6)$$

A is the amplitude of the profile, and c is the baseline. In the nonlinear regression, the Welsch weight of the form

$$w = \exp(-r^2) \qquad (6.7)$$

is applied with a default tuning constant of 2.985 in order to increase the robustness of the fitting. Here r is the normalized residual, and w is the robust weight. As can be seen, the emission profiles are well captured by the Voigt lineshape at all densities and detunings. We also plot the fitted linewidths σ and γ next to the emission profiles. The superimposed solid lines are best fits to a linear dependence. As can be seen, the homogeneous linewidth γ shows a strong density effect because the increase in the polariton density leads to more frequent collisions, and it is also reduced in magnitude when the detuning is negative where polaritons have high photonic components. On the other hand, the inhomogeneous linewidth σ remains approximately the same in the range of densities and detunings used in the measurements.
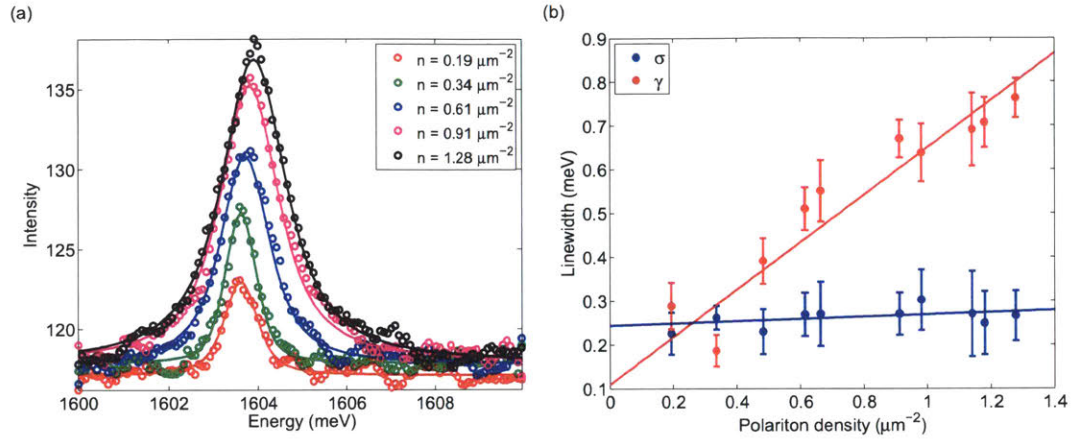
Figure 6-11: (a) Energy emission profiles at $k_\parallel = 0$ at different excitation densities for the detuning of $\delta = 10.11$ meV with a ring radius of 85 μm corresponding to Fig. 6-10. The dots are five-point running averages of the raw data, and the solid lines are the fits to the Voigt profile. (b) Gaussian linewidth σ and Lorentzian linewidth γ from the fitting in (a) at different excitation densities. The solid lines are best fits to a linear dependence using weighted least-squares estimates. The errorbars represent standard deviations in fitting σ and γ.
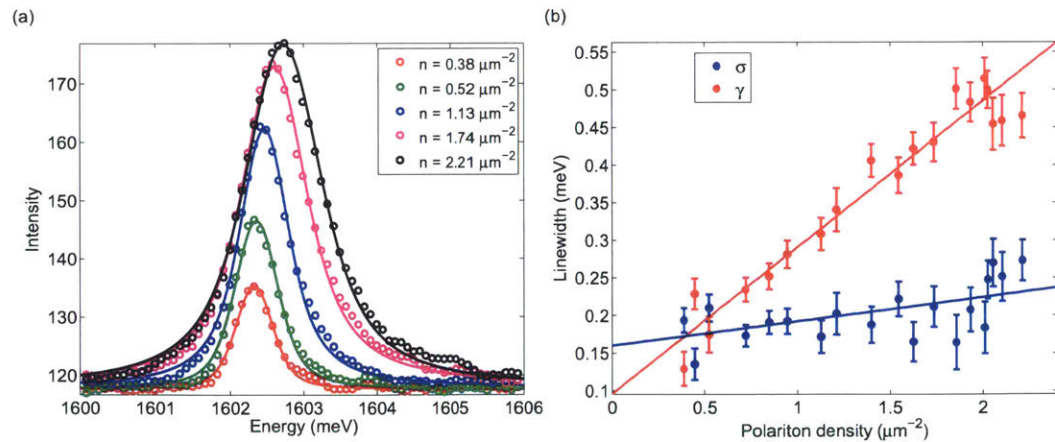
Figure 6-12: For the same conditions as Fig. 6-11 but with a the detuning of $\delta = 6.29$ meV.
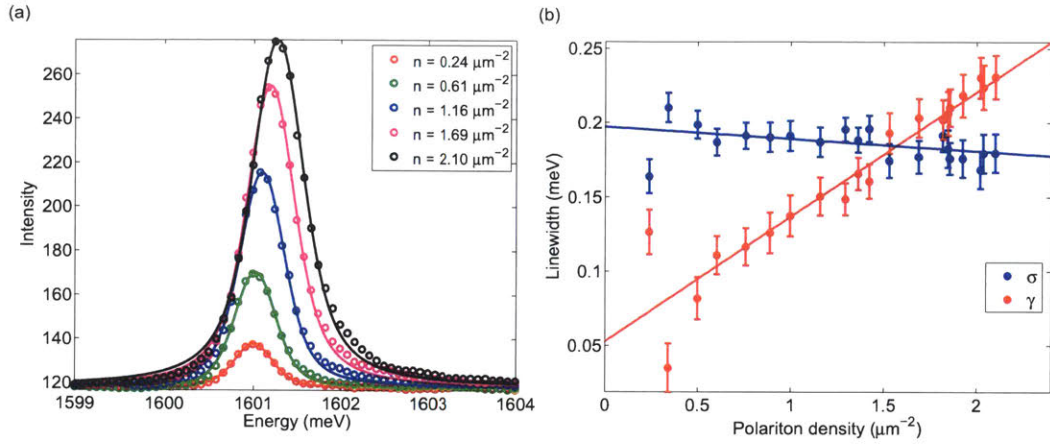
Figure 6-13: For the same conditions as Fig. 6-11 but with a the detuning of $\delta = 3.11$ meV.
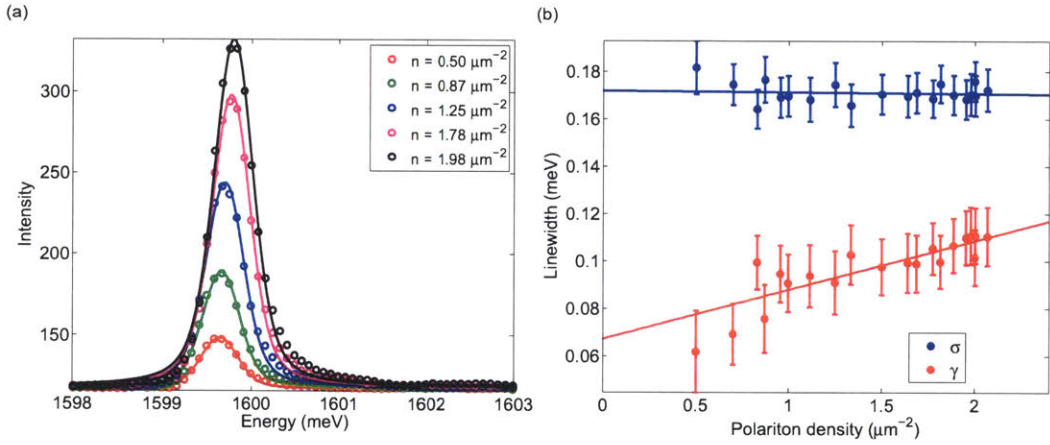
Figure 6-14: For the same conditions as Fig. 6-11 but with a the detuning of $\delta = 0.65$ meV.
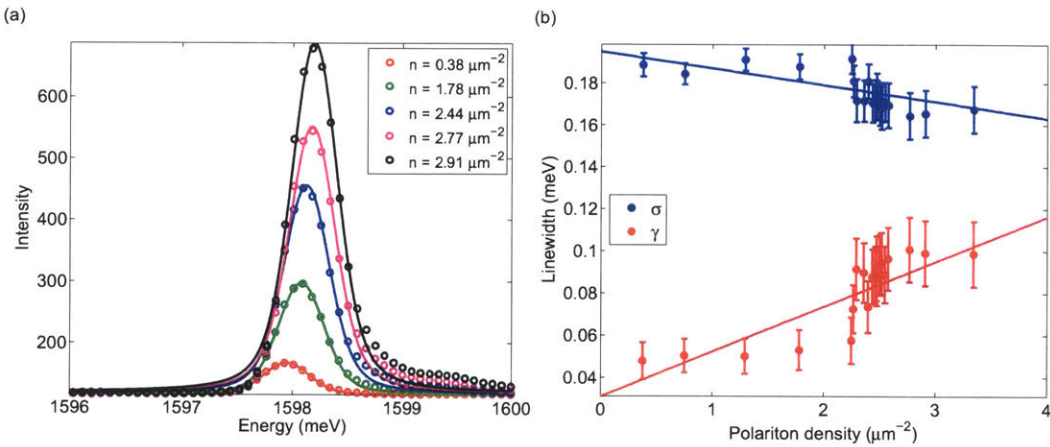
Figure 6-15: For the same conditions as Fig. 6-11 but with a the detuning of $\delta = -2.07$ meV.
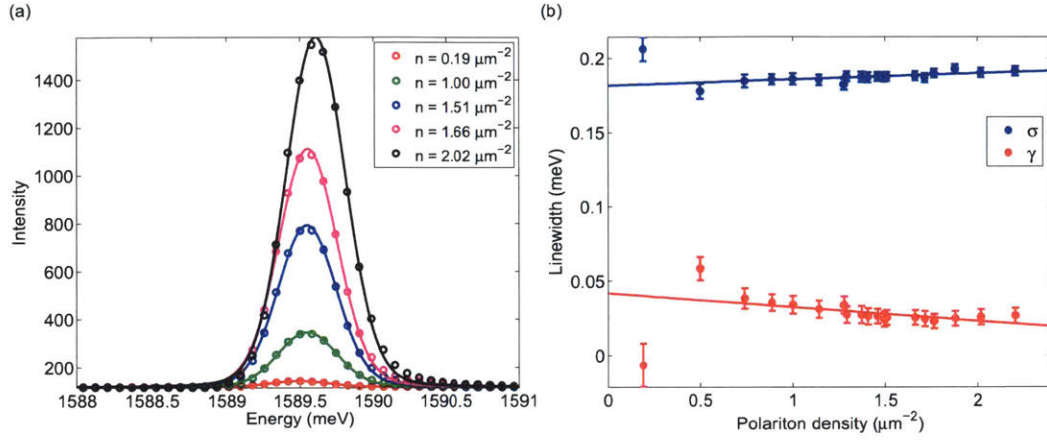
Figure 6-16: For the same conditions as Fig. 6-11 but with a the detuning of $\delta = -10.11$ meV.
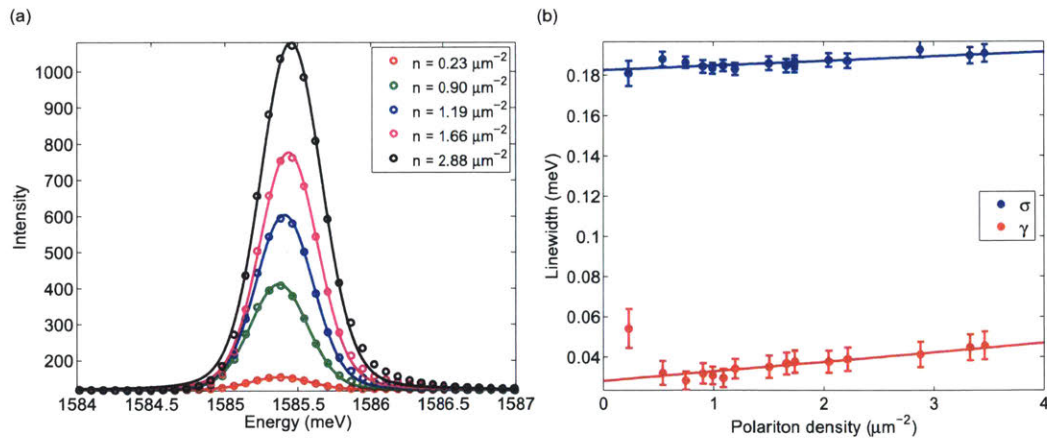
Figure 6-17: For the same conditions as Fig. 6-11 but with a the detuning of $\delta = -15.49$ meV.
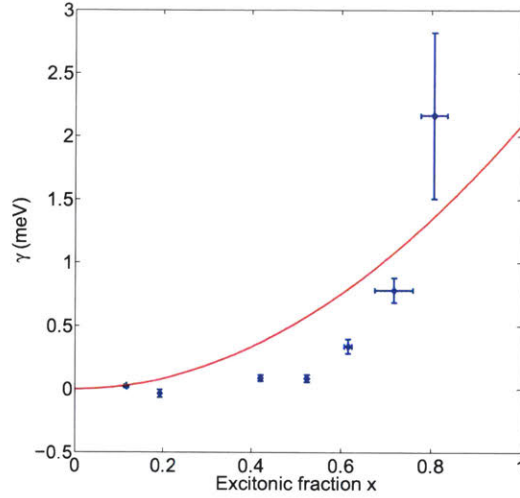
Figure 6-18: Interaction strength extracted from the slopes of linear fits to the homogeneous linewidth in Fig. 6-11 to 6-17. The red line is a fit to $\gamma \propto x^2$.

6.3.3 Determination of interaction strength based on the emission linewidth

In Fig. 6-18, we plot the slopes of linear fits to the homogeneous linewidths in Fig. 6-11 to 6-17. As can be seen, the linewidths increase as densities increase because increased density leads an increase in the collision frequency between polaritons, which is in turn manifested through broadened linewidths. The red line is a fit to $\gamma = ax^2$ with $a = 2.09 \pm 1.06$ meV$\cdot\mu$m^2, which quantitatively agrees with the interaction strength deduced from the energy shift in the following. The quadratic dependence comes from the fact that the polariton-polariton scattering is of two-body type.

6.4 Calibration of polariton density

Care was taken to ensure that the polaritons were nearly in spatial and thermal equilibrium. The spatial distributions of the polaritons in a trap are nearly spatially homogeneous as shown in Fig. 5-5. At high density when a condensate forms, there is evidence of self-trapping into a central region of the laser-generated trap. The data for detunings with significant exciton components have reasonable thermalization, as

are observed in Chapter 5. When polaritons are very photon-like, the spatial and energy profiles of the polaritons become quite inhomogeneous, but do not hinder the determination of the interaction strength.

The greatest uncertainty in these measurements is the determination of the polariton density, i.e., the total number of polaritons in the area of the field of view. We used two methods and found consistency between them. The first was to carefully determine the absolute collection efficiency of our photon detection system, as discussed in Chapter 4. The number of polaritons at a given momentum $k_\parallel$ was then deduced from the rate of photon emission knowing the cavity photon lifetime and the photonic fraction of the polaritons at that $k_\parallel$. Specifically, the total number of polaritons in the field of view can be computed using

$$N_{LP} = \sum_i \frac{N_i \tau_i}{\xi M_i} \tag{6.8}$$

where N_i is the counts per second on the CCD in the measurement, τ_i is the lifetime of polaritons, which is also angle-dependent, and ξ and M_i are the optical efficiency and the density of k states for pixel i, calculated in Chapter 4.

An independent check of the efficiency factor can be done by calculating the number of polaritons from integrating over the Bose-Einstein distributions as shown in Fig. 5-10(b) using

$$N_{LP} = \frac{gmS}{2\pi\hbar^2} \int_0^{E_{max}} N(E)dE \tag{6.9}$$

where S is the area of the field of view and E_{max} is the upper bound of the energy limit collected by the objective lens. From this way, we compute that the number of polaritons in the field of view at a pumping power of $P = 78$ mW is $N_{LP} = 1058$. By using Eq. (6.8), we get a quantity of $N_{LP} = 1012$, which is less than 5% different.

These methods give us an accurate calibration of the polariton density in the field of view in the annular trap. More generally, we do not have to rely on the details of the above calculations to get the approximate range of the polariton densities. We

know that we measure the polariton spectra up to the condensation threshold (as evidenced by the sharp spectral narrowing, discussed below and also reported in Ref. [140]). Quantum effects will be important when the thermal de Broglie wavelength is comparable to the interparticle spacing, i.e., when

$$\lambda_T = \sqrt{\frac{2\pi\hbar^2}{mk_BT}} \sim r_s = n^{-1/2} \tag{6.10}$$

where n is the particle density, and T is temperature of the particle. This implies $n \sim mk_BT/2\pi\hbar^2 \approx 4\times10^7$ cm^{-2} near the condensation threshold, for $k_BT \sim 20$ K and the polariton mass given above. Note the critical densities derived from these three different approaches are significantly smaller compared to what has been reported in previous literatures, which is typically on the order of $n = 10^9$ cm^{-2}. This suggests that earlier experimental measurements significantly underestimated the interaction strength of polaritons, by about two orders of magnitude.

6.5 Interaction strength of polaritons at low particle densities below the condensation threshold

In Fig. 6-19, we plot the measured blue shifts of the $k_{\parallel} = 0$ state as a function of polariton density at four representative detunings. As expected, polaritons experience higher blue shifts for excitonic detunings than for photonic detunings, since the energy renormalization presumably comes from the excitonic constituents. The solid lines show linear fits to the data using weighted least square estimates, as discussed in Chapter 4.

Figure 6-20 shows the extracted slopes at different cavity detunings versus their corresponding excitonic fractions. The interaction strength increases when excitonic fractions in polaritons are higher. The standard theory predicts that the interaction
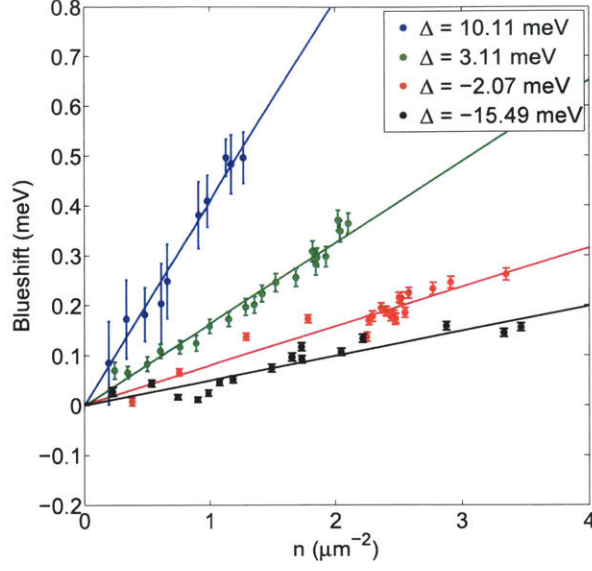
Figure 6-19: Blue shifts of the ground state energies as a function of polariton density at different cavity detunings. The solid points are measured blue shifts, the linear lines are fits to $\Delta E = gn$ using weighted least-squares estimates. The errorbars are standard deviations of estimated energy shifts.

between polaritons is governed by their underlying excitonic fractions x, given by

$$x = \frac{1}{2}\left(1 + \frac{\delta}{\sqrt{\delta^2 + \Omega^2}}\right), \qquad (6.11)$$

where Ω is the full Rabi splitting and δ is the cavity detuning, defined as $\delta = E_c(k_{||} = 0) - E_x$, where E_c and E_x are the cavity and exciton energies, respectively. The exciton fractions x are deduced for each data set from the effective mass of the lower polariton dispersion using the formula $x \simeq 1 - m_c/m_{LP}$, where m_c is the bare cavity photon mass, measured at very large photonic detuning (-22.5 meV). Since the interaction of exciton-polaritons is presumed to come exclusively from their underlying excitonic components, we fit the extracted slopes in Fig. 6-19 to a quadratic relation $g = ax^2$, as shown by the red line in Fig. 6-20. The dependence of the shift on exciton fraction is clearly superlinear, which is another indicator that the shift is not arising from polariton-exciton interactions; if interaction with excitons were the dominant cause of the blue shift, the shift would be linear with exciton fraction.

191

By extrapolation, the interaction strength in the limit of $x \rightarrow 1$ is determined as 0.44 ± 0.11 meV·μm^2. This value is quite surprising, in that it is two orders of magnitude larger than the absolute value calculated in Ref. [24], which has guided many theoretical investigations of polaritons. This theoretical work suggests the exciton-exciton interaction strength to be $g \sim 6E_B a_B^2$, where E_B is the excitonic binding energy, and a_B is the excitonic Bohr radius. Using the typical values for excitons in GaAs narrow quantum wells, namely $E_B \sim 10$ meV and $a_B \sim 100$ Å, gives $g \sim 6$ μeV·μm^2. This, in turn, implies that the polariton gas is intrinsically weakly interacting, as measured by the unitless parameter $\gamma = g/(\hbar^2/2m) \sim 0.01$ [207, 208], using the effective mass of polaritons $m \sim 10^{-4} m_0$, where m_0 is the vacuum electron mass. However, the measured interaction strength implies that the unitless parameter for the strength of the interactions is $\gamma = g/(\hbar^2/2m) \sim 1$, which means that the polariton gas cannot be treated by standard weakly interacting Bose gas theory. In particular, it implies that many-body correlations will play an important role at high densities.

The extrapolation to $x \rightarrow 1$ seems to imply that not only polaritons, but bare Wannier excitons also have this strong interaction. However, we note that in all the measurements here, the effective masses of the particles was very light, comparable to the polariton mass at resonance, as plotted in Fig. 6-21. The effective mass of the polaritons were deduced from the Hopfield coefficients used, which were derived from the detuning, as discussed above. It may be that the strong interactions seen here depend crucially on the light effective mass of the polaritons, and therefore it may be unwarranted to extrapolate this result to the pure exciton limit.

As noted above, the polariton-polariton interactions affect not only the blue shift (real self-energy) but also the line broadening (imaginary self-energy). The Lorentzian line broadening value of ~ 1 meV is also two orders of magnitude larger than what would be expected for the nominal exciton-exciton interaction strength. Using the semiclassical formula $\tau^{-1} = n\sigma\bar{v}$, where n is the density, $\sigma \sim a_B$ is the scattering cross section, and $\bar{v}$ is the average thermal velocity. It gives $\tau \sim 100$ ps, or $\hbar/\tau \sim 0.01$ meV with typical values for microcavity polaritons $n = 4 \times 10^7$ cm^{-2}, $\sigma = 100$ Å and

192
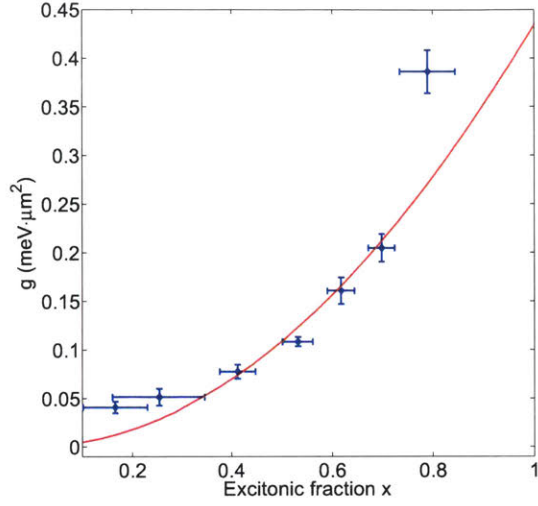
Figure 6-20: Measured interaction strength (g) as a function of excitonic fraction (x), which is deduced for each data set from the effective mass of the lower polariton dispersion using the formula $x \simeq 1 - m_c/m_{LP}$, where m_c is the bare cavity photon mass, measured at very large photonic detuning (-22.5 meV). Solid points are slopes extracted from Fig. 6-19. The red line is a best fit to a quadratic dependence using weighted least-squares estimates. The horizontal errors represent standard deviations of the calculated excitonic fraction using Eq. (6.11), and vertical errorbars represent standard deviations of interaction strengths from numerical fits.

$\bar{v} = 2 \times 10^8$ cm/s for $T = 20$ K. The measured Lorentzian broadening corresponds to a polariton-polariton scattering time of less than 1 ps.

Furthermore, the interactions between polaritons are predicted to be spin-dependent, and several experiments have studied this spin dependence. In the experiment reported here, we assume that the polaritons are equilibrated into a mixture of both spin states, and therefore the interaction strength we measure is an average value. Because the interaction of polaritons is stronger for spin-aligned polaritons, we expect that our measured interaction strength will be dominated by the spin-aligned contribution.
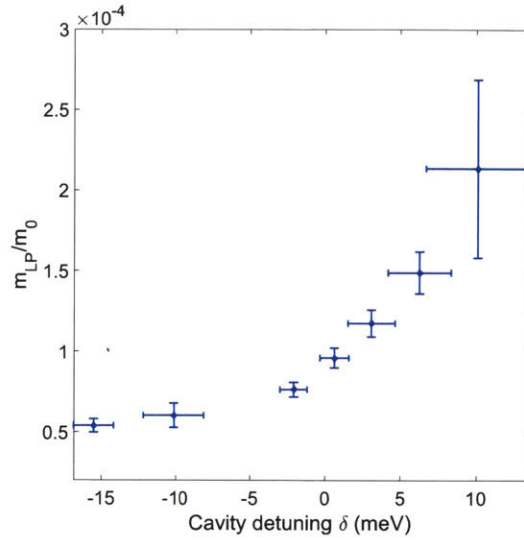
Figure 6-21: Effective mass of the polaritons as a function of the detuning, where m_0 is the vacuum electron mass deduced from the energy dispersions collected in a ring with a radius of 42 μm, corresponding to that in Fig. 6-19. Horizontal errorbars are standard deviations of cavity detunings from numerical fits, and vertical errorbars are standard deviations of calculated effective masses using the Hopfield formula.

6.6 Saturation of the interaction strength at high particle densities above the condensation threshold

Evidence of the importance of many-body correlations is seen in the behavior of the blue shift at the condensation threshold. In Fig. 6-22, we plot the blue shift of the ground state emissions at different polariton densities up to and above the condensation threshold in an annulus trap with a diameter of 72 μm, for an excitonic detuning of $\delta = 4.31$ meV. We also show the spectral width of the emission at $k_{||} = 0$. As discussed above, the condensation threshold is indicated by spectral narrowing.

At low densities, the blue shift scales linearly with the polariton density with a slope of 0.91 ± 0.13 meV$\cdot\mu$m^2, consistent with the value expected for this detuning. The linewidth of the emission also increases linearly with density because the larger population leads to more frequent incoherent collisions, and then narrows due to the emergence of coherence when condensation occurs. At the condensation threshold, the

194
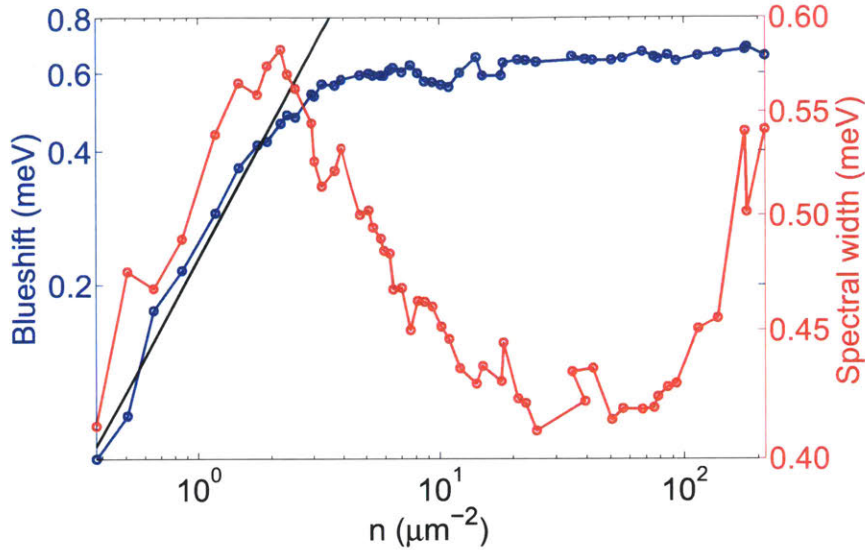
Figure 6-22: Measured blue shifts (blue circles) and spectral widths (red circles) of the $k_{||} = 0$ lower polariton emission as a function of polariton density at a cavity detuning of $\delta = 4.31$ meV in an annulus trap with a diameter of 36 μm. The straight line shows a linear dependence.

blue shift of the polariton emission becomes strongly sublinear with density, following a power law $\Delta E \sim n^{0.037}$. The simple mean-field prediction for a weakly interacting Bose gas is that the shift should still be linear with density when it condenses, with an overall slope that is reduced by a factor of two due to the nature of quantum indistinguishability [209]. The fact that the shift is strongly sublinear points to the importance of high-order correlations in the condensate regime, which have been shown to have a significant role in strongly interacting gases [210].

6.7 Why Are Polaritons Strongly Interacting?

Given that the measured value of the blue shift is so much larger than the theoretical expectation, we consider possible ways that the measurement could be misleading. First, one may ask whether excitons and/or free carriers generated by the non-resonant laser may indeed be diffusing into the region where the polaritons are observed. We are confident that this is not the case. As the diameter of the ring trap is increased up to 100 μm, the blue shift at fixed density has a constant value

independent of the trap radius, as seen in Fig. 6-5. If exciton or free carrier diffusion were playing an important role, the blue shift at the condensate density would depend strongly on the ring radius, as their diffusion length becomes much less than the radius. Also, the exciton diffusion length has been directly measured, as seen in Fig. 6-6 and Fig. 3(a) in Ref. [104], and is determined to be less than 10 μm. Furthermore, it is also known that the diffusion length of the polaritons decreases with increasing excitonic component as polaritons with higher excitonic components have greater effective mass and stronger interactions with phonons. This will lead to less exciton population far from the excitation region, while here we see that the blue shift increases with increasing excitonic fraction.

6.7.1 Phase-space filling

A blue shift may arise from phase-space filling, which leads to a reduction of the Rabi splitting between the upper and lower polariton branches. This is also predicted to give shifts of order $E_B a_B^2$ or less [211, 212], much less than what we observe here. Band-gap renormalization due to heating (i.e., phonon population) is known to give a red shift, not a blue shift, with increasing temperature.

6.7.2 Thermal up-conversion of free excitons

Another possibility is that the polaritons generate free excitons in the center of the trap via thermal up-conversion. In this model, excitons are present in the center of the trap, not due to diffusion from the laser excitation region, i.e., from the walls of the ring trap, but from migration of polaritons by themselves, which then turn back into free excitons by thermal excitation. For this to give the blue shift we see, assuming the standard interaction strength, there would need to be two orders of magnitude more excitons than polaritons. This would severely deplete the population of polaritons. Also, this effect should be exponentially dependent on the splitting ΔE between the polariton and exciton states, due to the Boltzmann $e^{-\Delta E/k_B T}$ factor, but in fact we see even more blue shift than expected when the lower polaritons are very photonic,

with large ΔE. We also see very little temperature dependence of the blue shift at constant ΔE as the lattice temperature is changed, as discussed in the following.

The temperature dependence of the blue shift under typical conditions is shown in Fig. 6-23. As seen in this figure, the shift at the pumping region is not strongly dependent on the lattice temperature. This is evidence against the mechanism discussed in the main text which conjectures that the polaritons generate excitons due to thermal excitation after they move to the center of the trap. Since a thermal excitation process is exponentially sensitive to the temperature due to the Boltzmann factor $e^{-\Delta E/k_B T}$, such a process would be strongly temperature dependent.

Additionally, the weak dependence on temperature also indicates that exciton diffusion from the generation region on the ring into the trap is not playing a major role, because the exciton diffusion constant should also be strongly dependent on the lattice temperature, with much higher diffusion at lower temperatures.

On the other hand, our experiments indicate that the blue shift at the Bose-Einstein condensation threshold varies roughly linearly with temperature. This can be understood as arising from the density dependence of the critical temperature of the condensation threshold. In two dimensions, the critical temperature should vary linearly with density. The mapping of the BEC threshold density as a function of temperature has already been discussed in Chapter 5.

6.7.3 Energy shift from quantum confinement

Figure 6-8 shows the complete view of the barrier measured under the same condition as in Fig. 6-9 with high k components filtered. As is seen, the potential profile around $x = 0$ is nearly flat in all the densities, due to the polariton population finding a common chemical potential in equilibrium. Meanwhile, the height of the barrier increases as the pump power is increased. This could contribute, in principle, an energy shift of the polariton states due to increasing quantum confinement in the trap region. However, the contribution is negligible. Using the result from a finite-
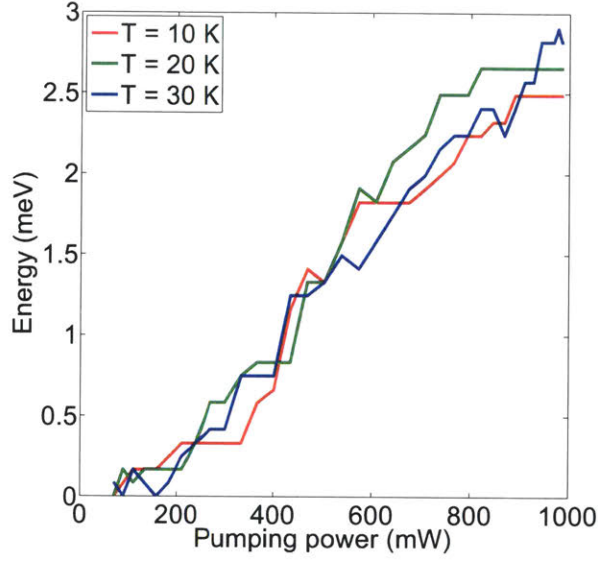
Figure 6-23: Blue shift of the $k_{||} = 0$ state at the pumping region in an annular trap with a diameter of 33 μm as a function of pump power for different temperatures, for $\delta = -0.16$ meV.

well potential, we have

$$E = \frac{2\eta^2\hbar^2}{L^2 m} \tag{6.12}$$

where m is the mass of polariton, L is the trap diameter, and η is the solution to the equation

$$\tan \eta = \sqrt{\frac{\zeta^2}{\eta^2} - 1} \tag{6.13}$$

with the trap strength being defined as

$$\zeta = \frac{L}{2}\sqrt{\frac{2m}{\hbar^2}V_0} \tag{6.14}$$

and V_0 is the height of the barrier. Plugging a typical parameter $m = 9 \times 10^{-5} m_0$, $L = 42$ μm, and $V_0 = 2$ meV, we find $E = 10$ μeV. On the other hand, the measured blue shift is typically on the order of 0.1 meV. Note that if we used a small trap, of order 10 micron diameter, as in the experiments of Ref. [213], then the quantum

198

confinement energy would be up to 20 times larger, and so could become comparable to the interaction blue shifts.

6.7.4 Other possible mechanisms

Assuming that the above mechanisms are ruled out, we can ask what mechanism could give us much stronger effective interactions at low density than predicted. One possibility is that the nearby biexciton resonance [214] significantly affects the interactions. We believe this is not the case, because the dependence of the interaction strength on detuning is not especially strong. Another possibility is a mechanism involving disorder, which has also been invoked as a way of explaining the larger-than-expected blue shift in previous experimental results [215, 216]. In our experiments, the photonic disorder is very low, but the excitonic disorder is approximately 2 meV (as measured by the inhomogeneous broadening of the bare exciton line). Jacob Taylor [217] has suggested that disorder may cause the excitons participating in the polariton states to be spatially correlated in "puddles" of much higher density than the average polariton density. This view requires no change to the standard exciton-exciton interaction strength. It is supported by the observation that both the blue shift and the Lorentzian line broadening are about 100 times larger than expected; both of these depend linearly on the effective density. Lastly, it could be that polaritons are really strongly interacting, and previous measurement is not incorrect. Polaritons have long de Broglie wavelengths, up to $1\,\mu m$, and the effective scattering cross section is much larger compared to excitons due to field-mediated interactions. This could in principle lead to much higher interactions compared to bare excitons. This might also explain the fact that we see significantly higher blue shift values when $x \to 0$, since field-mediated interactions could dominate over Coulomb interactions.

6.8   Conclusions

In conclusion, we have directly measured the polariton-polariton interaction strength by propagating polaritons to the center of a laser-generated annular trap. The inter-

action strength is independent of polariton density in the low-density regime. The measured value is two orders of magnitude larger than expected from prior theoretical calculations. The polariton-polariton interaction is effectively a $\chi^{(3)}$ nonlinearity [218], and is an important parameter for the design and theoretical modeling exciton-polaritonic optical devices. The large value measured here indicates that the efficiency of these devices may be much greater than anticipated, at least in the low-density regime. The saturation of the blue shift upon condensation calls for further theoretical analysis, and is likely due to coherent many-body effects of the condensate.

Chapter 7

Stable Mode Switching in Polariton Condensates

Microcavity polaritons provide unique testbeds for the study and manipulation of macroscopic quantum effects. Now that we have a high-Q microcavity structure which allows the formation of thermalized polaritons in a broad range of densities and temperatures, and the annular trap to spatially confine the polaritons, it is straightforward to investigate in detail the modes of condensates in the annular optical trap.

In this Chapter, the multistate optical switching among high-order bouncing-ball modes ("ripples") and whispering-gallery modes ("petals") of exciton-polariton condensates in laser-generated annular traps is presented. The formation of ripples and petals in the annular trap is discussed in Section 7.2. By tailoring the diameter and intensity of the annular trap, polariton condensates can be switched among different trapped modes, accompanied by a redistribution of spatial densities and a superlinear increase in emission intensities, implying that polariton condensates in this geometry could be exploited as multistate switches, as discussed in Section 7.3. A model based on non-Hermitian modes of the generalized Gross-Pitaevskii equation is proposed in Section 7.5. The model reveals that this mode switching arises from competition between pump-induced gain and in-plane polariton loss. We conclude the section by a survey of the experimental parameters for reproducible switching among trapped modes, and present the phase diagram for mode switching in Section 7.4. Taken to-

gether, the experimental results and theoretical modeling advance our fundamental understanding of the spontaneous emergence of coherence and move us toward its practical exploitation.

7.1 Experimental Methods

Previous experiments on Bose condensation of polaritons were usually performed with the photonic resonance close to the excitonic resonance, which resulted in highly excitonic characteristics in polaritons. Together with short cavity lifetimes, this severely limited the distance that polaritons could propagate [219, 213, 220]. The development of new structures with much longer cavity lifetimes, from 20–30 ps [184] to well over 100 ps [140, 98, 104], has allowed the possibility of polariton propagation over macroscopic distances. This property was used to measure the polariton-polariton interaction strength in a region with no free excitons [37], as discussed in Chapter 6.

In the work of this chapter, we generated polaritons with high photonic fractions by choosing a region of the wedged sample with a large negative cavity detuning. Their highly photonic nature allowed the polaritons to propagate coherently over long distances to form condensate states with spatial extent up to 50 μm inside an optical trap. Annular-shaped beams with diameters ranging from 21 μm to 54 μm were used to create the optical trap. The laser beam was tuned about 140 meV above the bandgap of the QW material. Therefore it essentially generated free carriers, which subsequently relaxed down to exciton and polariton states. Petals and ripples were formed inside the excitation annuli. In theory, if not limited by the pump power, higher-order condensate states with lengthscales on the order of millimeters could be realized in this high-Q microcavity structure, making them entirely visible to the naked eye.

While interactions of polaritons in this case are not strong enough for them to thermalize into equilibrium gases, they still play an important role. The interactions of polaritons with excitons in the pump region allow the polaritons to undergo condensation inside optical traps. Furthermore, nonlinear polariton-polariton inter-

actions result in switching among different condensate modes at high pump powers, as discussed further in Section 7.5.

7.2 Petals and Ripples in the Annular Trap

7.2.1 Spatial and spectral distributions of petals

Petals are whispering-gallery modes in the annular trap. Fig. 7-1 shows the emission patterns from an annular trap with a diameter of 41 μm. Polaritons remain in the vicinity of the pump region below the condensation threshold, as shown in Fig. 7-1(a). The asymmetry in the density distribution is largely due to inhomogeneity within the pump intensity profile. Fig. 7-1(c) shows the momentum distribution of the polaritons below the condensation threshold. Because the photonic mode in the microcavity we used has an energy gradient of $\sim$11 meV/mm along the white line in Fig. 7-1(a), there is a net flow of the polariton fluid along this energy gradient, as evidenced by the accumulation of the polariton densities with in-plane wavevector components at $k_x \approx 1\,\mu\text{m}^{-1}$ and $k_y \approx -1\,\mu\text{m}^{-1}$ in Fig. 7-1(c). The cavity gradient can also be identified from the spectrally and spatially resolved emission profile in Fig. 7-1(e) at low pump powers. In this plot, the $x = 0$ μm slice of Fig. 7-1(a) was projected onto the entrance slit of the spectrometer CCD and then spectrally dispersed. As can be seen, there is an energy difference of $\sim$0.5 meV between the emissions at $x = \pm 20$ μm. The propagation effect can also be identified in energy-resolved k-space emission profiles as smeared energy dispersions, which has been reported in Ref. [140] with the same sample structure.

When the excitation density is above the condensation threshold, polaritons propagate over 10 μm toward the center of the trap and form petal states inside the excitation ring. The center position of the pump annulus is plotted in Fig. 7-1(b) as white dashed lines, along with the spatial emission profile from petals. The petals demonstrate nodal structures similar to those of the high-order whispering-gallery modes in lasers, with the periodicity matching the density accumulation at $k_x = 1$
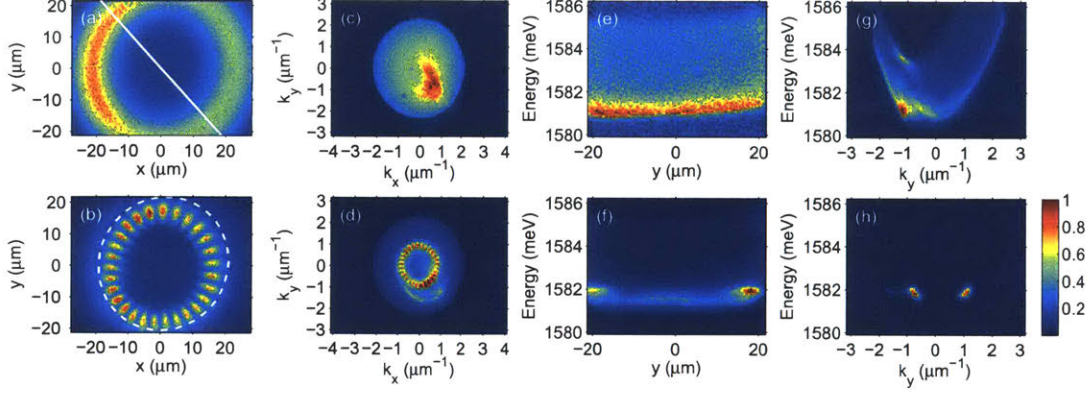
Figure 7-1: Petals in the annular trap with a diameter of 41 μm. (a)-(b) The polariton density distributions below (a) and above (b) condensation threshold in an annular trap. (c)-(d) The polariton momentum distributions below (c) and above (d) condensation threshold. (e)-(f) The energy-resolved polariton density distributions at $x = 0$ below (e) and above (f) condensation threshold. (g)-(h) The energy-resolved polariton momentum distributions at $k_x = 0$ below (g) and above (h) condensation threshold. The white solid line in (a) indicates the direction of the cavity energy gradient (the photon energy decreasing from upper right to lower left), and the white dashed line in (b) shows the center position of the annular pump.

μm^{-1} and $k_y = -1$ μm^{-1}. The petal structure is also observed in momentum space as expected since the condensate is a coherent state and the density distributions in real space and momentum space are Fourier-transform related. As expected, the energy-resolved measurements show far narrower emission spectra from the condensates (f and h) than from polaritons below the condensation threshold (e and g). Above the threshold, petals typically have higher energies than those polaritons that have flowed to the center of the annular trap, as seen in Fig. 7-1(f).

Patterns similar to petals in Fig. 7-1(b) have also been observed in structures with shorter polariton lifetime [103], but were attributed to the interference of two counter-propagating condensates in a channel formed by two concentric rings of excitation light beams. We find that the same patterns can be generated without the need for a channel formed from optical excitation beams. This indicates that the interactions of nonequilibrium condensates, but not the channel, play the most important role in determining the patterns that emerge.

7.2.2 Spatial and spectral distributions of ripples

Unlike petals, ripples are radially confined bouncing-ball modes in the annular trap. In Fig. 7-2(a), we plot the emission profile observed when a 33-μm annulus was used to excite the microcavity. Below the condensation threshold, the distributions of polaritons in real and momentum spaces show very similar signatures to those in the previous case. However, confined ripples appear when the excitation density is above the condensation threshold, as shown in Fig. 7-2(b). Similar patterns have been studied in quantum chaotic systems where they were termed as bouncing-ball modes [221]. In momentum space, we observed two large populations of polaritons at $k_x = \pm 1$ μm^{-1} indicative of a ripple mode, together with several states with smaller but not negligible amounts of polaritons. This suggests that the ripple pattern in Fig. 7-2(b) arises from the interference of these paired momentum states. Figures 7-2(f) and (h) show energy-resolved emission profiles along the vertical slices $x = 0$ and $k_x = 0$ in Figs. 7-2(b) and (d) respectively. The fact that the density at $k_y = 0$ is much higher than those at higher-momentum states can be attributed to the fact that we aligned the $k_x = 0$ slice of Fig. 7-2(d) to the entrance of the spectrometer CCD. Again the emission spectra narrow dramatically above the condensation threshold.

We observe that the high-order condensate states appear at lower thresholds than the lowest-order condensate state at $k_{||} = 0$, unlike the case in Ref. [37], where polaritons are composed of higher fractions of excitons. This confirms that interactions play a very important role in the formation of the lowest-order versus high-order condensate states. Polaritons have $\sim$5% of excitonic fractions in this measurement, and are weakly interacting with each other. At low powers, polaritons flow away from the pump region and meet in the center of the trap, and scattering to the $k_{||} = 0$ state is negligible due to the well known bottleneck effect [142]. As pump power increases, the interactions between reservoir excitons and bottleneck polaritons lead to the formation of metastable petals and ripples at finite momentum ($k_{||} = 1$ μm^{-1} in our case). However, when polaritons have higher excitonic fractions, in particular at resonance, where polaritons are equal mixtures of excitons and cavity photons, the
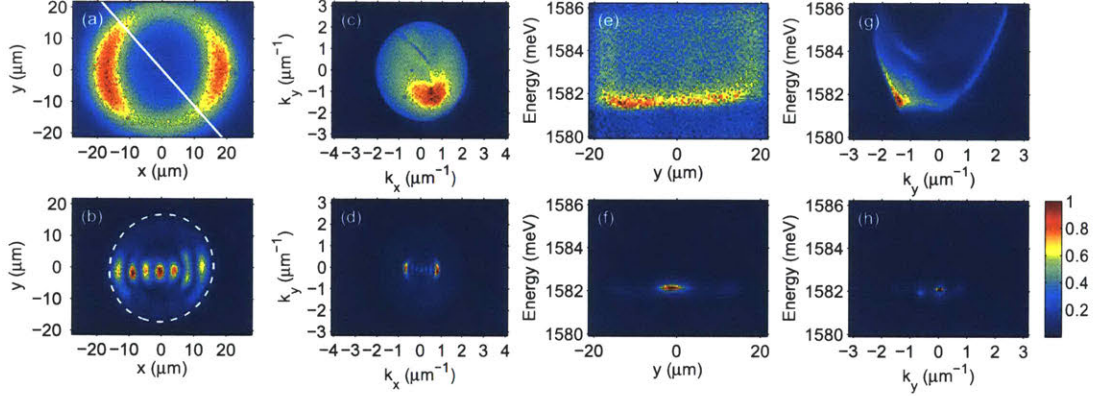
Figure 7-2: Ripples in the annular trap with a diameter of 33 μm. (a)-(b) The polariton density distribution below (a) and above (b) condensation threshold under annular-shaped beam excitation. (c)-(d) Polariton momentum distribution below (c) and above (d) condensation threshold. (e)-(f) Energy-resolved polariton density distribution at $x = 0$ below (e) and above (f) condensation threshold. (g)-(h) Energy-resolved polariton momentum distribution at $k_x = 0$ below (g) and above (h) condensation threshold. The white solid line in (a) indicates the direction of the cavity energy gradient (photon energy decreasing from upper right to lower left), and the white dashed line in (b) shows the center position of the annular pump.

interaction strength increases by approximately two orders of magnitude [37]. This leads to a less severe bottleneck effect [173], and favors the formation of the lowest-order condensate state. On the other hand, a balance of polariton leakage from the pump region against amplification from the reservoir determines that whether ripples or petals are the lowest-threshold mode; this is expanded upon in Section 7.5.

7.3 Stable Mode Switching in Condensates

The condensates can be switched among various petal and ripple states by varying the pump power continuously. In the top panel of Fig. 7-3, we show the integrated the emission intensity in the field of view as a function of pump power. The intensity undergoes several distinct superlinear increases, which are marked by the red lines, and increases by five orders of magnitude when the pump power is increased by a factor of only ~15. The real-space density distributions corresponding to the green dots in the upper panel are shown in Fig. 7-3(a)-(f). We clearly identify that the
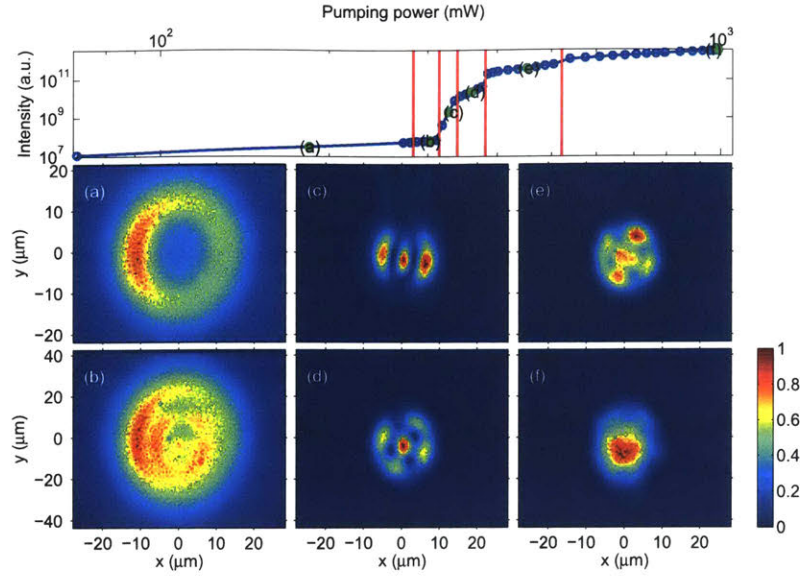
Figure 7-3: Top: the PL intensity as a function of pump power. The red lines indicate boundaries of different quantum states. The green dots are selected pump power levels for which the normalized real-space density distributions of the quantum states are shown in (a)-(f), respectively.

superlinear increases in emission intensity are accompanied by redistributions of the real-space densities, that is, by mode switching.

In Fig. 7-3(a), the excitation level was still below the condensation threshold, and a pattern similar to those in Figs. 7-1(a) and 7-2(a) was observed. Figure 7-3(b) demonstrates the onset of a higher-order state, but it was very difficult to resolve reliably. In Fig. 7-3(c), a two-node ripple mode appears. Figure 7-3(d) and (e) are mixtures of both petals and ripples. Numerical simulations discussed below suggest that petals and ripples coexist at this power due to interactions between these states. As shown in Fig. 7-3(f), when the system was pumped very hard, all high-order quantum states collapsed to the lowest-order condensate state. This power tunability of mode switching not only allows us to distinguish different high-order modes, but also suggests that polariton condensates in the annular trap could be implemented in device applications for stable multistate switches. With better control of the pump power, we believe more states can be accessed independently.

7.4 Phase boundaries of higher-order quantum states

In order to fully characterize the phase boundaries between different quantum states, we recorded the real-space polariton density distributions with excitation ring diameters ranging from 21 μm to 54 μm and pump powers ranging from 50 mW to 1 W. Note that we typically report the pump power before the AOM, and the actual power incident on the sample is 1000 times smaller, given by the duty cycle of the AOM, the shaping efficiency of the SLM and the optical efficiency of the excitation path. Because of the stability of the distributions and the superlinear increases in the emission intensities as shown in Fig. 7-3, we are able to classify different quantum states at different pump conditions. The resulting phase boundaries are shown in Fig. 7-4. In this plot, different colors are assigned to different types of states with distinct spatial distributions. The black-shaded region (0) in the upper left region indicates the uncondensed polaritons. Blue (2) and green (5) stand for ripples and petals, respectively. Both petals and ripples exist in a very narrow range of the phase diagram. This indicates that switching among polariton condensate states in the optical trap is very sensitive and reliable. The different regions of the staircase structure in the phase diagram show modes with different numbers of nodes that were observed with incremented values of the excitation ring size and power. The lowest-order condensate states, coded as red (7), occupy the lower right region of the phase map. The rest of the colors indicate patterns that are mixtures of high-order states, similar to those shown in Fig. 7-3(d) and (e).

Based on this phase diagram, we can see that as the excitation density and ring size are increased, ripples and petals appear successively as the lowest-threshold modes, and the phase boundary between the lowest-threshold modes and the uncondensed polaritons is approximately linear. Both features will be explained in the following section. The number of lobes in either petals or ripples can be easily tuned by changing the pump parameters, as shown in Fig. 7-4(b)-(e). This measured phase diagram should serve well to calibrate the implementation of exciton-polaritonic multistate switches using high-order condensate states.
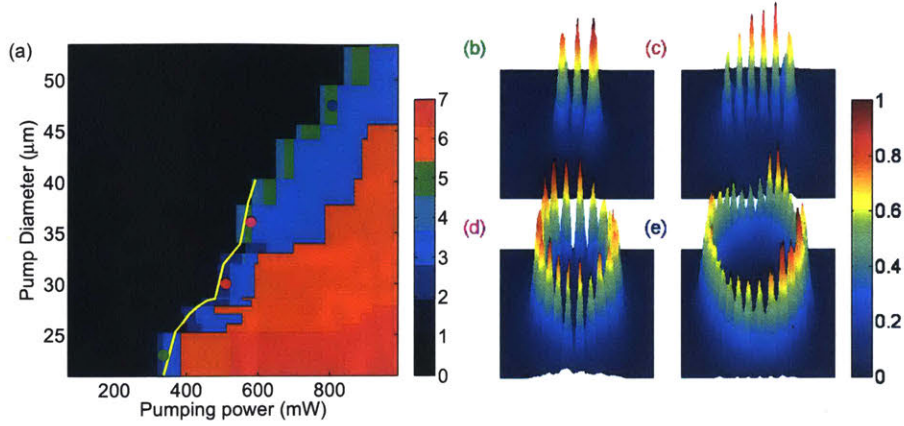
Figure 7-4: (a) Measured phase boundaries for condensate modes in annular optical traps. The yellow solid line is the simulated boundary for the lowest-threshold mode. Different colors correspond to different types of states, with blue, green and red indicating ripples, petals and lowest-order condensate state. The black-shaded region is uncondensed polaritons, and the other colors are mixtures of modes similar to those in Fig. 7-3(d) and (e). The spatial distributions of the modes indicated by colored dots are shown in (b)-(e) correspondingly.

7.4.1 Spatial distributions of mixed modes in the optical trap

Because of the interactions among high-order modes, a large set of mixed modes shows up in the phase diagram. In Fig. 7-5, we plot the spatial distributions for 12 mixed modes whose positions in the phase diagram are marked in Fig. 7-6. As can be seen, modes (1)-(3) have both ripple and petal characteristics, and modes (4)-(7) and (9)-(11) are petal-like and are quantized in the azimuthal direction, although the emission intensities from peaks and nodes are comparable. Modes (8) and (12) are ripple-like. Based on our numerical simulations, mixed modes are direct consequences of interactions between high-order modes with very close thresholds, rather than being artifacts from time-integrated measurements.

7.4.2 Evolution of node numbers of ripple and petal states in the optical trap

The number of nodes in either ripple or petal states can be varied by adjusting the pump diameter. The pump power also needs to be increased in order to reach
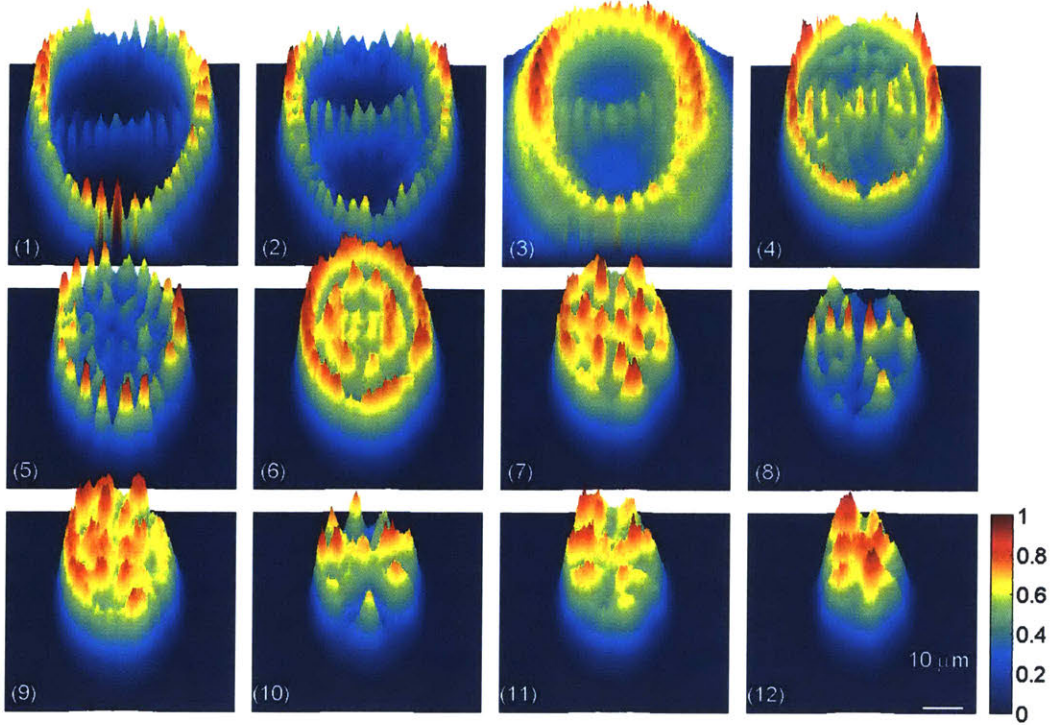
Figure 7-5: (1)-(12) Mixed modes for selected points in the phase diagram plot shown in Fig. 7-6. The scale bar in (12) indicates 10 μm.

condensation threshold as the diameter of the pump increases. In Fig. 7-7, we show the spatial distributions of 12 distinct modes with various nodes. As can be seen, by changing the pump parameter, we could switch from a 2-node ripple state up to an 8-node ripple state continuously. Similar switching behavior can also be realized by using petals as shown in Figs. 7-7(8)-(12).

7.5 Theory and Numerical Simulation of Pattern Formation

7.5.1 Gross-Pitaevskii equation and linearization

We use a generalized Gross-Pitaevskii equation (GPE) to describe the dynamics of polaritons under incoherent pumping. In this standard approach, the nonlinear in-
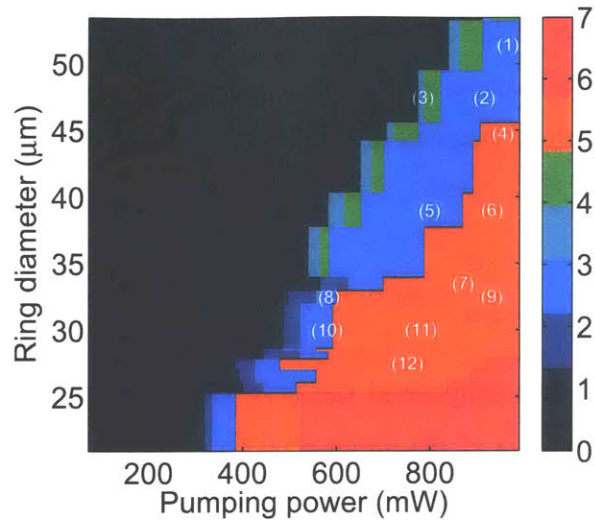
Figure 7-6: Phase diagram indicating the positions of the modes whose spatial distributions are shown in Fig. 7-5.
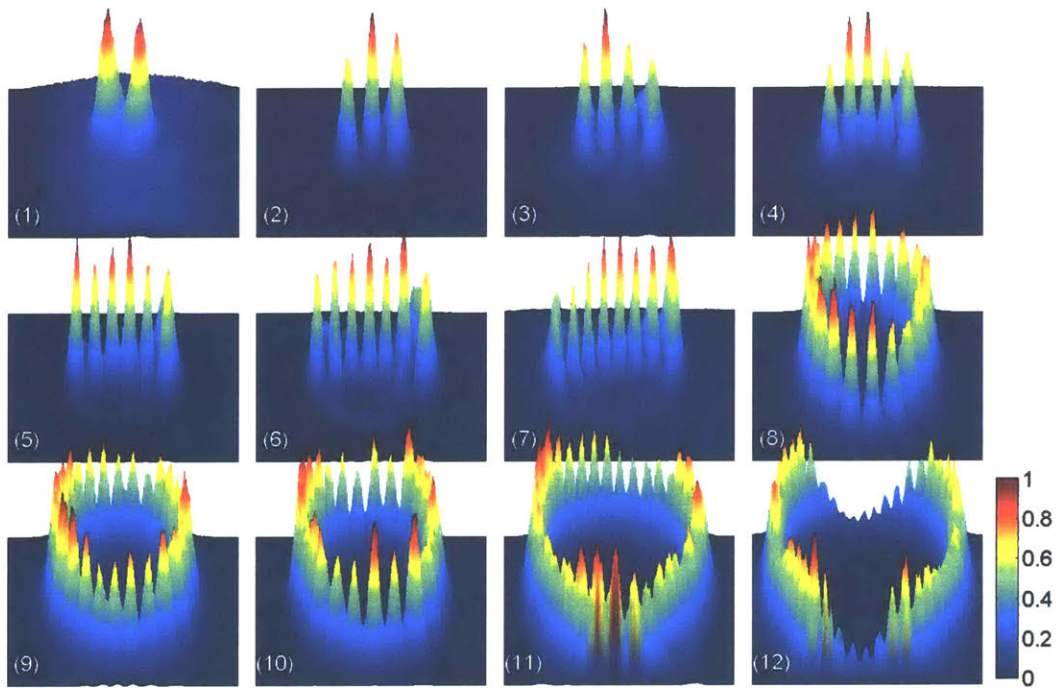
Figure 7-7: (1)-(12) Spatial distributions of ripple and petal states with different numbers of nodes obversed when the pump parameters are varied.

teractions of polaritons within the condensed fraction are treated at the mean-field level, while pumping and losses are introduced as complex-valued terms so that the generalized GPE for the dynamics of the condensate wavefunction $\Psi(\mathbf{r}, t)$ has the form:

$$i\frac{\partial \Psi}{\partial t} = \left[-\frac{\nabla^2}{2m} + g_R n_R + \frac{i}{2}\left(R n_R - \gamma_c \right) \right] \Psi + g|\Psi|^2 \Psi \qquad (7.1)$$

where for clarity we have suppressed the $(\mathbf{r}, t)$ dependence of the polariton wavefunction and the density n_R of the pump-generated exciton reservoir. This reservoir gives rise to a repulsive term describing the interaction of condensate polaritons with reservoir excitons, with a strength of g_R, together with an amplification of the condensed fraction via stimulated scattering from the reservoir at a rate of R. This latter gain contribution together with the inclusion of polariton mirror loss at rate γ_c make the effective generator describing condensate dynamics non-Hermitian in this case. Finally, the polariton-polariton repulsion within the condensate appears as the nonlinear term $\propto g$ at the mean-field level. The dynamics of the pump-induced reservoir must also be accounted for by a dynamical equation of the form:

$$\frac{\partial n_R}{\partial t} = Pf(\mathbf{r}) - R n_R |\Psi|^2 - \gamma_R n_R \qquad (7.2)$$

Here P and $f(\mathbf{r})$ are the pump strength and spatial profile, respectively. The aforementioned scattering from the exciton reservoir into the condensate at the rate R causes a depletion of the reservoir, which is encapsulated in the second term on the right-hand side. Reservoir losses that occur via mechanisms other than scattering into the reservoir (e.g. recombination losses) are described by γ_R.

For pumping powers below the condensation threshold, the system has a steady state with a pump-generated exciton density and an uncondensed polariton population. The steady state reservoir density in this regime can be obtained after linearizing Eq. (7.2) by dropping nonlinear terms of order $|\Psi|^2$; in this steady-state regime, the

exciton reservoir density adiabatically follows the pump:

$$n_R(\mathbf{r}, t \to \infty) = \frac{P}{\gamma_R} f(\mathbf{r}) \tag{7.3}$$

Below the condensation threshold, a linearization of the GPE is also valid; we can re-place $n_R(\mathbf{r}, t)$ by its linearized steady state value, and neglect the nonlinear polariton-polariton interactions $\propto g$. This yields the linearized GPE in Eq. (7.1) for condensate dynamics .

7.5.2 Linear threshold modes

We now analyze steady-state condensate formation in the linearized regime. In par-ticular, if we consider a single-frequency steady-state ansätz for the condensate wave-function:

$$\Psi(\mathbf{r}, t) = \varphi_n(\mathbf{r}) e^{-i\omega_n t}, \tag{7.4}$$

the linearized GPE in Eq. (7.1) becomes:

$$\mathcal{H}_{\mathrm{L}}(P)\varphi_n(\mathbf{r}) = \left[-\frac{\nabla^2}{2m} + \frac{g_R}{\gamma_R} P f(\mathbf{r}) + \frac{i}{2}\frac{R}{\gamma_R} P f(\mathbf{r}) - \frac{i}{2}\gamma_c \right] \varphi_n(\mathbf{r}) = \omega_n \varphi_n(\mathbf{r}) \tag{7.5}$$

The condensate wavefunction for a single-frequency ω_n condensate is therefore the nth eigenmode of the generator of the linearized dynamics, $\mathcal{H}_{\mathrm{L}}(P)$. We require ω_n to be a purely real frequency for the steady-state solution to correspond to a nontrivial condensate mode.

Let us now discuss how this requirement determines the power threshold for a given spatial mode. For simplicity, we rewrite the above eigenproblem in the form:

$$\left[-\nabla^2 + sP f(\mathbf{r}) \right] \varphi_n(\mathbf{r}) = q^2 \varphi_n(\mathbf{r}) \tag{7.6}$$

where we have introduced the pump-induced potential s:

$$\frac{s}{2m} = \frac{1}{\gamma_R}\left(g_R + \frac{i}{2}R\right) \tag{7.7}$$

and the 'wavevector' $q(\omega_n)$ is defined by:

$$\frac{q^2(\omega_n)}{2m} \equiv \omega_n + \frac{i}{2}\gamma_c \tag{7.8}$$

To determine the eigenmodes of $\mathcal{H}_{\mathrm{L}}(P)$, the above eigenproblem must be formulated as an appropriate boundary value problem (BVP). The following choice is made:

$$\left[-\nabla^2 + sPf(\mathbf{r})\right]\varphi_n(\mathbf{r}) = q^2(\omega_n)\varphi_n(\mathbf{r}) \ , \ \mathbf{r} \in \mathcal{P}$$
$$-\nabla^2\varphi_n(\mathbf{r}) = q^2(\omega_n)\varphi_n(\mathbf{r}) \ , \ \mathbf{r} \notin \mathcal{P} \tag{7.9}$$

where $\mathcal{P}$ is the region enclosed by the outer edge $\partial\mathcal{P}$ of the pump. Note here that we impose an 'outgoing' boundary condition with wavevector $q(\omega_n)$ at the pump edge $\partial\mathcal{P}$, as opposed to the more usual case of considering a boundary far from the pump region where the condensate wavefunction is vanishingly small and standard Dirichlet boundary conditions can be employed. For the large condensate sizes considered here, the latter approach would require simulating a very large spatial grid, making computation times inconveniently long. Our approach allows the use of a minimally relevant grid size. This occurs at a relatively minor expense: the outgoing wavevector imposed via this boundary condition depends on the unknown eigenvalue ω_n, and this BVP therefore needs to be solved self-consistently. To do so, we fix the outgoing wavevector by choosing an outgoing frequency Ω:

$$\left[-\nabla^2 + sPf(\mathbf{r})\right]\varphi_n(\mathbf{r}) = q^2(\omega_n)\varphi_n(\mathbf{r}) \ , \ \mathbf{r} \in \mathcal{P}$$
$$-\nabla^2\varphi_n(\mathbf{r}) = q^2(\Omega)\varphi_n(\mathbf{r}) \ , \ \mathbf{r} \notin \mathcal{P} \tag{7.10}$$

It is now straightforward to solve this BVP for a range of (increasing) values of the pump power at a fixed Ω. As a result, one obtains a set of eigenmodes $\{\varphi_n(\mathbf{r})\}$ and

214
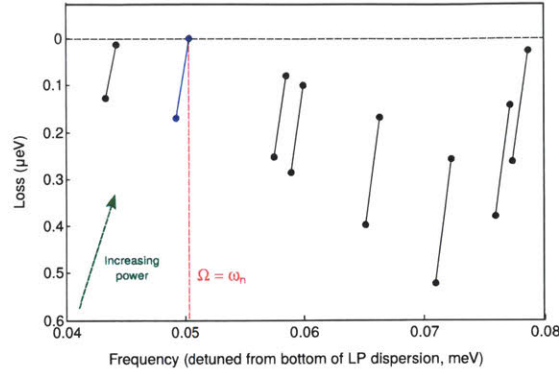
Figure 7-8: Flow of (complex) eigenvalues of the linear non-Hermitian generator $\mathcal{H}_{\mathrm{L}}(P)$ as a function of pump power P across the complex plane, computed for a fixed outgoing frequency Ω. The flow direction is indicated by the arrow. Eigenvalues approach the real axis from below as pump powers are increased. The lowest threshold mode is indicated in blue. It reaches the real line (loss = 0) for the smallest pump power, and has a real frequency ω_n equal to the imposed outgoing frequency Ω.

eigenfrequencies $\{\omega_n(P)\}$ of $\mathcal{H}_{\mathrm{L}}(P)$. These generally complex frequencies $\{\omega_n(P)\}$ flow across the complex plane as the pump power is varied; an example of this flow is shown in Fig. 7-8. For a certain pump power P_n, the nth eigenfrequency ω_n crosses the real axis (becomes real). The imaginary part of ω_n represents net loss, so its becoming zero implies that gain overcomes polariton loss at this pump power, and the associated eigenmode is an unstable fluctuation around the uncondensed polariton state. Furthermore, if the (now real) frequency is also equal to the imposed outgoing frequency, that is $\omega_n = \Omega$, the wavevector $q(\omega_n)$ is equal both inside and outside the pump region $\mathcal{P}$. The self-consistency condition is therefore simultaneously fulfilled, and the corresponding nth eigenmode $\varphi_n(\mathbf{r}; \omega_n, P_n)$ represents a true condensate mode with a real frequency ω_n and a linearized power threshold P_n. By varying the outgoing frequency Ω, and computing eigenvalues as a function of pump power, a set of such linear threshold modes $\{\varphi_n(\mathbf{r}; \omega_n, P_n)\}$ can be obtained.

215

7.5.3 Continuity equation and linear threshold formula

From the linearized dynamical equation for the condensate wavefunction, it is possible to obtain an equation for the dynamics of the condensate density, $|\Psi|^2$. In particular,

$$\frac{\partial |\Psi|^2}{\partial t} = \Psi^* \frac{\partial \Psi}{\partial t} + c.c. \tag{7.11}$$

From the generalized GPE in Eq. (7.1), it is easily found that:

$$\Psi^* \frac{\partial \Psi}{\partial t} = \frac{i}{2m} \Psi^* \nabla^2 \Psi + \left\{ -ig_R n_R - ig|\Psi|^2 + \frac{1}{2}(Rn_R - \gamma_c) \right\} |\Psi|^2 \tag{7.12}$$

and therefore,

$$\frac{\partial |\Psi|^2}{\partial t} = \frac{i}{2m} \left(\Psi^* \nabla^2 \Psi - \Psi \nabla^2 \Psi^* \right) + Rn_R |\Psi|^2 - \gamma_c |\Psi|^2 \tag{7.13}$$

The first term on the right hand side has the form of the divergence of a probability current; this can be made more explicit by defining the probability current $\vec{j}$ as:

$$\vec{j} = \frac{i}{2m} \left(\Psi \vec{\nabla} \Psi^* - c.c. \right) \tag{7.14}$$

following which the condensate density dynamics is governed by the equation:

$$\frac{\partial |\Psi|^2}{\partial t} = Rn_R |\Psi|^2 - \nabla \cdot \vec{j} - \gamma_c |\Psi|^2 \tag{7.15}$$

which has the well-defined form of a continuity equation. In particular, the above equation can be put into a more practical form by integrating over the area $\mathcal{P}$ of the region enclosed by the outer pump edge,

$$\frac{\partial}{\partial t} \int_{\mathcal{P}} d^2 \mathbf{r} \, |\Psi|^2 = R \int_{\mathcal{P}} d^2 \mathbf{r} \, n_R |\Psi|^2 - \oint_{\partial \mathcal{P}} \vec{j} \cdot d\vec{s} - \gamma_c \int_{\mathcal{P}} d^2 \mathbf{r} \, |\Psi|^2 \tag{7.16}$$

where the divergence theorem allows the term involving $\vec{j}$ to be rewritten as a flux integral. This equation has a simple interpretation: any increase in the total number of polaritons ($\propto \int_{\mathcal{P}} d^2 \mathbf{r} \, |\Psi|^2$) within the pump region comes from amplification via

the exciton reservoir, at a rate of R. Losses in the polariton number can be attributed to either the mirror loss γ_c or a leakage of the condensate from the pump edge. Since we integrate within the outer pump edge $\partial \mathcal{P}$, beyond which by definition no source of polariton formation exists, there can be no incoming probability current that would increase the polariton number within the pump region.

Now, we narrow our focus to the linearized regime, where the reservoir density $n_R = Pf(\mathbf{r})/\gamma_R$ is the same as shown earlier. Furthermore, we consider a single mode solution such that $\Psi(\mathbf{r}, t) = \varphi_n(\mathbf{r}; \omega_n, P_n)e^{-i\omega_n t}$, where $\varphi_n(\mathbf{r}; \omega_n, P_n)$ is the eigenmode of $\mathcal{H}_{\mathrm{L}}(P_n)$ that has (real) eigenfrequency ω_n. For simplicity, we suppress the parameters defining φ_n in the following discussion. With this ansätz, the condensate density is time-independent and the above continuity equation reduces to the form

$$\frac{R}{\gamma_R}P \int_{\mathcal{P}} d^2\mathbf{r}\; f(\mathbf{r})|\varphi_n|^2 = \oint_{\partial \mathcal{P}} \vec{j}[\varphi_n] \cdot d\vec{s} + \gamma_c \int_{\mathcal{P}} d^2\mathbf{r}\; |\varphi_n|^2 \tag{7.17}$$

The probability current $\vec{j}(\varphi_n)$ is now evaluated for the eigenmode φ_n. Defining the condensate density ρ_n, pump overlap $\mathcal{G}_n$, and in-plane loss γ_n respectively as the following:

$$\rho_n = \int_{\mathcal{P}} d^2\mathbf{r}\; |\varphi_n|^2\;, \quad \mathcal{G}_n = \frac{1}{\rho_n}\int_{\mathcal{P}} d^2\mathbf{r}\; f(\mathbf{r})|\varphi_n|^2\;, \quad \gamma_n = \oint_{\partial \mathcal{P}} \vec{j}[\varphi_n] \cdot d\vec{s} \tag{7.18}$$

we can recover the linear threshold formula:

$$\frac{P_n}{P_0} = \frac{1 + \gamma_n/(\rho_n\gamma_c)}{\mathcal{G}_n} \equiv \frac{1 + \Gamma_n}{\mathcal{G}_n} \tag{7.19}$$

where P_n is the linear threshold power for the nth mode, and $P_0 = (\gamma_c\gamma_R)/R$.

7.5.4 Competition between petals and ripples

Based on Eq. (7.19), for a given mode, the threshold is determined by: (i) relative loss Γ_n, which is defined as the ratio of in-plane loss γ_n to the total mirror loss $\rho_n\gamma_c$, the former being the flux of probability current $\vec{j}$ leaking across the outer pump edge $\partial \mathcal{P}$ (see Fig. 7-9(a)), and (ii) $\mathcal{G}_n$, a dimensionless measure of the overlap between
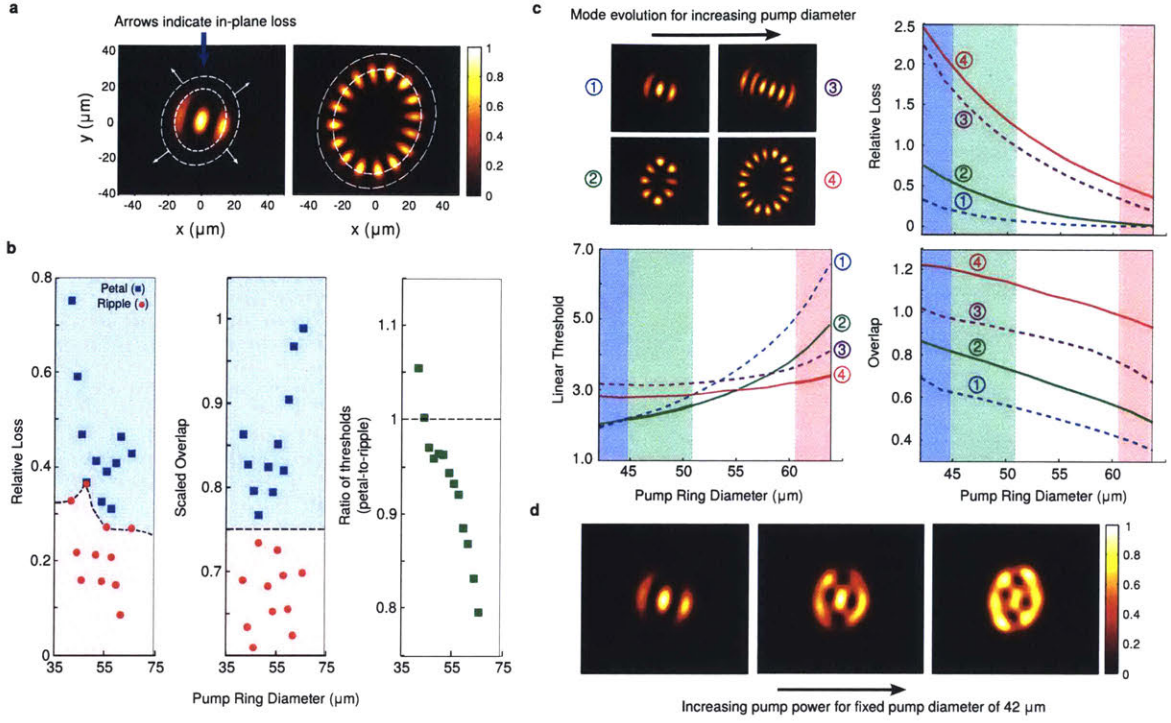
Figure 7-9: (a) Lowest-threshold modes for pump diameters 21 μm and 33 μm; white dashed lines indicate the inner and outer pump edges. (b) Loss-overlap characteristics for *lowest threshold* petal and ripple modes, and petal-to-ripple threshold ratio, versus pump diameter. Overlap is scaled by a dimensionless factor $\propto$ pump area A to highlight the separation between ripple and petal modes. (c) Loss, overlap, and threshold evolution for two ripple modes (dashed lines 1 and 3) and twp petal modes (solid lines 2 and 4) shown in the top panel. Red (blue) shaded area denotes pump diameters where ripple (petal) modes have lowest threshold. A thick line in the threshold plot indicates the lowest threshold mode; in the region with no thick lines, a mode other than those considered here has lowest threshold. (d) Simulation of condensate density for increasing pump power at a fixed pump diameter of 21 μm.

the mode and the pump within the region $\mathcal{P}$ enclosed by this pump edge. The lowest-threshold mode minimizes Eq. (7.19) by maximizing overlap with the pump to benefit from amplification, while still having low density near $\partial\mathcal{P}$ to reduce the relative loss Γ_n. Note that as relative loss for a mode becomes smaller, its overlap becomes increasingly important in determining the threshold.

By using the experimental pump profile as $f(\boldsymbol{r})$ in the nonlinear Gross-Pitaevskii equation, the petals and ripples observed in the experiment can be qualitatively reproduced. Fig. 7-10 shows the resulting polariton density distributions. The pump
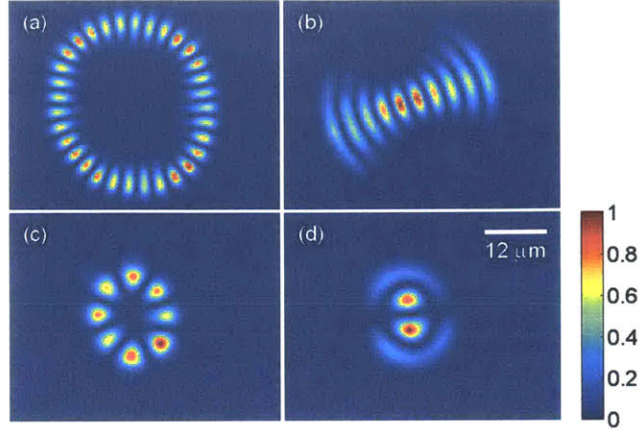
Figure 7-10: Simulated patterns using the generalized Gross-Pitaevskii equation.

profile that generated the pattern in Fig. 7-7(11) was used in the simulations for Figs. 7-10(a) and (b), and the number of lobes in each case was exactly reproduced using this method. The relative intensities of the peaks along the azimuthal direction were also qualitatively captured by this model. In the simulation, a ripple state showed up at a lower energy ($\sim$0.05 meV lower) but with significantly higher pump density ($\sim$50%). This mode was not observed in the experiment, due to the limited pump power we have. By using the pump profile corresponding to that of Fig. 7-7(2), the reproduced polariton density distributions agreed well with those observed in the experiments, shown in Fig. 7-10(c) and (d). Additionally, another two patterns were identified, and they have energies similar to the first mode (within 0.01 meV) with a difference in the pump threshold of less than 2%.

We study the linear modes of $\mathcal{H}_{\mathrm{L}}(P)$ for a range of pump diameters; the loss-overlap characteristics for the lowest-threshold ripple and petal modes are plotted in Fig. 7-9(b). While petal modes have stronger overlap and higher loss than ripple modes, their thresholds decrease below that of ripple modes as the pump diameter increases. To understand this, we focus for clarity on one low-order and one higher-order mode for petals (labeled 2 and 4) and ripples (1 and 3), and consider their loss, overlap, and threshold evolution as a function of pump diameter in Fig. 7-9(c). Crucially, we see that the relative loss decreases as the pump diameter increases. This

is because the in-plane loss scales as the circumference of the pump profile and the mirror loss scales as the area of the condensate mode, and the net dependence of the relative loss is $1/R$. Due to this effect, there exists for each mode a large enough pump diameter at which its relative loss is small enough such that the overlap $\mathcal{G}_n$ primarily determines its threshold. In this competition, petal modes have an advantage over ripple modes. Therefore, below a critical pump diameter petals are typically too lossy to have lower thresholds than ripples, even though their pump overlap is stronger. Beyond this critical diameter, Γ_n for petals decreases enough for their stronger overlap to pull their thresholds down below those of the competing ripple modes. For annular excitation profiles, a transition diameter will always exist due to this decrease of Γ_n; the particular diameter depends on details of the profile. By extension, for higher-order states with higher relative losses (see Fig. 7-9(c)), larger pump diameters are needed than those for lower-order states until Γ_n decreases sufficiently to encourage condensation into these modes, in agreement with observations here. Finally, we note that the overlap $\mathcal{G}_n$ decreases with growing pump diameter since the pump density $Pf(\mathbf{r})$ goes down as $1/R$ for a radius R annular pump with fixed FWHM. From Eqs. (7.19) and (7.18), the resultant decrease in $\mathcal{G}_n$ increases P_n^{th} linearly with pump diameter. This is apparent from the simulated lowest threshold boundary, in good agreement with the experimental phase diagram shown in Fig. 7-4.

Going beyond the condensation threshold requires full simulation of the nonlinear GPE over a large spatio-temporal grid. The large condensate sizes (up to $\sim$50 μm) observed in the current work, together with short polariton wavelengths ($\sim$1 μm), require fine spatial resolution, and make such simulations very computationally expensive. We circumvent this issue by expanding the condensate wavefunction in a pump power-dependent, non-Hermitian basis set $\{\varphi_n(\mathbf{r}; P, \omega_n)\}$ that accounts for the spatial complexity of the linearized condensate problem, with time-dependent coefficients. For discrete values of $P = P_n$, one mode in each set reduces to the corresponding threshold mode introduced before. Note that in general ω_n is complex, but for that particular threshold mode it is on the real axis. This reduces the full nonlinear GPE and reservoir dynamical equation to a set of coupled ODEs, an effective

nonlinear coupled-mode theory for reservoir-condensate dynamics. Applying to the specific case of a pump of diameter 42 μm, the coupled-mode theory reveals mixing of the lowest-threshold modes beyond threshold, when polariton-polariton interactions within the condensate become important. In particular, the coexistence of petal and ripple states shown in Fig. 7-9(d) was reproduced using this theory.

7.6 Conclusion and Outlook

We have seen the formation of high-order condensate states, including ripples, petals and their coherent mixtures, under non-resonant excitations, with a well defined phase diagram in the pump parameter space. Ripples are confined bouncing-ball modes while petals are whispering-gallery modes in the trap. The all-optical trapping allows facile switching among these condensate states in the annular trap, accompanied by superlinear increases in emission intensities.

The measured patterns bear some similarities to the multiple modes seen in standard vertical-cavity, surface-emitting lasers (VCSELs), e.g. the petal patterns seen in Ref. [222]. However, in typical lasers and VCSELs, the systems hop uncontrollably between different modes, leading to unwanted noise [223]). The nonlinear interactions in polariton condensate systems stabilize the modes to resist multimode behavior. This means that this system acts effectively as a multistable optical switch, in which transitions between states can be effected by small changes of the input light beam.

Chapter 8

Future Directions

Now that we have a system that has long enough lifetime to allow polaritons to fully thermalize and form equilibrium Bose-Einstein condensates, and we also know that polaritons are strongly interacting, it would not be a giant leap for us to apply coherent control to this fully quantum-mechanical system and study the dynamics between interacting condensates. In this Chapter, we will discuss possible directions that can be pursued in the future following the work of this dissertation.

8.1   Berezinskii-Kousterlitz-Thouless (BKT) Phase Transition

The long lifetime of our microcavity structure allows polaritons to reach full thermalization before coupling out of the cavity, leading to the formation of Bose-Einstein condensates in thermal equilibrium. In principle, it could also support the BKT phase transition in thermal equilibrium, which is unique to 2D systems [17]. As is well known, infinite 2D systems do not support BEC, but the BKT transition is possible. In physics, the BKT transition is a transition from bound vortex-antivortex pairs at low temperature to unpaired vortices and antivortices at the critical temperature.

At low enough temperature, the first-order spatial correlation function $g^{(1)}(s)$ decays slowly so that superfluid properties can be observed locally. In particular,

considering a small enough contour so that the superfluid phase can be defined at all points on it, the phase change $\delta\phi$ along the contour can only be a multiple of 2π. If $\delta\phi = 0$, a superfluid current will flow, which decays when $\delta\phi$ changes by 2π. This change can only occur when a quantized vortex moves across the contour, which is possible when free vortices exist in the system. Thus, a state with free vortices is non-superfluid. On the other hand, at very low temperature, vortices and antivortices gather in clusters of zero total vorticity. When one cluster moves across the contour, the total phase change $\delta\phi$ does not change, so supercurrents do not dissipate. This is the essential idea behind the BKT transition.

The BKT transition can also be understood from a thermodynamic perspective. In a 2D superfluid, the energy cost for the excitation of a quantized vortex [44] is

$$\Delta E = \pi \rho_{2s} \left(\frac{\hbar^2}{m} \right) \ln \frac{R}{r_c} \tag{8.1}$$

whereas the entropy of the system will increase by an amount of

$$\Delta S = 2k_B \ln \frac{R}{r_c} \tag{8.2}$$

accompanied by the formation of the vortex. Here R and r_c are the sizes of the system and vortex core, respectively, and ρ_{2s} is the 2D superfluid mass density. The free energy of the system could be lowered provided that

$$\Delta E - T\Delta S \leq 0 \tag{8.3}$$

Working out the algebra, we obtain

$$T \geq \frac{\pi}{2k_B} \rho_{2s} \left(\frac{\hbar}{m} \right)^2 = T_c \tag{8.4}$$

where the critical condition can be rewritten as

$$n_{2s} \lambda_T^2 = 4 \tag{8.5}$$

224

Here n_{2s} is the number density of the superfluid, and λ_T is the thermal de Broglie wavelength at the critical temperature. As can be seen, the BKT transition happens at similar but slightly higher temperatures than BEC.

It is straightforward to observe the BKT transition from a trapped BEC by spatial interferometry. Due to the existence of the vortex and antivortex, the wavefunction of the BKT state experiences phase singularities, which translates to a fork-like structure in the interferogram. However, the phase of the BEC state is locked to be uniform across the wavepacket. Furthermore, the first-order spatial correlation function $g^{(1)}(s)$ can be exploited to identify the BKT state. $g^{(1)}(s)$ of the BKT phase is predicted to be

$$g^{(1)}(s) \approx \left(\frac{s_T}{s}\right)^\nu \tag{8.6}$$

where

$$s_T = \frac{\lambda_T^2}{2\pi\xi} \tag{8.7}$$

and the exponent ν is temperature-dependent

$$\nu = \frac{T}{4T_c} \tag{8.8}$$

If the temperature of the system is T_c, $1/4$ is expected for the exponent. On the other hand, the first-order spatial correlation function of the BEC state follows a power decay with a temperature-independent exponent. By examining the short- and long-distance behaviors of the first-order spatial correlation function of the emission from a large condensate in short-lifetime samples, Roumpos et al. [224] reported that the BKT phase order survives in open-dissipative systems, particularly in exciton-polaritons. However, the observed exponent of the power law was in the range of 0.9 to 1.2, far away from the equilibrium prediction 0.25. Possible explanations include the nonequilibrium nature of the condensates and nonuniform spatial distributions of the condensates. It would be intriguing to unravel these different effects by performing

similar measurements using our long-lifetime microcavity structure.

8.2   Tonks-Girardeau Gas in 1D Confinement

Since polaritons are strongly interacting, the transition to Tonks-Girardeau gas might be possible in a 1D confinement. In physics, a Tonks-Girardeau gas (TGG) is a Bose gas in which the confined bosonic particles behave as if they were non-interacting fermions due to strong repulsive interactions. It is named after physicists Marvin D. Girardeau and Lewi Tonks. Strictly speaking, this is not a Bose-Einstein condensate as it does not demonstrate any of the characteristics, such as the off-diagonal long-range order or a unitary two-body correlation function, even in the thermodynamic limit.

The gradual transition between the BEC regime and the TGG regime is characterized by the dimensionless parameter γ, which is defined as

$$\gamma = \frac{E_{int}}{E_{kin}} \tag{8.9}$$

where E_{int} and E_{kin} are the interaction energy and kinetic energy of underlying particles, respectively. As illustrate in Fig. 8-1, when $\gamma \ll 1$, the healing lengths of particles are much larger than the interparticle spacing, and the system tries to minimize the kinetic energy, leading to the formation of BEC. When $\gamma \gg 1$, the healing length is much smaller than the interparticle spacing, the system tries to minimize the interaction energy, and particles become localized, forming TGG.

For microcavity polaritons, we know the interaction energy is on the order of 0.1 meV, as evidenced by the blueshfit of the polariton ground state energy. By appropriately engineering the potential, the kinetic energies of polaritons can be reduced to 1 meV or even less. Hence, $\gamma \geq 1$ could possibly be achieved for the preparation of a TGG. In the TGG regime, the sound velocity c scales linearly with the particle
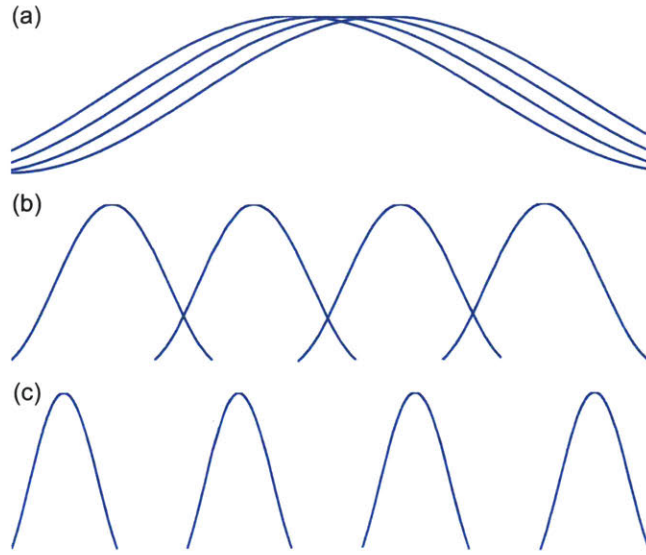
Figure 8-1: Schematic Illustration of the transition from BEC to TGG. (a) When $\gamma \ll 1$, particles are in the BEC state, forming a single-particle wave packet. (b) As γ increases, the size of the single-particle wavefunction decreases. (c) In the regime of $\gamma \gg 1$, TGG forms. Bosons that originally form BEC now behave like fermions, and become spatially distinct.

density n, explicitly expressed as

$$c = \frac{\pi \hbar n}{m} \tag{8.10}$$

whereas the sound velocity scales as the square root of underlying particle density in the BEC regime. Hence the scaling law can be used to determine if the system is in the TGG regime. The first-order spatial correlation function $g^{(1)}(s)$ can also be exploited to identify the TGG. $g^{(1)}(s)$ of the TGG is predicted to have an inverse square root dependence

$$g^{(1)}(s) = \sqrt{\frac{\xi}{s}} \tag{8.11}$$

where ξ is the healing length. As discussed in Chapter 1, for a 1D BEC, the dependence is exponential.

8.3 Trion-polariton Condensates and Bose-Fermi Mixtures

One of the striking features of polaritons is that their extremely light effective mass can allow quantum phenomena, in particular superfluidity, at much elevated temperatures up to room temperature, and thus could be possibly exploited for frictionless energy transport at easily obtainable temperatures. It would be more intriguing if charged polaritons, i.e., trion-polaritons, undergo superfluidity. Trions are two holes and one electron or two electrons and one hole, depending on the doping condition of the host semiconductor material, and trion-polaritons are light-matter mixtures, similar to exciton-polaritons. Superfluidity of charges will be superconducting, and if it is possible with trion-polaritons, room-temperature superconducting is not impossible.

Trion-polaritons are formed in a semiconductor microcavity with doped quantum wells. The presence of charges inside the quantum well could interact with the polaritons, and form a new composite system provided that the charge-polariton coupling is faster than the decay time of charges. Recently, the optical properties of trion-polaritons have been investigated in detail theoretically [225, 226].

On the other hand, conventional superconductivity occurs at low temperatures and can be described within the framework of the BCS theory [84], which relies on the formation of Cooper pairs. Cooper pairs are two electrons on top of the Fermi sea that are bound through phonon-mediated interactions, however small the attractive interaction between them [227, 228]. The phonon-mediated interaction can be partially understood as lattice screening of Coulomb interactions between the paired electrons. In cuprate-based high-T_c superconductors, electron pairing is also thought to be realized through a mediating boson, although probably not the phonon [229]. Excitons have been proposed as suitable mediating bosons to achieve high critical temperatures of superconductivity in specially designed heterostructures [230] (see Ref. [231] for a review). As compared to phonons, the characteristic cutoff energy above which the attractive character of the interaction is lost for the excitons is several orders of magnitude higher and the critical temperature is therefore expected

to be significantly increased with respect to the conventional BCS superconductors [230].

Since polaritons are bosons, they have been predicted to mediate the pairing of electrons in a microcavity structure where a two-dimensional electron gas is sandwiched between two undoped quantum wells [232]. In the past few years, two-dimensional semiconductor materials, such as MoS_2 and WS_2, have emerged as possible candidates for the realization of trion-polariton condensation. Given the two-dimensionality of the material, the phonon-electron interaction is significantly enhanced through the out-of-plane coupling. On the other hand, it has been demonstrated that the strong coupling of excitons in a two-dimensional material and light in a microcavity is possible [233], and a Rabi splitting of about 50 meV was realized, indicating the possibility of room-temperature condensation. As the next step, appropriate doping of charges can be introduced in bare quantum wells, and followed by a detailed investigation of the effects of charges on the light-matter coupling. Under appropriate conditions, polaritons, and possibly phonons and excitons could mediate the pairing of charges, leading to the formation of trion-polariton condensates.

8.4 Quantum Simulation with Polaritons and Their Condensates

Bose-Einstein condensation in optical lattices has been proved as a powerful tool to study the dynamics of complicated many-body systems. The observation of the Higgs boson in a superfluid due to spontaneous symmetry breaking [18] is one of the examples. On the other hand, the light-matter dual nature of polaritons permits the control and probing of the system in a direct way by examining the properties of those photons that couple out of the cavity. It is also straightforward to measure the spectral functions, $A(k, \omega)$, of polaritons, which can provide insights into the dynamics of many-body interactions in polariton systems. For cold atoms, the equilibrium occupation numbers can be measured [234], but the spectral functions are not readily

<div align="center">(a)   (b)</div>
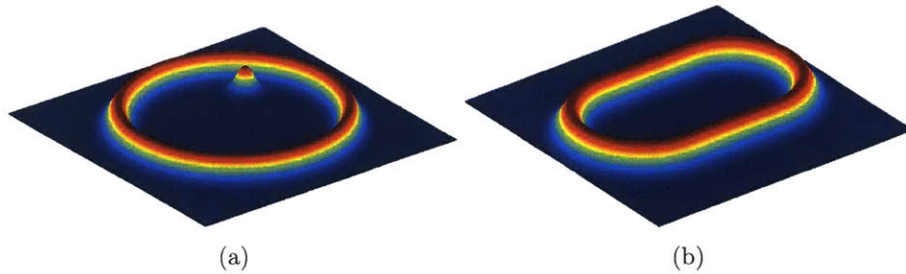
Figure 8-2: Quantum simulation with optically engineered confinement. (a) Ring superfluidity in annular confinement. (b) Quantum chaos in a stadium potential.

accessible. Additionally, the driven-dissipative nature of polariton systems allows an exploration of nonequilibrium quantum dynamics. By tuning the interaction strength of underlying polaritons through the cavity detuning, it is also possible to study the crossover dynamics between equilibrium and nonequilibrium phase transitions. Taking advantage of these unique characteristics, high-order condensation modes including p-wave [152] and d-wave [149] condensates have been demonstrated in periodic lattice structures. Observations of non-Hermitian physics [160] and phase frustration [235] have shown that polaritons are important complements to atomic condensates. We will briefly discuss two problems that could be studied with polaritons and their condensates.

8.4.1 Ring superfluidity

Owing to its connection to superconducting rings and persistent flows in superfluid helium, ring superfluidity has attracted much attention in the past few years [236, 237, 238, 239, 240, 104]. The polariton systems have been shown to allow superfluidity [99] and vortex structures [100, 101, 102]. It is thus a natural step to explore the possibility of ring superfluidity in polariton systems. Annular confinement developed in Chapter 5 can be exploited, shown in Fig. 8-2(a). By introducing a polariton fluid, shown as a tip inside the ring, using a resonant pulse with a controlled wavevector, different propagation behaviors can be anticipated. Let v denote the initial velocity vector of the resonant fluid, and v_c denote the Landau critical velocity for superfluidity. Hence,

1. If v is in the radial direction, and $|v| \leq v_c$, superfluidity propagation through the barrier is anticipated.

2. If v is in the radial direction, and $|v| \geq v_c$, the polariton fluid will scatter with the confinement barrier, and classical deflection with dissipation is anticipated. Since the lifetime of polaritons is sufficiently long, by engineering the size of the annular confinement, several deflections would be possible, leading to the formation of a stable density distribution. Given the wave nature of the quantum fluid, it will behave differently from a classical billiard ball elastically bouncing off a closed barrier.

3. If v is in the azimuthal direction, the ring superfluidity is expected. This is because the interaction between the barrier and the resonant fluid is repulsive, and can be effectively treated as a centripetal force.

Different propagation dynamics can be identified from time-resolved real-space and k-space images. Ring superfluidity allows the possibility of macroscopic superposition of states with different circulation, and is topologically distinct from a condensate in a simply connected region. Therefore, phase rotation of a multiple of π is anticipated. On the other hand, superfluidity in the radial direction leads to a suppression of the Rayleigh scattering, while normal propagation behavior through the barrier would lead to the generation of wake fields, both of which can be identified through momentum distributions using k-space imaging.

8.4.2   Quantum billiard in a stadium potential

Quantum chaos emerges as a branch of physics which studies the relationship between quantum mechanics and classical chaos. The correspondence principle states that classical mechanics is the classical limit of quantum mechanics. If this is true, then there must be quantum mechanisms underlying classical chaos. Quantum chaos typically deals with systems whose exact solutions are precluded by the fact that the constituents of the system influence each other in a complex way. Numerical

techniques or approximation schemes such as Dyson series are used to calculate the properties of the system. Soon after the realization of Bose-Einstein condensation, quantum simulation with condensates became a popular approach to quantum chaos given the classicality of the quantum condensation. Condensates are classical in the sense that they are macroscopic, and their dynamics can be well described by classical wave equations without resorting to quantum mechanics.

One of the intriguing questions concerns the dynamics of a quantum billiard in a stadium potential, as shown in Fig. 8-2(b). The chaotic behavior is determined by the length of the straight segments in the stadium. The quantum billiard finds some application in double-clad fibers. In such a fiber laser, the small core with a low numerical aperture confines the signal, and the wide cladding confines the multi-mode pump. In the paraxial approximation [241, 242], the complex fields of pumps in the cladding behave like wavefunctions of quantum billiards. The modes of the cladding with scarring may avoid the core, and symmetrical configurations could enhance this effect.

By shaping the above-band excitation beam into a stadium shape with the SLM, a stadium potential for polaritons can be created. A second resonant beam with a controlled wavevector can be used to create the billiard inside the stadium. The dynamics of the billiard can be studied using time-resolved real-space and k-space imaging techniques. By varying the excitonic fractions of polaritons through the cavity detuning, the effects of interactions on the dynamics of the quantum billiard can also be investigated.

8.5 Room-Temperature Polariton Condensation and Beyond

Quantum condensation of polaritons can occur at room temperature in principle. However, its operation temperature is limited by the small binding energy of excitons, $\sim$10 meV in GaAs quantum wells. Up until now, mostly studied polariton conden-

sates are still near liquid helium temperatures. On the other hand, the demand for polaritonics requires room-temperature operation. Using excitons with large binding energies in other systems, quantum condensation of polaritons has been observed at room temperature in GaN [77], polymer [79], and organic molecules [78]. Although the observed condensation has not been in equilibrium, it paves the way for the study of Bose-Einstein condensation at room temperature. Recently, strong coupling of light with an atomically thin monolayer material [243], MoS_2, has been demonstrated. The two-dimensional material is of the transition-metal-dichalcogenides (TMD) family, and has shown exceptional light-matter interaction strength (100 times larger oscillator strength than GaAs) [243, 244, 245], giant exciton binding energy (0.3-0.5 eV) [246, 247, 248, 249, 250, 251, 252], and large nonlinear optical susceptibility [253, 254, 255, 256], all of which can be exploited for realization of Bose-Einstein condensation of polaritons at photonic detunings and room temperature, enabling quantum simulation for a broad range of parameters and polaritonics at easily obtainable temperatures.

Appendix A

Generation and characterization of polarization-entangled photon states

A.1   Stokes Parameters for 2-qubit

Stokes parameters are a set of parameters that were originally used to describe the polarization states of electromagnetic radiation. Since the space of polarization states of electromagnetic radiation is isomorphic to the Hilbert space of a qubit, they have also been borrowed to describe a quantum state, relating the density matrix ρ in the following way, in particular for a 2-qubit,

$$\rho = \frac{1}{4} \sum_{m,n=0}^{3} S_{mn} \sigma_m \otimes \sigma_n \qquad (A.1)$$

where S is the Stokes parameter and σ is the Pauli matrix. We will write everything in $|H\rangle$ and $|V\rangle$ basis, which is the most natural basis set when we deal with the polarization of light. In practice, this relation can be generalized to a multiple-qudit system, where generalized Pauli matrices, the matrices of the generator of the $SU(n)$ group, can be used in place of the Pauli matrix.

A.2 Reconstruction of the Density Matrix

As is seen from Eq. (A.1), indices m and n appear in pairs. We can carefully reorder the tensor products and their related Stokes parameters so that one index can be used in the summation

$$\rho = \sum_{\nu=1}^{16} r_\nu \Gamma_\nu \qquad (A.2)$$

where Γ_ν is the tensor product of the Pauli matrices and r_ν is the corresponding projection coefficient. On the other hand, the measured counts n_ν can be computed as the expectation value of the density matrix projected to specific quantum states, which is,

$$n_\nu = N \langle \Psi_\nu | \Gamma_\nu | \Psi_\nu \rangle \qquad (A.3)$$

where N is a normalization factor, and Ψ_ν is the state in the measurement. Substituting Eq. (A.2) into Eq. (A.3), we obtain

$$n_\nu = N \sum_{\nu=1}^{16} r_\nu G_{\nu\mu} \qquad (A.4)$$

where

$$G_{\nu\mu} = \langle \Psi_\nu | \Gamma_\mu | \Psi_\nu \rangle \qquad (A.5)$$

Note that ν indexes the measurement and μ indexes the basis set. In order to get r_ν, we have to invert Eq. (A.4), which leads to

$$r_\nu = \frac{1}{N} \sum_{\nu=1}^{16} (G^{-1})_{\nu\mu} n_\mu \qquad (A.6)$$

This requires G to be nonsingular, which sets the constraint for the choice of projection states. Plugging Eq. (A.6) into Eq. (A.2), we obtain

$$\rho = \frac{1}{N} \sum_{\nu=1}^{16} M_\nu n_\nu \tag{A.7}$$

where

$$M_\mu = (G^{-1})_{\nu\mu} \Gamma_\nu \tag{A.8}$$

Based on (A.7), we can successfully reconstruct the density matrix up to a normalization factor from experimentally measurable coincidence counts. The related matrices, including Γ and M, are presented in the end of this appendix.

A.3   Maximum-Likelihood Estimation

Due to experimental inaccuracies in waveplate angles and statistical fluctuations of coincidence counts, the reconstructed density matrices are sometimes non-physical, that is, the matrices are not Hermitian and positive semidefinite. To get around this problem, the maximum-likelihood estimation of density matrices could be carried out. First, we generate an explicitly physical density matrix, i.e., a matrix that possess normalization, Hermiticity, and semidefinite-positivity. A smart choice would be

$$\rho_p(t) = T(t)^\dagger T(t) / \operatorname{Tr}\left(T(t)^\dagger T(t)\right) \tag{A.9}$$

and we take $T(t)$ as

$$T(t) = \sum_{\nu=1}^{16} t_\nu \Gamma_\nu \tag{A.10}$$

where t_ν is the projection coefficient. In the context of the maximum-likelihood estimation, we should find out a set of $\{t_\nu\}_{\nu=1,2,\dots,16}$ so that the constructed density matrix can lead to experimental measurements, usually coincidence counting, with

the most probable likelihood. Therefore, we need to construct a likelihood function. Given the physical density matrix ρ_p, we know that the measurement data consist of a set of 16 coincidence counts $\bar{n}_\nu$ whose expectation value is given by Eq. (A.2). Assuming that the coincidence measurements are independent and their measurement noise has a Gaussian probability distribution, the probability of obtaining this set of 16 counts is

$$P(n_1, n_2, \ldots, n_{16}) = \frac{1}{C} \prod_{\nu=1}^{16} \exp\left[-\frac{(n_\nu - \bar{n}_\nu)}{2\sigma_\nu^2}\right] \qquad (A.11)$$

where σ_ν is the standard deviation of the νth coincidence measurement, which can be approximately as $\sqrt{\bar{n}_\nu}$, and C is the normalization constant. In order to simplify the maximization, we seek to minimize the negative log-likelihood, given by

$$L = \sum_{\nu=1}^{16} \frac{\left[N \langle \Psi_\nu | \rho_p(t_1, t_2, \ldots, t_{16}) | \Psi_\nu \rangle - n_\nu\right]^2}{2N \langle \Psi_\nu | \rho_p(t_1, t_2, \ldots, t_{16}) | \Psi_\nu \rangle} \qquad (A.12)$$

To perform the numerical minimization, $t_1, t_2, \ldots, t_{16}$ are initialized to a series of randomly generated numbers in the range of [0,1]. Multiple trials of the minimization are performed in order to avoid any unwanted local minima. After minimizing the likelihood function, we obtain the T matrix, and based on Eq. (A.9), we can reconstruct a physical density matrix.

A.4 Error Analysis

The error analysis of tomographic density matrices is based on the Monte Carlo method, where additional numerically simulated data sets are used to obtain a statistical distribution of the elements of reconstructed density matrix ρ_p. Once we know that waveplate angles follow the Gaussian distribution and photon counts follow the Poisson process, we will be able to sample a set of coincidence counts. Based on experience, the error from waveplate angles is much smaller than the error from photon counts, so we only take into account the error from counting statistics. Then the

maximum likelihood method is used to obtain a set of physical density matrices from the simulated counts. The ensemble of reconstructed density matrices can be further used to calculate a set of physical quantities like fidelity, and the errors of these quantities are derived from the calculated set. Note that typically 100 simulations are used.

A.5 Physical Quantities to Characterize the Quantum States in 2-qubit Systems

Fidelity. Fidelity defines the overlap between two quantum states, which has the form

$$F(\rho_0, \rho) = \text{Tr}\left\{\sqrt{\sqrt{\rho_0}\rho\sqrt{\rho_0}}\right\} \tag{A.13}$$

Usually we choose ρ_0 to be the density matrix of a pure maximally entangled state. In this way, we could use the calculated fidelity as a measurement of entanglement. In the 2-qubit case, ρ_0 is chosen to be the Bell state.

Tangle and concurrence. Tangle and concurrence are measurements of non-classical properties of a quantum state. For the 2-qubit system, concurrence is defined as follows: consider the non-Hermitian matrix $R = \rho\Sigma\rho^T\Sigma$ where the superscript T denotes transpose, and Σ is the spin flip matrix in the basis of $|HH\rangle, |HV\rangle, |VH\rangle, |VV\rangle$ defined as

$$\Sigma = \begin{pmatrix} 0 & 0 & 0 & -1 \\ 0 & 0 & 1 & 0 \\ 0 & 1 & 0 & 0 \\ -1 & 0 & 0 & 0 \end{pmatrix} \tag{A.14}$$

239

If the eigenvalues of R, arranged in decreasing order, are given by $r_1 \geq r_2 \geq r_3 \geq r_4$, the concurrence is defined as

$$C = \max\left\{0, \sqrt{r_1} - \sqrt{r_2} - \sqrt{r_3} - \sqrt{r_4}\right\} \tag{A.15}$$

The tangle is calculated directly from the concurrence as

$$T = C^2 \tag{A.16}$$

Entanglement of formation is a similar quantity that measures the entanglement of a state, which is defined as

$$E = h\left(\frac{1 + \sqrt{1 - C^2}}{2}\right) \tag{A.17}$$

where

$$h(x) = -x \log x - (1 - x) \log(1 - x) \tag{A.18}$$

is the log-likelihood function of the Bernoulli distribution.

Entropy. Entropy quantifies the degree of mixture in a quantum system. More generally, it is defined as

$$S = -\operatorname{Tr}\left\{\rho \ln \rho\right\} \tag{A.19}$$

A more analytically convenient description is the linear entropy, which has the form

$$S_L = -\frac{4}{3}\left(1 - \operatorname{Tr}\left\{\rho^2\right\}\right) \tag{A.20}$$

240
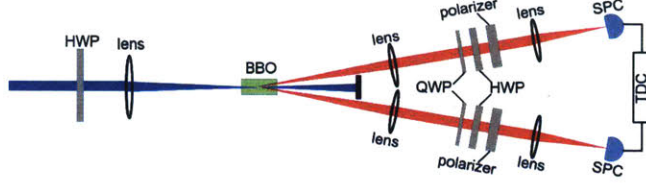
Figure A-1: Schematic illustration of the experimental setup for the generation and characterization of polarization-entangled photon pairs.

A.6 Experimental Design

A.6.1 Experimental layout

A schematic illustration of the experimental setup for the generation and characterization of polarization-entangled photon pairs is shown in Fig. A-1. A 390-nm blue light beam with appropriate polarization is focused onto a nonlinear crystal, typically BBO. Under type-II phase matching, the down-converted red photons are along two intersecting rings. By placing two pinholes at the positions of intersection, we pick up the streams of entangled photon pairs. The $\lambda/4$-waveplate (QWP), $\lambda/2$-waveplate and polarizer in the downstream are used to project entangled photons to a specific polarization state in state tomography measurements. The photons are detected by a pair of single photon counters (SPCs) and are converted to digital signals through the time-digital converter (TDC).

A.6.2 State characterization

State projection. In order to characterize the two-photon quantum state, a set of 16 projective measurements have to be carried out. We set the fast axes of both polarizers in the downstream to be horizontal. We use the Jones notation with the convention

$$|H\rangle = \begin{pmatrix} 1 \\ 0 \end{pmatrix} \qquad |V\rangle = \begin{pmatrix} 0 \\ 1 \end{pmatrix} \tag{A.21}$$

The corresponding matrices for a QWP and a HWP whose fast axes have angles about q and h with respect to the horizontal axis, respectively, are given as follows

$$U_{\text{QWP}}(q) = \frac{1}{\sqrt{2}} \begin{pmatrix} i + \cos 2q & \sin 2q \\ \sin 2q & i - \cos 2q \end{pmatrix} \tag{A.22}$$

and

$$U_{\text{HWP}}(h) = \begin{pmatrix} \cos 2h & \sin 2h \\ \sin 2h & \cos 2h \end{pmatrix} \tag{A.23}$$

respectively. The single-photon state will be projected as

$$|\Psi_{\text{proj}}^{(1)}(q, h)\rangle = U_{\text{QWP}}(q)U_{\text{HWP}}(h) \begin{pmatrix} 1 \\ 0 \end{pmatrix} = \begin{pmatrix} a(q, h) \\ b(q, h) \end{pmatrix} \tag{A.24}$$

with the coefficients

$$a(q, h) = \frac{1}{\sqrt{2}} \left(\cos 2(q - h) + i \cos 2h \right) \tag{A.25}$$

$$b(q, h) = \frac{1}{\sqrt{2}} \left(\sin 2(q - h) + i \sin 2h \right) \tag{A.26}$$

The projection state for the entangled photon pair is given by

$$|\Psi_{\text{proj}}^{(2)}(q_1, h_1, q_2, h_2)\rangle = |\Psi_{\text{proj}}^{(1)}(q_1, h_1)\rangle \otimes |\Psi_{\text{proj}}^{(1)}(q_2, h_2)\rangle \begin{pmatrix} a(q_1, h_1)a(q_2, h_2) \\ a(q_1, h_1)b(q_2, h_2) \\ b(q_1, h_1)a(q_2, h_2) \\ b(q_1, h_1)b(q_2, h_2) \end{pmatrix} \tag{A.27}$$

in the basis set $|HH\rangle, |HV\rangle, |VH\rangle, |VV\rangle$.

Measurement selection. In order to successfully reconstruct the density matrix of the two-photon state, the 16 independent measurements that are chosen have to yield an invertible G matrix. If the measurements are not independent, G will be

242

singular. One of the most convenient choices is listed in Table A.1.

ν	Mode 1	Mode 2	q_1	h_1	q_2	h_2
1	H	H	0	0	0	0
2	H	V	0	0	0	45
3	V	V	0	45	0	45
4	V	H	0	45	0	0
5	R	H	0	22.5	0	0
6	R	V	0	22.5	0	45
7	D	V	45	22.5	0	45
8	D	H	45	22.5	0	0
9	D	R	45	22.5	0	22.5
10	D	D	45	22.5	45	22.5
11	R	D	0	22.5	45	22.5
12	H	D	0	0	45	22.5
13	V	D	0	45	45	22.5
14	V	L	0	45	90	22.5
15	H	L	0	0	90	22.5
16	R	L	0	22.5	90	22.5

Table A.1: Measurements for the reconstruction of 2-qubit density matrix.

Related matrices for state tomography Γ matrices are the basis set of the density matrix to be reconstructed. Let us define the SU(2) generator as

$$\sigma_0 = |H\rangle\,|H\rangle + |V\rangle\,|V\rangle \tag{A.28}$$

$$\sigma_1 = |H\rangle\,|H\rangle - |V\rangle\,|V\rangle \tag{A.29}$$

$$\sigma_2 = |H\rangle\,|V\rangle + |V\rangle\,|H\rangle \tag{A.30}$$

$$\sigma_3 = i(|V\rangle\,|H\rangle - |H\rangle\,|V\rangle) \tag{A.31}$$

Note the order of the generator is not important. We can order Γ matrices in the following way (a factor of 1/2 is left out for simplicity, which has to be included in actual calculations)

243

$$\Gamma_1 = \sigma_0 \otimes \sigma_0 = \begin{pmatrix} 1 & 0 & 0 & 0 \\ 0 & 1 & 0 & 0 \\ 0 & 0 & 1 & 0 \\ 0 & 0 & 0 & 1 \end{pmatrix} \qquad \Gamma_2 = \sigma_0 \otimes \sigma_1 = \begin{pmatrix} 1 & 0 & 0 & 0 \\ 0 & -1 & 0 & 0 \\ 0 & 0 & 1 & 0 \\ 0 & 0 & 0 & -1 \end{pmatrix}$$

$$\Gamma_3 = \sigma_0 \otimes \sigma_2 = \begin{pmatrix} 0 & 1 & 0 & 0 \\ 1 & 0 & 0 & 0 \\ 0 & 0 & 0 & 1 \\ 0 & 0 & 1 & 0 \end{pmatrix} \qquad \Gamma_4 = \sigma_0 \otimes \sigma_3 = \begin{pmatrix} 0 & -i & 0 & 0 \\ i & 0 & 0 & 0 \\ 0 & 0 & 0 & -i \\ 0 & 0 & i & 0 \end{pmatrix}$$

$$\Gamma_5 = \sigma_1 \otimes \sigma_0 = \begin{pmatrix} 1 & 0 & 0 & 0 \\ 0 & 1 & 0 & 0 \\ 0 & 0 & 1 & 0 \\ 0 & 0 & 0 & 1 \end{pmatrix} \qquad \Gamma_6 = \sigma_1 \otimes \sigma_1 = \begin{pmatrix} 1 & 0 & 0 & 0 \\ 0 & -1 & 0 & 0 \\ 0 & 0 & -1 & 0 \\ 0 & 0 & 0 & 1 \end{pmatrix}$$

$$\Gamma_7 = \sigma_1 \otimes \sigma_2 = \begin{pmatrix} 0 & 1 & 0 & 0 \\ 1 & 0 & 0 & 0 \\ 0 & 0 & 0 & -1 \\ 0 & 0 & -1 & 0 \end{pmatrix} \qquad \Gamma_8 = \sigma_1 \otimes \sigma_3 = \begin{pmatrix} 0 & -i & 0 & 0 \\ i & 0 & 0 & 0 \\ 0 & 0 & 0 & i \\ 0 & 0 & -i & 0 \end{pmatrix}$$

$$\Gamma_9 = \sigma_2 \otimes \sigma_0 = \begin{pmatrix} 0 & 0 & 1 & 0 \\ 0 & 0 & 0 & 1 \\ 1 & 0 & 0 & 0 \\ 0 & 1 & 0 & 0 \end{pmatrix} \qquad \Gamma_{10} = \sigma_2 \otimes \sigma_1 = \begin{pmatrix} 0 & 0 & 1 & 0 \\ 0 & 0 & 0 & -1 \\ 1 & 0 & 0 & 0 \\ 0 & -1 & 0 & 0 \end{pmatrix}$$

$$\Gamma_{11} = \sigma_2 \otimes \sigma_2 = \begin{pmatrix} 0 & 0 & 0 & 1 \\ 0 & 0 & 1 & 0 \\ 0 & 1 & 0 & 0 \\ 1 & 0 & 0 & 0 \end{pmatrix} \qquad \Gamma_{12} = \sigma_2 \otimes \sigma_3 = \begin{pmatrix} 0 & 0 & 0 & -i \\ 0 & 0 & i & 0 \\ 0 & -i & 0 & 0 \\ i & 0 & 0 & 0 \end{pmatrix}$$

$$\Gamma_{13} = \sigma_3 \otimes \sigma_0 = \begin{pmatrix} 0 & 0 & -i & 0 \\ 0 & 0 & 0 & -i \\ i & 0 & 0 & 0 \\ 0 & i & 0 & 0 \end{pmatrix} \qquad \Gamma_{14} = \sigma_3 \otimes \sigma_1 = \begin{pmatrix} 0 & 0 & -i & 0 \\ 0 & 0 & 0 & i \\ i & 0 & 0 & 0 \\ 0 & -i & 0 & 0 \end{pmatrix}$$

$$\Gamma_{15} = \sigma_3 \otimes \sigma_2 = \begin{pmatrix} 0 & 0 & 0 & -i \\ 0 & 0 & -i & 0 \\ 0 & 1 & 0 & 0 \\ 1 & 0 & 0 & 0 \end{pmatrix} \qquad \Gamma_{16} = \sigma_3 \otimes \sigma_3 = \begin{pmatrix} 0 & 0 & 0 & -1 \\ 0 & 0 & 1 & 0 \\ 0 & 1 & 0 & 0 \\ -1 & 0 & 0 & 0 \end{pmatrix}$$

The G matrix is a 16×16 matrix. The row index is for measurements, and the column index is for the basis set. We show the matrix elements in table form in Table A.2. There are another 20 measurements, together with these 16 measurements, forming an over-complete set which is usually used to infer the density matrix by least-squares fit. Last, M matrices are used to connect the measurements directly to the reconstructed density matrix. The form of these matrices is independent of the chosen set of Γ matrices used to convert the density matrix into a vector. However, it does depend on the set of tomographic states $|\Psi_\nu\rangle$. With the order corresponding

	1	2	3	4	5	6	7	8	9	10	11	12	13	14	15	16
HH	1	1	0	0	1	1	0	0	0	0	0	0	0	0	0	0
HV	1	-1	0	0	1	-1	0	0	0	0	0	0	0	0	0	0
VV	1	-1	0	0	-1	1	0	0	0	0	0	0	0	0	0	0
VH	1	1	0	0	-1	-1	0	0	0	0	0	0	0	0	0	0
RH	1	1	0	0	0	0	0	0	0	0	0	0	1	1	0	0
RV	1	-1	0	0	0	0	0	0	0	0	0	0	1	-1	0	0
DV	1	-1	0	0	0	0	0	0	1	-1	0	0	0	0	0	0
DH	1	1	0	0	0	0	0	0	1	1	0	0	0	0	0	0
DR	1	0	0	1	0	0	0	0	1	0	0	1	0	0	0	0
DD	1	0	1	0	0	0	0	0	1	0	1	0	0	0	0	0
RD	1	0	1	0	0	0	0	0	0	0	0	0	1	0	1	0
HD	1	0	1	0	1	0	1	0	0	0	0	0	0	0	0	0
VD	1	0	1	0	-1	0	-1	0	0	0	0	0	0	0	0	0
VL	1	0	0	-1	-1	0	0	1	0	0	0	0	0	0	0	0
HL	1	0	0	-1	1	0	0	-1	0	0	0	0	0	0	0	0
RL	1	0	0	-1	0	0	0	0	0	0	0	0	1	0	0	-1

Table A.2: The G matrix in the state tomography.

to those in Table A.1, we can find M matrices to be

$$M_1 = \frac{1}{2} \begin{pmatrix} 2 & -1-i & -1+i & 1 \\ -1+i & 0 & -i & 0 \\ -1-i & i & 0 & 0 \\ 1 & 0 & 0 & 0 \end{pmatrix} \qquad M_2 = \frac{1}{2} \begin{pmatrix} 0 & -1-i & 0 & 1 \\ -1+i & 2 & -i & -i+i \\ 0 & i & 0 & 0 \\ 1 & -1-i & 0 & 0 \end{pmatrix}$$

$$M_3 = \frac{1}{2} \begin{pmatrix} 0 & 0 & 0 & 1 \\ 0 & 0 & -i & -1+i \\ 0 & i & 0 & 0 \\ 1 & -1-i & 0 & 0 \end{pmatrix} \qquad M_4 = \frac{1}{2} \begin{pmatrix} 0 & 0 & -1+i & 1 \\ 0 & 0 & -i & 0 \\ -1-i & i & 2 & -1-i \\ 1 & 0 & -1-i & 0 \end{pmatrix}$$

$$M_5 = \frac{1}{2}\begin{pmatrix} 0 & 0 & -2i & -1+i \\ 0 & 0 & 1+i & 0 \\ 2i & 1-i & 0 & 0 \\ -1-i & 0 & 0 & 0 \end{pmatrix} \qquad M_6 = \frac{1}{2}\begin{pmatrix} 0 & 0 & 0 & -1+i \\ 0 & 0 & 1+i & -2i \\ 0 & 1-i & 0 & 0 \\ -1-i & 2i & 0 & 0 \end{pmatrix}$$

$$M_7 = \frac{1}{2}\begin{pmatrix} 0 & 0 & 0 & -1+i \\ 0 & 0 & -1-i & 2 \\ 0 & 1+i & 0 & 0 \\ -1-i & 2 & 0 & 0 \end{pmatrix} \qquad M_8 = \frac{1}{2}\begin{pmatrix} 0 & 0 & 2 & -1+i \\ 0 & 0 & -1-i & 0 \\ 2 & 1+i & 0 & 0 \\ -1-i & 0 & 0 & 0 \end{pmatrix}$$

$$M_9 = \frac{1}{2}\begin{pmatrix} 0 & 0 & 0 & -i \\ 0 & 0 & i & 0 \\ 0 & -i & 0 & 0 \\ i & 0 & 0 & 0 \end{pmatrix} \qquad M_{10} = \frac{1}{2}\begin{pmatrix} 0 & 0 & 0 & 1 \\ 0 & 0 & 1 & 0 \\ 0 & 1 & 0 & 0 \\ 1 & 0 & 0 & 0 \end{pmatrix}$$

$$M_{11} = \frac{1}{2}\begin{pmatrix} 0 & 0 & 0 & -i \\ 0 & 0 & -i & 0 \\ 0 & i & 0 & 0 \\ i & 0 & 0 & 0 \end{pmatrix} \qquad M_{12} = \frac{1}{2}\begin{pmatrix} 0 & 2 & 0 & -1+i \\ 2 & 0 & -1+i & 0 \\ 0 & -1-i & 0 & 0 \\ -1-i & 0 & 0 & 0 \end{pmatrix}$$

$$M_{13} = \frac{1}{2}\begin{pmatrix} 0 & 0 & 0 & -1+i \\ 0 & 0 & -1+i & 0 \\ 0 & -1-i & 0 & 2 \\ -1-i & 0 & 2 & 0 \end{pmatrix} \qquad M_{14} = \frac{1}{2}\begin{pmatrix} 0 & 0 & 0 & -1-i \\ 0 & 0 & 1+i & 0 \\ 0 & 1-i & 0 & 2i \\ -1+i & 0 & -2i & 0 \end{pmatrix}$$

$$M_{15} = \frac{1}{2} \begin{pmatrix} 0 & 2i & 0 & -1-i \\ -2i & 0 & 1+i & 0 \\ 0 & 1-i & 0 & 0 \\ -1+i & 0 & 0 & 0 \end{pmatrix} \qquad M_{16} = \frac{1}{2} \begin{pmatrix} 0 & 0 & 0 & 1 \\ 0 & 0 & -1 & 0 \\ 0 & -1 & 0 & 0 \\ 1 & 0 & 0 & 0 \end{pmatrix}$$

Bibliography

[1] Baldo, M. & Stojanovic, V. Optical switching: Excitonic interconnects. *Nat. Photon.* **3**, 558–560 (2009).

[2] Yeh, C. *Applied Photonics* (Academic Press, 1994).

[3] Cvijetic, M. & Djordjevic, I. B. *Advanced Optical Communication Systems and Networks* (Artech House Applied Photonics, 2013).

[4] Al-Azzawi, A. *Photonics: Principles and Practices* (CRC Press, 2016).

[5] High, A. A., Novitskaya, E. E., Butov, L. V., Hanson, M. & Gossard, A. C. Control of exciton fluxes in an excitonic integrated circuit. *Science* **321**, 229–231 (2008).

[6] Grosso, G. *et al.* Excitonic switches operating at around 100 k. *Nat. Photon.* **3**, 577–580 (2009).

[7] Wang, Q. H., Kalantar-Zadeh, K., Kis, A., Coleman, J. N. & Strano, M. S. Electronics and optoelectronics of two-dimensional transition metal dichalcogenides. *Nat. Nano.* **7**, 699–712 (2012).

[8] High, A. A. *Indirect Excitons in GaAs coupled quantum wells: Development of optoelectronic logic devices and trapping potentials, and studies of low temperature phenomena in a bosonic condensed matter system.* Ph.D. thesis, Department of Physics, University of California, San Diego (2012).

[9] Kavokin, A., Baumberg, J. J., Malpuech, G. & Laussy, F. P. *Microcavities* (Oxford Science Publications, 2007).

[10] Amo, A. *et al.* Exciton-polariton spin switches. *Nat. Photon.* **4**, 361–366 (2010).

[11] Lagoudakis, K. G. *et al.* Observation of half-quantum vortices in an exciton-polariton condensate. *Science* **326**, 974–976 (2009).

[12] Sanvitto, D. *et al.* Persistent currents and quantized vortices in a polariton superfluid. *Nat. Phys.* **6**, 527–533 (2010).

[13] Roumpos, G. *et al.* Power-law decay of the spatial correlation function in exciton-polariton condensates. *Proc. Nat. Acad. Sci.* **109**, 6467–6472 (2012).

[14] Bloch, I., Dalibard, J. & Zwerger, W. Many-body physics with ultracold gases. *Rev. Mod. Phys.* **80**, 885–964 (2008).

[15] Weinberg, S. Approximate symmetries and pseudo-goldstone bosons. *Phys. Rev. Lett.* **29**, 1698–1701 (1972).

[16] Uchino, S., Kobayashi, M., Nitta, M. & Ueda, M. Quasi-nambu-goldstone modes in bose-einstein condensates. *Phys. Rev. Lett.* **105**, 230406 (2010).

[17] Hadzibabic, Z., Kruger, P., Cheneau, M. & Dalibard, B. B. J. Berezinski-ikosterlitzthouless crossover in a trapped atomic gas. *Nature* **441**, 1118–1121 (2006).

[18] Endres, M. *et al.* The higgs amplitude mode at the two-dimensional superfluid/mott insulator transition. *Nature* **487**, 454–458 (2012).

[19] Pollet, L. & Prokof'ev, N. Higgs mode in a two-dimensional superfluid. *Phys. Rev. Lett.* **109**, 010401 (2012).

[20] Volovik, G. E. *The Universe in Helium Droplet* (Oxford University Press, New York, 2003).

[21] Fukuyama, T. & Morikawa, M. Stagflation: Bose-einstein condensation in the early universe. *Phys. Rev. D* **80**, 063520 (2009).

[22] Harko, T. Cosmological dynamics of dark matter bose-einstein condensation. *Phys. Rev. D* **83**, 123515 (2011).

[23] Chavanis, P.-H. & Harko, T. Bose-einstein condensate general relativistic stars. *Phys. Rev. D* **86**, 064011 (2012).

[24] Tassone, F. & Yamamoto, Y. Exciton-exciton scattering dynamics in a semiconductor microcavity and stimulated scattering into polaritons. *Phys. Rev. B* **59**, 10830–10842 (1999).

[25] Bose, S. N. Plancks law and light quantum hypothesis. *Z. Phys.* **26**, 178 (1924).

[26] Einstein, A. Quantum theory of idea monoatomic gases. *Sitzber. Preuss. Akad. Wiss.* **23**, 3 (1925).

[27] Anderson, M. H., Ensher, J. R., Matthews, M. R., Wieman, C. E. & Cornell, E. A. Observation of bose-einstein condensation in a dilute atomic vapor. *Science* **269**, 198–201 (1995).

[28] Davis, K. B. *et al.* Bose-einstein condensation in a gas of sodium atoms. *Phys. Rev. Lett.* **75**, 3969 (1995).

[29] Bradley, C. C., Sackett, C. A., Tollett, J. J. & Hulet, R. G. Evidence of bose-einstein condensation in an atomic gas with attractive interactions. *Phys. Rev. Lett.* **75**, 1687–1690 (1995).

[30] Bradley, C. C., Sackett, C. A. & Hulet, R. G. Bose-einstein condensation of lithium: Observation of limited condensate number. *Phys. Rev. Lett.* **78**, 985–989 (1997).

[31] Demokritov, S. O. *et al.* Bose-einstein condensation of quasi-equilibrium magnons at room temperature under pumping. *Nature* **443**, 430–433 (2006).

[32] Deng, H., Weihs, G., Santori, C., Bloch, J. & Yamamoto, Y. Condensation of semiconductor microcavity exciton polaritons. *Science* **298**, 199–202 (2002).

[33] Kasprzak, J. *et al.* Bose-einstein condensation of exciton polaritons. *Nature* **443**, 409–414 (2006).

[34] Balili, R., Hartwell, V., Snoke, D., Pfeiffer, L. & West, K. Bose-einstein condensation of microcavity polaritons in a trap. *Science* **316**, 1007–1010 (2007).

[35] Sun, Y. *et al.* Bose-einstein condensation of long-lifetime polaritons in thermal equilibrium. *Phys. Rev. Lett.* **118**, 016602 (2017).

[36] Dunningham, J., Burnett, K. & Phillips, W. D. Bose-einstein condensates and precision measurements. *Philos. Trans. R. Soc. London, Ser. A* **363**, 2165–2175 (2005).

[37] Sun, Y. *et al.* Are polaritons not weakly interacting? direct measurement of the polariton-polariton interaction strength. *arXiv*:1508.06698 (2015).

[38] Dalfovo, F., Giorgini, S., Pitaeskii, L. P. & Stringari, S. Theory of bose-einstein condensation in trapped gases. *Rev. Mod. Phys.* **71**, 463–512 (1999).

[39] Leggett, A. J. Bose-einstein condensation in the alkali gases: Some fundamental concepts. *Rev. Mod. Phys.* **73**, 307–356 (2001).

[40] Pethick, C. & Smith, H. *Bose-Einstein Condensation in Dilute Gases* (University Press, Cambridge, 2002), 1 edn.

[41] Pitaeskii, L. P. & Stringari, S. *Bose-Einstein Condensation* (International Series of Monographs on Physics, 2003).

[42] Deng, H. Exciton-polariton bose-einstein condensation. *Rev. Mod. Phys.* **82**, 1489–1537 (2010).

[43] Lee, T. D. & Yang, C. N. Many-body problem in quantum mechanics and quantum statistical mechanics. *Phys. Rev.* **105**, 1119–1120 (1957).

[44] Yamamoto, Y. Bose-einstein condensation and lasers.

[45] Bagnato, V. & Kleppner, D. Bose-einstein condensation in low-dimensional traps. *Phys. Rev. A* **44**, 7439–7441 (1991).

[46] Landau, L. Theory of the superfluidity of helium ii. *Phys. Rev.* **60**, 356–358 (1941).

[47] Penrose, O. On the quantum mechanics of helium ii. *Philos. Mag.* **42**, 1373 (1951).

[48] Penrose, O. & Onsager, L. Bose-einstein condensation and liquid helium. *Phys. Rev.* **104**, 576–584 (1956).

[49] Bogoliubov, N. N. On the theory of superfluidity. *J. Phys. (USSR)* **11**, 23–32 (1947).

[50] Lee, T. D. & Yang, C. N. Eigenvalues and eigenfunctions of a bose system of hard spheres and its low-temperature properties. *Phys. Rev.* **106**, 1135–1145 (1957).

[51] Nozieres, P. *Bose-Einstein Condensation* (Cambridge University Press, 1995).

[52] Glauber, R. J. The quantum theory of optical coherence. *Phys. Rev.* **130**, 2529–2539 (1963).

[53] London, F. The λ-phenomenon of liquid helium and the bose-einstein degeneracy. *Nature* **141**, 643–644 (1938).

[54] London, F. On the bose-einstein condensation. *Phys. Rev.* **54**, 947–954 (1938).

[55] Cornish, S. L., Claussen, N. R., Roberts, J. L., Cornell, E. A. & Wieman, C. E. Stable ^{85}Rb bose-einstein condensates with widely tunable interactions. *Phys. Rev. Lett.* **85**, 1795–1798 (2000).

[56] Roati, G. *et al.* ^{39}K bose-einstein condensate with tunable interactions. *Phys. Rev. Lett.* **99**, 010403 (2007).

[57] Modugno, G. *et al.* Bose-einstein condensation of potassium atoms by sympathetic cooling. *Science* **294**, 1320–1322 (2001).

[58] Weber, T., Herbig, J., Mark, M., Nägerl, H.-C. & Grimm, R. Bose-einstein condensation of cesium. *Science* **299**, 232–235 (2003).

[59] Robert, A. *et al.* A bose-einstein condensate of metastable atoms. *Science* **292**, 461–464 (2001).

[60] Pereira Dos Santos, F. *et al.* Bose-einstein condensation of metastable helium. *Phys. Rev. Lett.* **86**, 3459–3462 (2001).

[61] Fukuhara, T., Sugawa, S. & Takahashi, Y. Bose-einstein condensation of an ytterbium isotope. *Phys. Rev. A* **76**, 051604 (2007).

[62] Takasu, Y. *et al.* Spin-singlet bose-einstein condensation of two-electron atoms. *Phys. Rev. Lett.* **91**, 040404 (2003).

[63] Fukuhara, T., Sugawa, S., Takasu, Y. & Takahashi, Y. All-optical formation of quantum degenerate mixtures. *Phys. Rev. A* **79**, 021601 (2009).

[64] Kraft, S., Vogt, F., Appel, O., Riehle, F. & Sterr, U. Bose-einstein condensation of alkaline earth atoms: ^{40}Ca. *Phys. Rev. Lett.* **103**, 130401 (2009).

[65] Stellmer, S., Tey, M. K., Huang, B., Grimm, R. & Schreck, F. Bose-einstein condensation of strontium. *Phys. Rev. Lett.* **103**, 200401 (2009).

[66] de Escobar, Y. N. M. *et al.* Bose-einstein condensation of ^{84}Sr. *Phys. Rev. Lett.* **103**, 200402 (2009).

[67] Stellmer, S., Tey, M. K., Grimm, R. & Schreck, F. Bose-einstein condensation of ^{86}Sr. *Phys. Rev. A* **82**, 041602 (2010).

[68] Mickelson, P. G., Martinez de Escobar, Y. N., Yan, M., DeSalvo, B. J. & Killian, T. C. Bose-einstein condensation of ^{88}Sr through sympathetic cooling with ^{87}Sr. *Phys. Rev. A* **81**, 051601 (2010).

[69] Fried, D. G. *et al.* Bose-einstein condensation of atomic hydrogen. *Phys. Rev. Lett.* **81** (1998).

[70] Griesmaier, A., Werner, J., Hensler, S., Stuhler, J. & Pfau, T. Bose-einstein condensation of chromium. *Phys. Rev. Lett.* **94**, 160401 (2005).

[71] Simsarian, J. E. *et al.* Magneto-optic trapping of ^{210}fr. *Phys. Rev. Lett.* **76**, 3522–3525 (1996).

[72] Lu, Z.-T. *et al.* Efficient collection of ^{221}fr into a vapor cell magneto-optical trap. *Phys. Rev. Lett.* **79**, 994–997 (1997).

[73] Guest, J. R. *et al.* Laser trapping of ^{225}Ra and ^{226}Ra with repumping by room-temperature blackbody radiation. *Phys. Rev. Lett.* **98**, 093001 (2007).

[74] Aspect, A., Cohen-Tannoudji, C., Arimondo, E., Vansteenkiste, N. & Kaiser, R. Laser cooling below the one-photon recoil energy by velocity-selective coherent population trapping. *Phys. Rev. Lett.* **61**, 826–829 (1988).

[75] Ketterle, W. & Van Druten, N. J. Evaporative cooling of trapped atoms. *Adv. At. Mol. Opt. Phy.* **37**, 181–236 (1996).

[76] Imamoglu, A., Ram, R. J., Pau, S. & Yamamoto, Y. Nonequilibrium condensates and lasers without inversion: Exciton-polariton lasers. *Phys. Rev. A* **53**, 4250–4253 (1996).

[77] Christopoulos, S. *et al.* Room-temperature polariton lasing in semiconductor microcavities. *Phys. Rev. Lett.* **98**, 126405 (2007).

[78] Kena-Cohen, S. & Forrest, S. R. Room-temperature polariton lasing in an organic single-crystal microcavity. *Nat. Photon.* **4**, 371–375 (2010).

253

[79] Plumhof, J. D., Stoferle, T., Mai, L., Scherf, U. & Mahrt, R. F. Room-temperature bose-einstein condensation of cavity exciton-polaritons in a polymer. *Nat. Mater.* **13**, 247–252 (2014).

[80] Moskalenko, S. A. Reversible optico-hydrodynamic effects in nonideal exciton gas. *Fiz. Tverd. Tela* **4**, 276 (1962).

[81] Blatt, J. M., Böer, K. W. & Brandt, W. Bose-einstein condensation of excitons. *Phys. Rev.* **126**, 1691–1692 (1962).

[82] DeMarco, B. & Jin, D. S. Onset of fermi degeneracy in a trapped atomic gas. *Science* **285**, 1703–1706 (1999).

[83] Regal, C. A., Ticknor, C., Bohn, J. L. & Jin, D. S. Creation of ultracold molecules from a fermi gas of atoms. *Nature* **424**, 47–50 (2003).

[84] Bardeen, J., Cooper, L. N. & Schrieffer, J. R. Microscopic theory of superconductivity. *Phys. Rev.* **106**, 162–164 (1957).

[85] Ginzburg, V. L. & Kirzhnits, D. A. On the superfluidity of neutron stars. *Sov. Phys. JETP* **20**, 1346–1348 (1965).

[86] Bahcall, J. N. & Wolf, R. A. Neutron stars. i. properties at absolute zero temperature. *Phys. Rev.* **140**, B1445–1451 (1965).

[87] Kaplan, D. B. & Nelson, A. E. Strange goings on in dense nucleonic matter. *Phys. Lett. B* **175**, 57–63 (1986).

[88] Pethick, C., Schaefer, T. & Schwenk, A. Bose-einstein condensates in neutron stars. *arXiv:*1507.05839 (2015).

[89] Opanchuk, B., Polkinghorne, R., Fialko, O., Brand, J. & Drummond, P. D. Quantum simulations of the early universe. *Annalen der Physik* **525**, 866–876 (2013).

[90] Langfeld, K., Markum, H., Pullirsch, R., Roberts, C. D. & Schmidt, S. M. Concerning the quark condensate. *Phys. Rev. C* **67**, 065206 (2003).

[91] Brodsky, S. J. & Shrock, R. Condensates in quantum chromodynamics and the cosmological constant. *Proc. Nat. Acad. Sci.* **108**, 45–50 (2011).

[92] Frenkel, J. On the transformation of light into heat in solids. i. *Phys. Rev.* **37**, 17–44 (1931).

[93] Wannier, G. The structure of electronic excitation levels in insulating crystals. *Phys. Rev.* **52**, 191 (1937).

[94] Mott, N. F. Conduction in polar crystals. ii. the conduction band and ultraviolet absorption of alkali-halide crystals. *Trans. Faraday Soc.* **34**, 500–506 (1938).

[95] Weisbuch, C., Nishioka, M., Ishikawa, A. & Arakawa, Y. Observation of the coupled exciton-photon mode splitting in a semiconductor quantum microcavity. *Phys. Rev. Lett.* **69**, 3314-3317 (1992).

[96] Houdré, R. *et al.* Measurement of cavity-polariton dispersion curve from angle-resolved photoluminescence experiments. *Phys. Rev. Lett.* **73**, 2043-2046 (1994).

[97] Steger, M. *et al.* Long-range ballistic motion and coherent flow of long-lifetime polaritons. *Phys. Rev. B* **88**, 235314 (2013).

[98] Steger, M., Gautham, C., Snoke, D. W., Pfeiffer, L. & West, K. Slow reflection and two-photon generation of microcavity exciton-polaritons. *Optica* **2**, 1-5 (2015).

[99] Amo, A. *et al.* Superfluidity of polaritons in semiconductor microcavities. *Nat. Phys.* **5**, 805-810 (2009).

[100] Lagoudakis, K. G. *et al.* Quantized vortices in an exciton-polariton condensate. *Nat. Phys.* **4**, 706-710 (2008).

[101] Nardin, G. *et al.* Hydrodynamic nucleation of quantized vortex pairs in a polariton quantum fluid. *Nat. Phys.* **7**, 635-641 (2011).

[102] Tosi, G. *et al.* Geometrically locked vortex lattices in semiconductor quantum fluids. *Nat. Comm.* **3**, 1243 (2012).

[103] Dreismann, A. *et al.* Coupled counterrotating polariton condensates in optically defined annular potentials. *Proc. Nat. Acad. Sci.* **111**, 8770-8775 (2014).

[104] Liu, G., Snoke, D. W., Daley, A., Pfeiffer, L. N. & West, K. A new type of half-quantum circulation in a macroscopic polariton spinor ring condensate. *Proc. Nat. Acad. Sci.* **112**, 2676-2681 (2015).

[105] Ballarini, D. *et al.* All-optical polariton transistor. *Nat. Comm.* **4**, 1778 (2013).

[106] Shah, J. & Dayem, A. H. Formation of electron-hole liquid in optically excited si: Results of fast time-resolved spectroscopy. *Phys. Rev. Lett.* **37**, 861-864 (1976).

[107] Hulin, D., Mysyrowicz, A., Combescot, M., Pelant, I. & a la Guillaume, C. B. Electron-hole liquid and biexciton pocket in agbr. *Phys. Rev. Lett.* **39**, 1497-1497 (1977).

[108] Hanamura, E. & Haug, H. Condensation effects of excitons. *Phys. Rep.* **33**, 209 (1977).

[109] Moskalenko, S. A. & Snoke, D. W. *Bose-Einstein Condensation of Excitons and Biexcitons* (Cambridge University Press, 2000).

[110] Purcell, E. M. Spontaneous emission probabilities at radio frequencies. *Phys. Rev.* **69**, 681 (1946).

[111] Goy, P., Raimond, J. M., Gross, M. & Haroche, S. Observation of cavity-enhanced single-atom spontaneous emission. *Phys. Rev. Lett.* **50**, 1903–1906 (1983).

[112] Gérard, J. M. *et al.* Enhanced spontaneous emission by quantum boxes in a monolithic optical microcavity. *Phys. Rev. Lett.* **81**, 1110–1113 (1998).

[113] Knight, J. C. *et al.* Mapping whispering-gallery modes in microspheres with a near-fieldprobe. *Opt. Lett.* **20**, 1515–1517 (1995).

[114] Lefevre-Seguin, V. & Haroche, S. Towards cavity-qed experiments with silica microspheres. *Mat. Sci. Eng. B* **48**, 53–58 (1997).

[115] Gorodetsky, M. L., Savchenkov, A. A. & Ilchenko, V. S. Ultimate q of optical microsphere resonators. *Opt. Lett.* **21**, 453–455 (1996).

[116] Vernooy, D. W., Ilchenko, V. S., Mabuchi, H., Streed, E. W. & Kimble, H. J. High-q measurements of fused-silica microspheres in the near infrared. *Opt. Lett.* **23**, 247–249 (1998).

[117] Vernooy, D. W., Furusawa, A., Georgiades, N. P., Ilchenko, V. S. & Kimble, H. J. Cavity qed with high-q whispering gallery modes. *Phys. Rev. A* **57**, R2293–R2296 (1998).

[118] Vahala, K. J. Optical microcavities. *Nature* **424**, 839–846 (2003).

[119] Gayral, B. *et al.* High-q wet-etched gaas microdisks containing inas quantum boxes. *Appl. Phys. Lett.* **75**, 1908–1910 (1999).

[120] Djordjev, K., Choi, S.-J., Choi, S.-J. & Dapkus, R. D. Microdisk tunable resonant filters and switches. *IEEE Phot. Technol. Lett.* **14**, 828–830 (2002).

[121] Rabiei, P., Steier, W. H., Zhang, C. & Dalton, L. R. Polymer micro-ring filters and modulators. *J. Lightwave Technol.* **20**, 1968 (2002).

[122] Srinivasan, K. *et al.* Experimental demonstration of a high quality factor photonic crystal microcavity. *Applied Physics Letters* **83**, 1915–1917 (2003).

[123] Hood, C. J., Lynn, T. W., Doherty, A. C., Parkins, A. S. & Kimble, H. J. The atom-cavity microscope: Single atoms bound in orbit by single photons. *Science* **287**, 1447–1453 (2000).

[124] Buck, J. R. & Kimble, H. J. Optimal sizes of dielectric microspheres for cavity qed with strong coupling. *Phys. Rev. A* **67**, 033806 (2003).

[125] Armani, D. K., Kippenberg, T. J., Spillane, S. M. & Vahala, K. J. Ultra-high-q toroid microcavity on a chip. *Nature* **421**, 925–928 (2002).

[126] Painter, O. *et al.* Two-dimensional photonic band-gap defect mode laser. *Science* **284**, 1819–1821 (1999).

[127] Akahane, Y., Asano, T., Song, B.-S. & Noda, S. Fine-tuned high-q photonic-crystal nanocavity. *Opt. Express* **13**, 1202–1214 (2005).

[128] Kwong, N. H., Takayama, R., Rumyantsev, I., Kuwata-Gonokami, M. & Binder, R. Third-order exciton-correlation and nonlinear cavity-polariton effects in semiconductor microcavities. *Phys. Rev. B* **64**, 045316 (2001).

[129] Yamamoto, Y., Tassone, F. & Cao, H. *Semiconductor Cavity Quantum Electrodynamics* (Springer Tracts in Modern Physics, 2000).

[130] Hopfield, J. J. Theory of the contribution of excitons to the complex dielectric constant of crystals. *Phys. Rev.* **112**, 1555–1567 (1958).

[131] Ashcroft, N. W. & Mermin, N. D. *Solid State Physics* (Thomson Learning, 1976).

[132] Vaughan, J. C. *Two-Dimensional Ultrafast Pulse Shapign and its Application to Coherent Control and Spectroscopy.* Ph.D. thesis, Massachusetts Institute of Technology (2005).

[133] Gerchberg, R. W. & Saxton, W. O. A practical algorithm for the determination of the phase from image and diffraction plane pictures. *Optik* **35**, 237 (1972).

[134] Grier, D. G. A revolution in optical manipulation. *Nature* **424**, 810–816 (2003).

[135] Jesacher, A. Full phase and amplitude control of holographic optical tweezers with high efficiency. *Opt. Exp.* **16**, 4479–4486 (2008).

[136] Zhu, L. & Wang, J. Arbitrary manipulation of spatial amplitude and phase using phase-only spatial light modulators. *Sci. Rep.* **4**, 7441 (2014).

[137] Wen, P. *Correlated Exciton Dynamics in Semiconductor Nanostructures.* Ph.D. thesis, Massachusetts Institute of Technology (2013).

[138] Goodman, J. W. *Introduction to Fourier optics* (McGraw-Hill, New York, 2005).

[139] Turner, D. *Investigating Exciton Correlations Using Multidimensional Optical Spectroscopy.* Ph.D. thesis, Massachusetts Institute of Technology (2010).

[140] Nelsen, B. *et al.* Dissipationless flow and sharp threshold of a polariton condensate with long lifetime. *Phys. Rev. X* **3**, 041015 (2013).

[141] Askary, F. & Yu, P. Y. Exciton-polariton bottleneck and the thermalization of polariton luminescence in cds and cdse. *Phys. Rev. B* **31**, 6643–6653 (1985).

[142] Tassone, F., Piermarocchi, C., Savona, V., Quattropani, A. & Schwendimann, P. Bottleneck effects in the relaxation and photoluminescence of microcavity polaritons. *Phys. Rev. B* **56**, 7554–7563 (1997).

[143] Tartakovskii, A. *et al.* Relaxation bottleneck and its suppression in semiconductor microcavities. *Phys. Rev. B* **62**, R2283 (2000).

[144] Stevenson, R. M. *et al.* Continuous wave observation of massive polariton redistribution by stimulated scattering in semiconductor microcavities. *Phys. Rev. Lett.* **85**, 3680–3683 (2000).

[145] Baumberg, J. J. *et al.* Parametric oscillation in a vertical microcavity: A polariton condensate or micro-optical parametric oscillation. *Phys. Rev. B* **62**, R16247–R16250 (2000).

[146] Savvidis, P. G. *et al.* Angle-resonant stimulated polariton amplifier. *Phys. Rev. Lett.* **84**, 1547–1550 (2000).

[147] Savvidis, P. G. *et al.* Off-branch polaritons and multiple scattering in semiconductor microcavities. *Phys. Rev. B* **64**, 075311 (2001).

[148] Jacqmin, T. *et al.* Direct observation of dirac cones and a flatband in a honeycomb lattice for polaritons. *Phys. Rev. Lett.* **112**, 116402 (2014).

[149] Kim, N. Y. *et al.* Dynamical d-wave condensation of exciton-polaritons in a two-dimensional square-lattice potential. *Nat. Phys.* **7**, 681–686 (2011).

[150] Cerda-Méndez, E. A. *et al.* Polariton condensation in dynamic acoustic lattices. *Phys. Rev. Lett.* **105**, 116402 (2010).

[151] Cerda-Méndez, E. A. *et al.* Exciton-polariton gap solitons in two-dimensional lattices. *Phys. Rev. Lett.* **111**, 146401 (2013).

[152] Lai, C. W. *et al.* Coherent zero-state and [pi]-state in an exciton-polariton condensate array. *Nature* **450**, 529–532 (2007).

[153] Kim, N. Y., Kusudo, K., Loffler, A., nad A. Forchel, S. H. & Yamamoto, Y. exciton-polariton condensates near the dirac point in a triangular lattice. *New J. Phys.* **15**, 035032 (2013).

[154] Ferrier, L. *et al.* Interactions in confined polariton condensates. *Phys. Rev. Lett.* **106**, 126401 (2011).

[155] Galbiati, M. *et al.* Polariton condensation in photonic molecules. *Phys. Rev. Lett.* **108**, 126403 (2012).

[156] Abbarchi, M. *et al.* Macroscopic quantum self-trapping and josephson oscillations of exciton polaritons. *Nat. Phys.* **9**, 275–279 (2013).

[157] Sturm, C. *et al.* All-optical phase modulation in a cavity-polariton mach-zehnder interferometer. *Nat. Comm.* **5**, 3278 (2014).

[158] Tanese, D. *et al.* Fractal energy spectrum of a polariton gas in a fibonacci quasiperiodic potential. *Phys. Rev. Lett.* **112**, 146404 (2014).

[159] Sun, Y. *et al.* Phase boundaries of multi-mode and single-mode quantum states in exciton-polariton condensates. In preparation.

[160] Gao, T. *et al.* Observation of non-hermitian degeneracies in a chaotic exciton-polariton billiard. *Nature* **526**, 554–558 (2015).

[161] Gander, W., Golub, G. H. & Strebel, R. Least-squares fitting of circles and ellipses. *BIT Numer. Math.* **34**, 558–578 (1994).

[162] Szymańska, M. H., Keeling, J. & Littlewood, P. B. Nonequilibrium quantum condensation in an incoherently pumped dissipative system. *Phys. Rev. Lett.* **96**, 230602 (2006).

[163] Wouters, M. & Carusotto, I. Superfluidity and critical velocities in nonequilibrium bose-einstein condensates. *Phys. Rev. Lett.* **105**, 020602 (2010).

[164] Keeling, J. Superfluid density of an open dissipative condensate. *Phys. Rev. Lett.* **107**, 080402 (2011).

[165] Smith, R. P., Beattie, S., Moulder, S., Campbell, R. L. D. & Hadzibabic, Z. Condensation dynamics in a quantum-quenched bose gas. *Phys. Rev. Lett.* **109**, 105301 (2012).

[166] Butov, L. V. Solid-state physics: A polariton laser. *Nature* **447**, 540–541 (2007).

[167] Butov, L. V. & Kavokin, A. V. The behaviour of exciton-polaritons. *Nat. Photon.* **6**, 2 (2012).

[168] Deveaud-Pledran, B. The behaviour of exciton-polaritons. *Nat. Photon.* **6**, 205 (2012).

[169] Posazhennikova, A. Weakly interacting, dilute bose gases in 2d. *Rev. Mod. Phys.* **78**, 1111–1134 (2006).

[170] Holzmann, M., Baym, G., Blaizot, J.-P. & Laloe, F. Superfluidity transition of homogeneous and trapped two-dimensional bose gases. *Proc. Nat. Acad. Sci.* **104**, 1476 (2007).

[171] Berman, O. L., Lozovik, Y. E. & Snoke, D. W. Theory of bose-einstein condensation and superfluidity of two-dimensional polaritons in an in-plane harmonic potential. *Phys. Rev. B* **77**, 155317 (2008).

[172] Kasprzak, J., Solnyshkov, D. D., André, R., Dang, L. S. & Malpuech, G. Formation of an exciton polariton condensate: Thermodynamic versus kinetic regimes. *Phys. Rev. Lett.* **101**, 146404 (2008).

[173] Deng, H. *et al.* Quantum degenerate exciton-polaritons in thermal equilibrium. *Phys. Rev. Lett.* **97**, 146402 (2006).

[174] Deng, H., Weihs, G., Snoke, D. W., Bloch, J. & Yamamoto, Y. Polariton lasing vs. photon lasing in semiconductor microcavities. *Proc. Nat. Acad. Sci.* **100**, 15318 (2003).

[175] Richard, M., Kasprzak, J., Romestain, R., Andre, R. & Dang, L. S. Spontaneous coherent phase transition of polaritons in cdte microcavities. *Phys. Rev. Lett.* **94**, 187401 (2005).

[176] O'Hara, K. E. & Wolfe, J. P. Relaxation kinetics of excitons in cuprous oxide. *Phys. Rev. B* **62**, 12909 (2000).

[177] Snoke, D. W., Wolfe, J. P. & Mysyrowicz, A. Evidence for bose-einstein condensation of excitons in cu2o. *Phys. Rev. B* **41**, 11171 (1990).

[178] Dagvadorj, G. *et al.* Nonequilibrium phase transition in a two-dimensional driven open quantum system. *Phys. Rev. X* **5** (2015).

[179] Byrnes, T., Kim, N. Y. & Yamamoto, Y. Exciton-polariton condensates. *Nat. Phys.* **10**, 803–813 (2014).

[180] Dominici, L. *et al.* Real-space collapse of a polariton condensate. *Nat. Comm.* **6** (2015).

[181] Sanvitto, D. & Kéna-Cohen, S. The road towards polaritonic devices. *Nat. Mater.* (2016).

[182] Altman, E., Sieberer, L. M., Chen, L., Diehl, S. & Toner, J. Two-dimensional superfluidity of exciton polaritons requires strong anisotropy. *Phys. Rev. X* **5**, 011017 (2015).

[183] Voronova, N. S., Elistratov, A. A. & Lozovik, Y. E. Detuning-controlled internal oscillations in an exciton-polariton condensate. *Phys. Rev. Lett.* **115**, 186402 (2015).

[184] Wertz, E. *et al.* Spontaneous formation and optical manipulation of extended polariton condensates. *Nat. Phys.* **6**, 860–864 (2010).

[185] Hartwell, V. E. & Snoke, D. W. Numerical simulations of the polariton kinetic energy distribution in gaas quantum-well microcavity structures. *Phys. Rev. B* **82**, 075307 (2010).

[186] Eastham, P. R. & Littlewood, P. B. Finite-size fluctuations and photon statistics near the polariton condensation transition in a single-mode microcavity. *Phys. Rev. B* **73**, 085306 (2006).

[187] Yuen-Zhou, J., Saikin, S. K., Yao, N. Y. & Aspuru-Guzik, A. Topologically protected excitons in porphyrin thin films. *Nat. Mater.* **13**, 1026–1032 (2014).

[188] Verger, A., Ciuti, C. & Carusotto, I. Polariton quantum blockade in a photonic dot. *Phys. Rev. B* **73**, 193306 (2006).

[189] Liew, T. C. H. & Savona, V. Single photons from coupled quantum modes. *Phys. Rev. Lett.* **104**, 183601 (2010).

[190] Bamba, M., Imamoğlu, A., Carusotto, I. & Ciuti, C. Origin of strong photon antibunching in weakly nonlinear photonic molecules. *Phys. Rev. A* **83**, 021802 (2011).

[191] Besga, B. *et al.* Polariton boxes in a tunable fiber cavity. *Phys. Rev. Applied* **3**, 014008 (2015).

[192] Romanelli, M., Karr, J. P., Leyder, C., Giacobino, E. & Bramati, A. Two-mode squeezing in polariton four-wave mixing. *Phys. Rev. B* **82**, 155313 (2010).

[193] Oka, H. & Ajiki, H. Light squeezing via a biexciton in a semiconductor microcavity. *Phys. Rev. B* **83**, 045305 (2011).

[194] Boulier, T. *et al.* Polariton-generated intensity squeezing in semiconductor micropillars. *Nat. Comm.* **5** (2014).

[195] Ciuti, C. Branch-entangled polariton pairs in planar microcavities and photonic wires. *Phys. Rev. B* **69**, 245304 (2004).

[196] Portolan, S., Stefano, O. D., Savasta, S. & Savona, V. Emergent entanglement of microcavity polariton pairs. *J. Phys. Conf. Series* **210**, 012033 (2010).

[197] Liew, T. C. H. & Savona, V. Multipartite polariton entanglement in semiconductor microcavities. *Phys. Rev. A* **84**, 032301 (2011).

[198] Pagel, D., Fehske, H., Sperling, J. & Vogel, W. Strongly entangled light from planar microcavities. *Phys. Rev. A* **86**, 052313 (2012).

[199] Pagel, D., Fehske, H., Sperling, J. & Vogel, W. Multipartite entangled light from driven microcavities. *Phys. Rev. A* **88**, 042310 (2013).

[200] Pagel, D. & Fehske, H. Entangled light from driven dissipative microcavities. *Phys. Rev. A* **92**, 022342 (2015).

[201] Einkemmer, L., Vörös, Z., Weihs, G. & Portolan, S. Polarization entanglement generation in microcavity polariton devices. *Phys. Status Solidi B* **252**, 1749–1756 (2015).

[202] Vörös, Z., Snoke, D. W., Pfeiffer, L. & West, K. Direct measurement of exciton-exciton interaction energy. *Phys. Rev. Lett.* **103**, 016403 (2009).

[203] Ramsteiner, M. *et al.* Influence of composition fluctuations in al(ga)as barriers on the exciton localization in thin gaas quantum wells. *Phys. Rev. B* **55**, 5239–5242 (1997).

[204] Zhao, H., Moehl, S., Wachter, S. & Kalt, H. Hot exciton transport in znse quantum wells. *Appl. Phys. Lett.* **80**, 1391–1393 (2002).

[205] Akselrod, G. M., Tischler, Y. R., Young, E. R., Nocera, D. G. & Bulovic, V. Exciton-exciton annihilation in organic polariton microcavities. *Phys. Rev. B* **82**, 113106 (2010).

[206] Akselrod, G. M. *et al.* Visualization of exciton transport in ordered and disordered molecular solids. *Nat. Comm.* **5**, 3846 (2014).

[207] Prokof'ev, N., Ruebenacker, O. & Svistunov, B. Critical point of a weakly interacting two-dimensional bose gas. *Phys. Rev. Lett.* **87**, 270402 (2001).

[208] Prokof'ev, N. & Svistunov, B. Two-dimensional weakly interacting bose gas in the fluctuation region. *Phys. Rev. A* **66**, 043608 (2002).

[209] Snoke, D. W. *Solid State Physics: Essential Concepts* (Cambridge University Press, 2008).

[210] Zimmermann, R. Dynamical t-matrix theory for high-density excitons in coupled quantum wells. *Phys. Stat. Sol. (b)* **243**, 2358–2362 (2006).

[211] Ciuti, C., Savona, V. & Quattropani, A. Role of the exchange of carriers in elastic exciton-exciton scattering in quantum wells. *Phys. Rev. B* **58**, 7926 (1998).

[212] Pavlovic, G. *Exciton-polaritons in low dimensional structures.* Ph.D. thesis, Université Blaise Pascal - Clermont-Ferrand (2010).

[213] Askitopoulos, A. *et al.* Polariton condensation in an optically induced two-dimensional potential. *Phys. Rev. B* **88**, 041308 (2013).

[214] Takemura, N., Trebaol, S., Wouters, M., Portella-Oberli, M. T. & Deveaud, B. Polaritonic feshbach resonance. *Nat. Phys.* **10**, 500–504 (2014).

[215] Marchetti, F. M., Keeling, J., Szymańska, M. H. & Littlewood, P. B. Thermodynamics and excitations of condensed polaritons in disordered microcavities. *Phys. Rev. Lett.* **96**, 066405 (2006).

[216] Marchetti, F. M., Keeling, J., Szymańska, M. H. & Littlewood, P. B. Absorption, photoluminescence, and resonant rayleigh scattering probes of condensed microcavity polaritons. *Phys. Rev. B* **76**, 115326 (2007).

[217] Taylor, J. private communication.

[218] Snoke, D. Polariton condensation and lasing. In Timofeev, V. & Sanvitto, D. (eds.) *Exciton-Polaritons in Microcavities*, vol. 172 of *Springer Series in Solid State Sciences* (Springer, 2012).

[219] Manni, F., Lagoudakis, K. G., Liew, T. C. H., Andre, R. & Deveaud-Pledran, B. Spontaneous pattern formation in a polariton condensate. *Phys. Rev. Lett.* **107**, 106401 (2011).

[220] Askitopoulos, A. *et al.* Robust platform for engineering pure-quantum-state transitions in polariton condensates. *Phys. Rev. B* **92** (2015).

[221] McDonald, S. W. & Kaufman, A. N. Wave chaos in the stadium: Statistical properties of short-wave solutions of the helmholtz equation. *Phys. Rev. A* **37**, 3067–3086 (1988).

[222] Li, M., Zhang, B., Chen, K., Snoke, D. & Heberle, A. Noncircular refractive index profile and breakdown of mode degeneracy of vertical cavity surface emitting lasers. *IEEE J. Quant. Electron.* **48**, 1065–1068 (2012).

[223] Pedaci, F., GiuDici, M., Tredicce, J. R. & Giacomelli, G. Experimental analysis of mode-hopping in bulk semiconductor lasers. *Appl. Phys. B* **81**, 993 (2005).

[224] Roumpos, G. *et al.* Single vortex-antivortex pair in an exciton-polariton condensate. *Nat. Phys.* **7**, 129–133 (2011).

[225] Averkiev, N. S. & Glazov, M. M. Light-matter interaction in doped microcavities. *Phys. Rev. B* **76**, 045320 (2007).

[226] Baeten, M. & Wouters, M. Many-body effects of a two-dimensional electron gas on trion-polaritons. *Phys. Rev. B* **91**, 115313 (2015).

[227] Bardeen, J. Electron-vibration interactions and superconductivity. *Rev. Mod. Phys.* **23**, 261–270 (1951).

[228] Cooper, L. N. Bound electron pairs in a degenerate fermi gas. *Phys. Rev.* **104**, 1189–1190 (1956).

[229] Giustino, F., Cohen, M. L. & Louie, S. G. Small phonon contribution to the photoemission kink in the copper oxide superconductors. *Nature* **452**, 975–978 (2008).

[230] Little, W. A. Possibility of synthesizing an organic superconductor. *Phys. Rev.* **134**, A1416–A1424 (1964).

[231] Ginzburg, V. L. *On Superconductivity and Superfluidity* (Springer New York, 2009).

[232] Laussy, F. P., Kavokin, A. V. & Shelykh, I. A. Exciton-polariton mediated superconductivity. *Phys. Rev. Lett.* **104**, 106402 (2010).

[233] Liu, X. *et al.* Strong light-matter coupling in two-dimensional atomic crystals. *Nat. Photon.* **9**, 30–34 (2014).

[234] Ensher, J. R., Jin, D. S., Matthews, M. R., Wieman, C. E. & Cornell, E. A. Bose-einstein condensation in a dilute gas: Measurement of energy and ground-state occupation. *Phys. Rev. Lett.* **77**, 4984–4987 (1996).

[235] Baboux, F. *et al.* Bosonic condensation and disorder-induced localization in a flat band. *Phys. Rev. Lett.* **116**, 066402 (2016).

[236] Ryu, C. *et al.* Observation of persistent flow of a bose-einstein condensate in a toroidal trap. *Phys. Rev. Lett.* **99**, 260401 (2007).

[237] Andersen, M. F. *et al.* Quantized rotation of atoms from photons with orbital angular momentum. *Phys. Rev. Lett.* **97**, 170406 (2006).

[238] Ramanathan, A. *et al.* Superflow in a toroidal bose-einstein condensate: An atom circuit with a tunable weak link. *Phys. Rev. Lett.* **106**, 130401 (2011).

[239] Wright, K. C., Blakestad, R. B., Lobb, C. J., Phillips, W. D. & Campbell, G. K. Driving phase slips in a superfluid atom circuit with a rotating weak link. *Phys. Rev. Lett.* **110**, 025302 (2013).

[240] Beattie, S., Moulder, S., Fletcher, R. J. & Hadzibabic, Z. Persistent currents in spinor condensates. *Phys. Rev. Lett.* **110**, 025301 (2013).

[241] Leproux, P., Fevrier, S., Doya, V., Roy, R. & Pagnoux, D. Modeling and optimization of double-clad fiber amplifiers using chaotic propagation of the pump. *Opt. Fiber Technol.* **7**, 324–339 (2001).

[242] Kouznetsov, D. & Moloney, J. Boundary behavior of modes of dirichlet laplacian. *J. Mod. Opt.* **51**, 1955–1962 (2004).

[243] Liu, X. *et al.* Strong light-matter coupling in two-dimensional atomic crystals. *Nat. Photon.* **9**, 30–34 (2015).

[244] Dufferwiel, S. *et al.* Exciton–polaritons in van der waals heterostructures embedded in tunable microcavities. *Nat. Comm.* **6**, 8579 (2015).

[245] Yu, H., Wang, Y., Tong, Q., Xu, X. & Yao, W. Anomalous light cones and valley optical selection rules of interlayer excitons in twisted heterobilayers. *Phys. Rev. Lett.* **115**, 187002 (2015).

[246] Chernikov, A. *et al.* Exciton binding energy and nonhydrogenic rydberg series in monolayer ws_2. *Phys. Rev. Lett.* **113**, 076802 (2014).

[247] He, K. *et al.* Tightly bound excitons in monolayer wse$_2$. *Phys. Rev. Lett.* **113**, 026803 (2014).

[248] Ugeda, M. M. *et al.* Giant bandgap renormalization and excitonic effects in a monolayer transition metal dichalcogenide semiconductor. *Nat. Mater.* **13**, 1091–1095 (2014).

[249] Wang, G. *et al.* Giant enhancement of the optical second-harmonic emission of wse$_2$ monolayers by laser excitation at exciton resonances. *Phys. Rev. Lett.* **114**, 097403 (2015).

[250] Ye, Z. *et al.* Probing excitonic dark states in single-layer tungsten disulphide. *Nature* **513**, 214–218 (2014).

[251] Zhang, C., Johnson, A., Hsu, C.-L., Li, L.-J. & Shih, C.-K. Direct imaging of band profile in single layer mos2 on graphite: Quasiparticle energy gap, metallic edge states, and edge band bending. *Nano Lett.* **14**, 2443–2447 (2014).

[252] Zhu, B., Chen, X. & Cui, X. Exciton binding energy of monolayer ws2. *Sci. Rep.* **5**, 9218 (2015).

[253] Kumar, N. *et al.* Second harmonic microscopy of monolayer mos$_2$. *Phys. Rev. B* **87**, 161403 (2013).

[254] Li, Y. *et al.* Probing symmetry properties of few-layer mos2 and h-bn by optical second-harmonic generation. *Nano Lett.* **13**, 3329–3333 (2013).

[255] Malard, L. M., Alencar, T. V., Barboza, A. P. M., Mak, K. F. & de Paula, A. M. Observation of intense second harmonic generation from mos$_2$ atomic crystals. *Phys. Rev. B* **87**, 201401 (2013).

[256] Seyler, K. L. *et al.* Electrical control of second-harmonic generation in a wse2 monolayer transistor. *Nat. Nano.* **10**, 407–411 (2015).